The Dynamical Structure Functions of Strongly Coupled Binary Charged Systems

Luciano Germano Silvestri

A dissertation

submitted to the Faculty of

the department of Physics

in partial fulfillment

of the requirements

for the degree of

Doctor of Philosophy

Boston College

Morrissey College of Arts and Sciences

Graduate School

March 2019

The Dynamical Structure Functions of Strongly Coupled Binary Charged Systems

Luciano Germano Silvestri

Advisor: Prof. Gabor J. Kalman, D.Sc.

ABSTRACT

Mixtures of charged particles, where the components have different charge numbers (Z_A), masses (m_A) and densities (n_A), with $A = 1, 2$ denoting the components, occur in Nature in a great variety. To be sure, even the simplest plasmas are necessarily multicomponent systems, consisting of negative and positive charges. This feature is, however, obscured within the centrally important and popular OCP (one component plasma) or jellium models, where the role of one of the components is reduced to providing a neutralizing background. When this background is inert, one is led to the Coulomb OCP model, while when the background is polarizable (such as an electron gas surrounding heavy particles), to a Yukawa OCP (YOCP), with a screened Yukawa potential replacing the Coulomb potential between the dynamically active particles. There are, however situations of physical importance, where the OCP description is inadequate and a genuine two component description of a plasma composed of two species is required.

This Thesis focuses on the study of the dynamics of many-body systems consisting of two components of like charges (all the Z_A-s being of the same signature) in a neutralizing background. The methodology is based upon parallel attacks through theoretical analysis and Molecular Dynamics (MD) simulations, the latter yielding the capability of instant verification of the former. The investigation involves the study of the partial (*i.e.* species by species) structure functions

$S_{AB}(\mathbf{k},\omega)$ and current-current correlation functions $L_{AB}(\mathbf{k},\omega)$. The Fluctuation–Dissipation Theorem (FDT) connects these quantities to the total and partial response functions $\chi_{AB}(\mathbf{k},\omega)$ (matrices in species space), which are instrumental in the description of the collective mode excitations of the system. This analysis has revealed an entirely novel feature: both $S_{11}(\mathbf{k},\omega)$ and $S_{22}(\mathbf{k},\omega)$ exhibit very sharp and deep (several orders of magnitude) minima in the strongly coupled liquid phase at robust characteristic frequencies of the system, which are virtually coupling independent. The FDT then demands that these anti-resonances show up as well in the imaginary part of the partial density response function $\chi_{AB}(\mathbf{k},\omega)$. Our theoretical analysis, based on the Quasi-Localized Charge Approximation (QLCA), has confirmed that this is indeed the case. These anti-resonant frequencies being related to the dissipative part of the response, require a physical description of the principal source of dissipation. This has been identified as the inter-species momentum transfer, governed by drag between the microscopic current fluctuations of the two species. The description of this effect was incorporated in the QLCA formalism, making it possible to derive a closed analytic representation of the fluctuation spectra in the frequency domain of interest and compare them with the results of the MD simulations. Other important novel concepts, such as the idea of coupling dependent effective mass, fast vs. slow sound, the mechanism of transition from short-range to long-range interaction have been identified and analyzed. Furthermore, the investigation of the dynamics has led to the first comprehensive description of the mode structures of classical binary Coulomb and Yukawa mixtures at arbitrary coupling values, which has been a longstanding problem in statistical plasma physics. Focusing on the longitudinal excitations, we describe the transition from weak coupling (where one is acquainted with the RPA result yielding only the single plasmon mode in the Coulomb case or a single acoustic mode in the Yukawa case) to strong coupling, with a doublet of modes that arise

from the complex relative motion between the two components, as affected by the interaction with the background.

ACKNOWLEDGEMENTS

The completion of this Ph.D. is due to the invaluable help of the people around me.

First on the list are the people closest to me: mom and dad, Pina and Elpidio, my brother Stefano, my uncle Secondo, partner Heather S. Fagnant, and true friend Konstadin Alargov for their unconditional love and unwavering support.

Next I thank my advisor Prof. Gabor J. Kalman who I admire for his incredible intellect and for bestowing upon me the ability to identify the fundamental physical principles of complex systems. The never ending group meetings proved invaluable to the formation of deep theoretical insights necessary for my scientific career.

Prof. Baldassare Di Bartolo holds a special place in this list. He treated me like his son and taught me more about being human and a good person than anybody else. His teaching on morality, faith, and modesty are the true Christian Principles on which Boston College claims to be founded. In addition, I thank him for giving me the opportunity of being part of his Erice team. I want to thank both Gabor and Rino for trying to teach me humility.

I want to thank the Hungarian team of the Wigner Research Centre: Dr. Zoltán Donkó, Peter Hartmann, and Ihor Korolov, for hosting me in the summer of 2015 to learn Molecular Dynamics simulations. I thank them also for providing the simulations data presented in this Thesis.

I thank my fellow graduate student Hong Pan, Prof. Kenneth I. Golden, from Uni-

versity of Vermont, Hanno Kählert from Christian–Albrechts–Universität in Kiel, Germany, Prof. Marlene Rosenberg, from University of California San Diego, USA, for the fruitful discussions about the physics of plasmas.

I thank the organizing committees of the Physics of Non–Ideal Plasmas (PNP), and the Strongly Coupled Coulomb Systems (SCCS) conferences in 2014 and 2017, especially Prof. Michael Bonitz, from Christian–Albrechts–Universität, for inviting me as a speaker in 2017.

I would like to thank my Thesis Defense Committee: Prof. Kevin Bedell, Prof. Krzystof Kempa, Prof. Baldassare Di Bartolo, Dr. Zoltán Donkó, and Prof. Kenneth I. Golden. Last, but not least, I want to thank the administrative staff of the Physics Dept.: Jane Carter, Nancy Chevry, Sile Ni Scanlain, and Scott Bortolotto for always being so kind and understanding.

TABLE OF CONTENTS

LIST OF FIGURES

Figure

LIST OF TABLES

Table

Nomenclature

$\bar{\chi}_{AB}(\mathbf{k},\omega)$ Partial Total (or Proper) Density Response Function aka Partial Polarization Function

$\bar{\Phi}_A(\mathbf{k},\omega)$ Total Perturbation Potential

$\breve{\Phi}_A(\mathbf{k},\omega)$ Partial Polarization Potential

$\chi^0_A(\mathbf{k},\omega)$ Vlasov Polarization Function of species A

Γ Coupling Parameter

$\hat{\chi}_{AB}(\mathbf{k},\omega)$, $\chi_{AB}(\mathbf{k},\omega)$ Partial External Density Response Function

$\hat{\Phi}_A(\mathbf{k},\omega)$, $\Phi_{AB}(\mathbf{k},\omega)$ Partial External Perturbation Potential

$\hbar$ Reduced Planck constant

$\omega_{*,A}$ Silvestri–Kalman frequency of species A

$\omega_{\pm}$ Eigenvalues/Collective modes. The $\pm$ subscripts indicate whether the particles are in–phase or out–of–phase respectively.

ω_{im} Important Silvestri–Kalman frequency

ω_{vaa} Virtual Average Atom frequency, aka Hydrodynamic frequency

$\Omega_{AB}/\sqrt{3}$ Einstein frequency of species A

ω_A Plasma frequency of species A

$\phi(k)$ Fourier Transform of the interaction potential

$\phi_{AB}(k) = Z_A Z_B \phi(k)$ Fourier Transform of the interaction potential between species A and B

$\varepsilon_{AB}(\mathbf{k}, \omega)$ Elements of the Dielectric Response Matrix

$c = c_1$ Concentration of Species 1

$L_{AB}(\mathbf{k}, \omega)$ Partial Longitudinal Microscopic Velocity Correlation Function

$m = m_2/m_1$ Mass ratio between the two species

$n = n_2/n_1$ Number density ratio between the two species

$S_{AB}(\mathbf{k}, \omega)$ Partial Dynamical Structure Function (DSF)

$Z = Z_2/Z_1$ Charge ratio between the two species

acoustic mode collective mode with linear dispersion $\omega(k \to 0) sk$

BIM Binary Ionic Mixture

DSF Dynamical Structure Function

FDT Fluctuation–Dissipation Theorem

MD Molecular Dynamics

OCP One Component Plasma

plasmon collective mode with finite frequency at $k = 0$

QLCA Quasi–Localized Charge Approximation

quasi–acoustic mode collective mode with square root dispersion $\omega(k \to 0) s\sqrt{k}$

RPA Random Phase Approximation

YBM Yukawa Binary Mixture

YOCP Yukawa One Component Plasma

CHAPTER I

Introduction

Plasma has a very broad definition, in the words of Harold Grad "A plasma is any electrically conducting medium whose electrical properties are sufficiently pronounced to react back on an external field. There is no end of materials that fit this description." (Grad, 1969). It is in the same of article that he coins the famous phrase that 99% of matter in the universe is in the plasma state. Another well known definition of plasma is the "Fourth State of Matter" and has been known as such since the beginning of the 19^{th} century (Jones, 1870). The Fourth place, with the first three being solid, liquid, and gas, is due to the observation that a gas heated to very high temperatures exhibits new interesting properties. Early researchers suggested that these systems were "the ultimate result of gaseous expansion" (Crookes, 1880; Crookes, 1879), *e.g.* a state in which the constituent particles are free and don't collide with each other. In technical terms, the mean free path of the particles is much longer that the size of the containing volume. This idea of a collisionless system was not too far fetched as it was shown in the following century by Vlasov. Concomitantly with the discovery of these new systems was the development of electromagnetic theory which lead to question the nature of these systems. Where they composed of matter or a manifestation of the aether? It can be said that the conclusive answer was presented by J. J. Thompson

in 1897 who demonstrated that cathode rays were a collection of electrical particles and as such subject to electric and magnetic fields (Thomson, 1897). Thus, by the end of the 19^{th} plasmas had obtained the definition given by Grad, but not their name yet. The word "plasma", in fact, was still used in connection to blood and it was Nobel Laureate Irwing Langmuir in 1929 who instead used it to denominate many-body systems of charged particles (Tonks, 1967).

1.1 Background: The One Component Plasma

Although, plasmas are necessarily multi-component systems composed by at least by two types of particles distinguished by their charge, their behavior, can, to first approximation, be described as a single component system. The simplest example is that of metals where the large mass difference between ions and electrons allows one to consider the dynamics of only one of the two while the other one is reduced to providing a neutralizing background. This model is commonly referred to as the One Component Plasma (OCP) if the dynamical particles are the ions, or "jellium" in the case of electrons.

Furthermore, plasmas are classified based on the strength of the interaction between the constituent particles. The coupling parameter is defined as the ratio of the average potential energy over the average kinetic energy of the particles and it is indicated by Γ (see below for the defining equation). Plasma with $\Gamma \ll 1$ are considered weakly coupled, $\Gamma \sim 1$ moderately coupled and $\Gamma > 10$ strongly coupled. Therefore, we have that plasmas at high temperatures and low number densities, as those produced in laboratory environments and in the sky during aurora borealis, are considered weakly coupled, while those with large number densities, as those found in the core of white dwarfs or the crust of neutron stars, are strongly coupled.

The OCP model has been a favourite of statistical physics for its defining characteristic: the long-range interaction between particles. The prominent properties of the OCP have been uncovered during the past decades via both theoretical and numerical studies (Baus and Hansen, 1980). The thermodynamic properties, pair correlations and the onset of crystallization of the system at a high coupling were first studied by Brush *et al.* using Monte Carlo simulations (Brush, Sahlin, and Teller, 1966). The crytallization temperature (coupling) has been refined in subsequent studies (e.g. (Slattery, Doolen, and DeWitt, 1980; Stringfellow, DeWitt, and Slattery, 1990)) that came up with values converging to $\Gamma_{\rm c} \cong 175$. Equilibrium, transport, and dynamical characteristics of the OCP have been investigated by Hansen *e*t al. in a series of Monte Carlo and Molecular Dynamics (MD) simulations (Hansen, 1973; Pollock and Hansen, 1973; Hansen, McDonald, and Pollock, 1975). Further advancements of computational resources has allowed for a more accurate determination of the above mentioned quantities and recent high performance computations provided accurate data for the self-diffusion coefficient (Daligault, 2012) and the shear viscosity (Daligault, Rasmussen, and Baalrud, 2014). Besides these, computer simulations have also given access to studies of the behavior of individual particles. In particular, the "caging", or "quasi–localization", of the particles was identified and quantified by Donkó and collaborators in early 2000 (Donkó, Kalman, and Golden, 2002; Donkó, Hartmann, and Kalman, 2003). Daligault subsequently connected this behavior to particle diffusion and showed that it is the root of some of the properties of the OCP in the liquid phase at Γ values exceeding ~ 50 (Daligault, 2006).

While all these studies have been motivated by the understanding of the strongly coupled ($\Gamma > 10$) domain, studies of the dynamical properties of plasmas were, actually, started much earlier, with the research by Lewi Tonks and Irving Langmuir (Tonks and Langmuir, 1929), who observed that the electron density, in a

low ionization degree plasma (which corresponds to an OCP with $\Gamma \to 0$), undergoes oscillations just like an harmonic oscillator with a characteristic frequency (the "plasma frequency"). This discovery presented interesting challenges from a theoretical perspective since these new phenomenon could not be explained by kinetic theory of gases. Only ten years after Tonks and Langmuir discovery Anatoly A. Vlasov showed that plasma particles are better described by a collisionless Boltzmann equation with an effective force created by the average electric field. The long range character of the Coulomb potential is the crucial element for the finite frequency density oscillations at infinite wavelengths (Vlasov, 1938; Vlasov, 1967). The importance of Vlasov intuition can only be understated because since then force will be classified as long-range or short-range.

The collisionless picture was later completed by the mathematical genius of Lev D. Landau, who showed that the plasma oscillations are damped by particle-wave interaction, the so called Landau damping. The idea to associate plasma oscillations with "collective excitations" was proposed by Bohm, Gross and Pines (Bohm and Gross, 1949a; Bohm and Gross, 1949b; Pines and Bohm, 1952; Bohm and Pines, 1953), and it was also Bohm and Gross (BG) (Bohm and Gross, 1949a; Bohm and Gross, 1949b) who determined the wave number (k) dependent positive dispersion of such oscillation ("plasmon"), caused by the thermal motion of the particles.

The first reliable results for the collective excitations in the strongly coupled domain were obtained by MD simulations of Hansen *et al.* (Hansen, McDonald, and Vieillefosse, 1979), who also verified the change of the positive slope of the dispersion curve at low coupling to a negative slope, the hallmark phenomenon of strong coupling which was already predicted theoretically (Kalman, Kempa, and Minella, 1991; Felde, Sprösser-Prou, and Fink, 1989; Singwi, Sjölander, et al., 1969; Vashishta and Singwi, 1972).

In conclusion, the OCP model and its short range couterpart, the nominal Yukawa

OCP, have been extensively studied and most of the interesting physics has been addressed. The Yukawa OCP, in particular, has seen a resurrection in recent years due to the wealth of experimentally available systems that can be modeled by it. Some of the most important are Ultracold Neutral Plasmas (UNP) (Killian et al., 2007; Strickler et al., 2016), Complex "Dusty" Plasmas (Merlino and Goree, 2004; Fortov et al., 2005; Morfill and Ivlev, 2009), and Warm Dense Matter (WDM) (Glenzer, Landen, et al., 2007; Glenzer and Redmer, 2009; Murillo, 2010; Gericke et al., 2010; Höll et al., 2004; Murillo, 2010; Thiele et al., 2008).

1.2 Binary Mixtures

Binary Mixtures, *i.e.* plasmas composed by two positive ions species and a negative electron background, are still an open research field. The most important example of strongly coupled plasmas are found in astrophysical systems. The core of white dwarfs is thought to be a mixture of completely ionzed Carbon and Oxygen atoms (Bildsten and Hall, 2001; Horowitz, Schneider, and Berry, 2010; Schneider et al., 2012; Hughto et al., 2012; Giammichele et al., 2018), the outer layer of the crust and the ocean of the neutron star are a multi-ion strongly coupled plasma surrounded by an ultrarelativistic degenerate electron gas (Brown, 2000; Peng, Brown, and Truran, 2007). Hence an investigation of the dynamics of plasma mixtures is in need. Furthermore, as it will be shown in this thesis, such systems exhibit novel physical effects, which have no equivalent in OCP systems. On the static equilibrium level, the issues of *a*) miscibility of the different components as functions of the various system parameters and of the temperature, *b*) competing liquid-solid phase transitions, *c*) the existence of ordered phases and *d*) the behavior of disordered phases *e*) thermodynamics and transport properties are in the forefront of interest (DeWitt, 1994; Igarashi and Iyetomi, 2003; Igarashi, Nakao, and Iyetomi, 2001; Ichimaru, Iyetomi, and Ogata, 1988). The latter is of

special interest as stages of inertial confinement fusion are considered strongly coupled and a precise determination of transport properties is necessary for the achievement of ignition (Atzeni and Meyer-ter-Vehn, 2004; Haxhimali et al., 2014; Haxhimali et al., 2015; Whitley et al., 2015; Stanton and Murillo, 2016; Ticknor et al., 2016; Diaw and Murillo, 2016).

On the dynamical level research has focused on the matrix of partial dynamic structure function (DSF) $S_{AB}(\mathbf{k},\omega)$ and its longitudinal and transverse current correlation counterparts $L_{AB}(\mathbf{k},\omega)$ and $T_{AB}(\mathbf{k},\omega)$. The frequency spectrum of strongly coupled binary mixtures has been a longstanding problem in statistical plasma physics. At weak coupling one is acquainted with the Vlasov result that yields the combination of the plasma frequencies of the two ionic species. Early MD simulations on binary Coulomb mixtures, performed by Hansen et al. (Hansen, McDonald, and Vieillefosse, 1979) showed that at strong coupling the longitudinal spectrum was again governed by one collective mode shifted to higher frequencies than the low coupling value. The observed higher frequency was initially identified as the hydrodynamic plasma frequency, *i.e.* the plasma frequency obtained by the average charge and average mass of the two components. Baus (Baus, 1977a; Baus, 1977b; Baus, 1977c; Baus, 1978), instead, suggested that the shift was due to a term proportional to the coupling parameter. However, in both cases discrepancies between MD and theory were observed. On the other hand Kalman and Golden proposed that the spectrum was characterized by two plasmon modes that arises from the complex relative motion between the two components (Kalman and Golden, 1990; Golden and Kalman, 2000; Golden and Kalman, 2001). The predicted high frequency mode showed good agreement with simulations, but the absence of the second low frequency mode cast doubt on the entire formulation. The existence of this mode was only recently confirmed by MD simulations (Kalman, Donkó, et al., 2014). In this same work Kalman

et al. suggested that the low frequency mode comes from the acoustic mode of a binary mixture whose particles interact via a short–range potential. They argued that as the long range interaction is turned on the acoustic mode acquires a mass by means of the Anderson mechanism (Anderson, 1963) to become the low frequency plasmon observed in binary Coulomb mixtures. How the low coupling single plasma frequency morphs into the strong coupling doublet as the system moves as a function of the increasing coupling parameter Γ, from the gaseous to the strongly coupled liquid phase, remains an intriguing question.

We arrive, then, at the topic of this thesis: the study of the Dynamical Structure Functions of Binary plasma mixtures via theoretical models and computer simulations. The rest of the Thesis is structured as follows: in the rest of this introductory Chapter I define the relevant parameters and equations used throughout the Thesis. The Chapter is concluded with Sec. 1.5 in which I give a brief description of the computational methods. The next Chapter introduces in more details the main theoretical model and its extension to address the dissipation in strongly coupled binary mixtures. Theory and simulations results are then presented for three systems: Binary mixtures of charged particles interacting via a Coulomb potential (BIM) in Chap. III, binary mixtures of charged particles interacting via a Yukawa potential (YBIM) in Chap. IV, and mass-asymmetric electronic bilayers in Chap. VI.

1.3 Definition of Parameters

Consider a plasma composed of two species of ions, $N = N_1 + N_2$ with charge number Z_A, masses m_A enclosed in a volume V, total density $n_0 = N/V$. The ions are surrounded by a rigid negative background that ensures charge neutrality $Z_1 e n_1 + Z_2 e n_2 - e n_e = 0$, with $e > 0$ being the electric charge and n_e the density. The concentrations of each species are given by $c_A = N_A/N$. The average of a

physical parameter, $\mathcal{O}$, is indicated by $\langle \mathcal{O}^{\alpha} \rangle = \sum_A \mathcal{O}_A^{\alpha} c_A$. The average charge number is

$$Z_{av} = \langle Z \rangle = Z_1 c_1 + Z_2 c_2, \tag{1.1}$$

average mass

$$m_{av} = \langle m \rangle = m_1 c_1 + m_2 c_2. \tag{1.2}$$

The entire system is at equilibrium temperature T ($\beta = 1/(k_B T)$). The Debye length and of ion species A

$$\lambda_{D,A} = \sqrt{4\pi n_A \beta}, \quad \mu_A = (\lambda_{D,A})^{-1} \tag{1.3}$$

The plasma parameter is defined as the number of particles in a Debye sphere. In the case of an OCP/electron gas it is denoted by

$$\Lambda = \frac{4\pi}{3} n_e \lambda_D^3, \tag{1.4}$$

[1] Plasmas with many particles within the Debye sphere, $\Lambda \gg 1$, are considered weakly coupled while plasmas with $\Lambda \ll 1$, with a Debye sphere sparsely populated, are considered strongly coupled. This idea is readily extended to binary mixture where

$$\Lambda_B = \frac{(\mu_1^2 + \mu_2^2)^{3/2}}{4\pi n_0}. \tag{1.5}$$

The above definitions are mostly used in the weakly coupled plasma literature since λ_D is the relevant length scale. When the correlations between particles become dominant, instead, the Ion–Sphere model proposed by Edwin Salpeter, in his work on nuclear reactions in the interior of stars, becomes more appropriate (Salpeter, 1954). In this case positive ions, strongly repel each other so to create

[1] In old literature the letter γ is used instead of Λ. However, I will use γ for describing collisional damping later on. Ichimaru uses N_D in his textbook (Ichimaru, 2004a).

a region around themselves where no other ion can be found, *e.g.* they create a *Coulomb hole*. The relevant length scale becomes then the average interparticle distance, aka the Wigner-Seitz (WS) radius, which, in the case of ions, we define as

$$a^3 = \frac{3}{4\pi n_0}, \tag{1.6}$$

and in the case of electrons as

$$a_e^3 = \frac{3}{4\pi n_e}. \tag{1.7}$$

. Using the above equation we define the ion coupling parameter of species A as

$$\Gamma_A = \frac{(Z_A e)^2 \beta}{a_A}, \quad a_A^3 = \frac{3}{4\pi n_A}. \tag{1.8}$$

The effective coupling parameter of the mixture is then given by an average of the single species coupling parameters

$$\Gamma_{\text{eff}} = c_1 \Gamma_1 + c_2 \Gamma_2, \tag{1.9}$$

which, by rewriting $a_A = a \left(Z/Z \left\langle Z \right\rangle\right)^{1/3}$, leads to

$$\Gamma_{\text{eff}} = \left\langle Z^{5/3} \right\rangle \left\langle Z \right\rangle^{1/3} \Gamma_{\text{ion}} \tag{1.10}$$

where

$$\Gamma_{\text{ion}} = \frac{e^2 \beta}{a}. \tag{1.11}$$

In order to be complete the we give the relation between Λ_B and Γ_{ion}

$$\Lambda_B = \frac{(3\Gamma_{\text{ion}})^{3/2}}{3}. \tag{1.12}$$

The coupling parameter $\Gamma_{\rm ion}$ is the parameter used in the computer simulations presented in this Thesis. The above equations show that $\Gamma_{\rm ion} < \Gamma_{\rm eff}$, however, this difference does not play an important role for the purpose of this research because the computer simulations span a wide range of parameters. The purpose of this research is to study the strong coupling effects on the mixture's dynamics and not the determination of a critical value of the coupling parameter, Γ_c.
The electron coupling parameter is defined similarly as

$$\Gamma_e = \frac{e^2}{a_e k_B T} = \langle Z \rangle^{1/3} \Gamma_{\rm ion}. \tag{1.13}$$

However, a more appropriate coupling parameter for the electrons is

$$r_s = a_e/a_0 \tag{1.14}$$

where $a_0 = \hbar^2/(m_e e^2)$ is the Bohr radius. This parameter depends entirely on the electron density; high (low) electron density leads to $r_s \ll 1$ ($r_s \gg 1$) and the electrons are considered weakly (strongly) coupled. For the sake of completeness we define Fermi wavenumber

$$k_F = \left(3\pi^2 n_e\right)^{1/3}, \tag{1.15}$$

the electron degeneracy parameter

$$\Theta = \frac{k_B T}{E_F}, \quad E_F = \frac{\hbar^2 k_F^2}{2m_e}, \tag{1.16}$$

and the relativistic parameter

$$x_F = \frac{\hbar k_F}{m_e c}. \tag{1.17}$$

Electron liquids with $\Theta \ll 1$ indicate a completely degenerate quantum electron gas in which the thermal deBroglie wavelength is much greater than the mean interparticle distance (*i.e.* the electrons' wavefunctions overlap over large distances). The relativistic parameter indicate whether the electrons have to be considered relativistic $x_F \approx 1$ or not $x_F \ll 1$. This parameter is usually found in astrophysical systems where the large mass of stars implies a high electron density hence $x_F \approx 1$. In particular, white dwarfs close to the Chandrasekar limit reach $x_F > 1$ and in this case the electrons become ultrarelativistic. In the limit $x_F \to \infty$ the coupling parameter $r_s \to e^2/\hbar c \simeq 1/137$ (Hartmann, Kalman, et al., 2009). The electrons in the mixtures considered in this Thesis form a completely relativistic degenerate quantum gas *i.e.* $r_s \ll 1$, $\theta \ll 1$, $x_F \approx 1$, therefore we neglect electron–ion interaction.

1.4 Statistical Mechanics Background

In this section we give formulas for the calculation of the relevant quantities. Neglecting the effects of the electronic background the ion-ion interaction Hamiltonian is

$$H_{ii} = \frac{1}{2V} \sum_{k \neq 0} \phi(k) \left[\rho(\mathbf{k}) \rho(-\mathbf{k}) - N \left\langle Z^2 \right\rangle \right] \tag{1.18}$$

where

$$\rho(\mathbf{k}) = \sum_A Z_A n_A(\mathbf{k}), \tag{1.19}$$

is the charge density operator and

$$\phi(k) = \frac{4\pi e^2}{k^2} \tag{1.20}$$

the Fourier transform of the Coulomb interaction. The number density operator of each ion species is

$$n_A(\mathbf{r},t) = \sum_i^{N_A} \delta[\mathbf{r} - \mathbf{x}_i(t)], \quad n_A(\mathbf{k}) = \sum_i^{N_A} e^{-i\mathbf{k}\cdot\mathbf{x}_i(t)} \tag{1.21}$$

and respective perturbation from the equilibrium density $n_A = N_A/V$

$$\delta n_A(\mathbf{r},t) = n(\mathbf{r},t) - n_A, \quad \delta n_A(\mathbf{k},t) = n_A(\mathbf{k},t) - N_A\delta_{\mathbf{k}}, \tag{1.22}$$

and $\delta_{\mathbf{k}}$ the Kronecker delta.

The focus of this research is on the species matrix of partial Dynamical Structure Functions, $S_{AB}(\mathbf{k},\omega)$. These are calculated from the Fourier transform of the density correlation functions

$$S_{AB}(\mathbf{k},\omega) = \frac{1}{\sqrt{n_A n_B}} \frac{1}{2\pi} \int d\tau \int d\mathbf{r} \, \langle n_A(\mathbf{x}+\mathbf{r}, t+\tau) n_B(\mathbf{x},t)\rangle \, e^{-i\mathbf{k}\cdot\mathbf{r}} e^{i\omega\tau}, \tag{1.23}$$

where the brackets $\langle\cdot\rangle$ indicate an ensemble average with the unperturbed Hamiltonian of eq. 1.18. The static structure functions are calculated by integrating over the entire frequency spectrum

$$S_{AB}(\mathbf{k}) = \int_{-\infty}^{\infty} d\omega S_{AB}(\mathbf{k},\omega), \tag{1.24}$$

which is related to the pair correlation function $h_{AB}(k)$

$$\begin{aligned} S_{AB}(\mathbf{k}) &= \frac{1}{\sqrt{N_A N_B}} \langle n_A(\mathbf{k}) n_B(-\mathbf{k})\rangle & (1.25)\\ &= \delta_{AB} + \sqrt{n_A n_B} h_{AB}(k). & (1.26) \end{aligned}$$

$h_{AB}(k)$ is the Fourier transform of the pair correlation function $h_{AB}(r) = g_{AB}(r) - 1$. Notice that $S_{AB}(\mathbf{k}, \omega)$ and $S_{AB}(\mathbf{k})$ have been defined with respect to particles numbers N_A and not the total number N, as found in textbooks Hansen and McDonald, 2013; Ichimaru, 2004a; Ichimaru, 2004b. The reason for this is because eqs. (1.23)–(1.26) are what is calculated in computer simulations.

$S_{AB}(\mathbf{k}, \omega)$'s and their static counterparts are proportional to the differential cross-section obtained from inelastic scattering experiments (Hansen and McDonald, 2013). In a mixture, scattering experiments are unable to distinguish between particles species and give information about the entire liquid. Fortunately, linear combinations of the partial DSF lead to total DSF. The charge density

$$S_{ZZ}(\mathbf{k}, \omega) = \langle \rho(\mathbf{k}, \omega) \rho(-\mathbf{k}, \omega) \rangle / N \tag{1.27}$$

can be rewritten as

$$S_{ZZ}(\mathbf{k}, \omega) = Z_1^2 c_1 S_{11}(\mathbf{k}, \omega) + Z_2^2 c_2 S_{22}(\mathbf{k}, \omega) + 2 Z_1 Z_2 \sqrt{c_1 c_2} S_{12}(\mathbf{k}, \omega), \tag{1.28}$$

the mass density as

$$S_{MM}(\mathbf{k}, \omega) = m_1^2 c_1 S_{11}(\mathbf{k}, \omega) + m_2^2 c_2 S_{22}(\mathbf{k}, \omega) + 2 m_1 m_2 \sqrt{c_1 c_2} S_{12}(\mathbf{k}, \omega). \tag{1.29}$$

In particular, the normalized charge density structure factor as

$$\tilde{S}_{ZZ}(\mathbf{k}) = \frac{1}{N \langle Z^2 \rangle} \langle \rho(\mathbf{k}) \rho(-\mathbf{k}) \rangle \tag{1.30}$$

$$= \frac{1}{N \langle Z^2 \rangle} \sum_{A,B} Z_A Z_B \sqrt{c_A c_B} S_{AB}(\mathbf{k}) \tag{1.31}$$

in the long-wavelength limit has to behave as

$$\tilde{S}_{ZZ}(\mathbf{k}) = \frac{k^2}{\mu_1^2 + \mu_2^2} + O(k^4) = \frac{(ka)^2}{3\Gamma \langle Z^2 \rangle} + O(k^4). \tag{1.32}$$

This follows from charge neutrality and perfect screening condition [2] (Hansen, McDonald, and Vieillefosse, 1979; Baus and Hansen, 1980).

In the case of Binary Yukawa Mixtures we will also consider the total DSF

$$S_{NN}(\mathbf{k}, \omega) = c_1 S_{11}(\mathbf{k}, \omega) + c_2 S_{22}(\mathbf{k}, \omega) + 2\sqrt{c_1 c_2} S_{12}(\mathbf{k}, \omega). \tag{1.33}$$

and concentration DSF

$$S_{CC}(\mathbf{k}, \omega) = c_1 c_2 \left[c_2 S_{11}(\mathbf{k}, \omega) + c_1 S_{22}(\mathbf{k}, \omega) - 2\sqrt{c_1 c_2} S_{12}(\mathbf{k}, \omega) \right] \tag{1.34}$$

as suggested by (Bhatia and Thornton, 1970; Bhatia and Thornton, 1971; Bhatia, Thornton, and March, 1974).

Additionally, we define the correlation function of the longitudinal microscopic velocities as

$$L_{AB}(\mathbf{k}, \omega) = \langle V_A^{(L)}(\mathbf{k}, \omega) V_B^{(L)}(\mathbf{k}, \omega) \rangle \,, \tag{1.35}$$

and transverse microscopic currents

$$T_{AB}(\mathbf{k}, \omega) = \langle V_A^{(T)}(\mathbf{k}, \omega) V_B^{(T)}(\mathbf{k}, \omega) \rangle \,, \tag{1.36}$$

where

$$V_A^{(L)}(\mathbf{k}, t) = \sum_i^{N_A} \mathbf{k} \cdot \mathbf{v}_i e^{-i\mathbf{k}\cdot\mathbf{x}_i(t)}, \quad V_A^{(T)}(\mathbf{k}, t) = \sum_i^{N_A} \mathbf{k} \times \mathbf{v}_i e^{-i\mathbf{k}\cdot\mathbf{x}_i(t)}. \tag{1.37}$$

[2] any external charge introduced in the plasma will be completely screened at large distances

From the above equations and the continuity equation for the number density we find the relations between $L_{AB}(\mathbf{k},\omega)$ and $S_{AB}(\mathbf{k},\omega)$

$$L_{AB}(\mathbf{k},\omega) = \frac{\omega^2}{k^2} S_{AB}(\mathbf{k},\omega). \tag{1.38}$$

For the sake of completeness we mention another important quantity used in the study of liquids is the velocity auto–correlation function for species A

$$Z_A(t) = \langle \mathbf{v}_A(t) \cdot \mathbf{v}_A(0) \rangle \,, \tag{1.39}$$

where $\mathbf{v}_A(t)$ is the velocity of a selected particle of species A and the brackets $\langle \cdot \rangle$ indicate and equilbrium ensemble average. It is related to the diffusion coefficient of species A via a Green–Kubo integral

$$D_A = \int_0^\infty dt Z_A(t), \tag{1.40}$$

and its $t = 0$ value is

$$Z_A(0) = \frac{k_B T}{m_A}. \tag{1.41}$$

In the case of mixtures we can define an inter–diffusion coefficient D_{12} as done in (Haxhimali et al., 2014),

$$D_{12} = \frac{\aleph}{3N c_1 c_2} \int_0^\infty dt \, \langle \mathbf{j}_{\text{int}}(t) \mathbf{j}_{\text{int}}(0) \rangle \,, \tag{1.42}$$

where the inter–species current $j_{\text{int}}(t)$ is given by

$$\mathbf{j}_{\text{int}}(t) = c_2 \sum_j^{N_1} \mathbf{v}_j - c_1 \sum_j^{N_2} \mathbf{v}_j, \tag{1.43}$$

and the prefactor $\aleph$

$$\aleph \equiv \lim_{k\to 0} \frac{c_1 c_2}{S_{CC}(k)} = c_1 c_2 \left[\frac{\partial^2(\beta G/N)}{\partial c_1^2}\right]_{P,T}, \tag{1.44}$$

with G being the Gibbs free energy. These quantities have not been investigated in the research presented in this Thesis because the main interest was on the dynamical properties and not on the calculation of transport coefficient. Notwithstanding a calculation of the above with a study of the static properties of binary liquids is in need and it is left as future work.

The most important relation that will be used in this Thesis is the Linear Fluctuation–Dissipation theorem (FDT), relating $S_{AB}(\mathbf{k},\omega)$ to the external density response functions $\hat{\chi}_{AB}(k,\omega)$. In a classical system we have

$$S_{AB}(\mathbf{k},\omega) = -\frac{1}{\pi\beta\sqrt{n_A n_B}} \frac{\mathrm{Im}\{\hat{\chi}_{AB}\}(\mathbf{k},\omega)}{\omega}. \tag{1.45}$$

The FDT is an important tool in statistical physics as it relates the thermal fluctuations (or else known as correlations) of a physical observable to the response of the system to a weak external perturbation affecting the physical observable. In simpler terms by weakly perturbing the system I can learn about its equilibrium correlations and vice versa. It has been a success of early non–equilibrium statistical physics pioneered by Harry Nyquist (Nyquist, 1928) and Herbert Callen and Theodore Welton (Callen and Welton, 1951) and later generalized by Ryogo Kubo (Kubo, 1957; Kubo, Yokota, and Nakajima, 1957). The adjective Linear is meant to distinguish it from its non–linear formulations originated from the work of Kenneth I. Golden, Gabor J. Kalman, and Michael B. Silevitch (Golden, Kalman, and Silevitch, 1972). Furthermore, Golden and Heath continued the work by calculating a cubic and quartic fluctuation–dissipation relation in the case of an un–magnetized OCP (Golden and Heath, 2016b; Golden and Heath, 2016a). This

work lead to the calculation of a hierarchy of FDT connecting a single $(p+1)$–point dynamical structure function to a linear combination of $(p+1)$–order p density response functions which was used again by Golden for the formulation of FDT of Binary Coulomb mixtures (Golden, 2018). Unfortunately, the beauty of such work is tainted by the cumbersome and tedious mathematical calculations that it requires and for this reason not much subsequent work has been done. An important work confirming the quadratic FDT has been presented by my Hungarian collaborators Zoltán Donkó, Peter Hartmann, and their student Peter Magyar in (Magyar et al., 2016; Donkó, Hartmann, Magyar, et al., 2017). In this Thesis I will limit to the use of the Linear FDT.

1.4.1 Plasma Response Functions

Response functions describe the dynamics of physical systems under the effects of an external perturbation. They provide a wealth of information on the dynamical properties of plasmas such as the dispersion relation, damping of the modes. Linear Response Theory applied to plasma physics has been reviewed by Golden and Kalman in Ref. (Golden and Kalman, 1969). In plasmas the dielectric function is the response function of interest as it is related to the density response function, polarization, and conductivity. In an OCP the dielectric function can be obtained response function from

$$\varepsilon^{-1}(k,\omega) = 1 + \phi(k)\hat{\chi}(k,\omega) \tag{1.46}$$

where $\phi(k)$ is the Fourier transform of the Coulomb interaction and $\hat{\chi}(k,\omega)$ is external density response function. At this point we need to distinguish between two density response functions: the external and screened response function. It is important to make this distinction as the two are different mathematical functions

with different physical implications (Martin, 1967).

Density response functions are defined as the coefficients of a series expansion in powers of the external potential $\hat{\Phi}(k,\omega)$. More precisely, they are the functional derivatives of the local density with respect of the external potential. In this thesis we are interested in the linear term of this expansion

$$\delta n(k,\omega) = \hat{\chi}(k,\omega)\hat{\Phi}(k,\omega) \tag{1.47}$$

At the same time, instead of considering the external potential as the perturbation, we can consider the total potential since this is the quantity measured in experiments (Giuliani and Vignale, 2005). The total potential is given by

$$\bar{\Phi}(k,\omega) = \hat{\Phi}(k,\omega) + \breve{\Phi}(k,\omega) \tag{1.48}$$

where $\breve{\Phi}(k,\omega)$ is the polarization field induced by $\hat{\Phi}(k,\omega)$. Using $\bar{\Phi}(k,\omega)$ we then define the total response function

$$\delta n(k,\omega) = \bar{\chi}(k,\omega)\Phi(k,\omega). \tag{1.49}$$

Note that the Total response function is indicate by a overhead bar $\bar{\chi}$ while the external response by a hat $\hat{\chi}$. In terms of $\bar{\chi}$ the dielectric function is calculated as

$$\varepsilon(k,\omega) = 1 - \phi(k)\bar{\chi}(k,\omega). \tag{1.50}$$

1.4.2 Partial Response Theory

The extension of linear response to multicomponent systems is presented in Ref. (Kalman and Golden, 1984). In the following I will reproduce the main formulas as they are key relations for the calculations of $\hat{\chi}(k,\omega)$. Although external

response functions are directly related to $S_{AB}(k,\omega)$, a description in terms of total response functions has the advantage of being more transparent. The generalization of response theory to a binary system is presented, however, it is valid for any multicomponent system (Kalman and Golden, 1984; Ichimaru, Mitake, et al., 1985).

Consider a system composed of two particles species that interact via the potential

$$\psi_{AB}(k) = Z_A Z_B \phi(k), \tag{1.51}$$

where $\phi(k)$ is the Fourier transform of the interaction. Introduce a weak charge Q at the origin which creates a pervading potential $V(r) = Q/r$. The external potential $\hat{\Phi}_1 = Z_1 eV$ will cause a response $\hat{\chi}_{11}$ in the species density n_1. At the same time, the external potential $\hat{\Phi}_2 = Z_2 eV$ will perturb the density n_2 which in turn will cause a response $\hat{\chi}_{12}$ in n_1. Mathematically,

$$\delta n_A(\mathbf{k},\omega) = \sum_B \hat{\chi}_{AB}(\mathbf{k},\omega)\hat{\Phi}_B, \tag{1.52}$$

or if we take the total potential $\bar{\Phi}_A = \hat{\Phi}_A + \breve{\Phi}_A$ as the perturbation

$$\delta n_A(\mathbf{k},\omega) = \sum_B \bar{\chi}_{AB}(\mathbf{k},\omega)\bar{\Phi}_B, \tag{1.53}$$

where $\breve{\Phi}_A = \sum_B \psi_{AB}\delta n_B(\mathbf{k},\omega)$ is the induced plasma field. The dielectric matrix is then defined as

$$\hat{\Phi}_A(k,\omega) = \sum_B \varepsilon_{AB}(k,\omega)\bar{\Phi}_B(k,\omega). \tag{1.54}$$

Using the above the definition we find (in matrix notation)

$$\begin{aligned} \varepsilon\bar{\Phi} &= \hat{\Phi} = \bar{\Phi} - \hat{\Phi} && (1.55)\\ &= \bar{\Phi} - \psi n && (1.56)\\ &= (\mathbb{1} - \psi\bar{\chi})\bar{\Phi} && (1.57) \end{aligned}$$

$$\Rightarrow \varepsilon = \mathbb{1} - \psi\bar{\chi} \qquad (1.58)$$

and defining $\eta = \varepsilon^{-1}$

$$\begin{aligned} \eta\hat{\Phi} &= \bar{\Phi} = \hat{\Phi} + \breve{\Phi} && (1.59)\\ &= \hat{\Phi} + \psi n && (1.60)\\ &= (\mathbb{1} + \psi\hat{\chi})\hat{\Phi} && (1.61) \end{aligned}$$

$$\Rightarrow \eta = \mathbb{1} + \psi\hat{\chi} \qquad (1.62)$$

where $\mathbb{1}$ is the 2x2 identity matrix. Finally, using $\eta\varepsilon = 1$ we obtain the relationships between the total and external response function

$$\hat{\chi} = \bar{\chi}\varepsilon^{-1} = \bar{\chi}\left[\mathbb{1} - \psi\bar{\chi}\right]^{-1}, \qquad (1.63)$$

$$\bar{\chi} = \hat{\chi}\eta^{-1} = \hat{\chi}\left[\mathbb{1} + \psi\hat{\chi}\right]^{-1}, \qquad (1.64)$$

The collective modes of the system are now solutions to the equation

$$\det\varepsilon = 0. \qquad (1.65)$$

Few words about symmetry. The external response $\hat{\chi}_{AB}$ must be a symmetric matrix since the matrix of S_{AB} is symmetric. The total response $\bar{\chi}_{AB}$, as derived from $\hat{\chi}_{AB}$, is also symmetric. This can be seen by expanding $(1 + \psi\hat{\chi})^{-1}$ in eq. (1.64)

via its infinite series. However, the symmetry of $\bar{\chi}$ does not imply a symmetric dielectric matrix which is, in general, asymmetric. This asymmetry of $\varepsilon(k,\omega)$ is not always verified and often overlooked as, in the end, one is interested $\hat{\chi}$. We can rewrite $\det\varepsilon$ as

$$\begin{aligned} \det\varepsilon &= \mathbb{1} - \mathrm{Tr}(\psi\bar{\chi}) + [\det\psi][\det\bar{\chi}] && (1.66)\\ &= \mathbb{1} - \psi_{11}\bar{\chi}_{11} - \psi_{22}\bar{\chi}_{22} - 2\psi_{12}\bar{\chi}_{12}, && (1.67) \end{aligned}$$

where in the last step we made use of the symmetry of $\bar{\chi}$ and the fact that $\det\psi = 0$. Notice, though, that in the case of bilayers (Chap. VI) $\det\psi \neq= 0$. We note, also, that here that dielectric matrix has been defined as the response of the potential, eq. (1.54), and not as the response of the field as it is usually done. The latter definition will cause $\sum\psi_{AC}\bar{\chi}_{CB} \to Z_B/Z_A\sum_C\psi_{AC}\bar{\chi}_{CB}$ which, however, does not have any impact in the quantity of interest, $\det\varepsilon$. It does, however, affect the polarizability $\alpha = \phi\bar{\chi}$ which is found in old literature and not currently used (Kalman and Golden, 1984).

1.5 Computer Simulations

Computer simulations have become an essential tool both in theoretical and experimental physics. In the field of strongly coupled plasmas Monte Carlo (MC) and Molecular Dynamics (MD) simulations are the most common techniques. MC simulations consist in sampling the phase space of the system by randomly changing the configuration of the particles. MD, on the other hand, follow a more deterministic approach by solving the equation of motion all the particles.

The simulations presented in this thesis have been performed by our collaborators Zoltán Donkó and Peter Hartmann from the Wigner Research Institute in Budapest, Hungary. A typical MD simulation is as follows. N particles are ini-

tialized with random initial positions and velocities. The system is let evolve in time by solving Newton's equations of motion

$$\ddot{x}_i(t) = \frac{F}{m_i} \tag{1.68}$$

for each particle. The equation is solved numerically using the Velocity Verlet algorithm. At each time step the positions and velocities are calculated as follows

1. Calculate $x(t + \Delta t) = x(t) + v(t)\Delta t + a(t)(\Delta t)^2/2$
2. Apply boundary conditions
3. Calculate the forces and acceleration on each particle: $a(t + \Delta t) = F/m$
4. Calculate $v(t + \Delta t) = v(t) + [a(t) + a(t + \Delta t)]\,\Delta t/2$.

The most expensive part of the simulation is the calculation of forces as this is done over each pair of particles, $\propto N(N-1)/2$. If the particles interact via the Yukawa potential we can calculate the forces on a particular particles from all the particles that fall within a sphere of radius R_{cut}. In the case of Coulomb interaction, the forces are calculated using the Particle–Particle–Particle–Mesh (P3M) algorithm (Hockney and Eastwood, 1981). This consists in dividing the force into a long range term and a short range term. The long range force is then Fourier transformed and used to solve Poisson equation. The solution is inverse Fourier transformed and added to the short range force. The thermalization of the system is achieved by rescaling the velocities, at each time step, to the desired temperature (Γ). Once the system has reached equilibrium the "measurement" phase is initiated. In Fig. 1.1 we show a sample plot of the calculated Γ as a function of the number of time steps. Notice that the line shows no oscillations in the first 30 000 steps indicating the thermalization phase. In the next 50 000 steps Γ oscillates around 300 as this was the chosen value. This is the measurement phase. If the

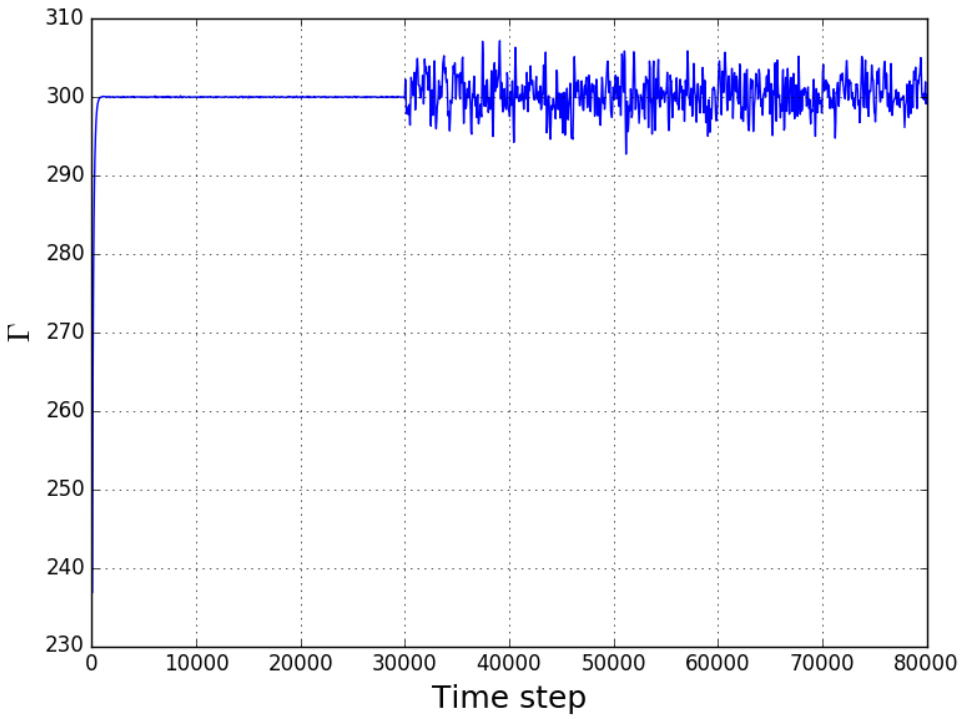

Figure 1.1: Calculated Γ as function of time step number. The simulation was of a 3D binary Yukawa mixture and performed on the BC cluster Pleiades.

system had not reached equilibrium Γ would have kept increasing to larger values. In measurement phase rescaling of the velocities is stopped and the positions and velocities of the particles are recorded at set interval of times. Therefore, at the end of the simulation, we have data sets containing the position and velocities of all the particles as a function of time. Physical observables are then calculated, assuming ergodicity, as time average of these data sets. For example, the Dynamical Structure Functions, $S_{AB}(\mathbf{k},\omega)$ are calculated from

$$S_{AB}(\mathbf{k},\omega) = \frac{1}{2\pi\sqrt{N_A N_B}} \lim_{\Delta T\to\infty} \frac{n_A(-\mathbf{k},\omega) n_B(\mathbf{k},\omega)}{\Delta T}, \tag{1.69}$$

where $n_A(\mathbf{k},\omega)$ is the Fourier transform of the number density operator

$$n_A(\mathbf{k},t) = \sum_i^{N_A} e^{i\mathbf{k}\cdot\mathbf{x}_{A,i}(t)} \tag{1.70}$$

and ΔT is the time span of recorded data.

The other important quantity calculated from MD is the pair distribution function $g(r)$. It gives information on the structure of the spatial distribution of the particles. The quantity $g(r)\delta V$, where δV is an infinitesimal volume, is the probability of finding two particles at a distance r from each other. In MD simulation this is calculated by counting the number of particles inside a sphere of radius r from each particle and then dividing it by the total number N. Obviously $g(r = 0) = 0$ since two classical particles cannot be in the same spot and $g(r \to \infty) = 1$ because the particles become uncorrelated at long distances. In a completely uncorrelated plasmas $g(r) = 1$, because the density is uniform. In a correlated liquid $g(r)$ will start from zero and show an oscillatory behavior around 1. The oscillations will decrease in amplitude as r increases and the strongest peak will be at the mean interparticles distance. As correlations become stronger the amplitude of the oscillations will increase and the oscillatory behavior will decay more slowly. When the system has crystallized $g(r)$ will be a series of delta function at r values corresponding to the lattice points. An example of a strongly coupled binary Yukawa mixture at $\Gamma = 300$ is shown in Fig. 1.2. In this plot we show the interspecies distribution function $g_{12}(r)$ normalized to $\sqrt{N_1 N_2}$. Notice that $g_{12}(r)$ has the strongest peak around $r = a$ and quickly approaches the value 1 at higher distances.

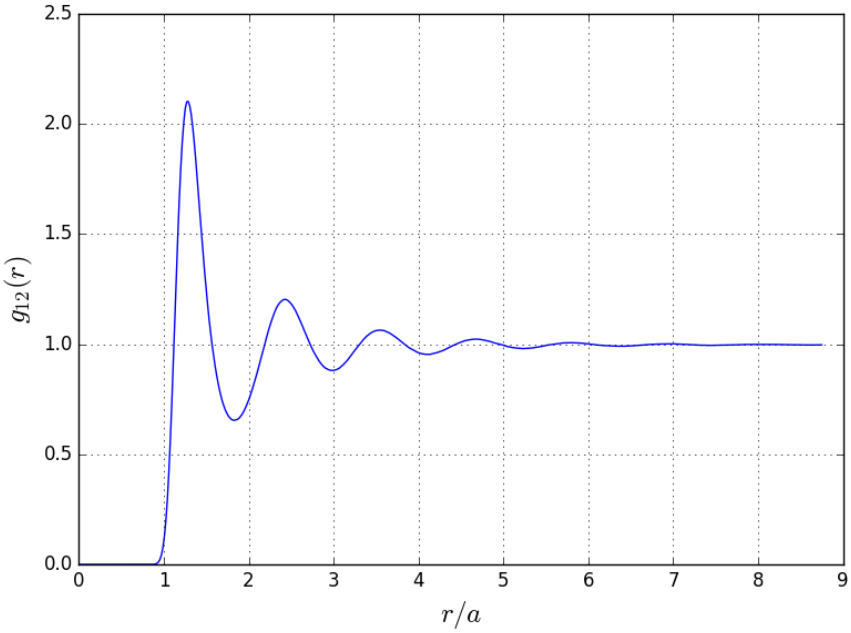

Figure 1.2: Calculated $g_{12}(r)$ from a simulation of a 3D binary Yukawa mixture performed on the BC cluster Pleiades.

CHAPTER II

Theoretical Methods in Plasma Physics

This chapter is devoted to the introduction of the principal theoretical model used in this thesis: the Quasi–Localized Charge Approximation (QLCA). Before describing the QLCA, I give a brief introduction of the different theoretical methods used in plasma physics in order to show how the QLCA fits in the among them. In the following, Sec. 2.1, I start from the early work of Vlasov, Landau, Bohm, Gross, and Pines. Although this can be found in many textbooks I will try to expand more on the physics and the reason their work has become so important. In Sec. 2.2 I will introduce the QLCA and its principal modification. I will show details of the calculation of response functions while details of the derivation of the dynamical QLCA matrix are given in App. B. Sec. 2.3 is the central piece of this Chapter and the Thesis. In here, I will demonstrate the existence of new characteristic frequencies of binary plasma mixtures: the Silvestri–Kalman frequencies. They appear as the zeros of density response functions. The Chapter concludes with Sec. 2.4 in which I present a simple toy model of two harmonic coupled oscillators illustrating the physics behind the Silvestri–Kalman frequencies.

2.1 Weakly Coupled Plasmas

As a many-body system of charged particles the study of the dynamics of plasmas was approached early on using kinetic equations. However, it soon became obvious that plasmas were different from normal fluids of neutral particles. In the latter we can identify a maximum interaction distance beyond which particles "effectively" do not interact[1]. In this case pairs of particles interact or "collide" only when they enter each other's range of action while for the rest they move on straight orbits described by $\mathbf{x} + \mathbf{v}t$. In a gas at high temperature and high density, thermal equilibrium is achieved and maintained by binary collisions. If we apply any pressure gradient to the system particle in regions at higher pressure will experience many more collisions than particles in low pressure regions. The perturbation is relaxed as fast particles escapes into low pressure regions and slow particles enter the high pressure region. In a microscopic description of such systems we talk of a particle interacting via an average field. In this case the average is carried over many short–time momentum transfers, hence the Boltzmann transport equation.

On the other hand, due to the slow decay of the Coulomb interaction, we cannot define a sphere of action in the case of plasmas. Here each charged particle is simultaneously under the influence of all the other particles. At high temperature and high density the field created by the charges exceeds any close encounter interaction between two particles. Therefore, particles do not move on straight lines, but on smooth orbits defined by the surrounding electric field, given by the solution of the Laplace equation. In this case we talk about a space average of the field in which fluctuations due to the point–like nature of the particles are removed. This average field is an important piece since it provides the restoring

[1]The simplest example is a gas of hard spheres. The potential is infinitely strong for distance smaller or equal the radius of the sphere and zero elsewhere.

force needed for the formation of plasma oscillations (Vlasov, 1968; Bohm and Gross, 1949a). The first to realize that the usual kinetic approach is inapplicable to plasmas was, of course, Lev D. Landau who showed that the Boltzmann collision operator, in this case, is tainted by divergences and thus it requires *ad hoc* cutoffs (Landau, 1965b). This lead to the famous Coulomb Logarithm

$$\ln \Lambda_c = \ln \left(\frac{b_{\min}}{b_{\max}} \right) = \ln \left(\frac{\lambda_D}{r_c} \right), \tag{2.1}$$

where the r_c is the classical distance of closest approach [2] and λ_D is the Debye wavelength. Anatoly A. Vlasov built upon Landau's work by separating the Coulomb interaction into a short–range and long–range part. He then showed that the long–range part greatly exceeds the short–range part and it is the main element in the description of the plasma oscillations (Vlasov, 1968). This, in turn, enormously simplifies the Boltzamnn transport equation by completely removing the collision integral. This is why the Vlasov equation is often referred to as the Collisionless Boltzmann equation. Landau, again, complemented Vlasov's work by showing that plasma oscillation continued to be damped even in the absence of collisions. This damping, also known as Landau Damping, is due to the interaction between the discrete aspect of plasma, *i.e.* particles, and their collective behavior (Landau, 1965a). The identification of the plasma oscillations as a collective excitation – in fact, the very idea of collective excitations and the notion of collective coordinates – is due to the pioneering series works by David Bohm, Eugene P. Gross and David Pines (Bohm and Gross, 1949a; Bohm and Gross, 1949b; Pines and Bohm, 1952; Bohm and Pines, 1953). Bohm and Gross (BG) determined the eponymous k–dependent positive dispersion of the plasmon, caused by the random thermal motion of the particles (Bohm and Gross, 1949a; Bohm and Gross, 1949b). Soon, however, it became clear that both the Vlasov treatment

[2] r_c is calculated by equating kinetic and potential energy, $mv^2/2 = e^2/r_c$

and the BG dispersion share an underlying theoretical foundation (which later was reformulated in many different guises (Pines and Bohm, 1952; Nozières and Pines, 1958; Gell-Mann and Brueckner, 1957; Sawada et al., 1957; Singwi, Tosi, et al., 1968) and has commonly become known as the Random Phase Approximation (RPA)) and are appropriate for weak coupling only. In the following we reproduce the Vlasov result as obtained from the Liouville equation. The reason for this is because the Vlasov (RPA) results will be used throughout this Thesis. In kinetic theory the Liouville equation of the full N–particle distribution function is reduced to a set of coupled equations known as the Bogoliubov-–Born–Green–Kirkwood–Yvon (BBGKY) hierarchy. The first of these equations gives the time evolution of the single–particle distribution, as a function of the two–particle distribution which in turn is a function of the three–particle distribution and so on. The above discussion, in the case of plasmas, translates in the charged particles being statistically independent so that the N–particle distribution can be expressed as the product of N single–particle distribution functions. This leads to, skipping some steps, the wavenumber and frequency dependent linearized Vlasov equation for the perturbed single–particle distribution function, of species A, $f_A(\mathbf{k},\omega,\mathbf{v}) = f_A^{(0)}(\mathbf{v}) + \delta f_A(\mathbf{k},\omega,\mathbf{v})$,

$$(\omega - \mathbf{k}\cdot\mathbf{v})\,\delta f_A(\mathbf{k},\omega,\mathbf{v}) + \left[\sum_B \psi_{AB}(\mathbf{k})\delta n_B(\mathbf{k},\omega) + \hat{\Phi}_A(\mathbf{k},\omega)\right]\mathbf{k}\cdot\frac{\partial}{\partial\mathbf{v}} f_A^{(0)}(\mathbf{v}) = 0 \tag{2.2}$$

where we recall that ψ_{AB} is any two–body interaction potential and $\hat{\Phi}_A$ is an external perturbation. Integrating $f_A(\mathbf{k},\omega,\mathbf{v})$ over the velocity $\mathbf{v}$ gives

$$\int d\mathbf{v} f_A(\mathbf{k},\omega,\mathbf{v}) = n_A + \delta n_A(\mathbf{k},\omega). \tag{2.3}$$

Now, if we consider $\hat{\Phi}_A(\mathbf{k},\omega)$ as the perturbation, δf_1 will be coupled, through $\delta n_2(\mathbf{k},\omega)$, to δf_2. However, by considering the total field $\bar{\Phi}_A$ as the perturbation

the two distributions will be independent of each and lead to

$$(\omega - \mathbf{k}\cdot\mathbf{v})\,\delta f_A(\mathbf{k},\omega,\mathbf{v}) + \bar{\Phi}_A(\mathbf{k},\omega)\mathbf{k}\cdot\frac{\partial}{\partial\mathbf{v}} f_A^{(0)}(\mathbf{v}) = 0, \tag{2.4}$$

which then gives a diagonal response matrix

$$\bar{\chi}(k,\omega) = \begin{pmatrix} \chi_1^{(0)}(k,\omega) & 0 \\ 0 & \chi_2^{(0)}(k,\omega) \end{pmatrix} \tag{2.5}$$

with

$$\chi_A^{(0)}(k,\omega) = -\frac{1}{m_A}\int \frac{d\mathbf{v}}{\mathbf{k}\cdot\mathbf{v} - \omega - i\delta}\mathbf{k}\cdot\frac{\partial}{\partial\mathbf{v}} f_A^{(0)}(\mathbf{v}) \tag{2.6}$$

being the familiar Vlasov polarization function. Using eq. (1.63) we can then calculate the elements of the external response $\hat{\chi}(k,\omega)$

$$\hat{\chi}_{11}(k,\omega) = \frac{\chi_1^{(0)}(k,\omega)\left[1 - \psi_{22}(k)\chi_2^{(0)}(k,\omega)\right]}{\varepsilon(k,\omega)} \tag{2.7}$$

$$\hat{\chi}_{12}(k,\omega) = -\frac{\chi_1^{(0)}(k,\omega)\psi_{12}(k)\chi_2^{(0)}(k,\omega)}{\varepsilon(k,\omega)} \tag{2.8}$$

$$\hat{\chi}_{22}(k,\omega) = \frac{\chi_2^{(0)}(k,\omega)\left[1 - \psi_{11}(k)\chi_1^{(0)}(k,\omega)\right]}{\varepsilon(k,\omega)} \tag{2.9}$$

and the dielectric matrix

$$\varepsilon_{11}(k,\omega) = 1 - \psi_{11}(k)\chi_1^{(0)}(k,\omega), \tag{2.10}$$

$$\varepsilon_{12}(k,\omega) = -\psi_{12}(k)\chi_2^{(0)}(k,\omega), \tag{2.11}$$

$$\varepsilon_{21}(k,\omega) = -\psi_{12}(k)\chi_1^{(0)}(k,\omega), \tag{2.12}$$

$$\varepsilon_{22}(k,\omega) = 1 - \psi_{22}(k)\chi_2^{(0)}(k,\omega), \tag{2.13}$$

whose determinant is

$$\det \varepsilon(k,\omega) = 1 - \psi_{11}(k)\chi_1^{(0)}(k,\omega) - \psi_{22}(k)\chi_2^{(0)}(k,\omega). \tag{2.14}$$

These equations explicitly show that $\varepsilon(k,\omega)$ is not symmetric ($\varepsilon_{12} \neq \varepsilon_{21}$) while $\hat{\chi}(k,\omega)$ is.

2.1.1 Moderately to Strongly Coupled Plasmas

The Vlasov equation, as mentioned, neglects correlations between particles and can be considered as the zeroth order of a perturbation expansion in terms of the coupling parameter (Liboff, 2003). Therefore, the next logical step is to calculate the next order term. This amounts to keeping the first two equations of the BBGKY hierarchy and expand to first order in perturbation the two–particle distribution function. This approach, carried out in different forms by many researchers (Guernsey, 1962; Oberman, Ron, and Dawson, 1962; Coste, 1965a; Coste, 1965b), leads to an exact calculation of the high frequency plasma conductivity and to the calculation of collisional damping, different than Landau damping, of the collective modes. Most importantly it was shown that electron–ion collisions dominates over electron–electron collisions in the damping of the modes (DuBois, Gilinsky, and Kivelson, 1962; Ogasawara, 1963). The reason for this can be explained in simple terms. Electron–electron collisions, in the $\mathbf{k} \to 0$ limit, do not affect the electron current because in the averaging process one cannot distinguish between two electrons, but can distinguish between ions and electron since each species carries a different current.[3]

[3]Here I would like to make a little side note. Parallel to the BBGKY hierarchy there is the European School of Iliya Prigogine. Their method consists in solving the full Liouville equation for f_N in terms of a resolvent (very similar to the more commonly known Green's function). The solution is a series of interaction integrals which can be associated with diagrams whose topology is connected with the order of interaction between particles. This method has not been used beyond Prigogine's students due to its mathematical complexity. However, its general formalism, I believe, is a good pedagogical tool as it is the classical equivalent of the Feynman

Another technique, more adequate for the calculation of transport coefficients, is to use the transport Boltzmann equation with an adequate collision operator. The most famous examples of this approach are the Landau integral (Landau, 1965b), Lenard–Balescu collision operator (Lenard, 1960; Balescu, 1960), and the Bhatnagar–Gross–Krook collision operator (Bhatnagar, Gross, and Krook, 1954) and its recent multispecies extension (Haack, Hauck, and Murillo, 2017). By extending this approach to finite and strong coupling, however, one readily encounters unphysical situations when the Coulomb logarithm becomes negative around $\Gamma \sim 1/3^{1/3} \approx 0.69$. One extension able to overcome this obstacle is the Effective Potential Theory of Baalrud and Daligault (Baalrud and Daligault, 2013).

The above approaches, however, are sullied by the complex mathematical landscape which makes it difficult to exctract a clear physical picture.

In the late 1960s and early 1970s mean-field theories started to make their way into plasma physics. The basic idea is to replace the polarization potential $\breve{\Phi}$ by an effective potential that incorporates all the correlational effects, that is

$$\breve{\Phi}(k,\omega) \to \breve{\Phi}(k,\omega) = \phi(k)\left[1 - G(\mathbf{k},\omega)\right]\delta n(\mathbf{k},\omega) \tag{2.15}$$

where $\phi(k)$ is the bare Coulomb interaction and $G(\mathbf{k},\omega)$ is called the Local Field Corrections. $G(\mathbf{k},\omega) = 0$ is entirely correlational dependent and by setting $G(\mathbf{k},\omega) = 0$ one recovers the RPA. This allows, then, the use of the Vlasov equation with the new effective potential leading to a dielectric function, looking at an OCP for simplicity,

$$\varepsilon(\mathbf{k},\omega) = 1 - \frac{\phi(k)\chi^{(0)}(\mathbf{k},\omega)}{1 + \phi(k)G(\mathbf{k},\omega)\chi^{(0)}(\mathbf{k},\omega)}, \tag{2.16}$$

diagrams.

a total response function

$$\bar{\chi}(\mathbf{k},\omega) = \frac{\chi^{(0)}(\mathbf{k},\omega)}{1+\phi(k)G(\mathbf{k},\omega)\chi^{(0)}(\mathbf{k},\omega)}, \tag{2.17}$$

and an external response function

$$\hat{\chi}(\mathbf{k},\omega) = \frac{\chi^{(0)}(\mathbf{k},\omega)}{1-\phi(k)\left[1-G(\mathbf{k},\omega)\right]\chi^{(0)}(\mathbf{k},\omega)}. \tag{2.18}$$

The problem now becomes to find a valid $G(\mathbf{k},\omega)$. This is easier than before since $G(\mathbf{k},\omega)$ must satisfy different conditions which are obtained from sum rules of $S(\mathbf{k},\omega)$. The most recent, and definitely the offspring of current times, is to use machine learning to calculate $G(\mathbf{k},\omega)$ as shown in (Dornheim et al., 2018). However, even though machines are more efficient than human in analyzing large datasets, the paper shows that human ingenuity play the main role in scientific research since the newly found $G(\mathbf{k},\omega)$ does not improve on those proposed in the early 1970's. The most famous of these mean-field theories is, perhaps, the STLS (Singwi, Tosi, et al., 1968; Singwi, Sjölander, et al., 1969; Singwi, Sjölander, et al., 1970) which uses a static LFC of the form

$$\phi(k)G(k,0) = -\sum_{\mathbf{q}} \frac{\mathbf{k}\cdot\mathbf{q}}{q^2}\phi(q)\left[S(\mathbf{k}-\mathbf{q})-1\right] \tag{2.19}$$

where $S(\mathbf{k})$ is the static structure function. This LFC is obtained from the following approximation of the two particle distribution function, f_2

$$f_2^{(STLS)}(\mathbf{r}_1,\mathbf{v}_1,\mathbf{r}_2,\mathbf{v}_2,t) = f_1(\mathbf{r}_1,\mathbf{v}_1,t)f_1(\mathbf{r}_2,\mathbf{v}_2,t)\left[1+h(\mathbf{r}_1,\mathbf{r}_2)\right], \tag{2.20}$$

and by the use of the linear FDT

$$S(\mathbf{k}) = 1 + h(\mathbf{k}) \tag{2.21}$$

Physically, this means that binary correlations relax on a much shorter time scales than single–particle distributions. The STLS was the first great improvement over the RPA and agreed very well with computer simulations and experiments. However, unphysical predictions appear at moderate coupling and it does not satisfy several of the required sum–rules (Giuliani and Vignale, 2005). Its main disagreement with the QLCA in the case of binary mixture has been elucidated by Kalman and Golden in (Kalman and Golden, 1998). The main difference being that the STLS is a static approximation while the QLCA a dynamical one, thus, leading to the correct prediction of the collective mode spectrum.

A recent improvement on the STLS, for application to inhomogeneous strongly coupled plasmas, has been proposed by Kählert *et al.* (Kählert, Kalman, and Bonitz, 2014; Kählert, Kalman, and Bonitz, 2015). It consists in keeping the time dependence of the pair correlation function.

$$f_2^{(ESTLS)}(\mathbf{r}_1, \mathbf{v}_1, \mathbf{r}_2, \mathbf{v}_2, t) = f_1(\mathbf{r}_1, \mathbf{v}_1, t) f_1(\mathbf{r}_2, \mathbf{v}_2, t) \left[1 + h(\mathbf{r}_1, \mathbf{r}_2, t)\right]. \tag{2.22}$$

Before concluding I cannot fail to mention the Velocity Average Approximation (VAA) proposed by Golden and Kalman in 1974 (Golden, Kalman, and Silevitch, 1974; Golden and Kalman, 1979; Golden and Kalman, 1982). It consists in the following approximation of the two–particle distribution function

$$\begin{aligned} f_2^{(VAA)}(\mathbf{r}_1, \mathbf{v}_1, \mathbf{r}_2, \mathbf{v}_2, t) &= \frac{1}{2}\left[\frac{f_1(\mathbf{r}_1, \mathbf{v}_1, t)}{n(\mathbf{r}_1, t)} \int d\mathbf{v}_1' f_2(\mathbf{r}_1, \mathbf{v}_1', \mathbf{r}_2, \mathbf{v}_2, t)\right. \\ &\left. + \frac{f_1(\mathbf{r}_2, \mathbf{v}_2, t)}{n(\mathbf{r}_2, t)} \int d\mathbf{v}_2' f_2(\mathbf{r}_1, \mathbf{v}_1, \mathbf{r}_2, \mathbf{v}_2', t)\right]. \end{aligned} \tag{2.23}$$

The VAA was very successful as it satisfied both the compressibility sum–rule and the first and third moment sum–rules. It lead to exact results in both the OCP and Binary Mixtures (Golden, 1982; Golden, Green, and Neilson, 1985a; Golden,

Green, and Neilson, 1985b), however, it required a great deal of mathematical effort which discouraged many researchers since it required the use of the Non–Linear FDT. The work on VAA, though, provided great insights to its originators who later proposed the QLCA which trades mathematical complexity and internal consistency for a clear physical picture.

2.2 Quasi–Localized Charge Approximation

The Quasi-Localized Charge Approximation was proposed almost three decades ago by Kalman and Golden (Kalman and Golden, 1990; Golden and Kalman, 2000; Golden and Kalman, 2001). Its basic assumption is that at strong coupling the liquid state closely resembles that of a disordered solid. That is charges are localized in deep potential minima whose positions are strongly correlated, but randomly distributed. The dynamics of the system are then dictated by the small amplitude oscillations that charges undergo around these minima. Notwithstanding, the liquid aspect is represented by the fact that the positions of the minima change over a time much longer than the period of oscillations. Inherent in the QLC model is the assumption that the two time scales are well separated and that for the description of the oscillating motion, the time average (converted into ensemble average) of the drifting quasi-equilibrium configuration is sufficient. This physical picture is supported by computer simulations which show that the pair distribution function is characterized by strong peaks at periodic space intervals, thermodynamic quantities, *e.g.* energy, of the strongly coupled liquid state do not change drastically from those of a solid (Baus and Hansen, 1980), and on a more dynamical level particles are effectively quasi-localized (Donkó, Kalman, and Golden, 2002; Donkó, Hartmann, and Kalman, 2003).

The strength of the QLCA is in its mathematical simplicity which provides a clear distinction of the roles played by the different physical effects. However, all of this

comes at the cost of self-consistency and various pitfalls. In fact, the QLCA requires the external input of the pair distribution function, obtained from computer simulations, it satisfies the first and third frequency sum rule, but fails to satisfy the compressibility sum rule, thermal effects while being small are completely absent, and finally it lacks a coherent description of the damping mechanism of the collective modes. It is on these last two points that this thesis tries to expand.

2.2.1 Collisional QLCA

In an OCP, to first order, we can identify two major damping mechanism: wave-particle interaction and particle-particle interaction. In the former plasma waves lose energy to particles that are slower than the wave speed and gain energy from particles that are faster. Since, at equilibrium, there are more slow particles than fast the wave becomes damped. This is known as Landau damping and is the only damping mechanism present for an OCP with $\Gamma = 0$ and dominates over collisional damping at very long wavelengths. At shorter wavelengths, instead, the individuality of particles becomes more and more relevant and collisions destroy the collective behavior. As correlations between particles increase one expect the second mechanism to become the dominant one even at very short wavelengths, however, both mechanisms vanish at infinite wavelengths ($k = 0$). If, instead, we were to consider a plasma mixtures we will have that collisional damping survives even at $k = 0$ due to distinguishability between the species composing the mixture. As a matter of fact, it was shown in the early days of plasma physics, that collisional damping due to like particles, *e.g.* electrons, vanishes as k^2, while collisions between different particles, *e.g.* electrons and ions, remains finite even at $k = 0$ (DuBois, Gilinsky, and Kivelson, 1962; Ogasawara, 1963). It is on this important difference that the Collisional QLCA relies on.

2.2.2 Derivation of relevant formulas

The system under consideration is composed of N charged particles of two species enclosed in a volume V with densities $n_A = N_A/V$. In the strong coupling regime the position of the i^{th} particle is defined as $\mathbf{X}_{A,i} = \mathbf{x}_{A,i} + \boldsymbol{\xi}_{A,i}(t)$, where $x_{A,i}$ indicates the quasi-static equilibrium positions and $\boldsymbol{\xi}_{A,i}$ small displacements around them. The introduction of damping in the original QLCA is achieved by adding a drag force term proportional to the relative velocities of the individual particles of species A in the microscopic equation of motion of $\boldsymbol{\xi}_{A,i}$

$$m_A\ddot{\xi}_{A,i} + \sum_B \sum_j \gamma_{AB}(\mathbf{r}_{AB,ij}) \left(\dot{\xi}_{A,i} - \dot{\xi}_{B,j}\right) + \sum_B \sum_j K_{A\bar{B},ij}\xi_{B,j} = Z_A e E(\mathbf{x}_{A,i}, t) \tag{2.24}$$

where $K_{AB,ij}$ is the (species matrix) element of the force obtained from the harmonic approximation of the potential, $\mathbf{E}$ is an external field acting only on species A, and $\mathbf{r}_{AB,ij} = \mathbf{x}_{A,i} - \mathbf{x}_{B,j}$. The new element is γ_{AB}, a symmetric two-body collisional matrix. Following the idea of the QLCA, the collisional matrix can now be averaged over all the pairs with the aid of the equilibrium pair distribution function and absorbed in a drag matrix $\mathbf{R}$ with elements

$$\begin{aligned} R_{AB}(\mathbf{k}) \;=\; & \sqrt{\frac{n_A n_B}{m_A m_B}} \left\{ \int d^3r \gamma_{AB}(\mathbf{r}) \left[1 + h_{AB}(r)\right] e^{-i\mathbf{k}\cdot\mathbf{r}} \right. \\ & \left. - \delta_{AB} \sum_C \frac{n_C}{n_A} \int d^3r \gamma_{AC}(\mathbf{r}) \left[1 + h_{AC}(r)\right] \right\}, \end{aligned} \tag{2.25}$$

where $h_{AB}(r)$ is the pair correlation function between species A and B. The $\mathbf{R}$ matrix describes the total drag force acting on a selected particle. The first term represents the force generated by the motion of all the other particles in the system on the selected particle, while the second is due to the velocity of the selected particle itself with the equilibrium environment of all the others (see eq. (B.2)). The drag matrix now combined with the original QLCA dynamical

matrix, $\mathbf{C}(\mathbf{k})$ from eq. (B.19), provides the collisional dynamical matrix

$$G_{AB}(\mathbf{k},\omega) = -i\omega R_{AB}(\mathbf{k}) + C_{AB}(\mathbf{k}). \tag{2.26}$$

The equation of motion, then, becomes

$$\left[\omega^2\delta_{AB} - G_{AB}(\mathbf{k},\omega)\right]\xi_{B,\mathbf{k}}(\omega) = -\frac{Z_A e n_A}{\sqrt{N_A m_A}} E_A(\mathbf{k},\omega), \tag{2.27}$$

from which we calculate the matrix elements of the external response functions

$$\chi_{AB}(\mathbf{k},\omega) = \sqrt{\frac{n_A n_B}{m_A m_B}}k^2[\omega^2\mathbf{I} - \mathbf{G}(\mathbf{k},\omega)]^{-1}_{AB}, \tag{2.28}$$

$\mathbf{I}$ being the identity matrix in species space. Using now the formalism of partial response functions presented in Sec. 1.4.2 we calculate the partial polarization function $\bar{\chi}_{AB}(\mathbf{k},\omega)$, and the dielectric matrix $\epsilon(\mathbf{k},\omega)$. The former is

$$\bar{\chi}_{AB}(\mathbf{k},\omega) = \sqrt{\frac{n_A n_B}{m_A m_B}}k^2[\omega^2\mathbf{I} - \mathbf{P}(\mathbf{k},\omega)]^{-1}_{AB}, \tag{2.29}$$

where

$$P_{AB}(\mathbf{k},\omega) = -i\omega R_{AB}(\mathbf{k}) + C_{AB}(\mathbf{k}) - \omega_A\omega_B k^2\phi(k), \tag{2.30}$$

is an entirely correlational dependent term. $\phi(k) = 1/k^2$ in the case of Coulomb interaction and $\phi(k) = 1/(k^2+\kappa^2)$ in the case of Yukawa. In other words $\mathbf{P}$ is calculated by removing the mean-field terms from the dynamical matrix $\mathbf{C}$. Nevertheless, by setting $\mathbf{P} = 0$ one does not recover the RPA, because of the underlying quasi–localization assumption. Using the the above equations we can calculate the dielectric matrix, however, we are not interested in the individual matrix elements, but only to the determinant of the dielectric matrix from which

we obtain the dispersion relation. This is given by

$$\det \varepsilon(\mathbf{k},\omega) = \frac{\det\{\omega^2\mathbf{I} - \mathbf{G}(\mathbf{k},\omega)\}}{\det\{\omega^2\mathbf{I} - \mathbf{P}(\mathbf{k},\omega)\}} = 0. \tag{2.31}$$

Given the fact that the primary quantity of interest in this thesis is the matrix of the external response functions below, for the sake of future reference, the explicit expressions of its elements. The diagonal elements are

$$\begin{aligned}\chi'_{11}(k,\omega) &= \frac{n_1}{m_1}\frac{k^2}{|\mathcal{D}|^2}\left\{\left(\omega^2 - C_{22}\right)\left[(\omega^2-\omega_+^2)(\omega^2-\omega_-^2) - \omega^2\det\mathbf{R}\right]\right. \\ &\left. +(\omega R_{11})^2\left(\omega^2-\omega_{*2}^2\right) + (\omega R_{12})^2\left(\omega^2 - C_{11} + \frac{R_{11}}{R_{12}}C_{12}\right)\right\}, \end{aligned}\tag{2.32}$$

$$\chi''_{11}(k,\omega) = \frac{n_1}{m_1}\frac{k^2}{|\mathcal{D}|^2}\left\{\omega R_{11}\left(\omega^2-\omega_{*2}^2\right)^2 + \omega R_{22}\left(\omega^2 + \frac{C_{12}^2}{R_{11}R_{22}}\right)\det\mathbf{R}\right\}, \tag{2.33}$$

and the off diagonal elements

$$\begin{aligned}\chi'_{12}(k,\omega) &= -\sqrt{\frac{n_1 n_2}{m_1 m_2}}\frac{k^2}{|\mathcal{D}|^2}\left\{C_{12}\left[(\omega^2-\omega_+^2)(\omega^2-\omega_-^2) - \omega^2\det\mathbf{R}\right]\right. \\ &\left. -\omega^2 R_{12}\left[R_{22}\left(\omega^2-\omega_{*1}^2\right) + R_{11}\left(\omega^2 - C_{22} + \frac{R_{22}}{R_{12}}C_{12}\right)\right]\right\}, \end{aligned}\tag{2.34}$$

$$\begin{aligned}\chi''_{12}(k,\omega) &= -\sqrt{\frac{n_1 n_2}{m_1 m_2}}\frac{k^2}{|\mathcal{D}|^2}\frac{\omega R_{11}R_{22}}{R_{12}}\left\{\left(\omega^2-\omega_{*1}^2\right)\left(\omega^2-\omega_{*2}^2\right)\right. \\ &\left. -\omega R_{12}\left[\omega^2 - \frac{(\omega^2-C_{11})(\omega^2-C_{22})}{R_{12}^2}\right]\det\mathbf{R}\right\}. \end{aligned}\tag{2.35}$$

$\chi_{22}(k,\omega)$ is obtained by the exchange $1 \to 2$ in the formulas of $\chi_{11}(k,\omega)$ and $\chi_{21}(k,\omega) = \chi_{12}(k,\omega)$. In the above expressions the term $\mathcal{D}$ in the denominator is given by

$$\mathcal{D}(k,\omega) = \det\left\{\omega^2\mathbf{I} - \mathbf{G}(k,\omega)\right\}, \tag{2.36}$$

and its zeros give the dispersion of the collective modes. The explicit expression, in terms of R_{AB} and C_{AB} is

$$\begin{aligned}\mathcal{D}(k,\omega) &= \left[\omega^2-\omega_+^2(k)\right]\left[\omega^2-\omega_-^2(k)\right]-\omega^2\det\mathbf{R}(k)\\ &\quad -i\omega\left\{R_{11}(k)\left[\omega^2-\omega_{*2}^2(k)\right]+R_{22}(k)\left[\omega^2-\omega_{*1}^2(k)\right]\right\},\end{aligned} \tag{2.37}$$

where $\omega_\pm(k)$ are the eigenvalues of the $\mathbf{C}$-matrix and we have defined

$$\omega_{*1}^2(k)=C_{11}(k)-\frac{R_{12}(k)}{R_{22}(k)}C_{12}(k), \tag{2.38}$$

$$\omega_{*2}^2(k)=C_{22}(k)-\frac{R_{12}(k)}{R_{11}(k)}C_{12}(k). \tag{2.39}$$

Further simplification of the imaginary part of the determinant leads to

$$\begin{aligned}\mathcal{D}''(k,\omega) &= -\omega\left\{R_{11}(k)\left[\omega^2-\omega_{*2}^2(k)\right]+R_{22}(k)\left[\omega^2-\omega_{*1}^2(k)\right]\right\}\\ &= -\omega\left[R_{11}(k)+R_{22}(k)\right]\left[\omega^2-\omega_{im}^2(k)\right]\end{aligned} \tag{2.40}$$

with a zero at

$$\omega_{\rm im}^2(k)=\frac{R_{11}\omega_{*2}^2(k)+R_{22}\omega_{*1}^2(k)}{R_{11}+R_{22}}. \tag{2.41}$$

For future reference we rewrite the entire determinant as

$$\mathcal{D}(k,\omega)=\left[\omega^2-\omega_+^2(k)\right]\left[\omega^2-\omega_-^2(k)\right]-\omega^2\det\mathbf{R}-i\omega\left(R_{11}+R_{22}\right)\left[\omega^2-\omega_{\rm im}^2(k)\right]. \tag{2.42}$$

This formula is different from the original QLCA in the fact that it is a complex function and thus allows for the calculation of damping of the collective modes. We conclude this section with two important points. First, the matrix $\mathbf{G}(\mathbf{k},\omega)$ should not be confused with the dynamical local field corrections talked about in the previous section. The same labeling is due to be consistent with the current

literature. Nevertheless, the LFC is more closely related to the matrix $\mathbf{P}(k,\omega)$ and shown in (Kalman, Golden, Donkó, et al., 2005). The second important point is that the above equations have been obtained via simple algebra and no specific property of the $\mathbf{R}$ or $\mathbf{C}$ has been used. This indicates that the "frequencies" $\omega_{*1,2}$ are not specific to strongly coupled plasmas, but general formulas of 2×2 matrices. Furthermore, this suggests that similar relations should exist for larger symmetric matrices and it is indeed so. However, a generalization of this formulas to $N \times N$ is out of the scope of this thesis and it is left as future work. A preliminary work on this topic can be found in (Belbasi, Ebrahim Foulaadvand, and Joe, 2014) in which the authors consider a one dimensional chain of identical driven coupled oscillators.

2.2.3 Extended Collisional QLCA

In 2005 Kalman and Golden (Kalman, Golden, Donkó, et al., 2005) proposed an extension of the QLCA in order to try to include thermal effects. The extension amounts in recognizing that the multiplying factor

$$\frac{n_1}{m_1}k^2 \tag{2.43}$$

in (B.19) is the high frequency expansion of the Vlasov polarization function

$$\chi_A^{(0)}(k,\omega) = -\frac{1}{m_A}\int d^3v \frac{1}{\mathbf{k}\cdot\mathbf{v}-\omega-i\delta}\mathbf{k}\cdot\frac{\partial f^{(0)}}{\partial \mathbf{v}} \approx \frac{n_A}{m_A}\frac{k^2}{\omega^2}. \tag{2.44}$$

This leads to

$$\bar{\chi}_{AB}(\mathbf{k},\omega) = \sqrt{\bar{\chi}_A^{(0)}\bar{\chi}_B^{(0)}}\left[\mathbf{I}-\mathcal{P}(\mathbf{k},\omega)\right]^{-1}_{AB} \tag{2.45}$$

$$\mathcal{P}_{AB}(\mathbf{k},\omega) = -i\omega\mathcal{R}_{AB}(\mathbf{k},\omega)+\mathcal{H}_{AB}(\mathbf{k},\omega), \tag{2.46}$$

$$\mathcal{R}_{AB}(\mathbf{k},\omega) = \sqrt{\bar{\chi}_A^{(0)}\bar{\chi}_B^{(0)}}\frac{1}{k^2}\left[\bar{\gamma}_{AB}(k) - \delta_{AB}\sum_C \frac{n_A}{n_C}\bar{\gamma}_{AC}(0)\right], \tag{2.47}$$

$$\begin{aligned}\mathcal{H}_{AB}(\mathbf{k},\omega) &= \sqrt{\bar{\chi}_A^{(0)}\bar{\chi}_B^{(0)}}\frac{1}{k^2}\frac{1}{V}\sum_{\mathbf{q}} q^\alpha q^\beta \Big\{\phi_{AB}(q)h_{AB}\left(|\mathbf{k}-\mathbf{q}|\right) \\ &\quad -\delta_{AB}\sum_C \frac{n_C}{n_A}\phi_{AC}(q)h_{AC}(q)\Big\},\end{aligned} \tag{2.48}$$

and $\bar{\gamma}_{AB}(k)$ is defined below. From the above equations it is evident that the matrices of the external response χ_{AB}, polarization function $\bar{\chi}_{AB}$, and dielectric matrix ε_{AB} are all symmetric. While this is not an issue for χ_{AB} and $\bar{\chi}_{AB}$, it certainly is for ε_{AB}. However, this discrepancy has often been ignored in the past and in other strong coupling theories since one is, in the end, interested in the external response χ_{AB} and it is, tacitly, expected that the asymmetry in ε_{AB} vanishes when one calculates the determinant. This discrepancy is also found in the STLS and in the dynamical field correction of Ichimaru and co-workers. Furthermore, the most drastic flaw is in the square root of term in the off-diagonal terms $\bar{\chi}_{12}(\mathbf{k},\omega)$. At low frequencies $\chi_A^{(0)}(\mathbf{k},\omega)$ are negative and change sign at higher frequencies. However, the frequency at which $\chi_1^{(0)} = 0$ is different than the frequency at which $\chi_2^{(0)} = 0$. Therefore there is a region for which $\bar{\chi}_{12}(\mathbf{k},\omega)$ is ill-defined. This flaw is not present in $\chi_{AB}(\mathbf{k},\omega)$ and $\det\varepsilon(\mathbf{k},\omega)$ were only the product $\bar{\chi}_1^{(0)}\bar{\chi}_2^{(0)}$, and not its square root, appears. Finally, a first principle derivation on the lines of (Kalman, Golden, Donkó, et al., 2005) does not recover the correct dispersion relation nor a symmetric χ_{AB}. Thus, the Extended QLCA for Binary systems can be considered only as phenomenological approximation of the external response $\chi_{AB}(\mathbf{k},\omega)$.

2.3 The Silvestri–Kalman Frequencies

We arrive now at the central point of this thesis. Let's look at the damping matrix $\mathbf{R}$ in more details, by defining

$$\bar{\gamma}_{AB}(k) = \int d^3r \gamma_{AB}(\mathbf{r}) \left[1 + h_{AB}(r)\right] e^{-i\mathbf{k}\cdot r} \tag{2.49}$$

we can rewrite the $\mathbf{R}$-matrix elements as

$$R_{11}(k) = \frac{n_1}{m_1}\left[\bar{\gamma}_{11}(k) - \bar{\gamma}_{11}(0) - \frac{n_2}{n_1}\bar{\gamma}_{12}(0)\right], \tag{2.50}$$

$$R_{12}(k) = \sqrt{\frac{n_1 n_2}{m_1 m_2}}\bar{\gamma}_{12}(k). \tag{2.51}$$

This shows that the diagonal elements are composed by two terms: a term describing collisions between particles of the same species and a term indicating collisions between particles of different species. In the long wavelength limit ($k \to 0$) conservation of momentum causes the intra–species term to vanish and leaving only the inter–species term. This, then, leads to the matrix elements being all proportional to each other and the damping matrix becomes a singular matrix

$$\mathbf{R}(0) = -\bar{\gamma}_{12}\begin{pmatrix} n_2/m_1 & -\sqrt{\frac{n_1 n_2}{m_1 m_2}} \\ -\sqrt{\frac{n_1 n_2}{m_1 m_2}} & n_1/m_2 \end{pmatrix}. \tag{2.52}$$

Exploiting the fact that $\det \mathbf{R} = 0 \Rightarrow R_{11}/R_{12} = R_{12}/R_{22}$, the real parts of χ_{AB} become

$$\begin{aligned} \chi'_{11}(k,\omega) &= \frac{n_1}{m_1}\frac{k^2}{|\mathcal{D}(k,\omega)|^2}\left\{\left[\omega^2 - C_{22}(k)\right]\left[\omega^2 - \omega_+^2(k)\right]\left[\omega^2 - \omega_-^2(k)\right]\right. \\ &\quad \left. + \omega^2 R_{22}\left(R_{11} + R_{22}\right)\left[\omega^2 - \omega_{\rm im}^2(k)\right]\right\}, \end{aligned} \tag{2.53}$$

$$\chi'_{22}(k,\omega) = \frac{n_2}{m_2}\frac{k^2}{|\mathcal{D}(k,\omega)|^2}\left\{\left[\omega^2 - C_{11}(k)\right]\left[\omega^2-\omega_+^2(k)\right]\left[\omega^2-\omega_-^2(k)\right] + \omega^2 R_{11}\left(R_{11}+R_{22}\right)\left[\omega^2-\omega_{im}^2(k)\right]\right\}, \tag{2.54}$$

$$\chi'_{12}(k,\omega) = -\sqrt{\frac{n_1 n_2}{m_1 m_2}}\frac{k^2}{|\mathcal{D}(k,\omega)|^2}\left\{C_{12}(k)\left[\omega^2 - \omega_+^2(k)\right]\left[\omega^2-\omega_-^2(k)\right] - \omega^2 R_{12}\left(R_{11}+R_{22}\right)\left[\omega^2-\omega_{im}^2(k)\right]\right\}, \tag{2.55}$$

and the imaginary parts

$$\chi''_{11}(k,\omega) = \frac{n_1 k^2}{m_1}\frac{\omega R_{11}}{|\mathcal{D}(k,\omega)|^2}\left[\omega^2-\omega_{*2}^2(k)\right]^2, \tag{2.56}$$

$$\chi''_{22}(k,\omega) = \frac{n_2 k^2}{m_2}\frac{\omega R_{22}}{|\mathcal{D}(k,\omega)|^2}\left[\omega^2-\omega_{*1}^2(k)\right]^2, \tag{2.57}$$

$$\chi''_{12}(k,\omega) = \sqrt{\frac{n_1 n_2}{m_1 m_2}}\frac{\omega R_{12} k^2}{|\mathcal{D}(k,\omega)|^2}\left[\omega^2-\omega_{*1}^2(k)\right]\left[\omega^2-\omega_{*2}^2(k)\right]. \tag{2.58}$$

We notice that the numerators of all the above expressions vanish at specific frequencies. These are commonly referred to as anti–resonances. Specifically, the numerators of $\chi'_{11}(k,\omega)$ and $\chi'_{22}(k,\omega)$ vanish at $C_{22}(k)$ and $C_{11}(k)$ respectively, only when terms of $O(\bar{\gamma}_{12}^2)$ are neglected, while those of $\chi''_{11}(k,\omega)$, $\chi''_{22}(k,\omega)$, and $\chi''_{12}(k,\omega)$ have exact zeros at ω_{*2} and ω_{*1}. The important thing to notice is that the zeros of $\chi''_{AB}(k,\omega)$, by means of the Fluctuation–Dissipation theorem eq. (1.45), become also the zeros of $S_{AB}(k,\omega)$. For future reference, the explicit expressions of $S_{AB}(k,\omega)$ are

$$S_{11}(k,\omega) = -\frac{k^2}{\pi\beta m_1}\frac{R_{11}}{|\mathcal{D}(k,\omega)|^2}\left[\omega^2-\omega_{*2}^2(k)\right]^2, \tag{2.59}$$

$$S_{22}(k,\omega) = -\frac{k^2}{\pi\beta m_2}\frac{R_{22}}{|\mathcal{D}(k,\omega)|^2}\left[\omega^2-\omega_{*1}^2(k)\right]^2, \tag{2.60}$$

$$S_{12}(k,\omega) = -\frac{k^2}{\pi\sqrt{\beta m_1 \beta m_2}} \frac{R_{12}}{|\mathcal{D}(k,\omega)|^2} \left[\omega^2 - \omega_{*1}^2(k)\right] \left[\omega^2 - \omega_{*2}^2(k)\right]. \tag{2.61}$$

In the next chapters we will show that ω_{*A}, to first order in k

- are independent of the absolute value of $\bar{\gamma}_{12}$,
- are independent of the coupling parameter, Γ, and therefore on the strength of correlations. Their derivation, however, is contingent on the quasi–localization of the charges.

They are, then, new characteristic frequencies of strongly coupled plasmas, dependent only on system's parameters *e.g.* charge, mass, and concentration of the species. We baptize these frequencies, with perhaps forgivable measure of self–indulgence, the **Silvestri–Kalman (SK)** frequencies.

2.4 Toy Model

In this section we present a simple toy model in order to elucidate on the physics of the anti–resonances. Consider two damped harmonic oscillators with different natural resonant frequencies, $\omega_1 = \sqrt{k_1/m_1}$ and $\omega_2 = \sqrt{k_2/m_2}$, coupled by a spring of constant q. Furthermore, assume that one of the two oscillators is driven by a small periodic force. The equations of motions are

$$\ddot{x}_1 + \frac{\gamma}{m_1}(\dot{x}_1 - \dot{x}_2) + \frac{k_1}{m_1}x_1 + \frac{q}{m_1}(x_1 - x_2) = a_1 e^{i\omega t}, \tag{2.62}$$

$$\ddot{x}_2 + \frac{\gamma}{m_2}(\dot{x}_2 - \dot{x}_1) + \frac{k_2}{m_2}x_2 - \frac{q}{m_2}(x_1 - x_2) = 0. \tag{2.63}$$

In order to simplify the notation we define the Fano frequency $\tilde{\omega}_A$ as

$$\tilde{\omega}_1^2 = \omega_1^2 + \sigma_{12}^2,, \quad \sigma_{12}^2 = \frac{q}{m_1}, \tag{2.64}$$

and the respective frequencies of the second oscillator are obtained by exchanging $1 \rightarrow 2$. The crucial assumption here is that the drag force is proportional to the relative velocity between the two oscillators. The solutions of this system of equations is given by the sum of the homogeneous solution ($a_1 = 0$) and the particular solution ($a_1 \neq 0$). Starting from the homogeneous equation, the normal modes of the system are

$$\Omega_{\mp}^2 = \frac{1}{2}\left\{\tilde{\omega}_1^2 + \tilde{\omega}_2^2 \pm \sqrt{\left(\tilde{\omega}_1^2 - \tilde{\omega}_2^2\right)^2 + 4\nu_{12}^2\nu_{21}^2}\right\}. \tag{2.65}$$

The $\mp$ subscript indicate whether the two oscillators move in-phase or out-of-phase with each other. The presence of damping (considered small) leads to a decaying exponential factor $e^{-\gamma_{\pm}t}$ to the homogeneous solution

$$x_1 = b_1 e^{-\gamma_+ t} e^{-i\Omega_+ t} + d_1 e^{-\gamma_- t} e^{-i\Omega_- t}. \tag{2.66}$$

In the case $a_1 \neq 0$, after an initial transient part ($\gamma_{\pm}t \gg 1$), the system will oscillate at the frequency ω of the driving force and the dynamical matrix, rewritten in terms of the $\mathbf{C}$ and $\mathbf{R}$ matrices, is

$$\omega^2\mathbf{I} - \mathbf{G} = \begin{pmatrix} \omega^2 - i\omega R_{11} - C_{11} & -i\omega R_{12} - C_{12} \\ -i\omega R_{21} - C_{21} & \omega^2 - i\omega R_{22} - C_{22} \end{pmatrix} \tag{2.67}$$

where

$$\mathbf{R} = \begin{pmatrix} -\gamma/m_1 & \gamma/m_1 \\ \gamma/m_2 & -\gamma/m_2 \end{pmatrix}, \qquad \mathbf{C} = \begin{pmatrix} \tilde{\omega}_1^2 & -\nu_{12}^2 \\ -\nu_{21}^2 & \tilde{\omega}_2^2 \end{pmatrix}. \tag{2.68}$$

The solutions of the system are then

$$x_1(t) = c_1(\omega)e^{i\omega t}, \quad x_2(t) = c_2(\omega)e^{i\omega t} \tag{2.69}$$

where

$$c_1(\omega) = -a_1 \left\{ \frac{(\omega^2 - C_{22})\,\mathcal{D}' + \omega R_{22}\mathcal{D}''}{|\mathcal{D}(\omega)|^2} + i\omega R_{22} \frac{(\omega^2 - \omega_{*2}^2)^2}{|\mathcal{D}(\omega)|^2} \right\}, \tag{2.70}$$

$$c_2(\omega) = a_1 \left\{ \frac{C_{21}\mathcal{D}' + \omega R_{21}\mathcal{D}''}{|\mathcal{D}(\omega)|^2} - i\omega \frac{R_{11}R_{22}}{R_{12}} \frac{(\omega^2 - \omega_{*1}^2)\,(\omega^2 - \omega_{*2}^2)}{|\mathcal{D}(\omega)|^2} \right\}, \tag{2.71}$$

and $\mathcal{D}$ is the determinant of $\omega^2\mathbf{I} - \mathbf{G}$. Looking at the real part we notice that, by neglecting terms of $O(\gamma^2)$, the amplitude c_1 vanishes at the resonant frequency of the second oscillator $\tilde{\omega}_2 = \sqrt{(k_2 + q)/m_2}$ while c_2 never vanishes. On the other hand, the imaginary part $\mathrm{Im}\{c_1(\omega)\}$ vanishes at the natural frequency of the second oscillator

$$\begin{aligned} \omega_{*2}^2 &= C_{22} - \frac{R_{12}}{R_{11}} C_{21} \\ &= \tilde{\omega}_2^2 - \nu_{21}^2 \\ &= \frac{k+q}{m_2} - \frac{q}{m_2} \\ &= \omega_2^2. \end{aligned} \tag{2.72}$$

Similarly, $\omega_{*1}^2 = \omega_1$ is the natural frequency of the first oscillator.

Plots of the absolute value of the amplitudes and their imaginary parts together with their phases are shown in the Fig. 2.1. Notice that the zeros of the imaginary parts corresponds to the frequencies at which each oscillator undergoes a phase change of π. In other words, for frequencies $\omega < \omega_{*1}$ the two oscillators move in phase with the driving force. At $\omega = \Omega_+$ the entire system is at resonance and the two oscillators are in phase with each other (symmetric mode). As the frequency is increased past the first resonance, $\omega > \Omega_+$, both oscillators move out of phase with the driving force until $\omega = \omega_{*2} \approx 1.5$ where the second oscillators starts moving out–of–phase with the driving force. At $\omega = \tilde{\omega}_2 \approx 1.68$ the amplitude c_1 vanishes at the first oscillator stops. At this frequency the first

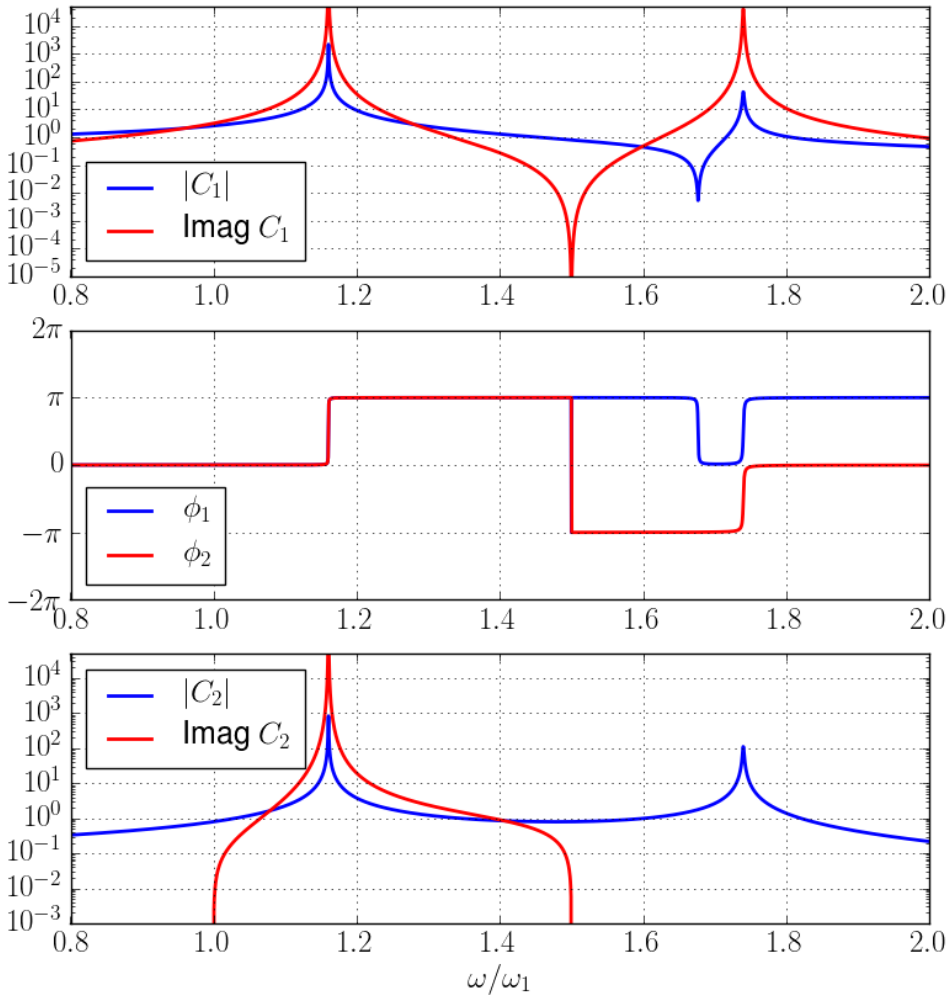

Figure 2.1: Plots of the complex amplitude of the two harmonic oscillators

oscillator experiences two equal and opposite forces that cancel each other: the driving force and the response of the second oscillator. Finally, further increasing the driving frequency the system reaches the second resonance, $\omega = \Omega_-$, where the two oscillators move out–of–phase with each other (anti-symmetric mode). Belbasi *et. al.* have given an alternative interpretation of the $\tilde{\omega}_{*2}$ frequency (Belbasi, Ebrahim Foulaadvand, and Joe, 2014). We can think of the equilibrium position of the first oscillator as being one of the nodes of the standing wave created by the right propagating wave of the driving force and the left propagating wave of the response of the second oscillator. However, in their investigation they do not consider the ω_{*2} frequency.

The important point to notice is that the zeros of the real and imaginary part of $c_1(\omega)$ are different from each other. In the literature, this toy model of driven coupled oscillators is often considered to be the classical analog of the quantum Fano effect (Joe, Satanin, and Kim, 2006; Miroshnichenko, Flach, and Kivshar, 2010). However, it must be said that this is somewhat erroneous since the Fano effect is the interference between a discrete state and a continuum of states (Fano, 1935; Fano, 1961), while in the case of two harmonic oscillators we have an interference between two discrete states.

We conclude this section by returning to our crucial assumption that the damping term is proportional to the relative velocities of the particles. If each oscillator were damped only by its own velocity then $R_{12} = 0$ which leads to $\omega_{*2} = C_{22}$ and no anti-resonance would be visible in the imaginary part of c_1 since $\det \mathbf{R} \neq 0$.

2.5 Coulomb Drag and Anti–resonances

The physical picture suggested by the Collisional QLCA is, in other words, of one species dragging the other. This, obviously, is reminiscent of a well known effect in GaAs electronic bilayer; the Coulomb Drag. In order to study elelectron–

electron interaction Russian physicist M. Pogrebinski proposed the following experiment (Pogrebinskii, 1977; Narozhny and Levchenko, 2016). Imagine two 2D conducting layers separated by a distance d and a driving current I_1 is ran through the first (active) layer. Due to the long range Coulomb interaction a current will be induced in the other (passive) layer. If the passive layer acts as an open circuit then a voltage drop V_2 would be measured, otherwise a current I_2 will be measured. Thus,the charge carriers in the active layers "drag" the charge carriers of the passive layer. The ratio

$$R_D = -\frac{V_2}{I_1} \tag{2.73}$$

defines the transresistance between the two layers and consequently the inter–layer interaction. Pogrebinskii derived a Drude-like formula for the two resistivities

$$\rho_D = -\rho_{xx}^{(12)} = \frac{m_2}{e^2 n_1 \tau_D}, \quad \rho_{xx}^{(11)} = \frac{m_1}{e^2 n_1}\left(\frac{1}{\tau} + \frac{1}{\tau_D}\right) \tag{2.74}$$

where 1,2 denote the two layers, τ is a relaxation time due to impurities in the system, and τ_D is the drag relaxation time of the drift currents between the two layers (Narozhny and Levchenko, 2016). In those years the semiconducting industry was booming and researcher started to study this phenomenon using GaAs double quantum well structures. Ref. (Rojo, 1999; Narozhny and Levchenko, 2016) are review papers dedicated entirely to the Coulomb drag effect showing the immense amount of interest that this phenomenon attracts. Nowadays, so called van der Waals materials have allowed for the creation of better and more robust electronic bilayers and thus, increasing the interest in Coulomb drag (Geim and Grigorieva, 2013). Most of the research is focused on the calculation of transport properties, specifically, on the transresistivity ρ_D and a qualitative understanding of the phenomenon can be claimed. In the case of semiconductor electronic bilayers, the driving current in the active layer creates electron-hole pairs with finite momen-

tum which is then transferred to the passive layer via the Coulomb interaction, creating again electron-hole pairs. However, creation of electron–hole pairs does not automatically creates a current in the passive layer since electrons and holes "move" opposite to each other thus leading to a zero total momentum. The net current is obtained thanks to the different effective masses of electrons and holes in semiconductors (Kamenev and Oreg, 1995).

The extensive research on Coulomb drag, however, has not mentioned the presence of anti–resonances in the response function (or at least I am not aware of any papers). The physical picture presented above is, obviously, specific to a quantum electron liquid, which is not what is being investigated in this thesis, but it has the basic element, asymmetry between constituent particle, for the existence of anti–resonances. Furthermore, much work has been done on what, in this thesis would be called, a weakly to moderately coupled electron liquid and research is ongoing in the case of a strongly coupled electron liquid. I am aware of only one paper which mentions the anti–resonance in the context of a 2D electron liquid and it is the one in Ref. (Kreil et al., 2018). The asymmetry in this system is given by two different spin orientations of the electron. A 3D strongly coupled electron liquid has also been investigated in terms of the Collisional QLCA and preliminary results are shown in Ref. (Kalman, Golden, and Silvestri, 2016).

CHAPTER III

Binary Coulomb Plasmas

In this chapter we will study plasmas composed of two positive ions species immersed in a neutralizing background of negative electrons. The system's variables and parameters are given in Sec. 1.3 of Chap. I. In here we recall only that $c = N_1/N$ is the concentration of species 1 and the coupling parameter Γ is given in eq. (1.11), and the asymmetry parameters are

$$p^2 = \frac{Z_2}{Z_1}\frac{(1-c)}{c}, \qquad q^2 = \frac{Z_2}{Z_1}\frac{m_1}{m_2}. \tag{3.1}$$

The particles interact via the unscreened Coulomb potential

$$\tilde{\phi}_{AB}(r) = \frac{Z_A Z_B e^2}{r}, \qquad \phi_{AB}(k) = \frac{4\pi Z_A Z_B e^2}{k^2}. \tag{3.2}$$

The rest of the chapter is structured as follows: Theoretical predictions are presented in Sec. 3.1, for the weakly coupled regime, and in Sec. 3.2 for the strongly coupled regime. These results are then compared with MD simulation in Sec. 3.3. The transition from weak to strong coupling is investigated in Sec. 3.4. Finally the chapter concludes with a computer experiment for the verification of the physics behind the Silvestri–Kalman frequencies in Sec. 3.5.

3.1 Weak Coupling Regime

In the weak coupling regime the external response functions, calculated using the RPA, are

$$\chi_{11}(k,\omega) = \frac{\chi_1^0(k,\omega)\left[1-\phi_{22}(k)\chi_2^0(k,\omega)\right]}{\varepsilon(k,\omega)}, \tag{3.3}$$

$$\chi_{12}(k,\omega) = -\frac{\chi_1^{(0)}(k,\omega)\phi_{12}(k)\chi_2^{(0)}(k,\omega)}{\varepsilon(k,\omega)}, \tag{3.4}$$

$$\chi_{22}(k,\omega) = \frac{\chi_2^0(k,\omega)\left[1-\phi_{11}(k)\chi_1^0(k,\omega)\right]}{\varepsilon(k,\omega)}, \tag{3.5}$$

where $\varepsilon(k,\omega)$ is the dielectric function

$$\varepsilon(k,\omega) = 1-\phi_{11}(k)\chi_1^0(k,\omega)-\phi_{22}(k)\chi_2^0(k,\omega), \tag{3.6}$$

and $\chi_A^0(k,\omega)$ the Vlasov polarization function which expressed in terms of the Plasma Dispersion function $W(x)$ is

$$\chi_A^0(k,\omega) = -\beta n_A\left[1+\zeta_A\mathcal{Z}(\zeta_A)\right], \quad \zeta_A = \frac{\omega}{k}\sqrt{\frac{\beta m_A}{2}}. \tag{3.7}$$

For references purposes the Plasma Dispersion function $\mathcal{Z}(\zeta)$ is

$$\mathcal{Z}(\zeta) = \frac{1}{\sqrt{\pi}}\int_{\infty}^{\infty}\frac{e^{-t^2}}{t-\zeta}dt, \quad \zeta = x+iy. \tag{3.8}$$

In the case of a real argument $y=0$ it can be expressed in terms of the Dawson integral, $\mathcal{D}(x)$, as

$$\mathcal{Z}(x) = -2\mathcal{D}_+(x)+i\sqrt{\pi}e^{-x^2}, \quad \mathcal{D}_+(x) = e^{-x^2}\int_0^x e^{t^2}dt. \tag{3.9}$$

Nowadays there exist a wealth of computer programs that calculate $\mathcal{Z}(x)$ directly, in this Thesis, we make use of the `SciPy` packages which uses the Faddeeva function $\mathcal{W}(z)$, defined by the complementary error function and related via the imaginary error function to the Dawson integral,

$$\mathcal{W}(z) = e^{-z^2}\mathrm{erfc}(-iz), \quad D(x) = \frac{\sqrt{\pi}}{2}e^{-x^2}\mathrm{erfi}(x), \tag{3.10}$$

Using $\mathcal{W}(z)$ the Vlasov response function becomes (*The Plasma Dispersion Function* 1961)

$$\chi_A^0(\zeta_A) = -\beta n_A \left[1 + i\sqrt{\pi}\mathcal{W}(\zeta_A)\right]. \tag{3.11}$$

The collective modes of the system are found from the solutions of the dispersion equation $\det \varepsilon(k,\omega) = 0$. At high frequencies ($\omega/k \gg \sqrt{1/\beta m_2} > \sqrt{1/\beta m_1}$, species 2 is the lighter species) the system supports a single plasmon mode with a finite frequency at $k = 0$ and positive k^2-dispersion. The explicit dispersion in the long–wavelength limit is

$$\omega_0^2(k \to 0) = \omega_p^2 + 3\frac{\omega_1^2 v_1^2 + \omega_2^2 v_2^2}{\omega_p^2}k^2, \tag{3.12}$$

where $\omega_p^2 = \omega_1^2 + \omega_2^2$ is the nominal total plasma frequency and $v_A^2 = 1/(\beta m_A)$ the thermal speeds of the particles. Since the system is considered to be collisionless, damping is due to wave-particle interactions and it is

$$\gamma_0(k) = \sqrt{\frac{\pi}{8}}\frac{\omega_0^2}{k^3}\left\{\frac{\omega_1^2}{v_1^3}\exp\left[-\frac{\omega_0^2}{k^2 v_1^2}\right] + \frac{\omega_2^2}{v_2^3}\exp\left[-\frac{\omega_0^2}{k^2 v_2^2}\right]\right\}. \tag{3.13}$$

The multi-component aspect of the system allows for a second solution to the dispersion equation in the regime $\sqrt{1/(\beta m_1)} \ll \omega/k \ll \sqrt{1/(\beta m_2)}$, however, this mode is highly damped and never really observed. Only in the case of a plasma

mixture with species at different temperatures, $T_2 \gg T_1$, one finds the solution

$$\omega_s(k \to 0) = v_{th} k, \qquad v_{th} = \sqrt{\frac{T_2}{m_1} + 3\frac{T_1}{m_1}}. \tag{3.14}$$

with the corresponding damping

$$\gamma_s(k) = \sqrt{\frac{\pi}{8}} v_{th} k \left\{ \sqrt{\frac{m_2}{m_1}} + \left(\frac{T_2}{T_1}\right)^{3/2} \exp\left[-\frac{T_2}{2T_1} - \frac{3}{2}\right] \right\}. \tag{3.15}$$

This mode is usually found in an electron–ion plasma and it is commonly called the "ion–acoustic mode". It is associated with plasma oscillations of the ions screened by the surrounding electron cloud. It can be rewritten also as

$$\omega_s(k \to 0) = \frac{\omega_{i,p}}{\varepsilon_e(k)} \tag{3.16}$$

where $\omega_{i,p}$ is the plasma frequency of the ions and $\varepsilon_e(k)$ the static dielectric function of the electrons.

Without further ado we calculate the partial dynamic structure functions $S_{AB}(k,\omega)$, using the Fluctuation–Dissipation theorem (1.45),

$$S_{11}(k,\omega) = -\frac{1}{\pi\beta n_1 \omega} \left[\frac{\mathrm{Im}\{\chi_1^0\} \left|1 - \phi_{22}\chi_2^0\right|^2}{|\varepsilon(k,\omega)|^2} + \frac{\phi_{22}\tilde{\phi}_{11} \,\mathrm{Im}\{\chi_2^0\} \left|\chi_2^0\right|^2}{|\varepsilon(k,\omega)|^2} \right], \tag{3.17}$$

$$\begin{aligned} S_{12}(k,\omega) \;=\; & -\frac{\phi_{12}(k)}{\pi\beta\sqrt{n_1 n_2}\omega} \left[\frac{(\mathrm{Im}\{\chi^0\}_1 \,\mathrm{Re}\{\chi_2^0\} + \mathrm{Im}\{\chi_2^0\} \,\mathrm{Re}\{\chi_1^0\}) \,\mathrm{Re}\{\varepsilon\}}{|\varepsilon(k,\omega)|^2} \right. \\ & \left. - \frac{(\mathrm{Re}\{\chi_1^0\} \,\mathrm{Re}\{\chi_2^0\} - \mathrm{Im}\{\chi_1^0\} \,\mathrm{Im}\{\chi_2^0\}) \,\mathrm{Im}\{\varepsilon\}}{|\varepsilon(k,\omega)|^2} \right], \end{aligned} \tag{3.18}$$

$$S_{22}(k,\omega) = -\frac{1}{\pi\beta n_2 \omega} \left[\frac{\mathrm{Im}\{\chi_2^0\} \left|1 - \phi_{11}\chi_1^0\right|^2}{|\varepsilon(k,\omega)|^2} + \frac{\phi_{11}\tilde{\phi}_{22} \,\mathrm{Im}\{\chi_1^0\} \left|\chi_1^0\right|^2}{|\varepsilon(k,\omega)|^2} \right]. \tag{3.19}$$

its line plots for four low values of ka in Fig. 3.1 and intensity plots in Fig. 3.2. In

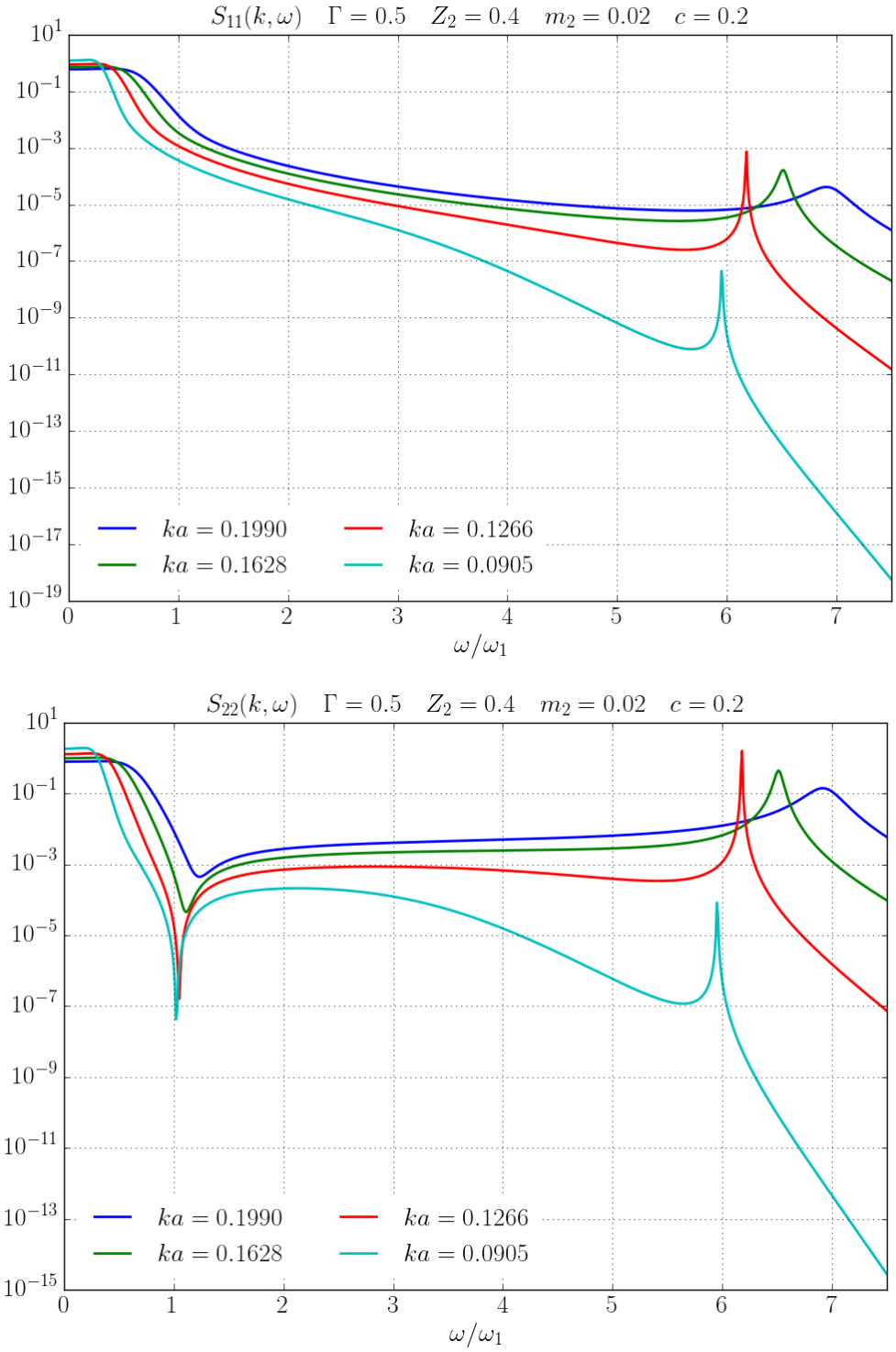

Figure 3.1: Line plots of $S_{11}(k,\omega)$ (top) and $S_{22}(k,\omega)$ (bottom) at four different ka values. The asymmetry parameters are indicated in the plots' titles.

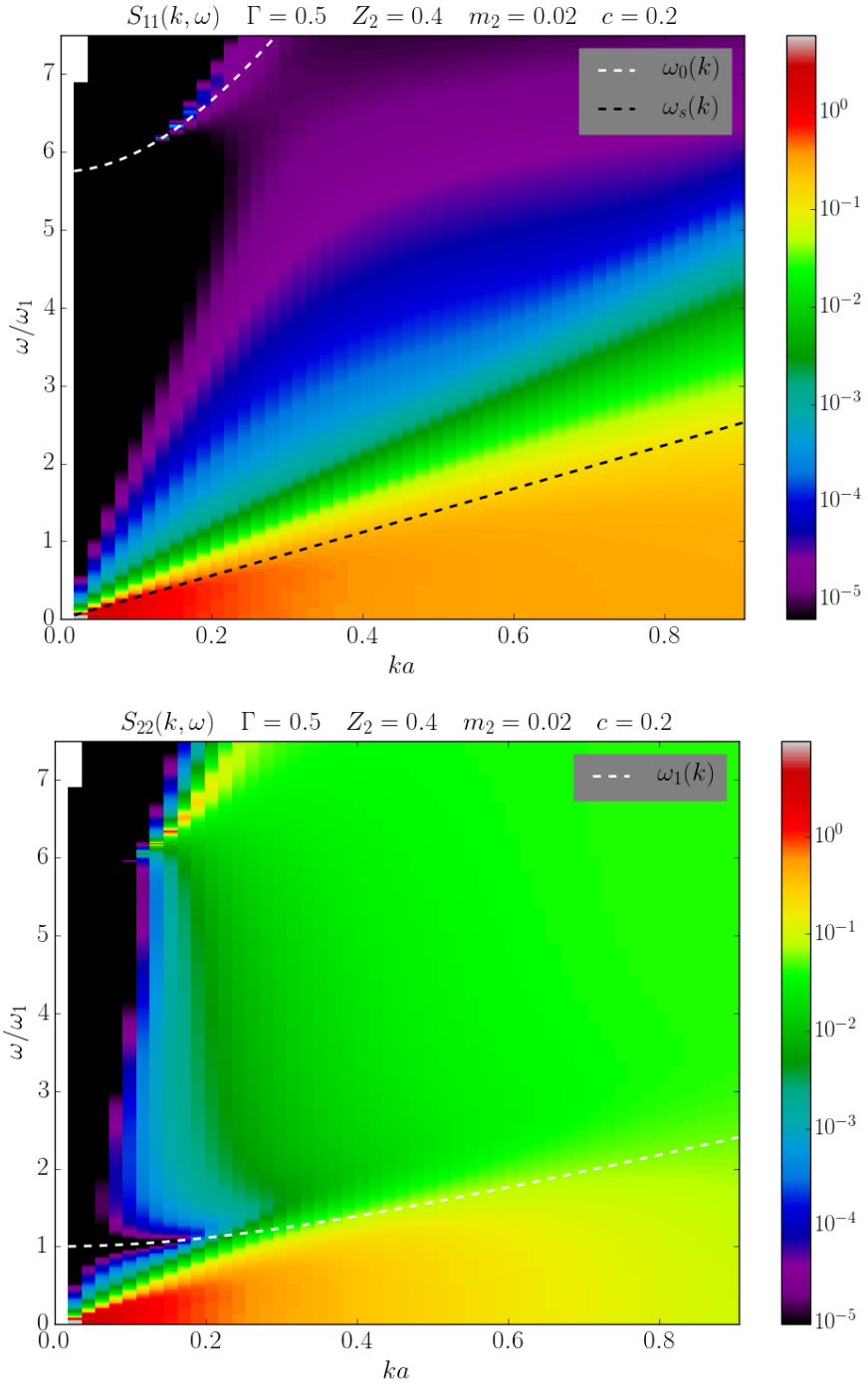

Figure 3.2: Intensity plots of $S_{11}(k,\omega)$ (top) and $S_{22}(k,\omega)$ (bottom) for the set of asymmetry parameters indicated in the plots' titles. White dashed lines and black dashed lines are described in the text. Notice that the lowest ka is 0.0189, therefore the white column at $ka = 0.0$ is the empty part of the plots.

both plots we observe the RPA plasmon mode $\omega_0(k)$ at $\omega \approx 6\omega_1$ moving rightward to higher frequencies with increasing ka. The interesting feature is the sharp minimum found in $S_{22}(k,\omega)$ at $\omega = \omega_1$. This is not the Silvestri–Kalman anti–resonance, but its equivalent in a weakly coupled mixture. Looking at eq. (3.19) we immediately notice that, neglecting the second term, $S_{22}(k,\omega)$ has a zero whenever $1 - \tilde{\phi}_{11}(k)\chi_1^0(k,\omega) = 0$. This is none other than the dispersion relation of an OCP composed by species 1. The second term is negligibly small due to the large mass difference since

$$\mathrm{Im}\{\chi_1^0\}/\,\mathrm{Im}\{\chi_2^0\} \propto m_2/m_1 \ll 1. \tag{3.20}$$

The zero of $S_{22}(k,\omega)$ is at

$$\omega_1^2(k) = \omega_1^2 + 3v_1^2k^2. \tag{3.21}$$

No anti–resonance is visible in $S_{11}(k,\omega)$ because its second term in eq. (3.17) is non–negligible. The above dispersion relations are visible in color maps of $S_{AB}(k,\omega)$ shown in Fig. 3.2. In these plots peaks of $S_{AB}(k,\omega)$ are identified with a red-white color, while anti-resonances with a purple-black color. Both plots show the positive k^2 plasmon dispersion at high frequencies. The white dashed line in the plot of $S_{11}(k,\omega)$ represents dispersion (3.12). In the plot of $S_{22}(k,\omega)$ we observe the anti–resonance as a dark region around $\omega/\omega_1 \approx 1$ which becomes narrower as ka increases up to 0.2. The white dashed line in the plot of $S_{22}(k,\omega)$ represents dispersion (3.21).

We would like to point out the similarity with the toy model presented in Sec. 2.4 of the previous chapter. As mentioned at the end of it the zeros of the real and imaginary part of the response functions coincide whenever there is no inter–species damping. We conclude by noting that no "ion–acoustic" peak is visible in any of the above plots. This mode, in fact, is masked by the large damping as represented by the wide red–yellow region below the black dashed line representing dispersion

(3.14). We conclude this section with Table. 3.1 indicating the numerical values of the frequencies discussed above.

ω_1	ω_2	ω_p
1	5.657	5.744

Table 3.1: Tabulated values of the relevant frequencies for the mixture shown in Figs. 3.1– 3.2 (in units of ω_1). $Z_1 = m_1 = 1$.

3.2 Strong Coupling Regime

Strong coupling brings new features in the Dynamic Structure Factor and in this section we will use the Collisional QLCA to identify and describe them. Similar to the weak coupling case we start by calculating the collective modes from the dispersion relation and we conclude with the calculation of the Silvestri–Kalman frequencies.

The principal quantity of interest is the dynamical matrix $\mathbf{G}(\mathbf{k},\omega) = -i\omega\mathbf{R}(\mathbf{k}) + \mathbf{C}(\mathbf{k})$. The elements of $\mathbf{C}(\mathbf{k})$ are

$$C_{11}(k) = \omega_1^2\left[1+\frac{1}{3}p^2-2D_{11}(k)\right], \tag{3.22a}$$

$$C_{12}(k) = \omega_1^2\left[\frac{2}{3}pq-2pqD_{12}(k)\right], \tag{3.22b}$$

$$C_{22}(k) = \omega_1^2\left[q^2p^2+\frac{1}{3}q^2-2q^2p^2D_{22}(k)\right], \tag{3.22c}$$

with

$$D_{AB}(k) = \int \frac{dr}{r}h_{AB}(r)\left[\frac{\sin(kr)}{kr}+3\frac{\cos(kr)}{(kr)^2}-3\frac{\sin(kr)}{(kr)^3}\right]. \tag{3.23}$$

Details of the derivation of the above formulas are given in Appendix C.1.

3.2.1 Collective Modes

As shown in the previous chapter the solutions of the $\det \varepsilon(k,\omega) = 0$ are equivalent to those of

$$\mathcal{D}(k,\omega) = \left[\omega^2 - \omega_+^2(k)\right]\left[\omega^2 - \omega_-^2(k)\right] - i\omega\left(R_{11} + R_{22}\right)\left[\omega^2 - \omega_{\rm im}^2(k)\right], \quad (3.24)$$

where $\omega_\pm(k)$ are the eigenvalues of the $\mathbf{C}(k)$ matrix

$$\omega_\pm^2 = \frac{\omega_1^2}{2}\left\{\mathrm{Tr}\,\mathbf{C}(k) \pm \sqrt{\mathrm{Tr}\,\mathbf{C}(k)^2 - 4\det\mathbf{C}(k)}\right\}, \quad (3.25a)$$

$$\mathrm{Tr}\,\mathbf{C}(k) = 1 + q^2p^2 + \frac{p^2+q^2}{3} - 2\left[D_{11}(k) + q^2p^2D_{22}(k)\right], \quad (3.25b)$$

$$\begin{aligned}\det\mathbf{C}(k) &= \frac{q^2\left(1+p^2\right)^2}{3}\left[1 - 2\frac{D_{11} + 2p^2D_{12} + p^4D_{22}}{\left(1+p^2\right)^2}\right] \\ &\quad -2q^2p^2\left[D_{11} - 2D_{12} + D_{22} - 2\left(D_{11}D_{22} - D_{12}^2\right)\right]. \quad (3.25c)\end{aligned}$$

Since $\det\mathbf{C}(k=0) \neq 0$ we find two plasmon modes with finite frequencies given by

$$\omega_\pm^2(0) = \frac{\omega_1^2}{2}\left\{1 + q^2p^2 + \frac{q^2+p^2}{3} \pm \sqrt{\left(1 + q^2p^2 + \frac{q^2+p^2}{3}\right)^2 - \frac{4}{3}q^2(1+p^2)^2}\right\}, \quad (3.26)$$

which rewritten in terms of characteristic frequencies become

$$\omega_\pm^2(0) = \frac{\omega_p^2}{2} + \frac{\Omega_{12}^2 + \Omega_{21}^2}{6} \pm \frac{1}{2}\sqrt{\left(\omega_p^2 + \frac{\Omega_{12}^2 + \Omega_{21}^2}{3}\right)^2 - 4\omega_{\rm vaa}^2\frac{\Omega_{12}^2 + \Omega_{21}^2}{3}}, \quad (3.27)$$

$$\Omega_{AB}^2 = \frac{4\pi Z_A}{m_A}Z_B n_B e, \quad (3.28)$$

$$\omega_{\rm vaa}^2 = \frac{4\pi\left\langle Z^2\right\rangle n_0 e^2}{\langle m\rangle} \quad (3.29)$$

with $\omega_p^2 = \omega_1^2 + \omega_2^2$ being the total plasma frequency. Ω_{AB} represents the oscillation frequency of a particle of species A in the frozen environment of particles of species B. ω_{vaa} is the called the hydrodynamic frequency or Virtual Average Atom (VAA) frequency and it corresponds to the plasma frequency of an OCP created by the average charge and mass of the components (Hansen, McDonald, and Vieillefosse, 1979). In the above equation we recall that $\langle A \rangle = Ac_1 + Ac_2$ which leads to $\omega_{vaa} < \omega_p$.

The diagonalization of the matrix $\omega^2 \mathbf{I} - \mathbf{C}(\mathbf{k}, \omega)$ allows us to retrieve information on the "polarization" of these modes. The high frequency mode ω_+, represents the mode in which particles of different species move in–phase, while the out–of–phase motion corresponds to the low frequency mode ω_-.

At the other end of the spectrum, $k \to \infty$, the $\mathbf{C}(k)$ matrix becomes diagonal and the collective modes become exactly the nominal Einstein frequencies

$$\omega_+^2(k \to \infty) = \frac{\omega_1^2 + \Omega_{12}^2}{3}, \quad \omega_-^2(k \to \infty) = \frac{\omega_2^2 + \Omega_{21}^2}{3}, \tag{3.30}$$

which, similar to eq. (3.28), represent the oscillation frequency of a particle of species A in the frozen environment of particles of species A and B. This short wavelength behaviour is somewhat expected since at such short wavelength $\lambda \ll a$ the wave couples only to the single particle motion.

3.2.2 Silvestri–Kalman Frequencies

As shown in the previous chapter the main frequencies of interest are the zeros of the real and imaginary part of the external response functions. These anti-resonances are easily calculated from the elements of the dynamical matrix. Neglecting terms of $O(R_{AB}^2)$ in eq. (2.53)-(2.57), at $k = 0$, the zeros of the real

part of $\chi_{AB}(k,\omega)$ are

$$C_{11}(0) = \omega_1^2 + \frac{\Omega_{12}^2}{3}, \tag{3.31}$$

$$C_{22}(0) = \omega_2^2 + \frac{\Omega_{21}^2}{3}. \tag{3.32}$$

which we name Fano frequencies. The anti–resonances of the imaginary part, $\omega_{*1,2}$, are calculated from eqs. (2.38)–(2.39). As mentioned before at $k = 0$ the term in R_{AB} representing the intraspecies collision vanishes while the interspecies term remains finite. Thus, all the elements of $\mathbf{R}$ become proportional to a single collisional frequency, $\bar{\gamma}_{12}$. Rewriting $\mathbf{R}$ in unit of ω_1 and casting all the details in a nominal collisional frequency ν we have

$$\mathbf{R} = -\nu \begin{pmatrix} n & -\sqrt{n/m} \\ -\sqrt{n/m} & 1/m \end{pmatrix}, \tag{3.33}$$

which when used in conjunction with eq. (2.38) and eq. (2.39) leads to the Silvestri–Kalman (SK) frequencies

$$\omega_{*1}^2(0) = \omega_1^2(1+p^2) = \omega_1^2 + \Omega_{12}^2, \tag{3.34}$$

$$\omega_{*2}^2(0) = \omega_1^2 q^2(1+p^2) = \omega_2^2 + \Omega_{21}^2 \tag{3.35}$$

As mentioned before they are independent of the collisional frequency, ν, and are entirely defined by the physical parameters of the system. We also notice that, using the neutrality condition $Z_1 n_1 e + Z_2 n_2 e - e n_e = 0$, each frequency can be rewritten in terms of the electronic background density

$$\omega_{*A}^2(0) = \frac{4\pi Z_A e n_A}{m_A}\left(Z_1 n_1 e + Z_2 n_2 e\right) = \frac{4\pi Z_A e n_A}{m_A} n_e e. \tag{3.36}$$

We point out that the SK frequency should not be confused with the oscillation frequency of an ion A in the frozen negative background, as this frequency contains a factor $1/\sqrt{3}$

$$\omega_{*A}^2 = 3\Omega_{E,A}^2, \quad \Omega_{E,A}^2 = \frac{4\pi}{3}\frac{Z_A e n_A}{m_A} n_e e \tag{3.37}$$

The other relevant frequency is the zero of the imaginary part of the dispersion relation, $\omega_{\rm im}$. Using eq. (2.41) at $k = 0$, we find

$$\omega_{\rm im}^2(0) = \omega_1^2 \frac{q^2(1+p^2)^2}{q^2+p^2} = \frac{\omega_{*1}^2(0)\omega_{*2}^2(0)}{\Omega_{12}^2 + \Omega_{21}^2} = \frac{4\pi \langle Ze \rangle^2 n_0}{\langle m \rangle} = \omega_{\rm vaa}^2. \tag{3.38}$$

discussion of the implication of this equality is left for later.

At finite k intra–species and inter–species collisional become relevant and knowledge of the functional form of $\nu_{AB}(k)$ is needed for the calculations of the SK frequencies. However, assuming for the moment that these effects can be neglected we can look at the short wavelength limit of these frequencies, which, similarly to the collective modes, become the nominal Einstein frequencies at short wavelengths

$$\omega_{*A}^2(k \to) = C_{AA}(k \to \infty) = \frac{\omega_A^2 + \Omega_{AB}^2}{3} \tag{3.39}$$

and

$$\omega_{\rm im}^2(k \to \infty) = \frac{\omega_{vaa}^2}{3}. \tag{3.40}$$

In Fig. 3.3 we show the dispersion of all the frequencies (collective modes, Fano, Silvestri–Kalman, etc.) in order to show their positions with respect to each other. The pair distribution $g_{AB}(r)$ computed in MD simulations has been used for making of this plot. At $k = 0$ we notice the hierarchy

$$\omega_-(0) < \sqrt{C_{11}(0)} < \omega_{*1}(0) < \omega_{\rm im}(0) < \omega_+(0) < \sqrt{C_{22}(0)} < \omega_{*2}(0), \tag{3.41}$$

as confirmed by the above equations and it remains valid for any set of asymmetry parameters q, p. At $k \to \infty$ all the frequencies reach their Einstein frequencies $\omega_{E1,2}$. It is interesting to note that the collective modes and SK frequencies intersect in multiple ka values which correspond to $C_{12}(ka) = 0$, more about this will be discussed later. As for $\omega_{\rm im}$ no intersection is found as expected since it represents a weighted average of the SK frequencies.

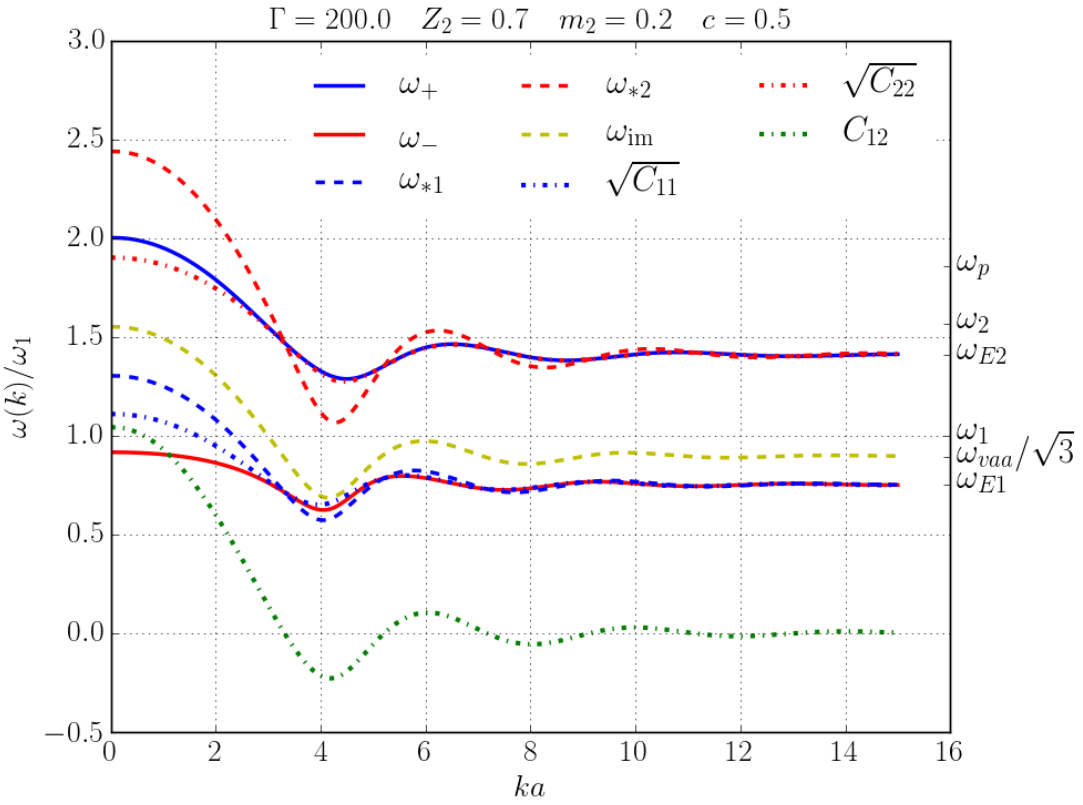

Figure 3.3: Dispersions of the relevant QLCA frequencies in units of ω_1. The collective mode are indicated by solid lines, Silvestri–Kalman frequencies by dashed lines, QLCA Dynamical matrix elements by dashed-dot lines. On the right side of the plot the values of characteristic frequencies are indicated.

3.3 Results and Discussion

In this section we will compare the theoretical results with MD simulations starting with the weak coupling regime followed by the strong coupling regime. Before moving on we point out a discrepancy, noticed too late to rectify. The Γ value reported in plots' titles does not correspond to $\Gamma_{\rm ion}$ defined in eq. (1.11). The Γ reported in the plots' titles is

$$\Gamma = \Gamma_1 = \frac{e^2\beta}{a_1}, \quad a_1^3 = \frac{3}{4\pi n_1}. \tag{3.42}$$

This means that

$$\Gamma_{\rm ion} = \Gamma\frac{a_1}{a} = \Gamma(1+n)^{1/3} \Rightarrow \Gamma_{\rm ion} > \Gamma. \tag{3.43}$$

Furthermore, we recall that neither Γ nor $\Gamma_{\rm ion}$ are representative of the real effective coupling of the mixture. However, the difference between $\Gamma, \Gamma_{\rm ion}, \Gamma$eff is not crucial for the purpose of this Thesis, where we are only concerned with strong coupling effects in general and not in the determination of an exact coupling parameter.

3.3.1 Weak Coupling

In Figs. 3.4–3.5 we show plots of $S_{AB}(k,\omega)$ at the lowest coupling values, available from MD simulations, for two sets of asymmetry parameters. Solid lines represent MD data while dashed lines, $S_{AB}(k,\omega)$ calculated using the RPA. The latter have been multiplied by a factor of 2 in order to lay on top of the MD lines (likely due to a normalization factor in simulations). Furthermore, plots for the second and third ka values have been shifted upwards for better viewing, both MD and RPA. In the plots of $S_{22}(k,\omega)$ we indicate the location of the plasmon $\omega_0(k)$. The plots show very good agreement between RPA and MD overall. This is somewhat unexpected since the RPA is considered exact at $\Gamma = 0$ and at finite Γ one

expects some disagreement due to the presence of correlational effects neglected by the RPA. The only disagreement is found in the profile of the plasmon peak which is predicted to be narrower by the RPA. A slight shift to lower frequencies is also observed at $\Gamma = 0.5$ in Fig. 3.5 likely due to correlational effects. The important feature is the presence of an anti–resonance in the dynamic structure function of the light component, $S_{22}(k,\omega)$, while no anti–resonance is found in $S_{11}(k,\omega)$. As explained in Sec. 3.1 this is due to the small mass ratio $m_2/m_1 = 0.02$ which causes the second term in $S_{22}(k,\omega)$ to be negligible while it is non–negligible in $S_{11}(k,\omega)$. Both the plasmon peak and the anti–resonance are clearly visible only at the lowest ka and are immediately broadened in the next two lowest ka values.

In the Figures we note also the faint presence of a low frequency peak at $\omega/\omega_1 < 1$. This peak is better visible in the total $S_{ZZ}(k,\omega)$ as shown by Fig. 3.6. While its existence is arguable for the second set of asymmetry parameters (bottom plot), a peak is evident at the lowest ka value in the first set (top plot). This peak is the "ion–acoustic mode" $\omega_s(k)$ of eq. (3.14) and like the plasmon is highly damped at higher ka. The dispersion of both the plasmon and "ion–acoustic" mode is shown in color maps of $L_{AB}(k,\omega)$ in Figs. 3.7–3.8, with the plasmon dispersion indicated by a solid white line and the dispersion of the "ion–acoustic" mode by a dashed white line.

$\omega_{F1}(ka_{min})$	$\omega_{*1}(0)$	$\omega_{F2}(ka_{\min})$	$\omega_{*2}(0)$	ω_p	$\omega_0(ka_{min})$	ω_{vaa}
1.1028	1.1255	4.6337	7.1181	3.4156	4.6437	1.2625
1.0915	1.6125	6.4475	7.2111	5.7446	6.5028	2.5019

Table 3.2: Tabulated values of all the frequencies of the system (in units of ω_1). $Z_1 = m_1 = 1$. The first row represent Set 1: $\Gamma = 0.2$, $Z_2 = 0.8$, $m_2 = 0.02$, $c = c_1 = 0.75$. Second row Set 2: $\Gamma = 0.5$, $Z_2 = 0.4$, $m_2 = 0.02$, $c = c_1 = 0.2$

Before moving on we spend few words on the polarization of these two modes. As said before, in an OCP the plasmon mode represents the out-of–phase motion

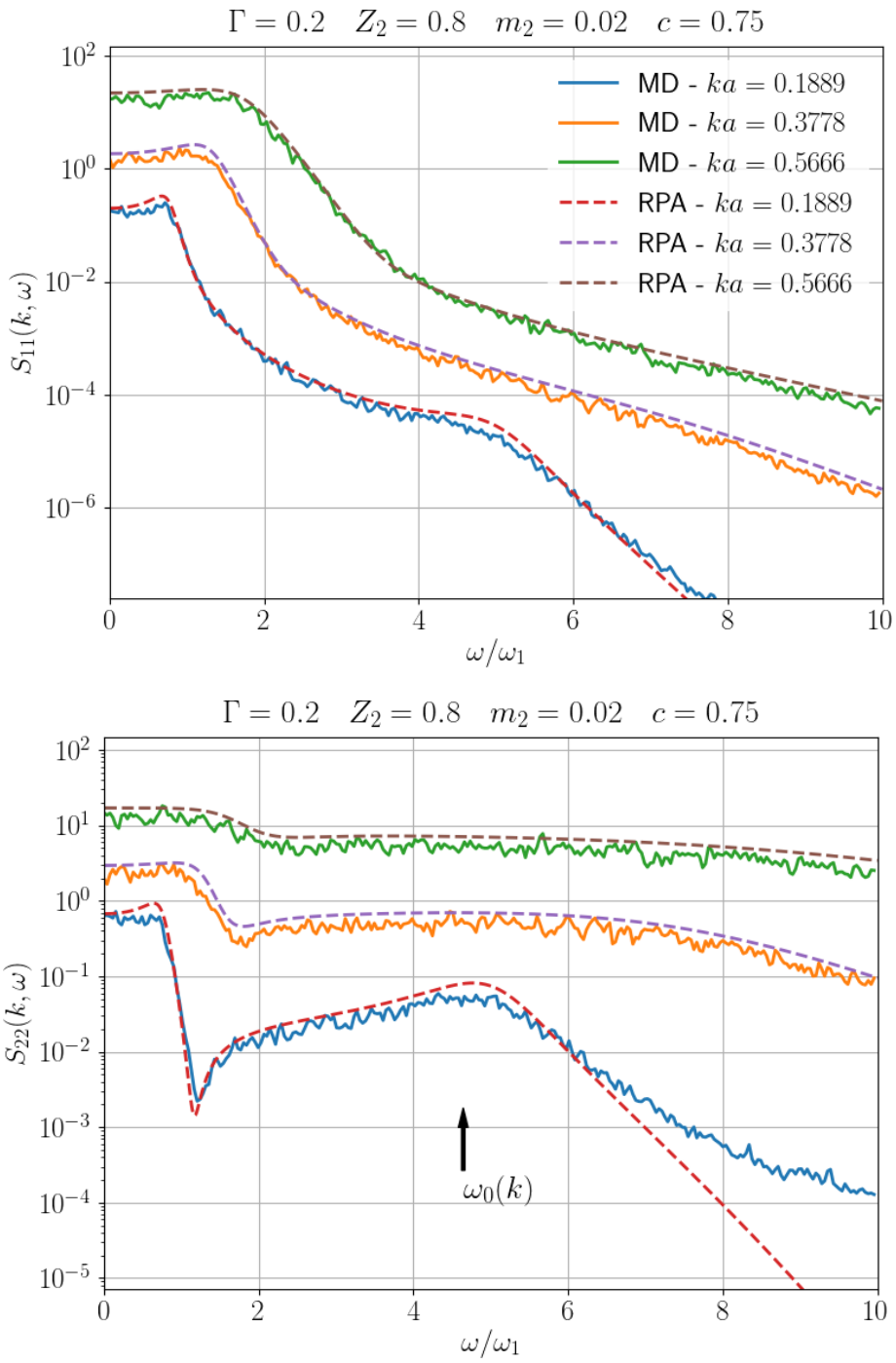

Figure 3.4: Comparison between the RPA and MD $S_{11}(k,\omega)$ (top) and $S_{22}(k,\omega)$ (bottom) for the lowest three values of ka reached in simulations. The asymmetry parameters are shown in the titles. Solid lines represent MD data, dashed lines RPA calculations. The second (third) ka line have been multiplied by a factor of 10 (100) for better viewing.

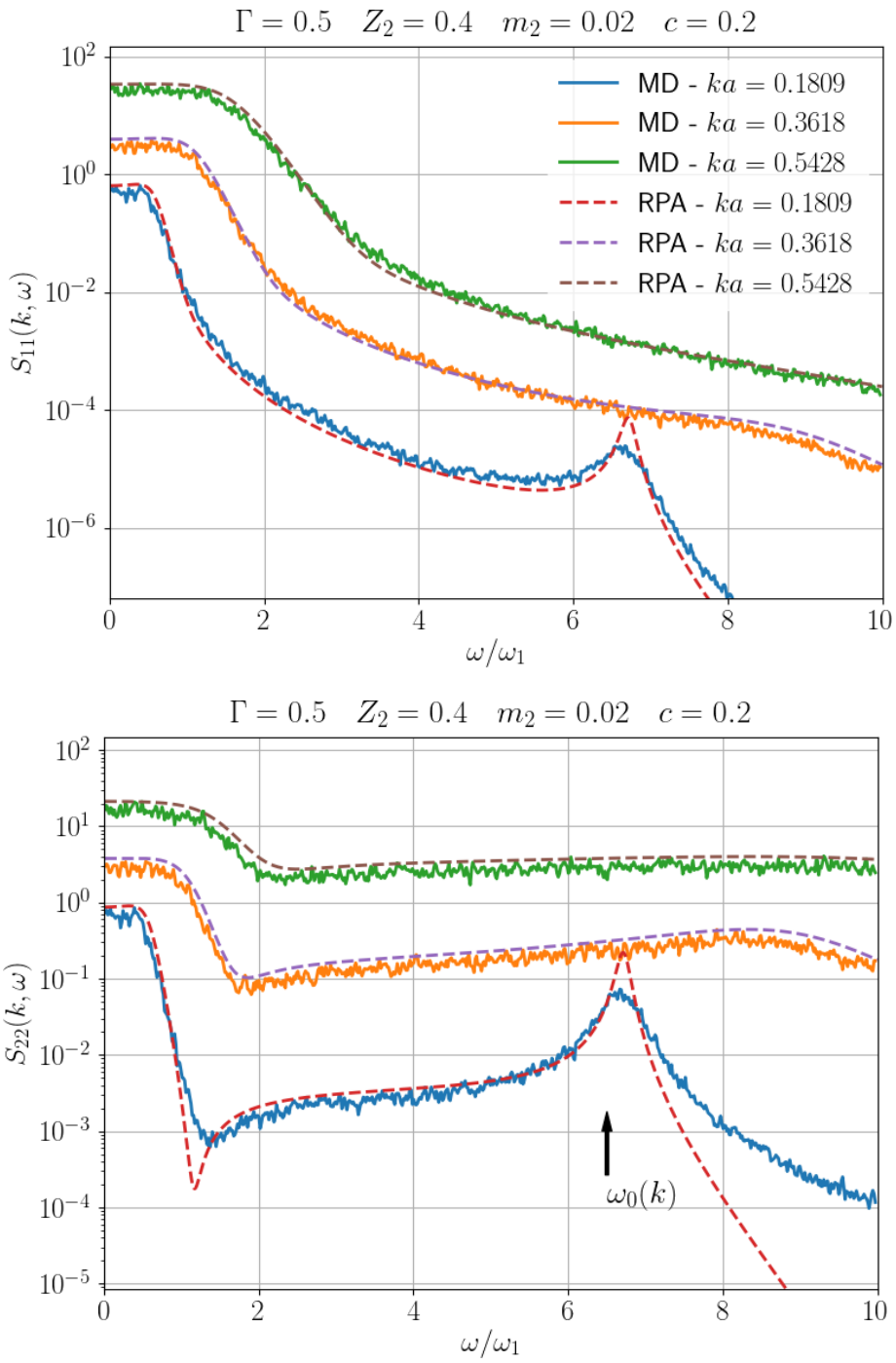

Figure 3.5: Comparison between the RPA and MD $S_{11}(k,\omega)$ (top) and $S_{22}(k,\omega)$ (bottom) for the lowest three values of ka reached in simulations. The asymmetry parameters are shown in the titles. Solid lines represent MD data, dashed lines RPA calculations. The second (third) ka line have been multiplied by a factor of 10 (100) for better viewing.

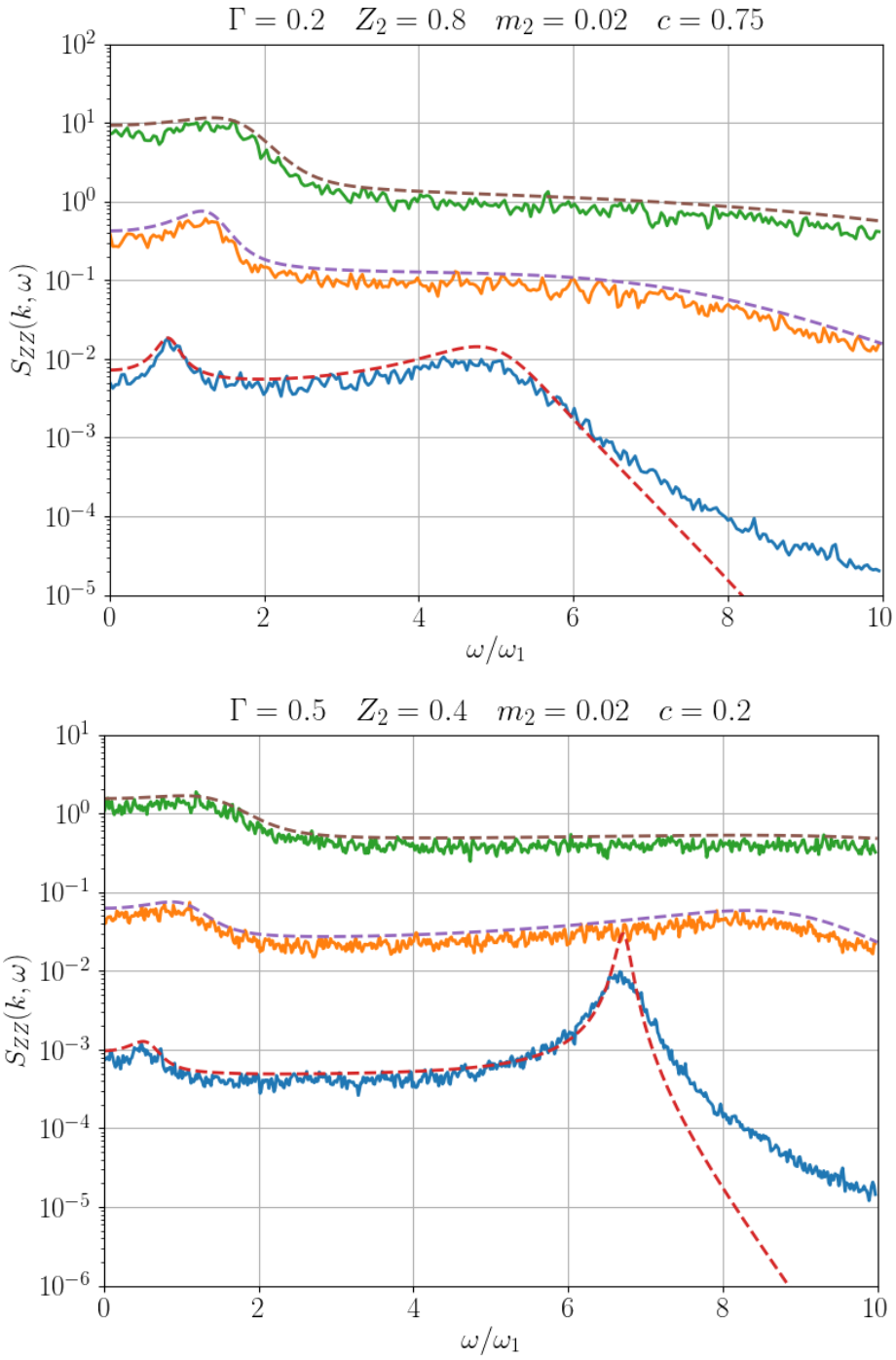

Figure 3.6: Plot of $S_{ZZ}(k,\omega)$ for the asymmetry parameters shown in Figs. 3.4–3.5.

of all the ions with respect to the negative electronic background, while the "ion–acoustic" mode of an electron–ion plasma to plasma oscillation of the ions screened by the electron cloud. Direct comparison with the OCP leads to the interpretation of $\omega_0(k)$, in the binary ionic mixture, to the in–phase motion between the two ion species (while the still being out–of–phase with respect to the negative electronic background). This leads then to the identification of the acoustic mode $\omega_s(k)$ with the out–of–phase motion between the two ion species. This physical picture can be checked and confirmed by looking at the inter-species correlation functions $S_{12}(k,\omega)$ and $L_{12}(k,\omega)$. Plots of MD $L_{12}(k,\omega)$ are shown in Fig. 3.9. In here we notice a negative peak at low frequencies, representative of $\omega_s(k)$, and a positive one at high frequencies, representative of $\omega_0(k)$. We must note that this is different than the coupled harmonic oscillator model in which the high frequency mode is the out–of–phase mode. This is because $\omega_0(k)$ is the only mode that survives at $T = 0$, hence, it is the multi–component counterpart of the plasmon of an OCP. For the sake of completeness we report all the values of the relevant frequencies of the asymmetry parameters used in the plots in Table 3.2.

We conclude this part by mentioning a special case. The acoustic solution, $\omega_s(k)$, exists only in a binary mixture at finite temperature and within the range $v_1 \ll \omega/k \ll v_2$. In our case given that the two masses are different the two thermal speeds are different, however, we can also have the case $m_1 = m_2$ and $T_1 \neq T_2$. This is a less realistic situation in classical plasma, but it is realizable in a quantum electron gas. The duality of the system is obtained by considering the electron gas as composed by two species: one with spin up and one with spin down. The difference in temperature is then achieved by different populations of each spin species (recall that temperature is proportional to the electron density). Such a system has been considered by Agarwal *et al.* in Ref. (Agarwal et al., 2014) in which $\omega_s(k)$ is called the spin-plasmon.

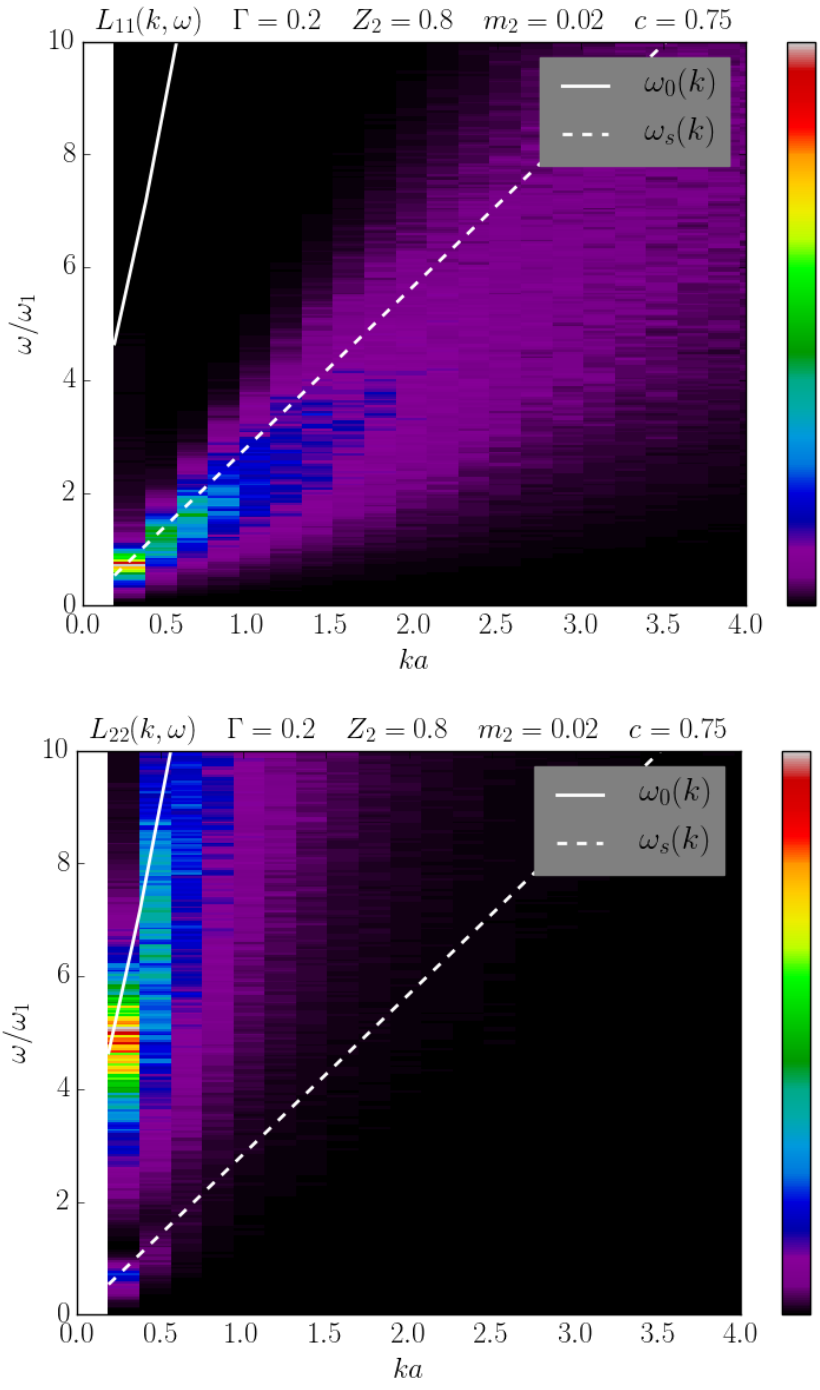

Figure 3.7: Intensity plots of $L_{11}(k,\omega)$ (top) and $L_{22}(k,\omega)$ (bottom) for the asymmetry parameters shown in the titles. The dashed white lines indicate the dispersion calculated from eq. (3.12).

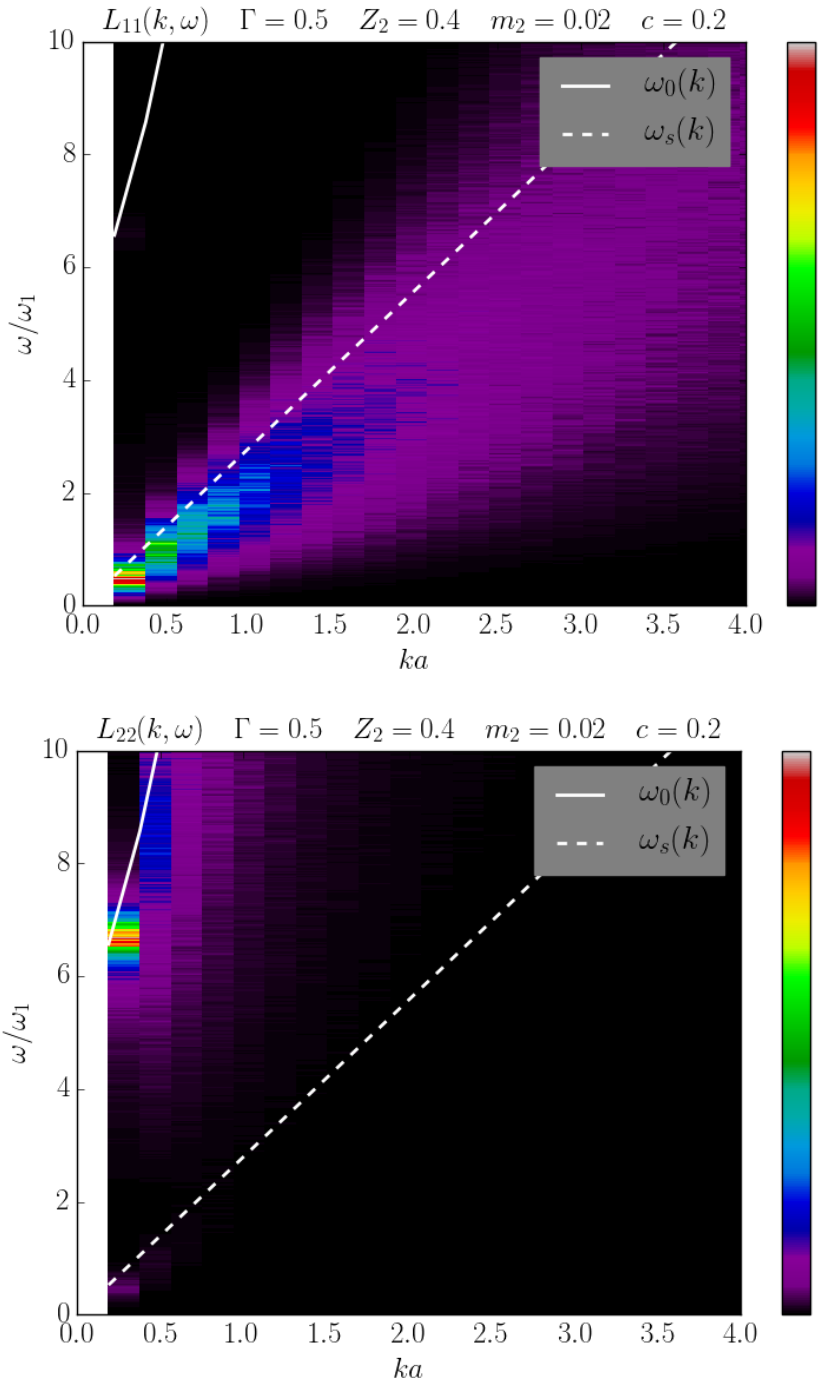

Figure 3.8: Intensity plots of $L_{11}(k,\omega)$ (top) and $L_{22}(k,\omega)$ (bottom) for the asymmetry parameters shown in the titles. The dashed white lines indicate the dispersion calculated from eq. (3.12).

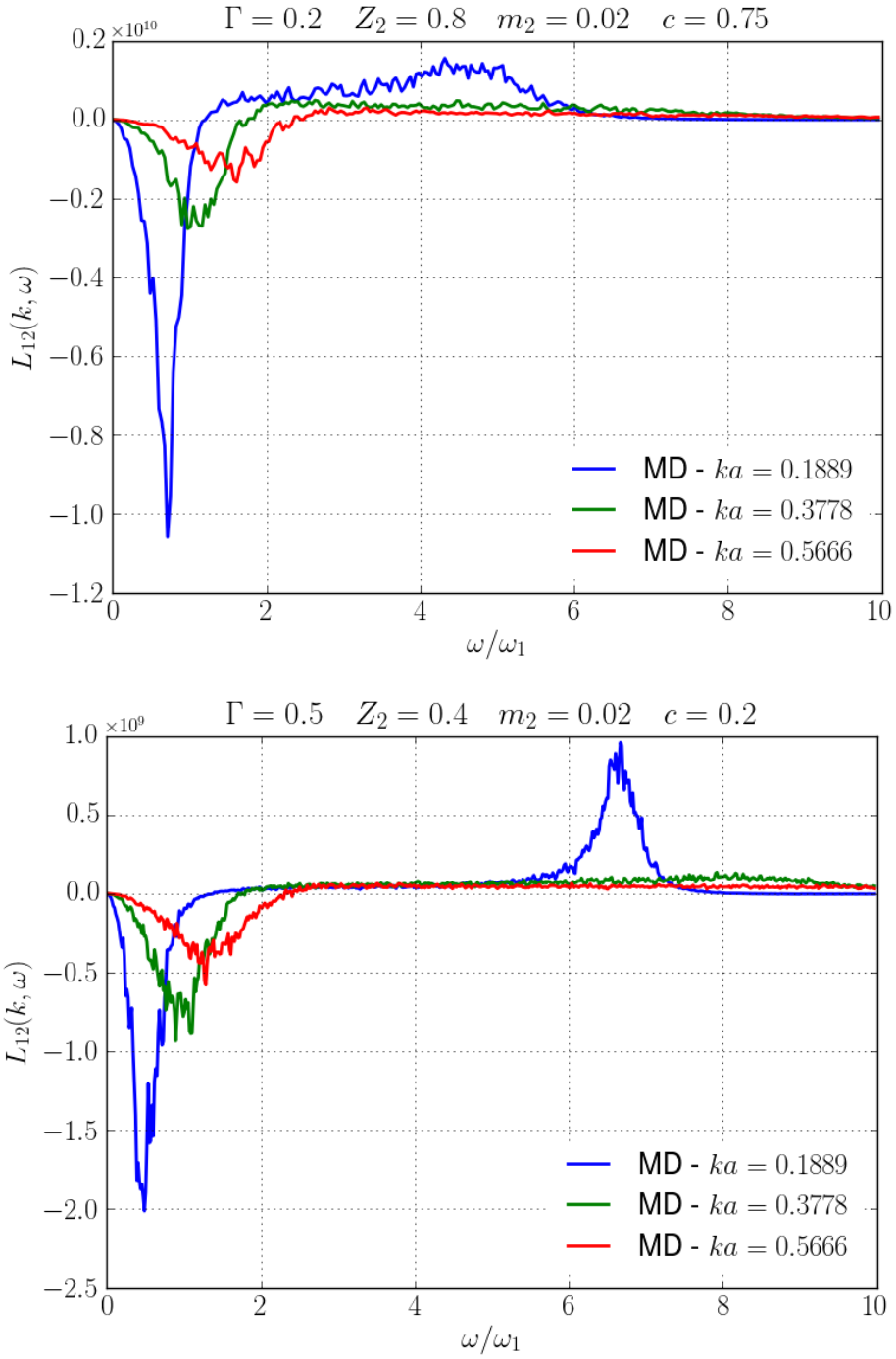

Figure 3.9: Plot of $L_{12}(k, \omega)$ for the asymmetry parameters shown in Figs. 3.4–3.5.

3.3.2 Strong Coupling

In Fig. 3.10 we show plots of $S_{AB}(k,\omega)$ at the lowest ka values with $\Gamma = 10\,000$ comparing MD and Collisional QLCA calculations. Given the large Γ the particles were initialized in a bcc lattice, so to reduce the thermalization time, and remained in this configuration for the entirety of the simulation. This high Γ is chosen so to reduce thermal effects to the minimum and therefore representative of the QLCA assumptions. The agreement between MD (solid lines) and collisional QLCA (dashed lines) is very good. The Collisional QLCA correctly predicts the locations of the collective modes and of the anti–resonance in $S_{22}(k,\omega)$. No anti-resonance is instead visible in $S_{11}(k,\omega)$. However, the fast decay of $S_{11}(k,\omega)$ to the left of the ω_{*2} suggests that the anti–resonance is still present it is masked by the high frequency tail.

In Figs. 3.11–3.17 we show plots for few different asymmetry parameters with liquid values of the coupling parameter Γ. The nominal collisional frequency ν used is shown in the plots' legends. In these plots it is evident the existence of both anti–resonances. We stress that the values of $|\nu|$ are only indicative and should not be considered as the best fit. The reason being that the QLCA was originally formulated for the calculation of the collective modes and not meant for an accurate reproduction of $S_{AB}(k,\omega)$. The Collisional QLCA is to be considered as a first step toward a reproduction of $S_{AB}(k,\omega)$. As a matter of fact, eqs. (2.59)–(2.61) show that $S_{AB}(k,\omega)$ is approximated as a product of two Lorentzians. From the plots it is evident that such an approximation is very crude, nontheless it captures some of the main features of $S_{AB}(k,\omega)$: the collective modes and anti–resonances. The main drawbacks of the QLCA, and consequently of the Collisional QLCA, is the lack of consideration of thermal effects. This causes the QLCA to fail to reproduce the diffusive peak at $\omega = 0$ for coupling parameters Γ indicative of a moderately coupled liquid. As mentioned above a disordered lattice structure

is the closest representation of the QLC formalism hence the good agreement at $\omega = 0$ in Fig. 3.10. Furthermore, the Collisional QLCA poorly reproduces the high frequency tail of $S_{AB}(k,\omega)$ in all cases. MD simulations studies on the OCP have shown that the high frequency tail decays with a power law and the exponents becomes very large as Γ increase $\sim \omega^{-10}$ (Korolov et al., 2015).

Moving on to the strengths of the Collisional QLCA we find an overall good agreement with MD simulations. The Collisional QLCA correctly identifies the collective mode and anti–resonance frequencies in all cases. The main purpose of these plots is to show the existence of both anti–resonances at any $\Gamma > 10$ and the effects of the collisional frequency ν on the collective modes. Fig. 3.12 is obtained by using two values of the collisional frequency, namely $|\nu| = 0.5\omega_1$ and $|\nu| = 0.05\omega_1$. The large value of $|\nu|$ causes the disappearance of the low frequency plasmon $\omega_- = 0.7769\omega_1$. The high frequency plasmon $\omega_+ = 1.3568\omega_1$, on the other hand, is clearly visible and its widths appears unaffected by ν. The chosen asymmetry parameters lead to

$$\omega_{*1} = 1.4142\omega_1, \quad \omega_{*2} = 1.2910\omega_1 \tag{3.44}$$

respectively, to the right and left of ω_+. This feature of the SK–frequencies being above and below of the in–phase collective mode is an interesting feature that is found in the entirety of this Thesis. The effects of $|\nu|$ on the collective modes are evident by looking at the denominator of $S_{AB}(k,\omega)$, rewriting $|\mathcal{D}(,\omega)|^2$ from eq. (3.24) in terms of ν we have

$$\mathcal{D}(k,\omega) = \left[\omega^2 - \omega_+^2(k)\right]^2 \left[\omega^2 - \omega_-^2(k)\right]^2 + \omega^2\nu^2 \left(n + 1/m\right)^2 \left[\omega^2 - \omega_{\rm im}^2(k)\right]. \tag{3.45}$$

The frequencies $\omega_\pm(k)$ are the eigenvalues of the real matrix $\mathbf{C}(k)$ and we claimed these to be the collective modes of the system under the assumption of small

damping $|\nu| \ll 1$. Obviously, $|\nu| = 0.5$ does not satisfy this condition and the peaks in $S_{AB}(k,\omega)$ are now given by the complex solution of

$$\det|\omega^2\mathbf{I} - i\omega\mathbf{R} - \mathbf{C}(k)| = 0. \tag{3.46}$$

Furthermore these solutions are the eigenfrequencies of the matrix $\chi(k,\omega)$ related to the displacement fields, $_{,A}$. In general, the collective modes of a plasma are given by the zeros of the $\varepsilon(k,\omega)$ which is the response of a plasma to external electric field. Plots of the Real and Imaginary part of $\det\varepsilon(k,\omega)$ for the simulation parameters of Fig. 3.12 is shown in Fig. 3.18. Notice that the Real part of crosses the zero line only at $\omega = \omega_+$. At $\omega = \omega_-$ the Real part shows an asymmetric peak for the lowest $|\nu|$. From these results we argue that for the simulations parameters of Fig. 3.12 there exists only one collective mode: the high frequency plasmon ω_+. The second low frequency plasmon predicted by the QLCA is instead annihilated due to the large collisional frequency $|\nu|$ and only at much higher Γ, where $|\nu| \ll 1$, this second plasmon will be observed. A more thorough study of $\det\varepsilon(k,\omega)$ will be given in the next Chapter.

Figs. 3.13–3.15 are meant to show how the low frequency plasmon is affected by the collisional frequency. Notice that ω_- becomes visible in $S_{11}(k,\omega)$ when the concentration is increased. We note that Γ_{eff}, as given by eq. (1.9), does not change appreciably with the concentration, $\Gamma_{\text{eff}} = \{96.8, 92.6, 95.2\}$ for $c = c_1 = \{0.25, 0.5, 0.75\}$. Indication that the collisional frequency increase with Γ is shown in Figs. 3.16–3.17 where the same asymmetry parameters are shown for two Γ values.

A final feature of note is that the SK frequencies appear only in the partial DSF and not in the total DSF's such as the charge-charge $S_{ZZ}(k,\omega)$ and mass-mass, $S_{MM}(k,\omega)$, hence, would not be visible in any scattering experiment unable to

probe a single species. $S_{MM}(k,\omega)$ and $S_{ZZ}(k,\omega)$ calculated using the Collisional QLCA are

$$\begin{aligned} S_{MM}(k,\omega) &= c_1 m_1^2 S_{11}(k,\omega) + 2\sqrt{c_1 c_2} m_1 m_2 S_{12}(k,\omega) + c_2 m_2^2 S_{22}(k,\omega) \\ &= \frac{\nu k^2}{\beta\pi}\frac{m_1 c_1}{|\mathcal{D}|^2}\left[\left(\omega^2-\omega_{*2}^2\right)^2 - 2\frac{|R_{12}|}{R_{11}}\sqrt{mn}\left(\omega^2-\omega_{*2}^2\right)\left(\omega^2-\omega_{*1}^2\right)\right. \\ &\quad \left. + mn\frac{R_{22}}{R_{11}}\left(\omega^2-\omega_{*1}^2\right)^2\right] \\ &= \frac{k^2}{\beta\pi}\frac{m_1 c_1 \nu}{|\mathcal{D}|^2}\left(\omega_{*2}^2-\omega_{*1}^2\right)^2 \end{aligned} \tag{3.47}$$

$$\begin{aligned} S_{ZZ}(k,\omega) &= c_1 Z_1^2 S_{11}(k,\omega) + 2\sqrt{c_1 c_2} Z_1 Z_2 S_{12}(k,\omega) + c_2 Z_2^2 S_{22}(k,\omega) \\ &= -\frac{k^2 R_{11}}{\beta\pi|\mathcal{D}|^2}\frac{Z_1^2 c_1}{m_1}\left[\left(\omega^2-\omega_{*2}^2\right)^2 + 2\frac{R_{12}}{R_{11}}\sqrt{\frac{Z^2 n}{m}}\left(\omega^2-\omega_{*2}^2\right)\left(\omega^2-\omega_{*1}^2\right)\right. \\ &\quad \left. + \frac{Z^2 n}{m}\frac{R_{22}}{R_{11}}\left(\omega^2-\omega_{*1}^2\right)^2\right] \\ &= \frac{k^2\nu\omega_1}{\beta\pi|\mathcal{D}(k,\omega)|^2}\frac{Z_1^2 c_1}{m_1}(1-q^2)^2\left(\omega^2 - \frac{\omega_{*2}^2 - q^2\omega_{*1}^2}{1-q^2}\right)^2 \\ &\xrightarrow{k\to 0} \frac{k^2\nu\omega_1}{\beta\pi|\mathcal{D}(k,\omega)|^2}\frac{Z_1^2 c_1}{m_1}(1-q^2)^2\omega^4 \end{aligned} \tag{3.48}$$

where the last expression is obtained by recalling that $\omega_{*2}^2(k) = q^2\omega_{*1}^2(k)$ to $O(1)$ in k (compare eqs. (3.34)–(3.35)). Plots of $S_{MM}(k,\omega)$ and $S_{ZZ}(k,\omega)$ with a lattice Γ are shown in Fig. 3.19, while plots of $S_{ZZ}(k,\omega)$ only are shown in Figs. 3.20–3.21. The disagreement between Collisional QLCA and MD simulations is again expected in this case. In particular we point out that $S_{ZZ}(k,\omega=0)$ calculated from MD approaches a finite value, while the Collisional QLCA predicts $S_{ZZ}(k,\omega\to 0)\to 0$. Finally, in Fig. 3.22 we show a list $L_{AB}(k,\omega)$ for the range $\Gamma = 10-300$ to further confirm the Γ–independence of the Silvestri–Kalman frequencies as given in eqs. (3.34)–(**??**)

The mode dispersion are shown in Fig. 3.23 via intensity plots of $L_{AB}(k,\omega)$ for the

highest Γ shown in Fig. 3.22. In Figs. 3.24-3.25 a collection of intensity plots for different concentrations. Solid white lines represent the dispersion of the QLCA collective modes $\omega_{\pm}$, eq. (3.25), while dashed white lines the dispersion of the SK frequencies, eqs. (2.38) – (2.39), with $R_{AB}(k) = R_{AB}(0)$. We notice that the high frequency plasmon is always present, while the low frequency plasmon appears only in the case of mixtures with a high concentration of heavy particles. In the opposite case, instead, we notice the presence of an acoustic-like mode. However, this is not a real collective mode and it is only an artifact of the intensity plots since $L_{AB}(k, \omega)$ vanishes at $\omega = 0$. Confirmation that this is not a real mode is given by looking at Fig. 3.26 where we show plots of $S_{AB}(k, \omega)$ for the first few ka. Notice that there is no presence of an acoustic–like mode. As mentioned above the absence of the low frequency plasmon is likely due to a large concentration of light particles.

Overall all the plots show qualitatively good agreement between the QLCA and MD. The QLCA correctly predicts the main features of the dispersion of the two plasmons. Both modes start at finite frequencies at $k = 0$ and show a negative dispersion at finite k, a hallmark of strong coupling. The dispersions reach a minimum around $ka \sim 4$. In the literature, this is identified as the "roton minimum", another feature of strongly correlated liquids (Kalman, Kyrkos, et al., 2012). We notice that the location of the minimum appears to be independent of the asymmetry parameters. This is due to the fact that all the simulations use $N = 10\,000$ particles and a simulation box of side $L = 1e - 5$, the Wigner–Seitz radius is then defined by the total density N/L^3 which is the same for all the asymmetry parameters. As suggested in (Kalman, Kyrkos, et al., 2012) the location of the minimum can be interpreted as the location of the boundary of the first Brillouin zone of a bcc lattice. In fact, if we consider a bcc lattice with lattice constant $b = \sqrt[3]{2\pi/3}a$ (a the liquid WS radius) we find that when $kb = 2\pi$, $ka = 4.9$ close

to the minimum in the plots. The presence of the roton minimum in these mixture further corroborates that the roton minimum is a feature of strongly coupled liquid and not only a quantum effects (Kalman, Kyrkos, et al., 2012). At short wavelengths, around $ka = 8$, the QLCA and MD start to deviate from each other. As described before the QLCA modes approach the nominal Einstein frequencies of each species with almost flat dispersion. The MD dispersions, instead, bend upward suggesting that the modes enter the "single particle continuum". This behaviour is less evident in the plots of $Z_2 = 0.5$, $m_2 = 0.02$, and $c = 0.90$ and it is likely due to the larger concentration of species 1 and the higher Γ value. The most important feature of these plots is the qualitatively good agreement of the QLCA calculations. This is unexpected because, as mentioned in the appendix of (Kalman and Golden, 1990), the QLC formalism can be justified for $ka\omega_1/\omega < 1$. Finally we look at the dispersion of the SK frequencies. We recall that both SK frequencies are the zeros of $S_{12}(k,\omega)$ and $L_{12}(k,\omega)$ therefore, both their dispersion will be evident in color maps of $-L_{12}(k,\omega)|$. In Fig. 3.27–3.29 we show color maps of $|L_{12}(k,\omega)|$, for three asymmetry parameters. The zeroes of these functions are represented by black regions. The low frequency anti–resonance is clearly visible in all Figures and very good agreement is found between Collisional QLCA and MD up to $ka = 3$. This is somewhat surprising since the SK dispersion is calculated with the assumption $R_{AB}(k) = R_{AB}(0)$, *i.e.* neglecting k-dependent effects of the collisional damping. The high frequency SK anti–resonance, instead, does not show the same good agreement. In fact, the large black region at high frequencies masks its exact location and it appears to have a positive k dispersion. This is somewhat expected since the high frequencies SK anti–resonance appears as a wide minimum in plots of $L_{AB}(k,\omega)$ and not as sharp as the low frequency one. Furthermore, MD data for $L_{12}(k,\omega)$ becomes very small and noisy at high frequencies and low values are indistinguishable from zero in this color code. However,

the presence of the high frequency SK anti–resonance is visible at much higher ka where we notice an alternating pattern between colored and dark regions. This is especially evident in Fig. 3.27. This oscillating behaviour is an interesting feature as it represents sign oscillations of $L_{12}(k,\omega)$. To better investigate this feature we show line plots of $L_{12}(k,\omega)$ in Fig. 3.30. Similar to the weak coupling regime the low frequency mode is associated with an out–of–phase motion of the two particle species, while the high-frequency mode with an in-phase motion. As ka increases the peaks of $L_{12}(k,\omega)$ at $\omega = \omega_{\pm}$ change sign. Furthermore, the ka values at which $L_{12}(k,\omega)$ changes sign are to be the crossing points between the collective modes and SK anti–resonances.

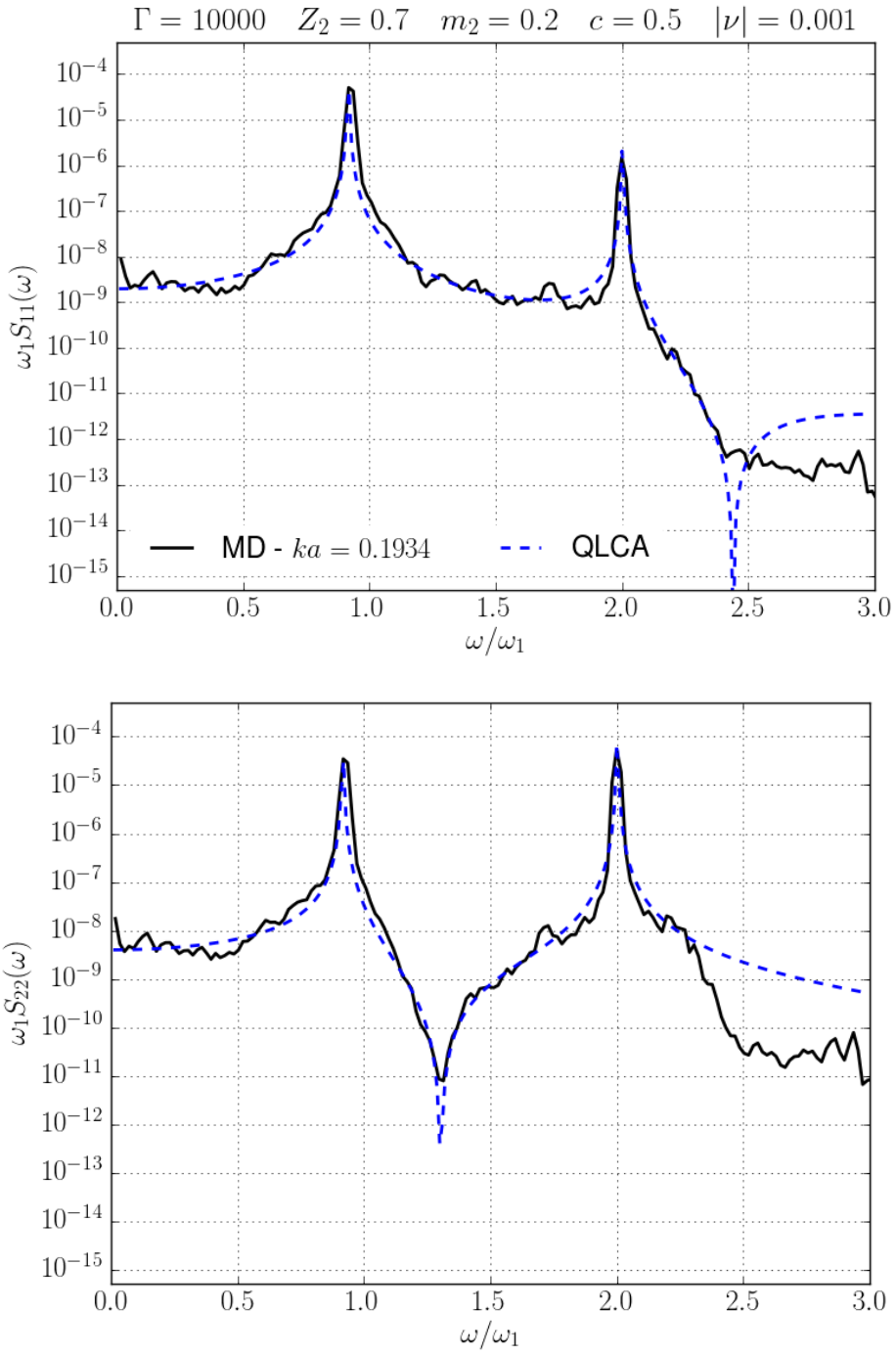

Figure 3.10: Comparison between the QLCA and MD $S_{AB}(ka, \omega)$ for the asymmetry parameters shown in the title. Solid black lines represent MD data, dashed blue lines Collisional QLCA calculations.

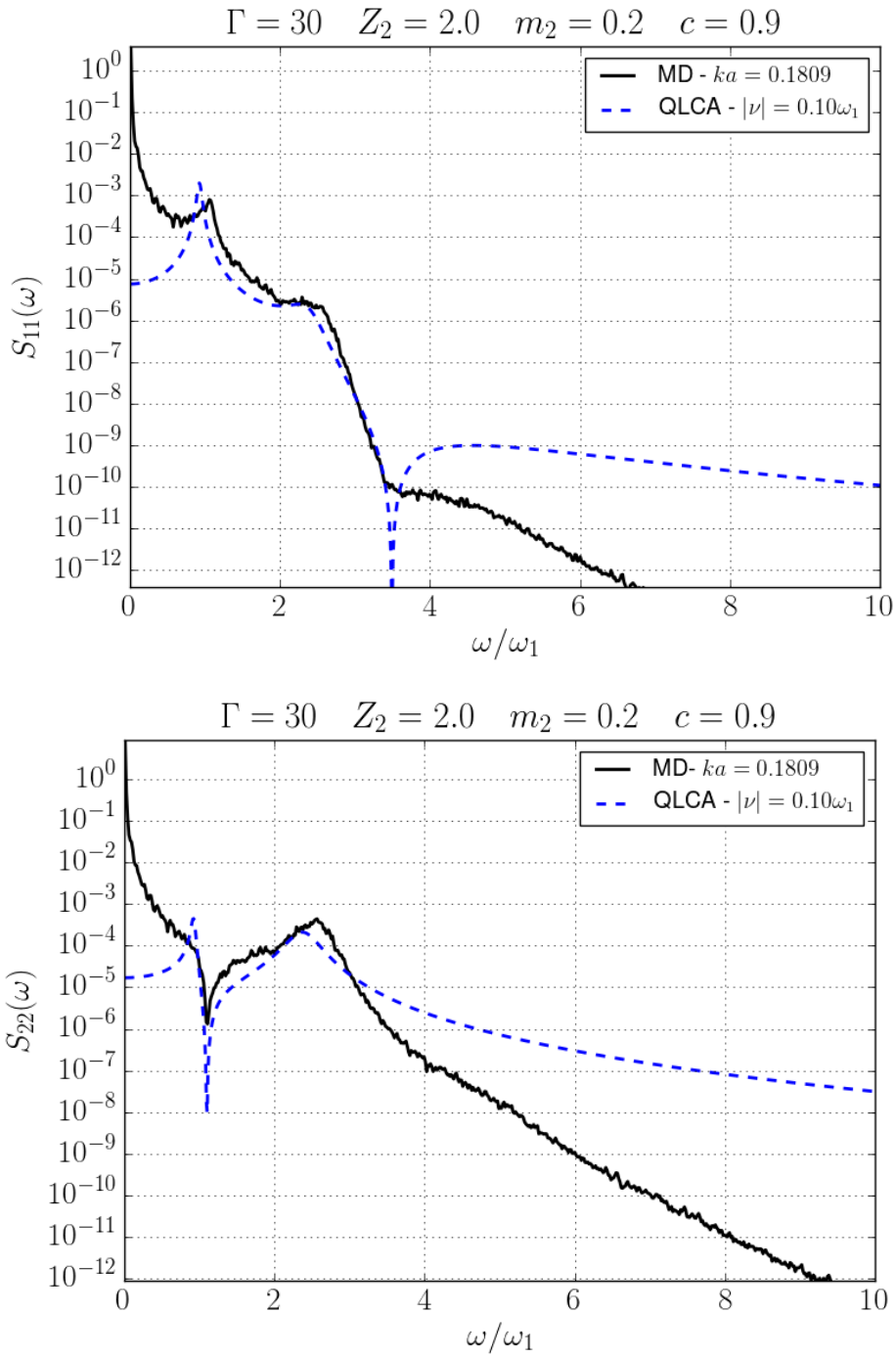

Figure 3.11: Comparison between the QLCA and MD $S_{AB}(ka, \omega)$ for the asymmetry parameters shown in the title. Solid black lines represent MD data, dashed blue lines Collisional QLCA calculations.

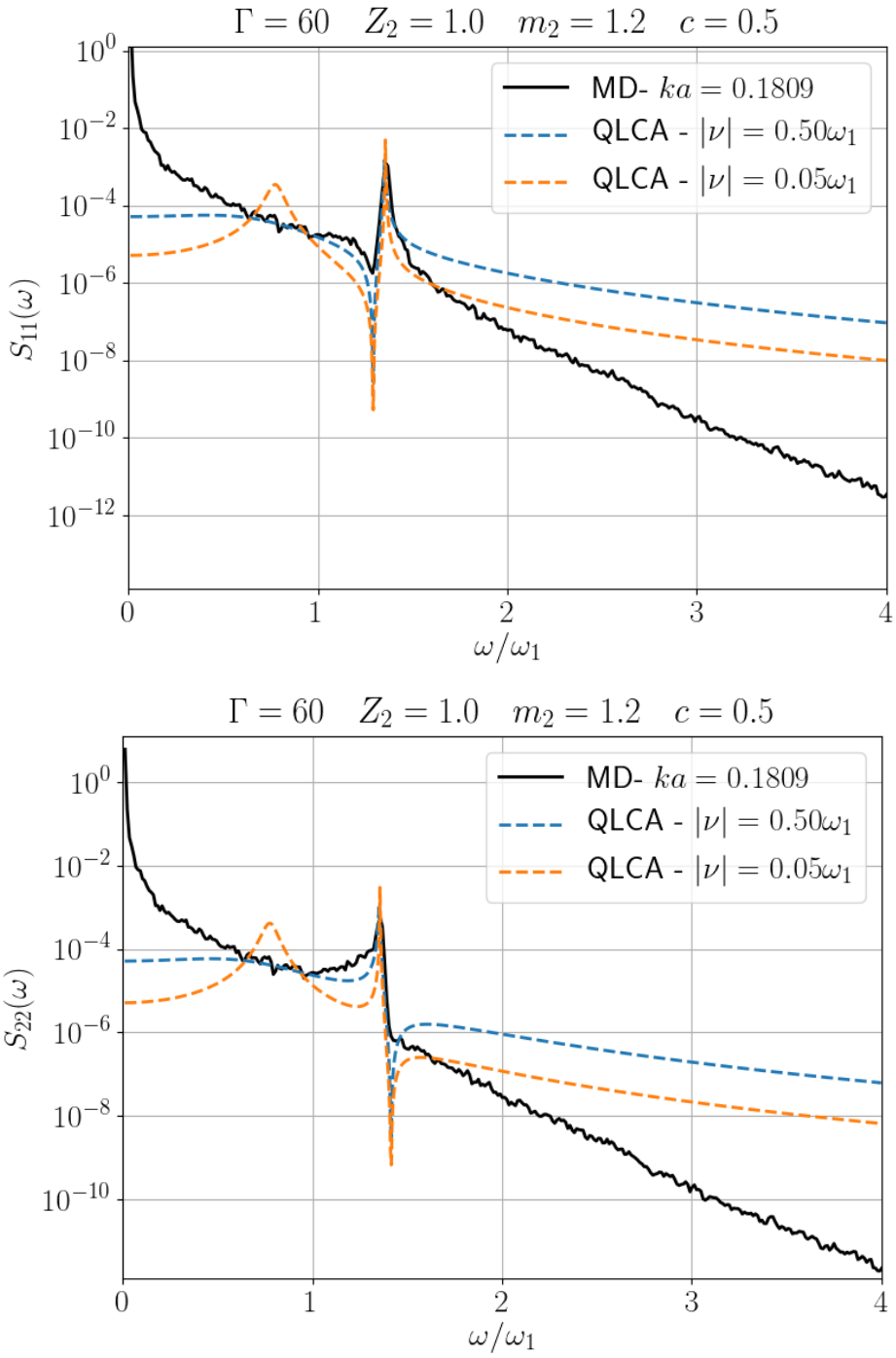

Figure 3.12: Comparison between the QLCA and MD $S_{AB}(ka, \omega)$ for the asymmetry parameters shown in the title. Solid black lines represent MD data, dashed blue lines Collisional QLCA calculations.

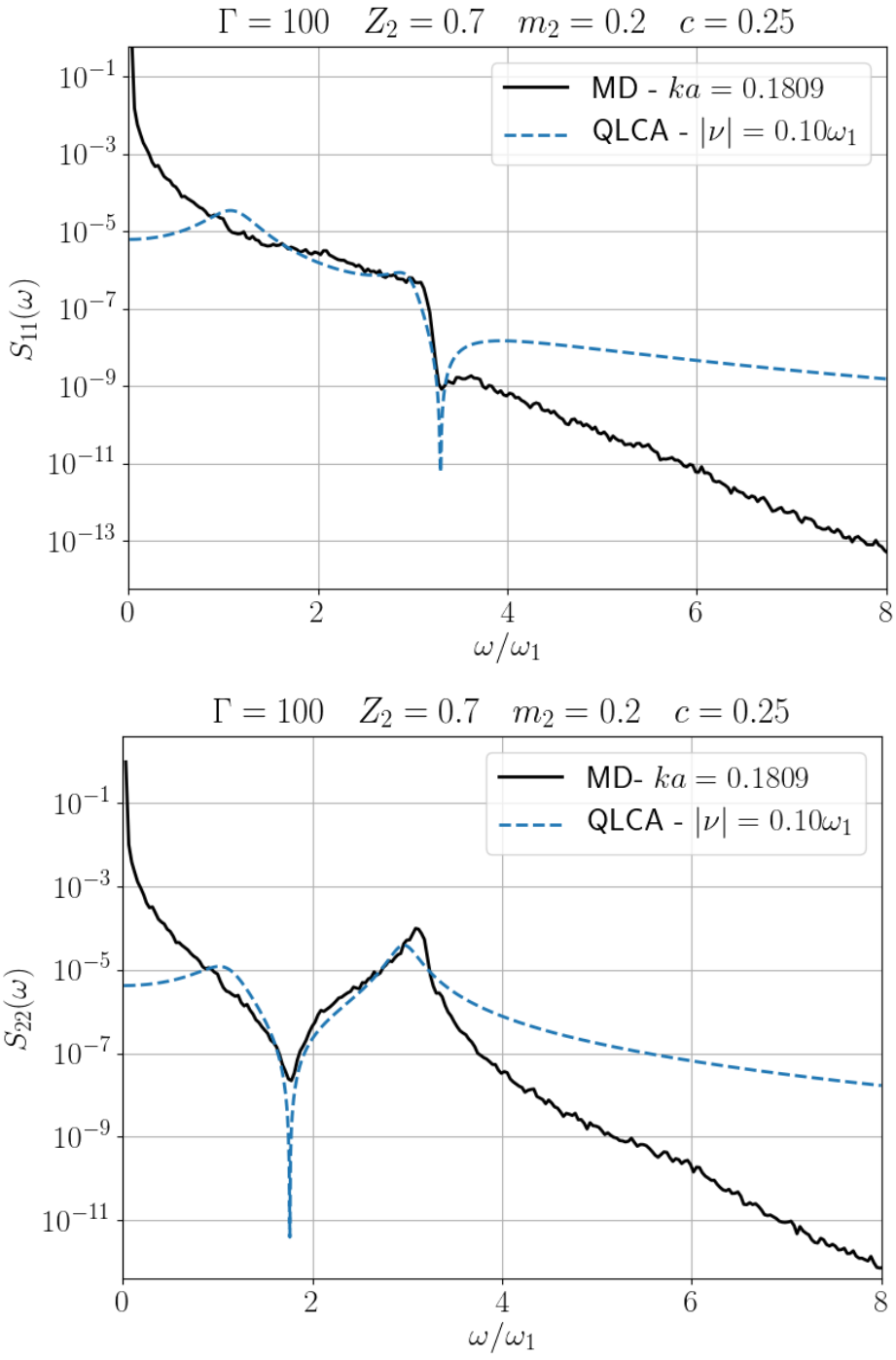

Figure 3.13: Comparison between the QLCA and MD $S_{AB}(ka, \omega)$ for the asymmetry parameters shown in the title. Solid black lines represent MD data, dashed blue lines Collisional QLCA calculations.

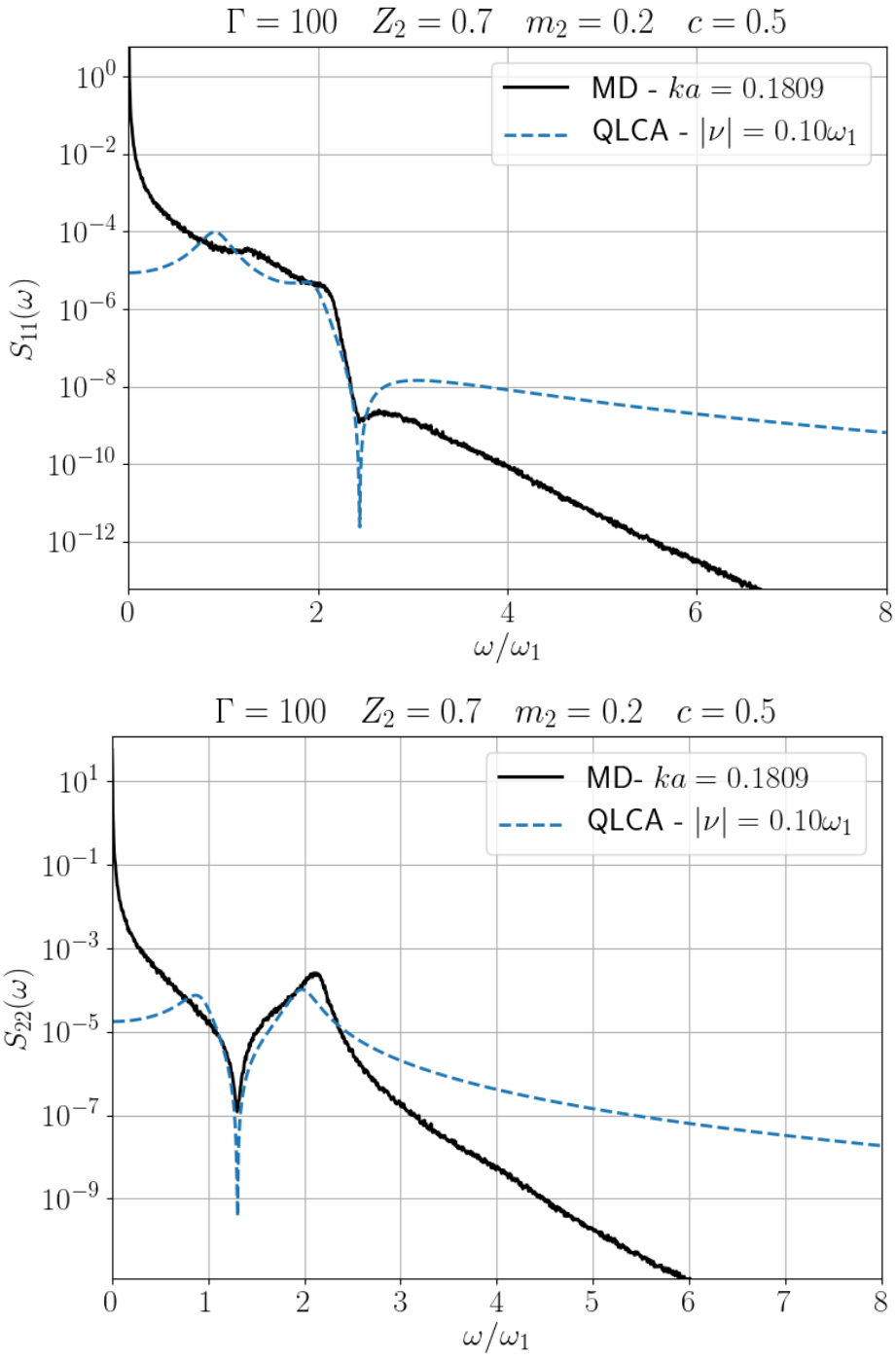

Figure 3.14: Comparison between the QLCA and MD $S_{AB}(ka, \omega)$ for the asymmetry parameters shown in the title. Solid black lines represent MD data, dashed blue lines Collisional QLCA calculations.

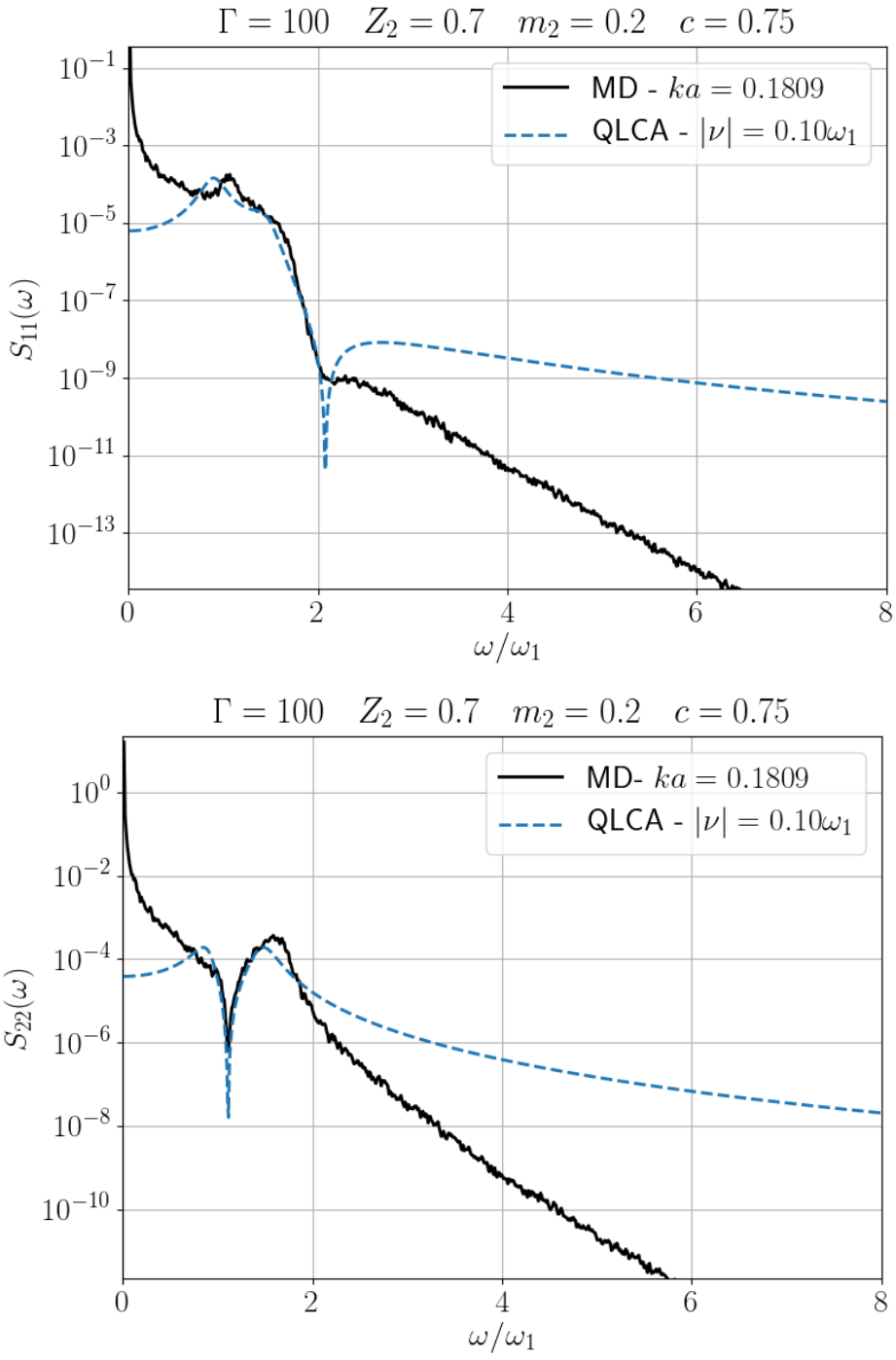

Figure 3.15: Comparison between the QLCA and MD $S_{AB}(ka, \omega)$ for the asymmetry parameters shown in the title. Solid black lines represent MD data, dashed blue lines Collisional QLCA calculations.

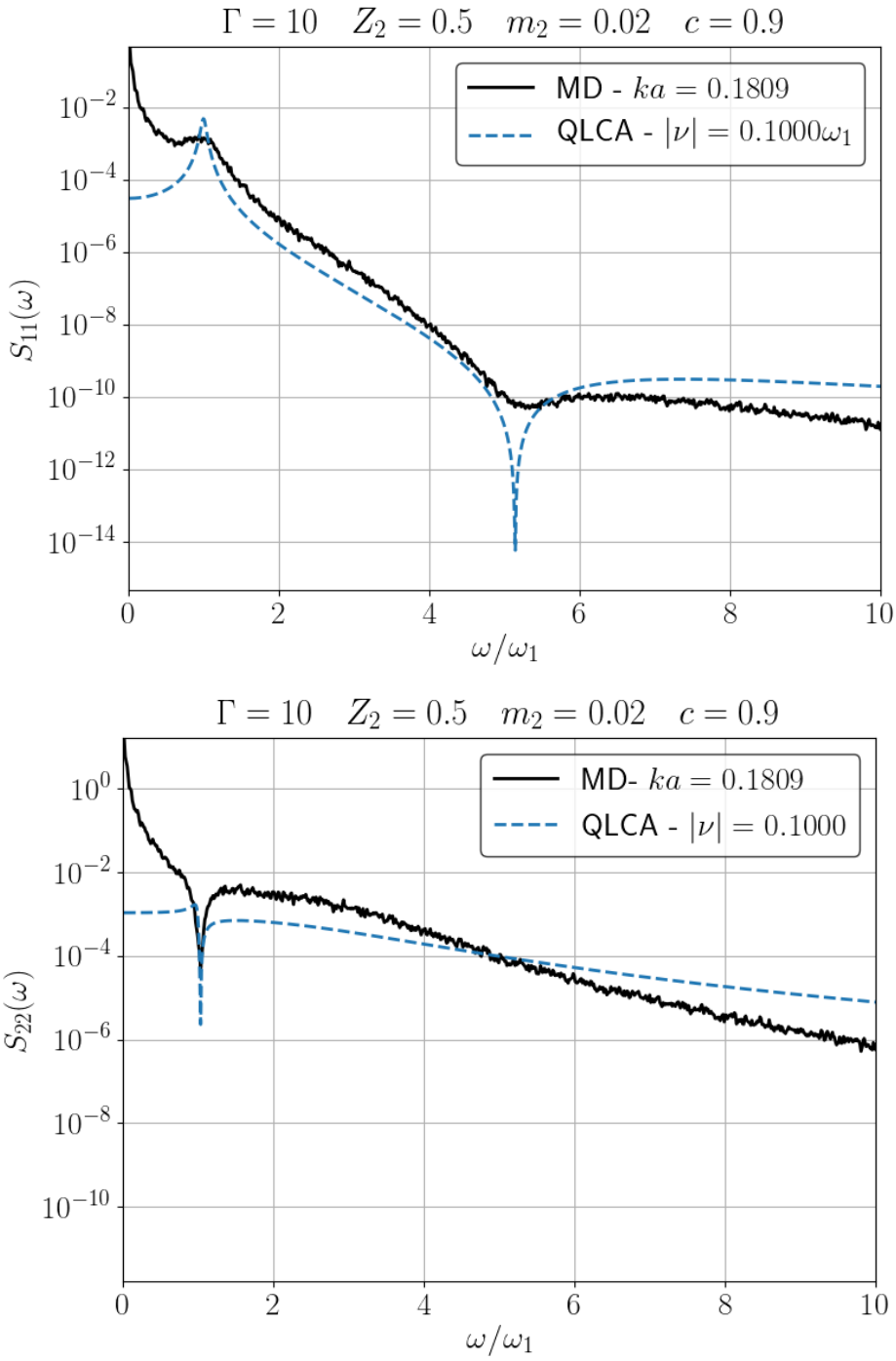

Figure 3.16: Comparison between the QLCA and MD $S_{AB}(ka, \omega)$ for the asymmetry parameters shown in the title. Solid black lines represent MD data, dashed blue lines Collisional QLCA calculations.

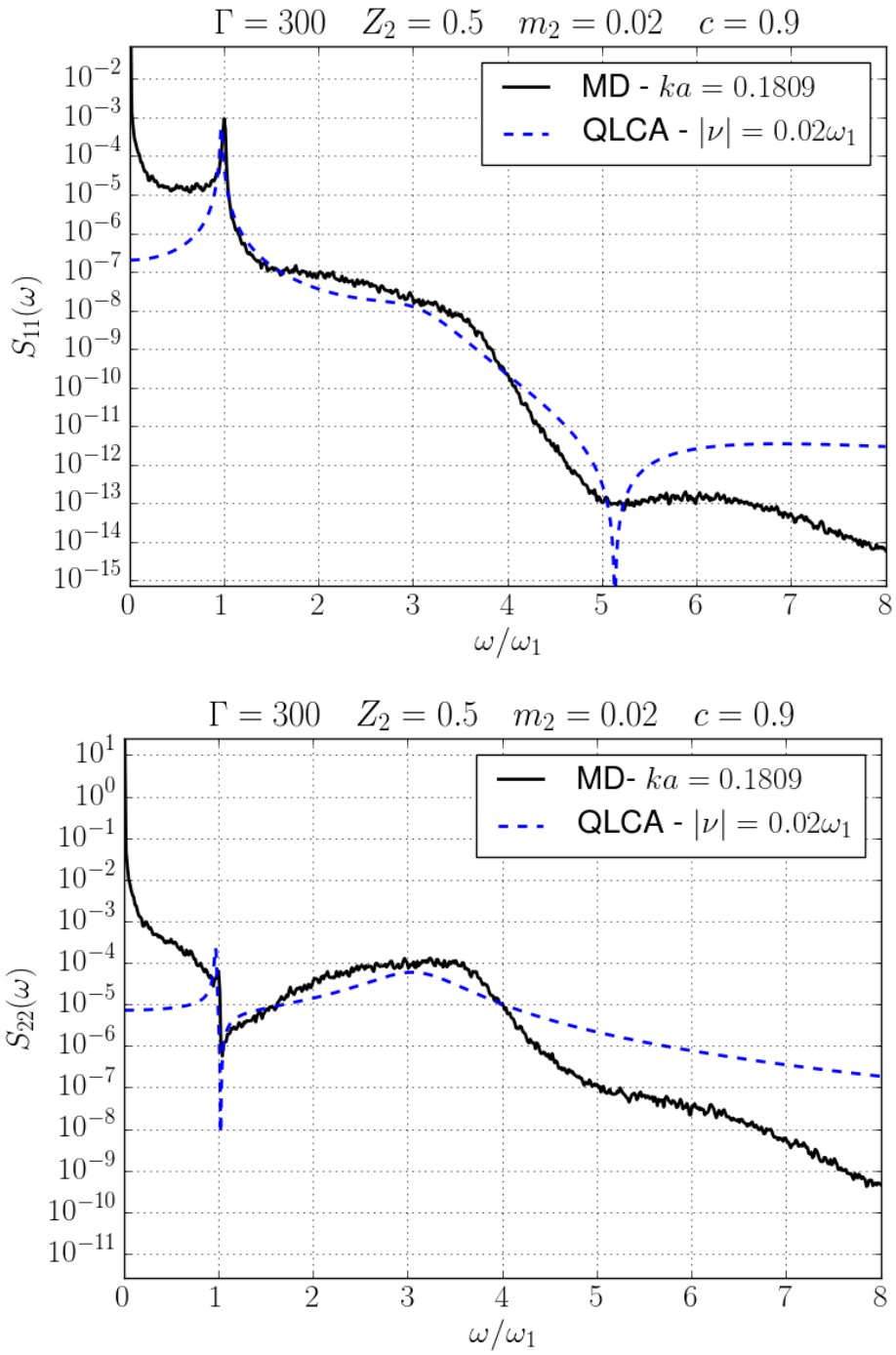

Figure 3.17: Comparison between the QLCA and MD $S_{AB}(ka, \omega)$ for the asymmetry parameters shown in the title. Solid black lines represent MD data, dashed blue lines Collisional QLCA calculations.

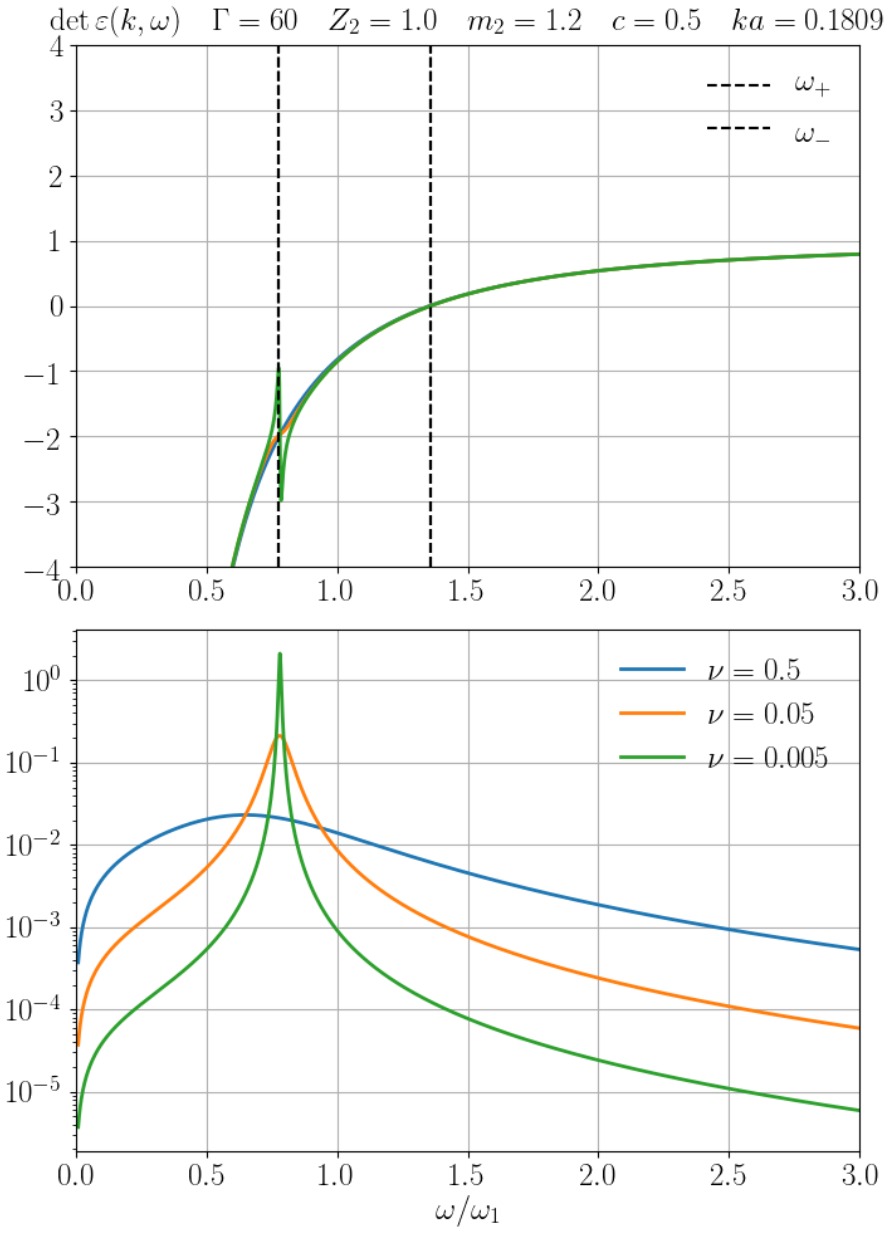

Figure 3.18: Plot the Real (top) and Imaginary (bottom) part of $\det \varepsilon(k, \omega)$ for the simulation parameters of Fig. 3.12 for three $|\nu|$ values

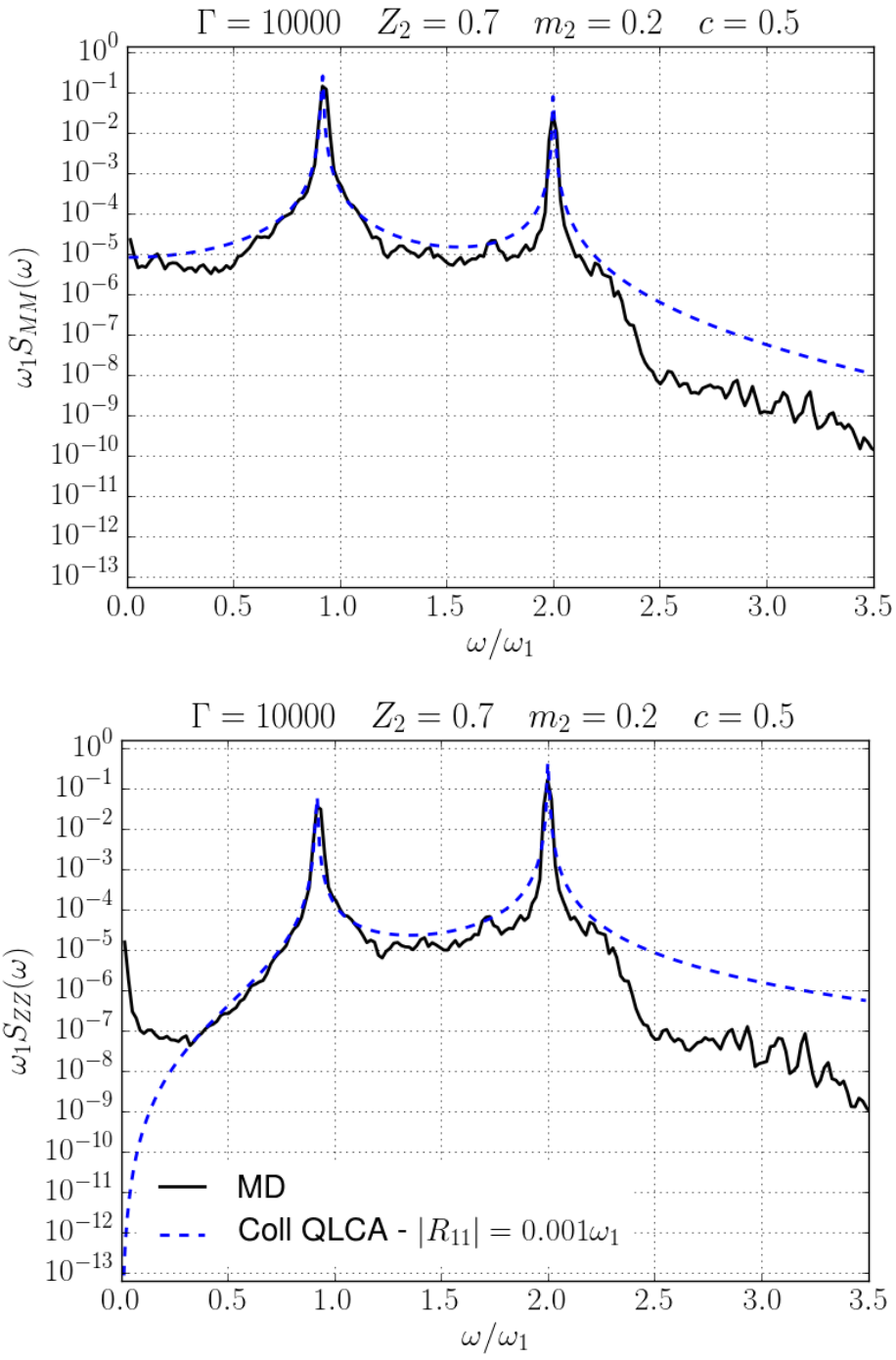

Figure 3.19: Comparison between the QLCA and MD $S_{AB}(ka_{\min}, \omega)$ for the asymmetry parameters shown in the titles. Solid black lines represent MD data, dashed blue lines QLCA calculations

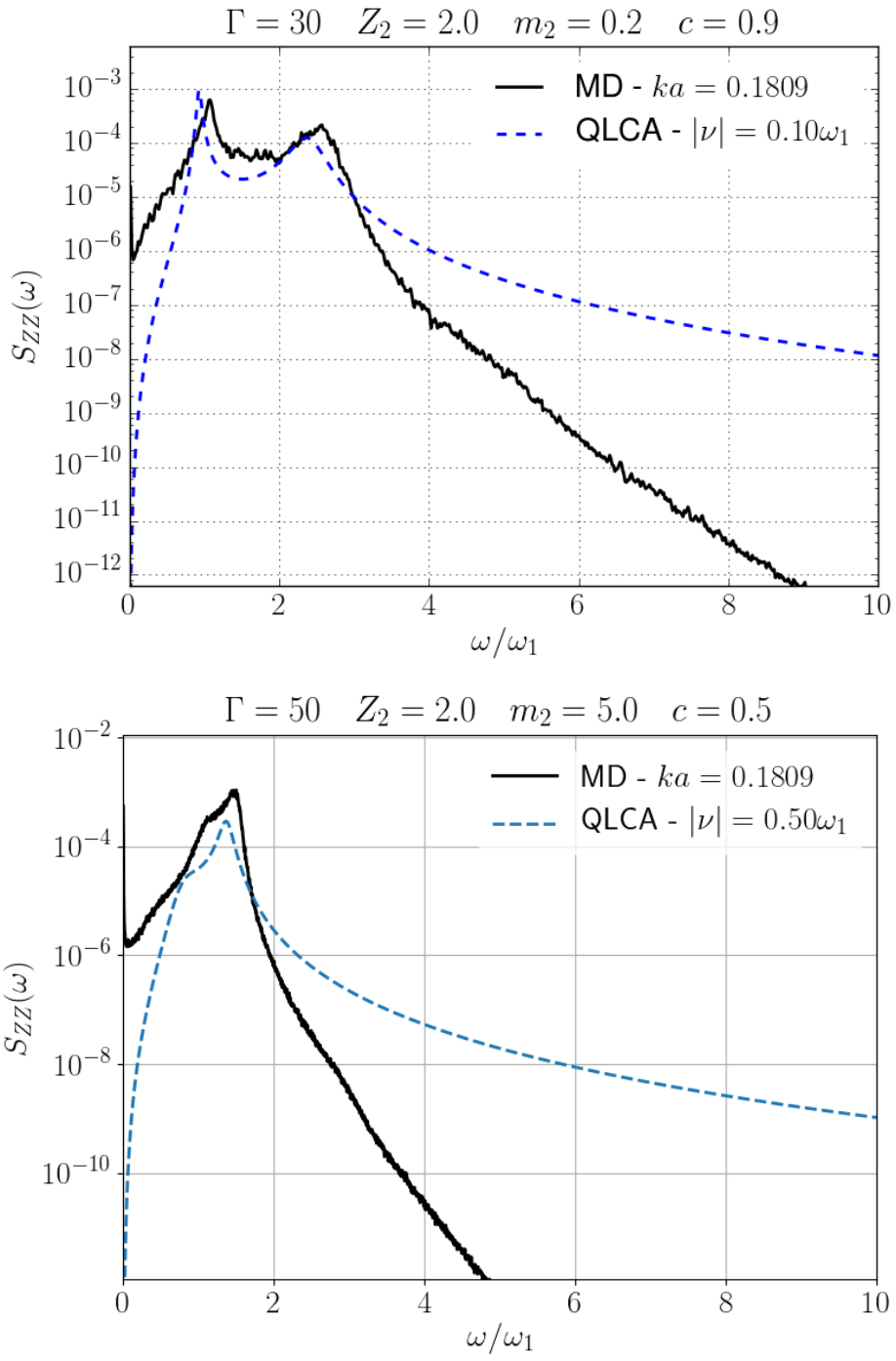

Figure 3.20: Comparison between the QLCA and MD $S_{AB}(ka_{\min}, \omega)$ for the asymmetry parameters shown in the titles. Solid black lines represent MD data, dashed blue lines QLCA calculations

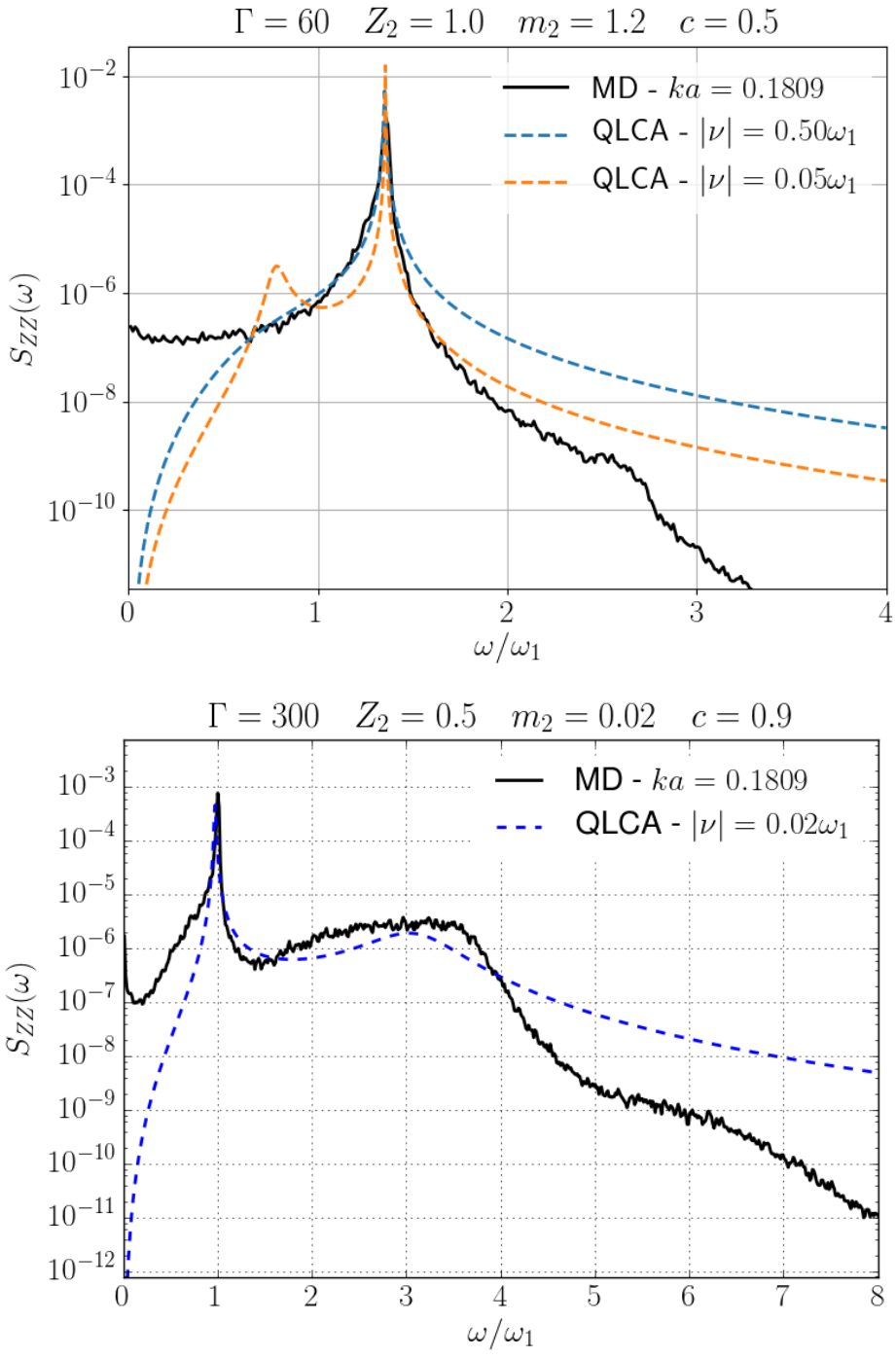

Figure 3.21: Comparison between the QLCA and MD $S_{AB}(ka_{\min}, \omega)$ for the asymmetry parameters shown in the titles. Solid black lines represent MD data, dashed blue lines QLCA calculations

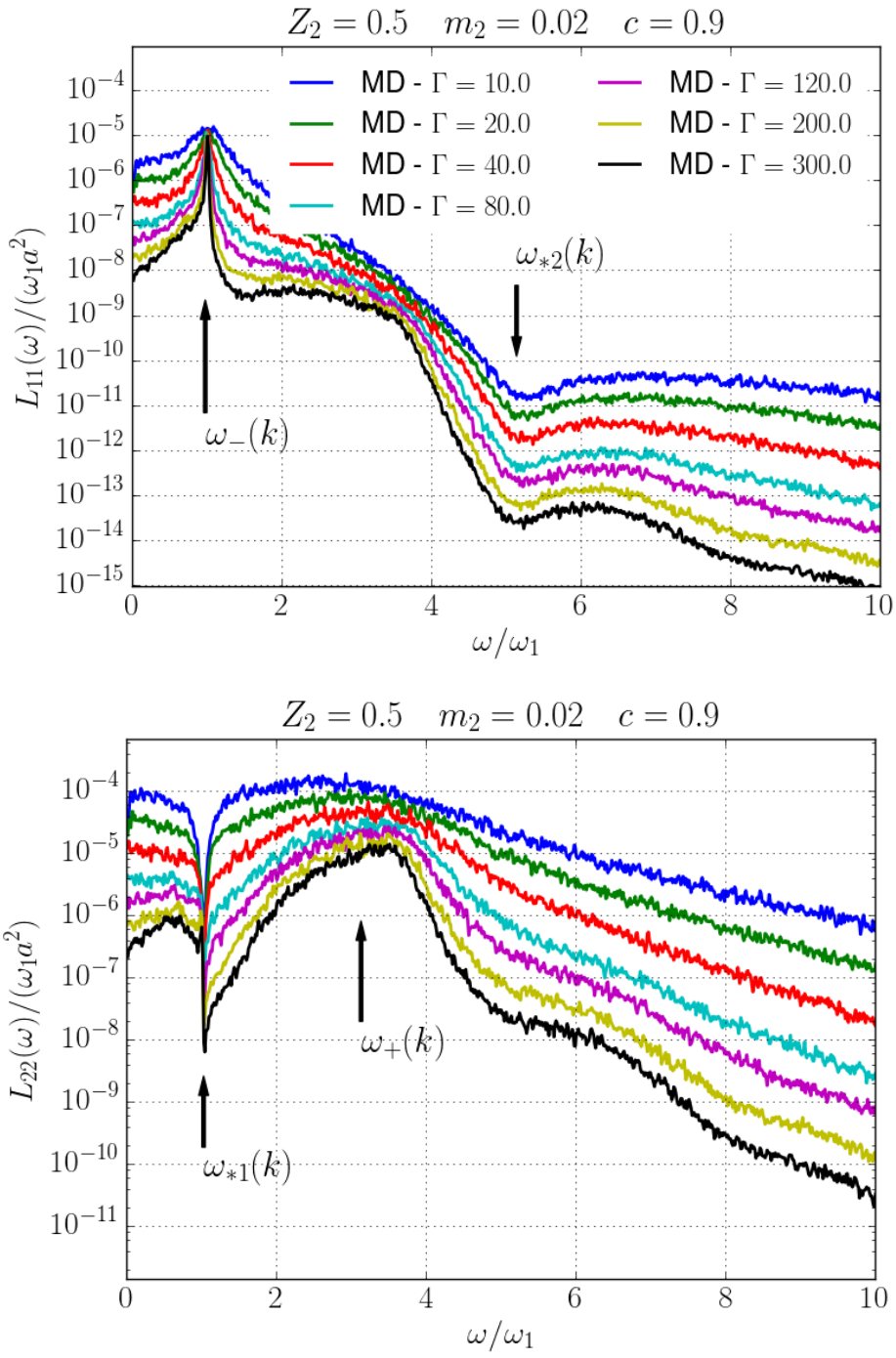

Figure 3.22: Plots of MD $L_{AB}(k,\omega)$ for a set of strongly coupled Γ values at the lowest ka obtainable from simulations. The QLCA collective modes and the Silvestri-Kalman frequencies are shown.

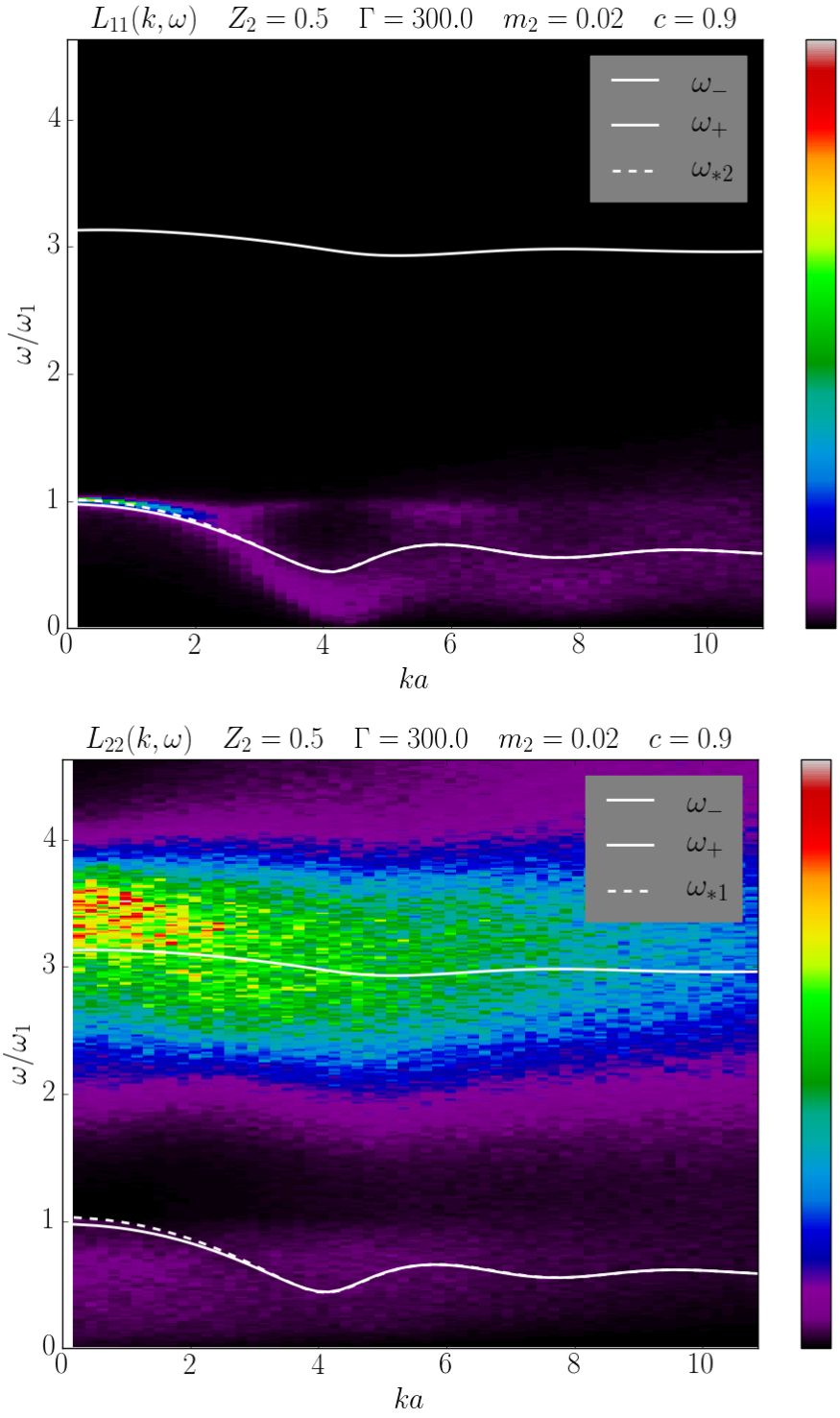

Figure 3.23: Intensity plots of MD $L_{AB}(k,\omega)$ to show the mode dispersion.

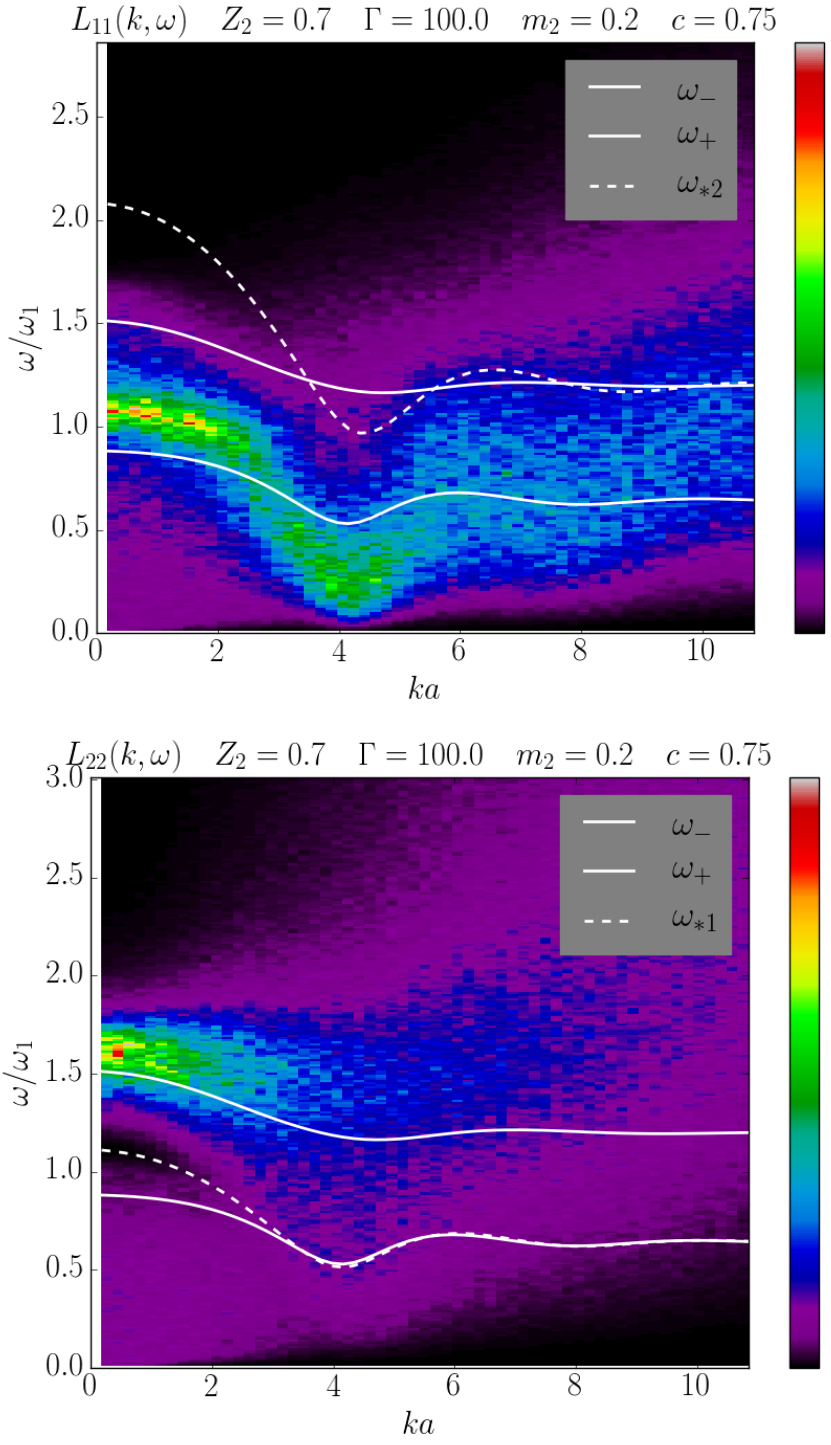

Figure 3.24: Intensity plots of MD $L_{AB}(k,\omega)$ for a binary mixture with a high concentration of heavy particles.

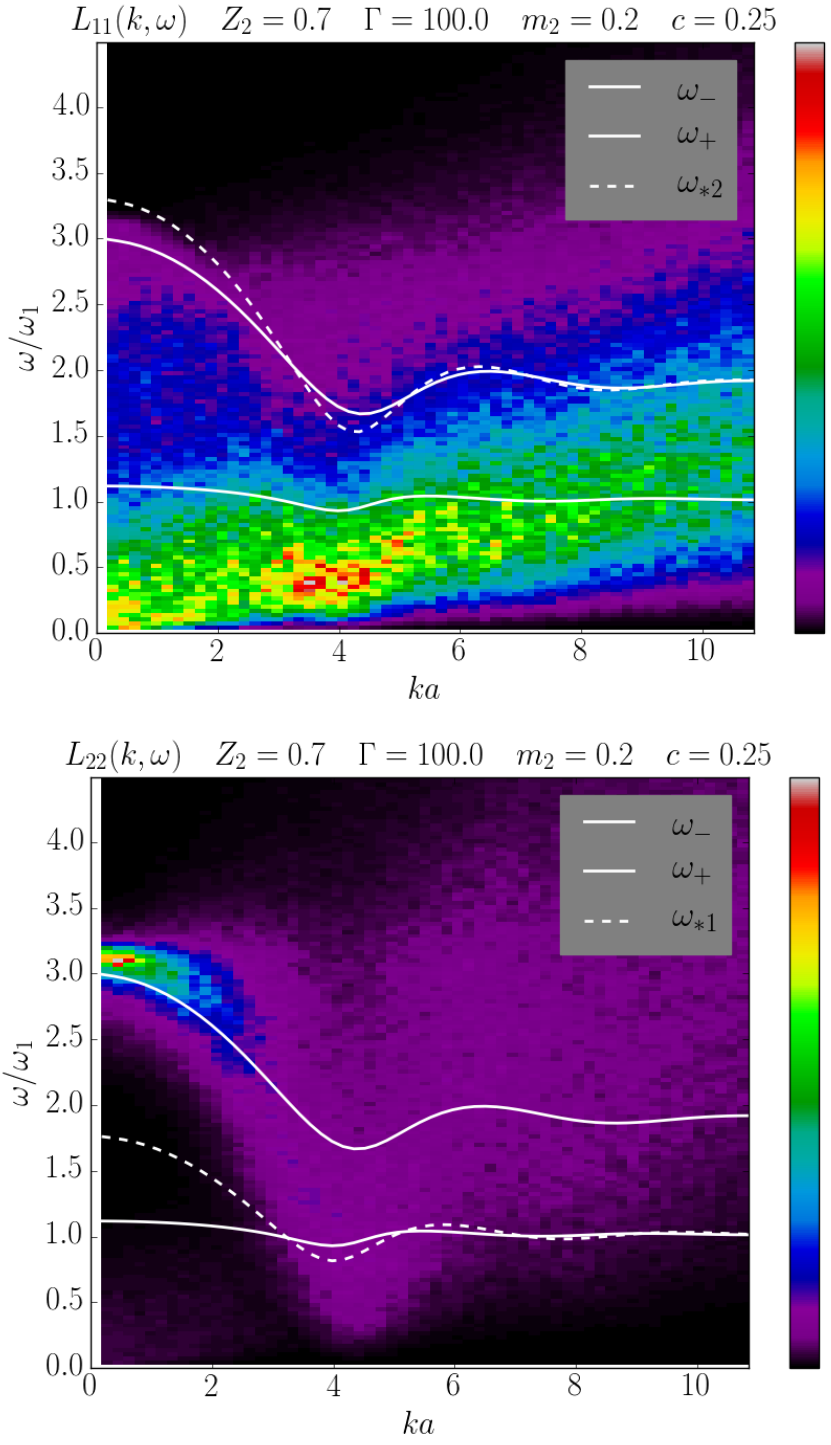

Figure 3.25: Intensity plots of MD $L_{AB}(k,\omega)$ for a binary mixture with a high concentration of light particles.

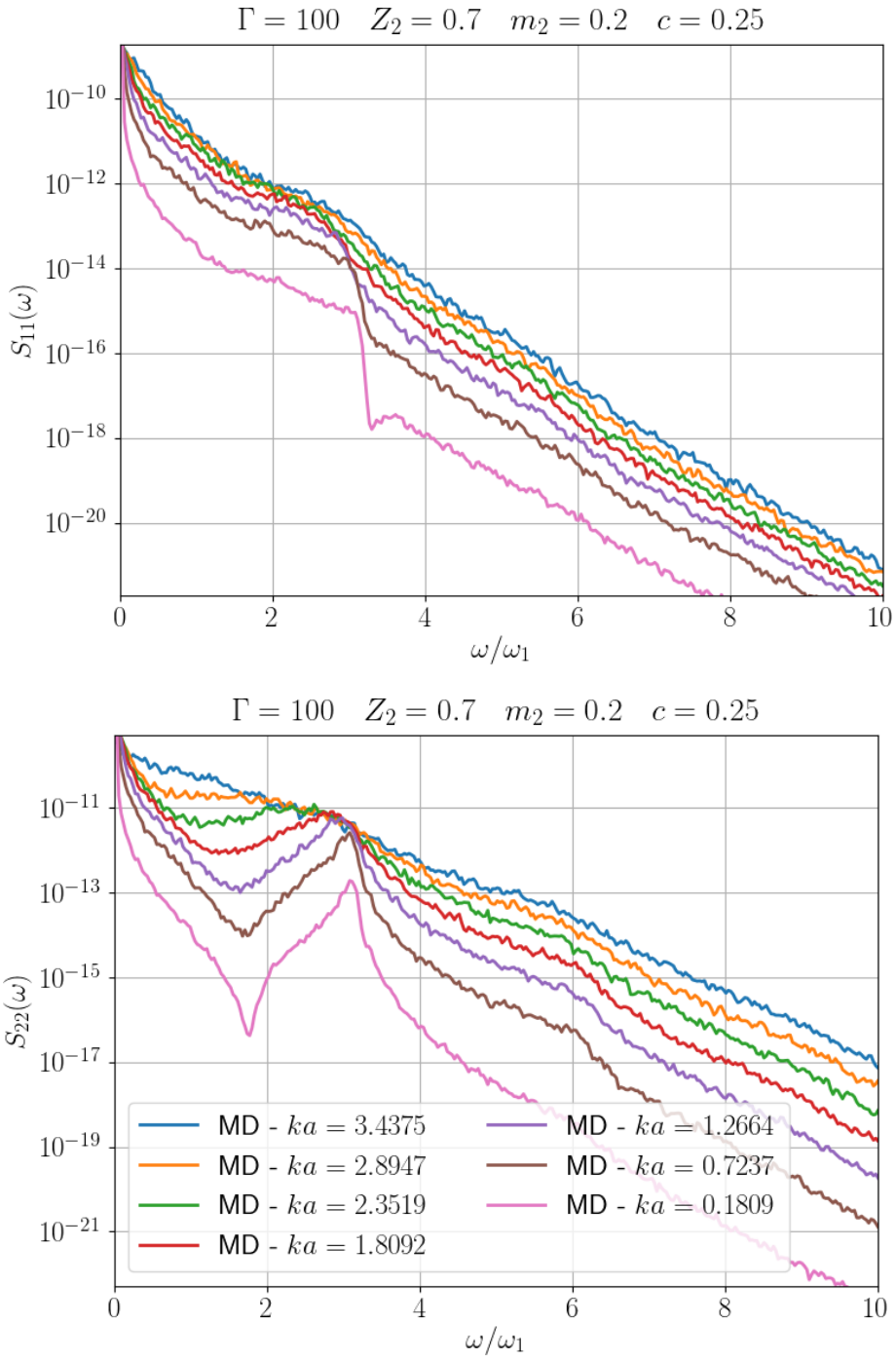

Figure 3.26: Line plots of $S_{AB}(k, \omega)$ for the first few ka values indicating the absence of an acoustic–like mode.

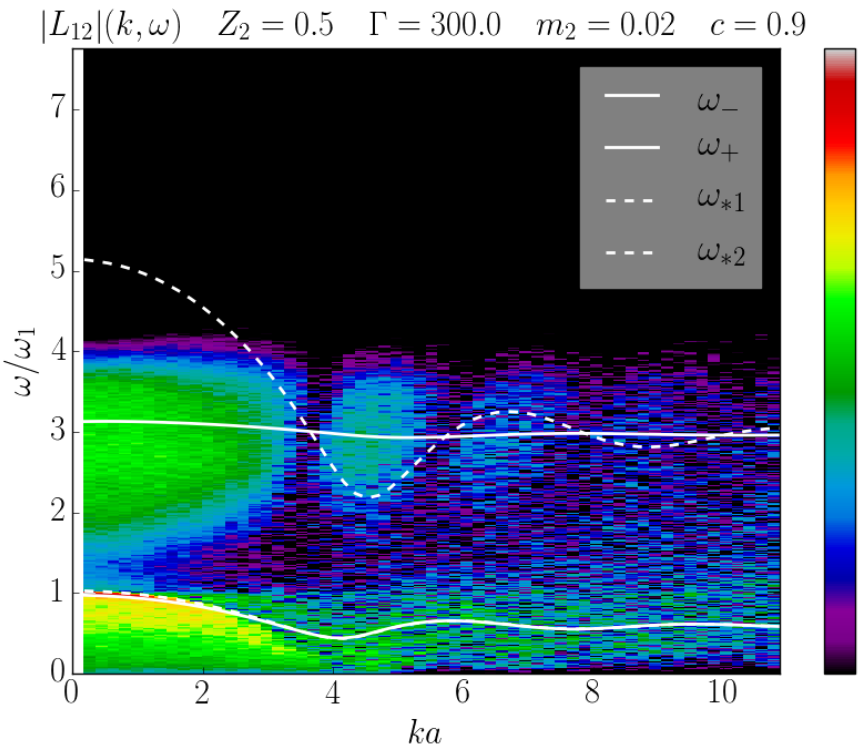

Figure 3.27: Density Plot of $L_{12}9k,\omega)$ to show the dispersion of the SK frequencies indicated by dashed white lines

3.4 Weak to Strong Coupling Transition

Before concluding this chapter few words on the transition from weak to strong coupling are needed. In Fig. 3.31 we show line plots of $S_{ZZ}(k,\omega)$ at the lowest ka value for the available range of Γ. The frequencies of interest are indicated in the plots. We notice that as Γ increases the RPA plasmon peak ω_0 widens and shifts to lower frequencies, indicating a decrease in the temperature dependent k^2–term of the dispersion. The region between $1 < \Gamma < 20$ seems to be a "no man's land" with no signatures of a plasmon mode, but only a very wide shoulder. At around $\Gamma = 10$ (yellow line) the high frequency tail starts to decay much faster suggesting the presence of the high frequency QLCA plasmon, which becomes evident at $\Gamma > 40$ (blue line). At low frequencies instead, we notice the faint presence of the "ion–acoustic" mode only for $\Gamma < 1$. As mentioned before this is

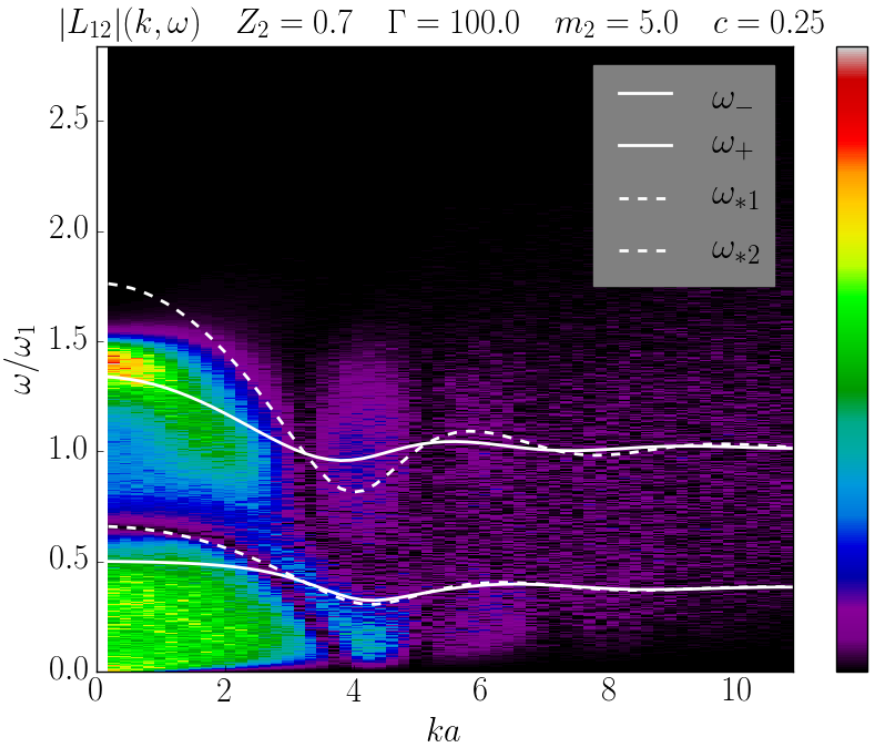

Figure 3.28: Density Plot of $L_{12}9k,\omega)$ to show the dispersion of the SK frequencies indicated by dashed white lines

not a plasmon mode as it disappears at $T = 0$. At intermediate Γ we find again no sign of a collective mode and only at $\Gamma = 20$ we start noticing a low frequency peak at $\omega = \omega_-$. The left most peak at $\Gamma = 200$ is the low frequency phonon mode of a fcc lattice. In fact, the MD simulation for $\Gamma = 200$ was initialized with particle distributed on a fcc lattice and no melting was observed for the entire simulation time. The "no man's land" at $1 < \Gamma < 20$ suggests a non continuous transition from weak to strong coupling. A possible interpretation of this behavior is that the system becomes more and more collisional with increasing Γ leading to a maximum damping at $\Gamma > 5$. As Γ increases further particles become quasi–localized leading to the appearance of two QLCA plasmons for $\Gamma > 20$. The set of parameters shown in Fig. 3.31 is the only set available at this time, due to the very long relaxation time required for low Γ. We expect that with advancement

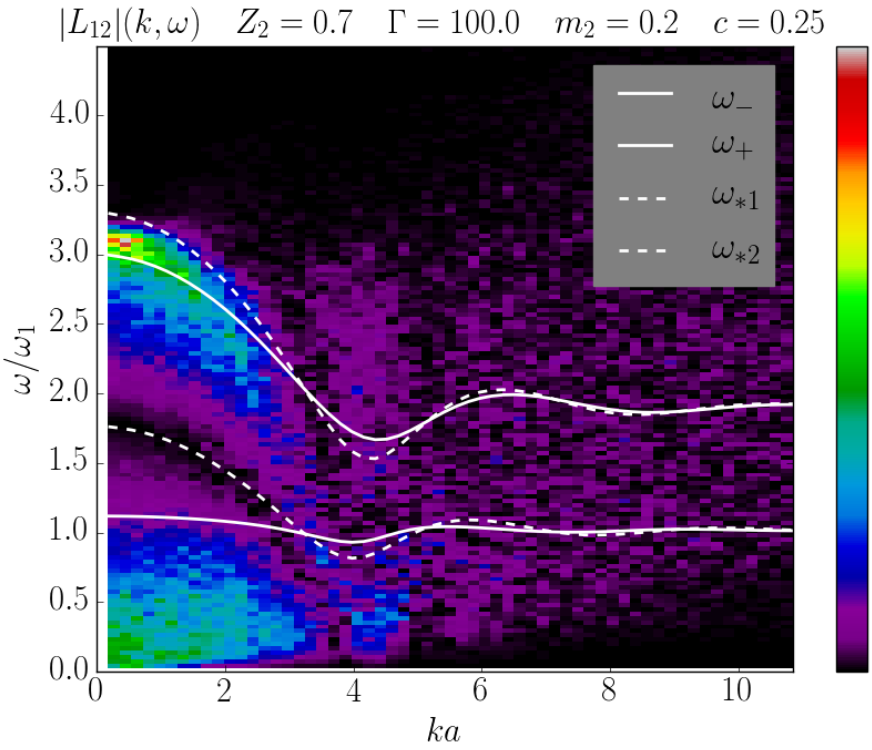

Figure 3.29: Density Plot of $L_{12}9k, \omega)$ to show the dispersion of the SK frequencies indicated by dashed white lines

in computer technology a large set of simulations will be able to show a clearer transition of the modes from weak to high coupling. In order to reach a more conclusive description of the transition more simulations are in need.

In the mean time, though, Kalman *et al.* investigated the origin of the second plasmon from another perspective (Kalman, Donkó, et al., 2014). In their paper they argue that ω_- originates from the acoustic mode of a Yukawa binary mixture by means of the Anderson–Higgs mechanism (Anderson, 1963), while ω_+ from the optic mode. This is true only partially as we will see in the later Chapters. As a teaser we leave with the following question. In an OCP there exists only one longitudinal excitation at $k = 0$. This represents the oscillation of the positive ions with respect to the negative electronic background. When the interaction becomes short range, as in the case of a Yukawa OCP (YOCP), the plasmon

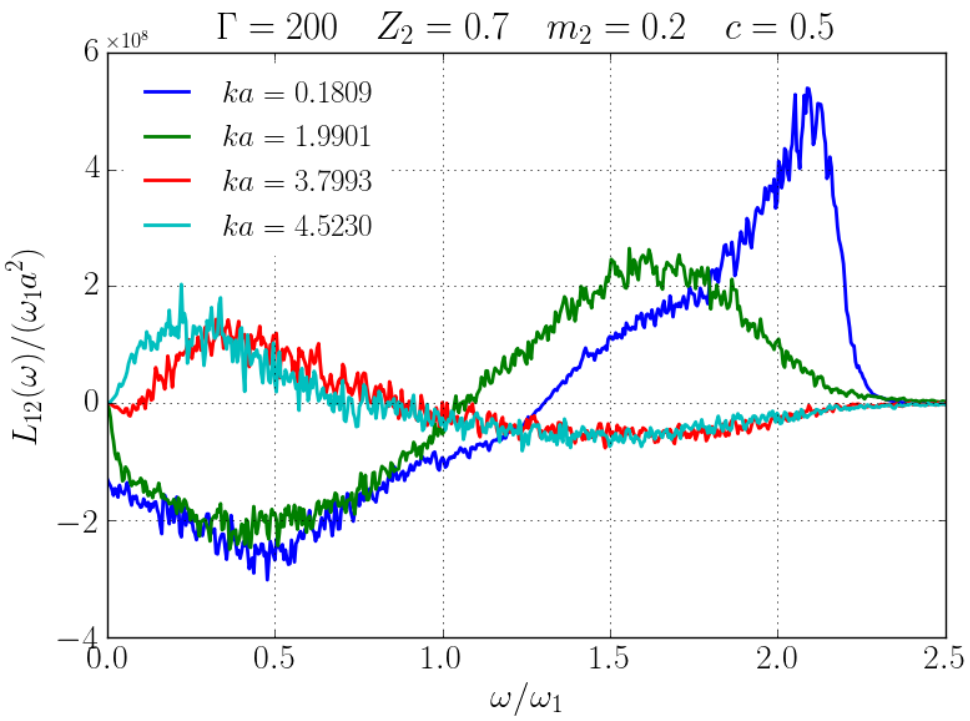

Figure 3.30: Plot of L_{12} at four different ka values showing how the sign change after the collective mode has intersected with the anti-resonance

mode becomes acoustic, *i.e.* vanishes as $\omega \approx sk$ as $k \to 0$ with sound speed s. In a binary mixture we have showed that the high frequency plasmon ω_+ is the binary mixture counterpart of the OCP plasmon, in which both positive ions species are in–phase with each other and oscillate out–of–phase with the negative background. The low frequency plasmon ω_-, instead, is an entirely new correlational–dependent plasmon representative of out–of–phase oscillations between the two ion species. In a Yukawa mixture we will find again two modes: an acoustic mode, typical of in–phase motion, and an optic mode, typical of out–of–phase motion. The question then is: if it is true that the low frequency plasmon comes from the acoustic mode, how do you explain the different polarization?

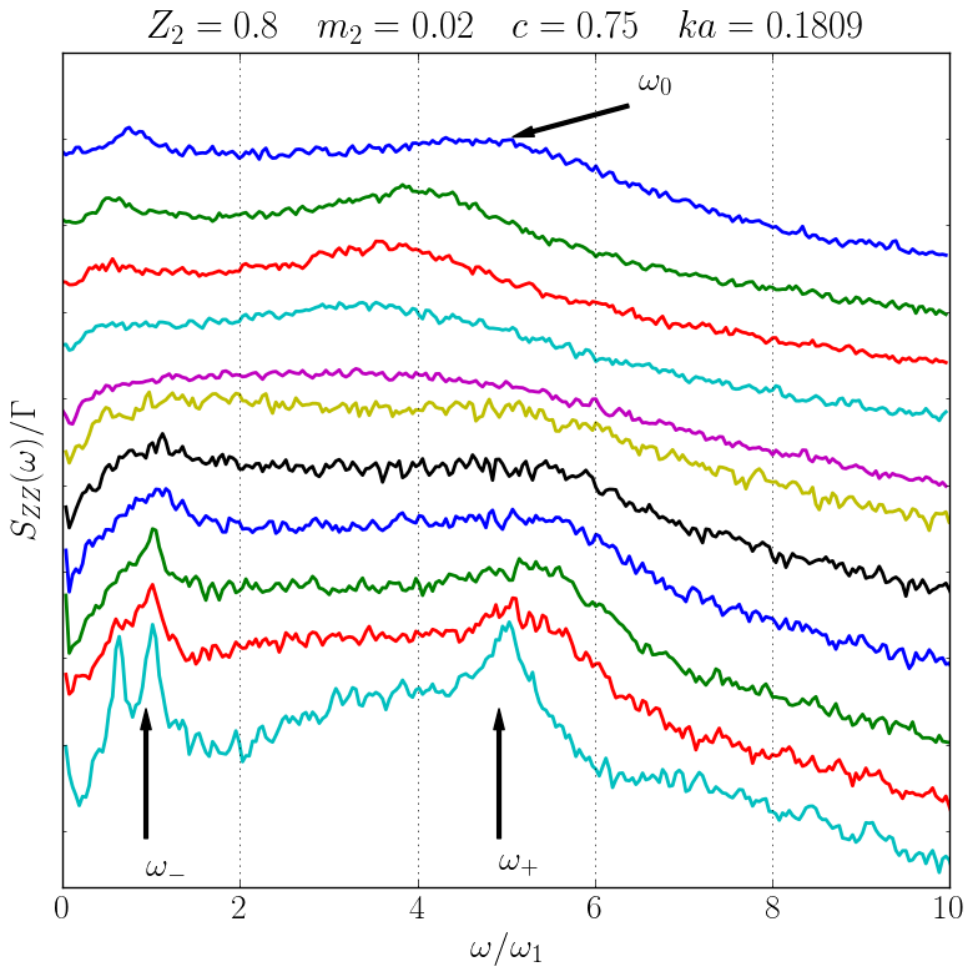

Figure 3.31: From top to bottom $\Gamma = \{0.2, 0.5, 1, 2, 5, 10, 20, 40, 80, 120, 200\}$

3.5 Computer Experiment

We conclude this chapter with a computer experiment. In order to see how the classical Fano effect manifests itself in the binary ionic mixture we investigate the response of the system to an external pertubation. We performed MD simulations of a bcc lattice of $N = 2000$ point-like particles of species 1 and 2 and thermalized to $\Gamma = 10\,000$. An external electric field acting along the x direction only on species A is applied in the form of $E_A(x_i, t) = \sin(\omega_x t)\sin(2\pi\ x_i/L)$. The amplitude of this field is chosen to be small (linear response regime), while the excitation frequency is linearly increased in time starting from $\omega_x = 0.4\omega_1$ up to $\omega_x = 4\omega_1$.

$c = c_1$	$\omega_-(0)$	$\omega_+(0)$	$\omega_{*1}(0)$	$\omega_{*2}(0)$	Ω_{12}	Ω_{21}	ω_p	ω_{vaa}
0.1	1.6199	4.8675	2.7019	5.0547	1.5599	2.9183	4.8010	4.3626
0.25	1.1182	2.9944	1.7607	3.2939	1.0165	1.9017	2.8896	2.4508
0.5	0.9171	2.0022	1.3038	2.4393	0.7528	1.4083	1.8574	1.5519
0.75	0.8814	1.5114	1.1106	2.0777	0.6412	1.1995	1.3478	1.1942
0.9	0.9099	1.2794	1.0382	1.9422	0.5994	1.1213	1.1279	1.0660

Table 3.3: Tabulated values of all the frequencies of the system (in units of ω_1). $Z_1 = m_1 = 1$. $\Gamma = 100$, $Z_2 = 0.7$, $m_2 = 0.2$

During the simulation a small friction term, $-fv$, is added to the equation of motion to compensate for the heating due to the external field. The friction coefficient f is continuously adjusted to provide stable temperature ($\Gamma \approx$ const). The time evolution of the x component of the velocities is recorded to obtain $\langle v_x \rangle^B = \sum_i v_{i,x}^B \sin(2\pi\ x_i/L)$ of species B: this measures $\mathrm{Re}\{\chi_{BA}\}$. In Fig. 3.32 we report $\langle v_x \rangle^2$ when only the second species is perturbed ($\mathrm{Re}\{\chi_{22}\}$). The peaks in Fig. 3.32 are at the poles of $\hat{\chi}_{22}$ which, for the chosen parameters values, are in the vicinity of $\omega_- = 0.917\omega_1$ and $\omega_+ = 2.002\omega_1$. A significant decrease in the oscillation is evident around $\omega_{01} = 1.11\omega_1$, which corresponds to the zero of the numerator, $\sqrt{C_{11}} = 1.1106\omega_1$, thus confirming the consistency of the model (the zeros of $\mathrm{Re}\{\mathcal{D}\}$ are masked by the nearby zeros of the denominator). Tabulated values of all the relevant frequencies are shown in Table 3.3.

3.6 Extra: 2D Binary Coulomb Mixtures

In the above we have investigated 3D Coulomb mixtures only, meanwhile the QLCA was formulated for the description of the collective modes of Coulomb liquids also in 2D (Kalman and Golden, 1990; Golden and Kalman, 2000; Golden and Kalman, 2001). Therefore, in this section we present preliminary results of the Collisional QLCA applied to the case of a binary 2D mixtures of particles interacting via the Coulomb potential. The collisional extension also in this case

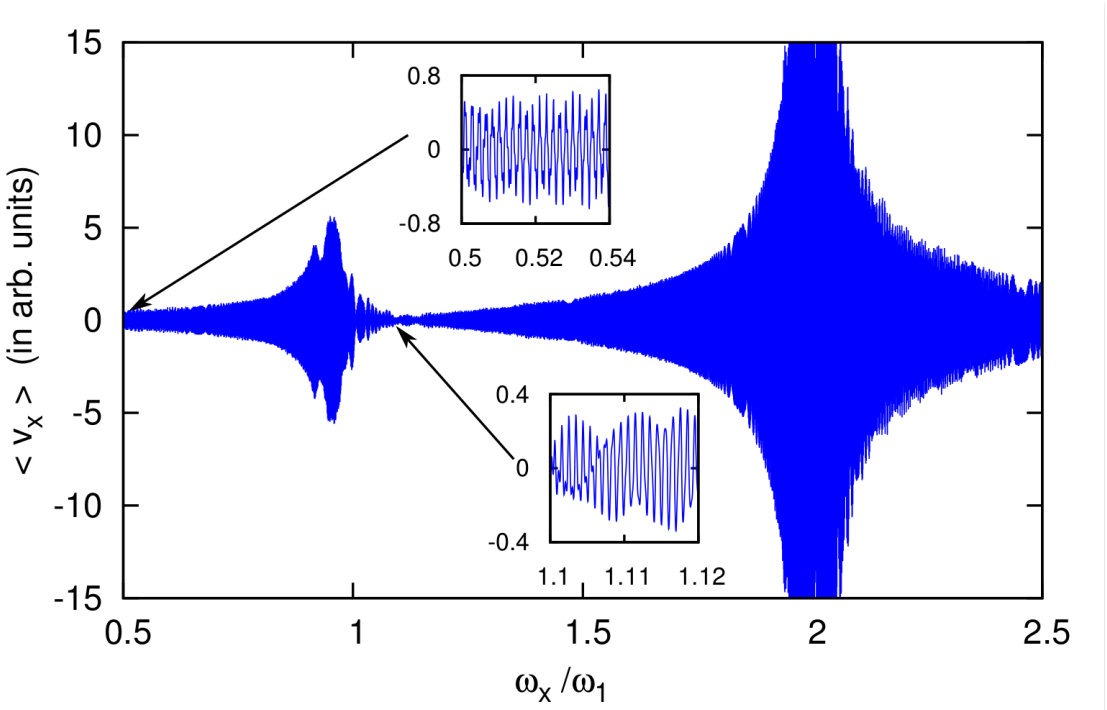

Figure 3.32: Amplitude of the oscillations of the longitudinal velocity of species 2 plotted against the excitation frequency of the fictitious driving force acting on the same species. The insets are magnification of the oscillations showing a decrease in amplitude at $\omega_{02} = \sqrt{C_{11}}$. $\Gamma = 10\,000$, $Z = 0.7$, $m = 0.2$, $c = 0.5$.

predicts the existence of the Silvestri-Kalman frequencies. This is somewhat expected since the expressions of the SK frequencies arise from algebraic properties of complex symmetric matrices. Without going into the details of the calculations of the QLCA 2D dynamical matrix we show in Figs. 3.33-3.34 we show intensity plots of $L_{AB}(k,\omega)$ of a 2D Binary Ionic Mixtures. Plots of $L_{11}(k,\omega)$ and $L_{22}(k,\omega)$ show the collective modes dispersion while the plot of $|L_{12}(k,\omega)|$ is meant to show the dispersion of the SK frequencies. We find good agreement also in this case. This further supports the fact that anti-resonances in asymmetric binary mixtures are due only to asymmetry in the mass/charge of the components. These results are presented here, but are meant to be compared with results in Chap. VI.

3.7 Conclusions

In this Chapter we have investigated a plasma mixture composed by two species of charged ions in a negative neutralizing background. The particles interacted via the long–range Coulomb potential. We have investigated both the weak and strong coupling limits. In the former the dynamics have been studied via the RPA formalism while the Collisional QLCA has been used in the latter. The main result of this chapter is the discovery of anti–resonances in the partial DSF of these mixtures and the excellent agreement with MD simulations. It was shown that the weak coupling anti–resonances are different from their strong coupling counterparts, which have been named as Silvestri–Kalman frequencies. MD simulations have been used to support theoretical predictions. We have shown that the SK frequencies do not depend on the strength of the damping, but they rely on the existence of interspecies damping. The strength of the damping appears to affect only the collective modes. Large damping leads to the broadening and disappearance of one of the two modes. Preliminary results on the calculation of $\det \varepsilon(k, \omega)$ have supported this picture. More discussion on this phenomenon is investigated in the next Chapter. It was also shown that the SK frequencies are also coupling independent, while still relying on the underlying assumption of the quasi–localization of the particles. A computer experiment has been presented in order to confirm the physical mechanism behind the SK frequencies. We conclude this chapter arguing that the Collisional QLCA captures the main features of the dynamics of Strongly Coupled Binary Ionic Mixtures: collective modes and anti–resonances. In addition, the Collisional QLCA allows for the study of the complex dielectric function and a more accurate collisional frequency will lead to an exact calculation of the damping of the modes.

As a reference for future research we list the new features found at strong coupling (vs. weak coupling)

- Two entirely correlational dependent plasmon modes (vs. one single plasmon at weak coupling)
- Negative dispersion at finite ka (vs. positive at weak coupling)
- Roton Minimum
- Silvestri–Kalman frequencies (vs. Fano frequencies at weak coupling)
- The role of ω_{vaa} in the mode dispersion
- Collisional Damping (vs. Landau Damping)

The above features have been investigated in this Chapter, but many more remain to be investigated, just to mention a few

- Behavior of $S_{AB}(k,\omega)$ at $\omega = 0$
- Behavior of $S_{AB}(k,\omega)$ as $\omega \to \infty$
- Collective Mode structure dependence on the charge asymmetry parameter Z
- Transverse Collective Modes

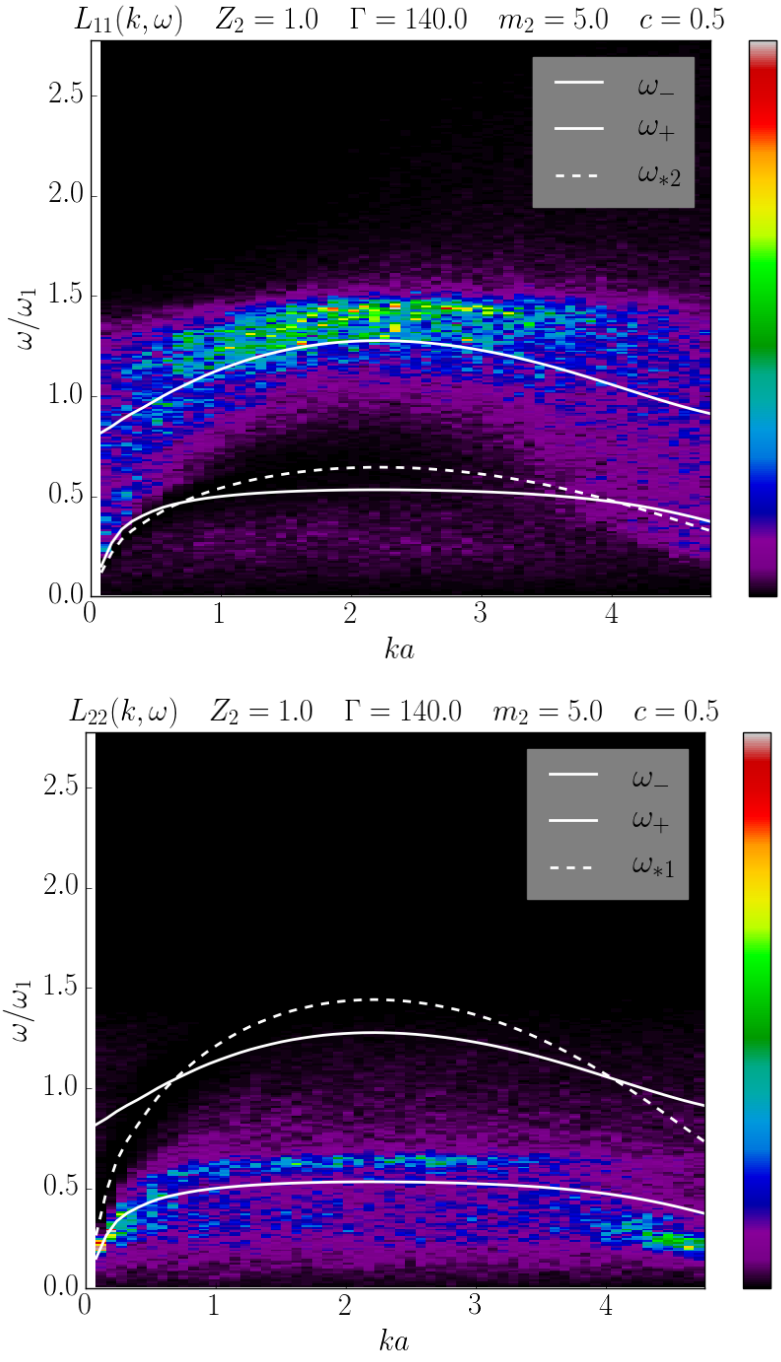

Figure 3.33: Intensity plots of $L_{11}(k,\omega)$ (top) and $L_{22}(k,\omega)$ (bottom) for a 2D Binary Coulomb Mixture

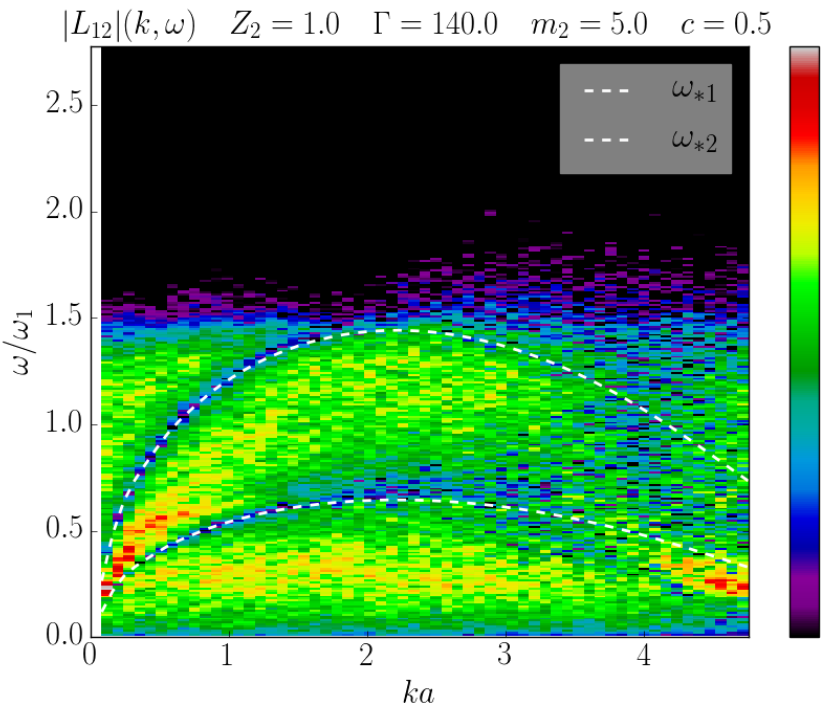

Figure 3.34: Intensity plot of $|L_{12}(k,\omega)|$ for a 2D Binary Coulomb Mixture

CHAPTER IV

Yukawa Binary Mixtures

In the previous Chapter we have investigated mixtures of charges interacting via the long-range Coulomb potential. Here we extend our results to mixtures with short range interaction which we name Yukawa Binary Mixtures (YBM). This model gives a more accurate representation of real physical systems since the negative background is not rigid anymore, but it interacts with the positive ions by effectively screening the Coulomb potential. The most notable system that can be modeled as one component Yukawa plasma is called a dusty plasma. The name dusty comes from the semiconductor industry. In the 80's the semiconductor industry was spending large amount of money on clean room facilities in order to remove dirt and other impurities on the chip in the manufacturing process. Until one day by pure luck (Selwyn, Singh, and Bennett, 1989; Merlino and Goree, 2004) showed that impurities or "dust" in a plasma chamber was getting deposited on the chip. In practice when a plasma is created inside a chamber neutral micron-sized particles become charged due to the high mobility of electrons. The particles acquire large amount of charge, of the order of 10^4 e, and the low kinetic energy makes the particles strongly coupled. Other systems that can be modeled as YOCP are ultracold atoms, colloids, and more recently Warm Dense Matter (Murillo, 2010). The dynamics of strongly coupled YOCP has been exten-

sively studied. Salin (Salin, 2007) derived an expression for the dynamic structure factor (DSF) $S(k,\omega)$ from linearized hydrodynamics equations. Salin showed that $S(k,\omega)$ is given by the sum of three lorentzian centered at $\omega = 0$, $\omega = \pm c_s k$, representing the diffusive peak and two propagating acoustic mode with sound speed c_s respectively. Mithen *et al.* (Mithen, Daligault, and Gregori, 2011) have shown that such description well reproduces the DSF of YOCP for wavelength $k < 0.43\kappa$, while at higher wavenumbers a more sophisticated approach, based on memory functions, is needed (Mithen, Daligault, Crowley, et al., 2011). These works, as stated said, have focused on the Dynamic Structure Function of the YOCP and relied on different formulas for the calculation of the sound speed. Recently, Khrapak and Thomas (Khrapak and Thomas, 2015) have shown how a simple fluid description complemented with a sufficiently general equation of state valid across coupling regimes is sufficient to provide a good estimate for the sound speed. From a fundamental point of view, a substantial amount of work has been done on the collective mode structure of the YOCP using the Quasi-Localized Charge Approximation (QLCA) (Rosenberg and Kalman, 1997; Kalman, Rosenberg, and DeWitt, 2000).

Thus, it is logical to extend the merit of the QLCA to binary mixtures of particles interacting via a Yukawa potential. Kalman *et al.* (Kalman, Hartmann, Donkó, Golden, and Kyrkos, 2013) studied the collective mode structure of 2D Yukawa binary mixtures comparing theoretical predictions with Molecular Dynamics (MD) simulations. In this chapter, I will expand their work on to 3D Yukawa binary mixtures. In Sec. 4.1 I will introduce the parameters that define YBM, in Sec. 4.2 will review and expand on the weak coupling regime, while in Sec. 4.3 will look at the strong coupling regime, and finally compare with MD simulations in Sec. 4.4.

4.1 Model and definitions

We consider a 3D plasmas composed $N = N_1 + N_2$ particles of two species with charges, Z_A, masses, m_A, and concentrations $c_A = N_A/N$. The particles interact via the Yukawa potential

$$\phi(r) = \frac{Z_A Z_B e^2}{r} e^{r/\lambda_Y} \tag{4.1}$$

where λ_Y is the screening length. The entire system is characterized by two parameters: the screening length

$$\kappa = a/\lambda_Y, \tag{4.2}$$

and the coupling parameter

$$\Gamma = \frac{\beta e^2}{a} \tag{4.3}$$

where a is the interparticle distance defined by the Wigner–Seitz radius of each species

$$a = \sqrt{a_1 a_2}, \quad a_A^3 = \frac{3}{4\pi}\frac{1}{n_A} \tag{4.4}$$

with n_A the number density of species A. Notice that a has been defined differently than the Binary Coulomb Mixtures. Furthermore, we define the charge $Z = Z_2/Z_1$, mass $m = m_2/m_1$ and density ratio $n = n_2/n_1 = c_2/c_1$ which are cast together in the two parameters

$$p^2 = Zn, \qquad q^2 = \frac{Z}{m}. \tag{4.5}$$

4.2 Weak Coupling

Following the structure of the BIM chapter we calculate the collective modes in the weakly coupled regime using the Vlasov equation and in the strongly coupled

regime the QLCA. While the validity of the Vlasov equation in the weak coupled regime is tacitly assumed, it has been shown that for the Yukawa OCP (YOCP) this assumption is valid with some limitations (Golden, Kalman, and Silvestri, 2018). Depending on the values of Γ and κ and $w = s/v_{th}$ (*i.e.* the ratio between the phase velocity of the wave and thermal speed of the particles) we have identified five different domains in the (κ, Γ) parameter space in which the physical behavior of the YOCP exhibits different features.

Generalizing the formalism of (Golden, Kalman, and Silvestri, 2018) we find, at $\Gamma \ll 1$, the collective modes from the (complex) solutions of

$$\varepsilon(k,\omega) = 1 - \sum_A \phi_A(k)\bar{\chi}_A(k,\omega) \tag{4.6}$$

$$\phi_A(k) = \frac{4\pi(Z_A e)^2}{k^2+\kappa^2}, \tag{4.7}$$

where $\bar{\chi}_A$ is the usual Vlasov polarization function

$$\bar{\chi}_A(k,\omega) = -\frac{1}{m_A}\int d^3v \frac{\mathbf{k}\cdot\partial_{\mathbf{v}} f_M(\mathbf{v})}{\mathbf{k}\cdot\mathbf{v} - (\omega + i\delta)}, \tag{4.8}$$

$f_M(v)$ the Maxwell-Boltzmann distribution

$$f_M(\mathbf{v}) = n_A\left(\frac{m_A}{2\pi T_A}\right)^{3/2}\exp\left(-\frac{mv^2}{2T_A}\right) \tag{4.9}$$

which gives

$$\bar{\chi}_A(k,\omega) = -\frac{n_A}{m_A}\frac{m_A}{T_A}\left[1 + \zeta_A \mathcal{Z}(\zeta_A)\right], \quad \zeta_A = \frac{\omega}{k}\sqrt{\frac{m_A}{2T_A}} \tag{4.10}$$

where $\mathcal{Z}(\zeta)$ is the Plasma Dispersion Function defined in the previous Chapter. We can rescale $\phi_A(k)\bar{\chi}_A(k,\omega)$ by their Debye wavelengths

$$\mu_1^2 = 4\pi e^2 Z_1^2 n_1 \beta = \frac{3\Gamma}{a^2\sqrt{n}} Z_1^2, \quad \mu_2^2 = 4\pi e^2 Z_2^2 n_2 \beta = \frac{3\Gamma}{a^2\sqrt{n}} Z_2^2 n \tag{4.11}$$

where $\sqrt{n} = \sqrt{n_2/n_1}$ in the denominator is due to the fact that $a = \sqrt{a_1 a_2}$. Thus, the dielectric function becomes

$$\begin{aligned} \varepsilon(k,\omega) &= 1 - \frac{3\Gamma}{\sqrt{n}} \frac{1}{(ka)^2+\kappa^2} \left\{ Z_1^2 \left[1 + \zeta_1 \mathcal{Z}(\zeta_1)\right] + Z_2^2 n \left[1 + \zeta_2 \mathcal{Z}(\zeta_2)\right] \right\} & (4.12) \\ &= 1 - \frac{3\Gamma}{\sqrt{n}} \frac{Z_1^2 + Z_2^2 n}{(ka)^2+\kappa^2} \Pi(\zeta_1) & (4.13) \end{aligned}$$

The dispersion relation, assuming small damping, then reads

$$\mathrm{Re}\Pi(\zeta_1) = \frac{k^2+\kappa^2}{3\Gamma} \frac{\sqrt{c_1 c_2}}{\langle Z^2 \rangle} \tag{4.14}$$

In Figs. 4.2–4.2 we show plots of $\mathrm{Re}\{\Pi(\zeta_1)\}$ for different values of the asymmetry parameters. The RHS of eq. (4.14) will appear as a horizontal line on the same plot. The intersection points are the collective modes and the propagating mode will be the intersection point on the right of the maximum. Thus, only those values of κ and Γ for which the horizontal line is below the maximum of $\mathrm{Re}\{\Pi(\zeta_1)\}$ allow for the existence of an acoustic mode. The largest maximum value of $\mathrm{Re}\{\Pi\}$ is $\Pi_{\max} = 0.2848$ at $m = 1$ for any concentration and charge ratio (since it has been normalized to 1). Using this value we can find the sufficient condition

$$\Gamma > \frac{\kappa^2}{3\Pi_{\max}} \frac{\langle Z^2 \rangle}{\sqrt{c_1 c_2}} = 1.17\kappa^2 \frac{\langle Z^2 \rangle}{\sqrt{c_1 c_2}}. \tag{4.15}$$

which, as one would expect, is closely related to the YOCP condition, see eq. (12) in (Golden, Kalman, and Silvestri, 2018). For the sake of completeness we report

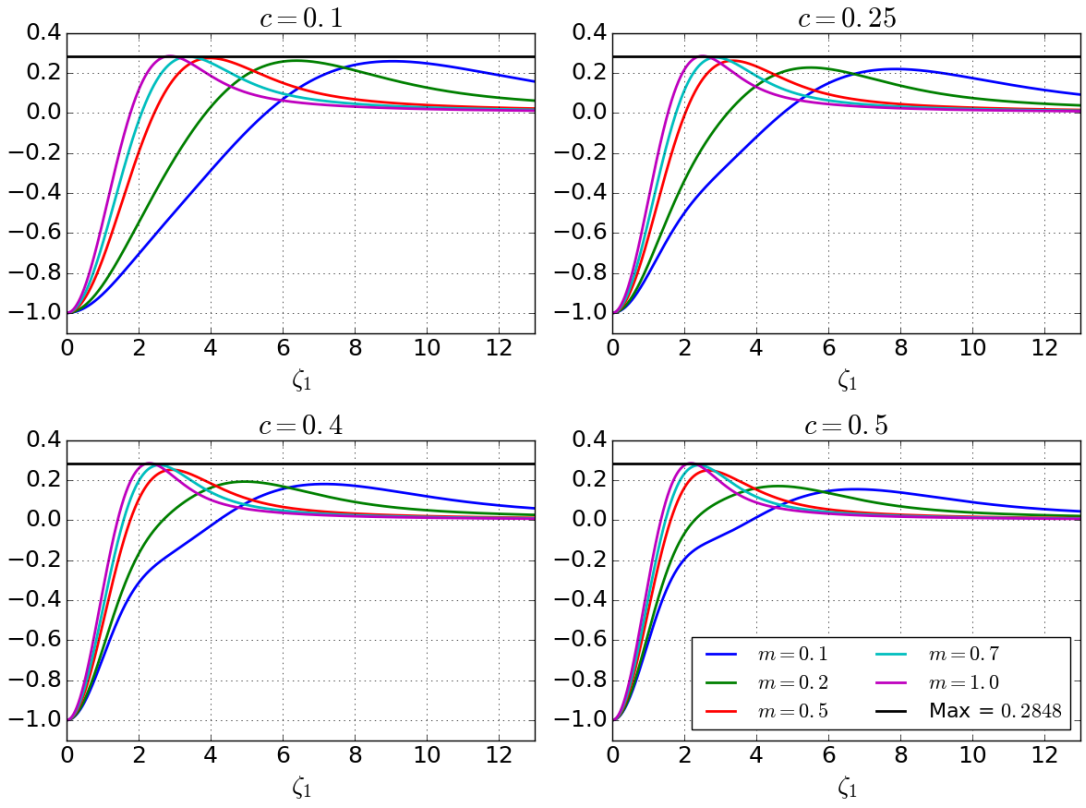

Figure 4.1: Plot of $\mathrm{Re}\{\Pi(\zeta_1)\}$ with $Z_1 = Z_2 = 1$ for different mass ratios at four different concentrations and $\Gamma = 0.3$. The black line indicates the maximum value reached at $m = 1$. Note that $c = c_1$.

the maximum values of $\mathrm{Re}\{\Pi\}(\zeta_1)$ for the plotted mass ratios in Table 4.1. In Figs. 4.2–4.4 we show contour maps of the quantity

$$Y_c(\kappa, \Gamma) = \frac{\kappa^2}{3\Gamma} \frac{\sqrt{c_1 c_2}}{\langle Z^2 \rangle} \tag{4.16}$$

The color indicates the value of $Y_c(\kappa, \Gamma)$. The color code has been limited to $Y_c = 0.5$ for better viewing. The black lines indicate specific contours of Y_c. The contour line in between $0.1 < Y_c < 0.5$ indicate the maximum value $Y_c(m = 1)$ and $Y_c(m = 0.2)$. Comparing this with Table 4.1 we see that the allowed values of Γ and κ are those below the line $Y_c = 0.2848$ in the green-blue region.

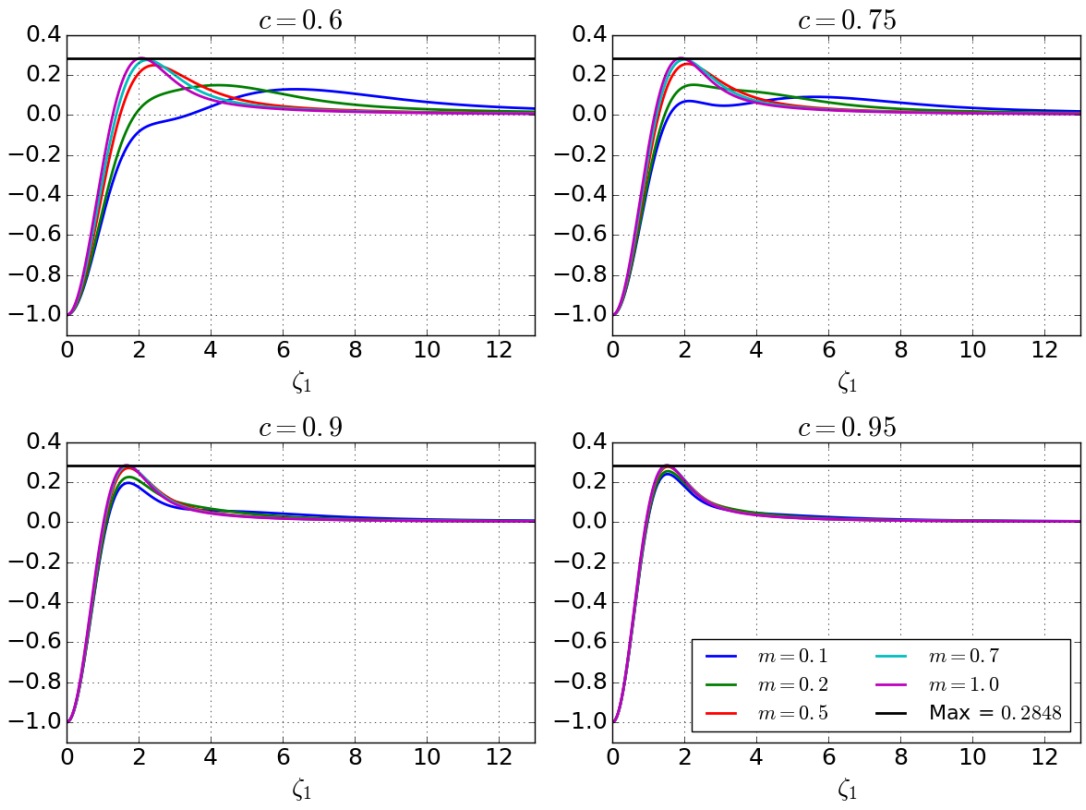

Figure 4.2: Plot of $\mathrm{Re}\{\Pi(\zeta_1)\}$ with $Z_1 = Z_2 = 1$ for different mass ratios at four different concentrations and $\Gamma = 0.3$. The black line indicates the maximum value reached at $m = 1$. Note that $c = c_1$.

The collective mode can be calculate using the $\zeta_1 \to \infty$ expansion of $\mathcal{Z}(\zeta_1)$

$$\mathcal{Z}(x) \approx -\frac{1}{x}\left[1 + \frac{1}{2x^2} + \frac{3}{4}\frac{1}{x^4} + \frac{15}{8}\frac{1}{x^6} + ...\right] + i\pi e^{-x^2}, \tag{4.17}$$

to find

$$\begin{aligned} \varepsilon &= 1 + \frac{1}{k^2+\kappa^2}\left[\mu_1^2 v_1^2 \frac{k^2}{\omega^2} + 3\mu_1^2 v_1^4 \frac{k^4}{\omega^4} + \mu_2^2 v_2^2 \frac{k^2}{\omega^2} + 3\frac{k^4}{\omega^4}\mu_2^2 v_2^4\right] \\ &= 1 + \frac{\omega_p^2}{k^2+\kappa^2}\left[\frac{k^2}{\omega^2} + 3\frac{\omega_1^2 v_1^2 + \omega_2^2 v_2^2}{\omega_p^2}\frac{k^4}{\omega^4}\right] \end{aligned} \tag{4.18}$$

m	0.1	0.2	0.5	0.7	1.0
$c = 0.25$	0.2196	0.2269	0.2614	0.2776	0.2848
$c = 0.4$	0.1805	0.1927	0.2519	0.2753	0.2848
$c = 0.5$	0.1546	0.1704	0.2487	0.2747	0.2848
$c = 0.6$	0.1287	0.1490	0.2487	0.2749	0.2848
$c = 0.75$	0.0904	0.1508	0.2555	0.2769	0.2848
$c = 0.9$	0.1962	0.2258	0.2706	0.2809	0.2848
$c = 0.95$	0.2402	0.2547	0.2773	0.2827	0.2848

Table 4.1: Table of the maximum value of $\mathrm{Re}\{\Pi\}(\zeta_1)$ for the different concentration and mass ratios.

whose solution is an acoustic mode

$$\omega_0(k) = sk \tag{4.19}$$

with the sound speed

$$\begin{aligned} s^2_{\mathrm{Th,RPA}} &= \frac{c_0^2}{\sqrt{2}}\left[1+\sqrt{1+12\frac{\omega_1^2 v_1^2+\omega_2^2 v_2^2}{\omega_p^4}\kappa^2}\right] \\ &= \frac{s_0^2}{2}\left[1+\sqrt{1+12\frac{\kappa^2}{3\Gamma/\sqrt{n}}\left(1+\frac{q^2p^2}{m}\right)\left(1+q^2p^2\right)^{-4}}\right], \end{aligned} \tag{4.20}$$

$s_0 = \omega_p/\kappa$ is the $T = 0$ sound speed. In the last passage we have expressed it in terms of the asymmetry parameters $Z = Z_2/Z_1$, $n = n_2/n_1$, $m = m_2/m_1$.

At the same time we can calculate the sound speed following the procedure in (Golden, Kalman, and Silvestri, 2018). Using the expansion (4.17) again we can write Π as

$$\Pi(w) = \frac{1}{1+Z^2 n}\left\{\frac{w}{2}+\frac{3w^2}{4}+\frac{15w^3}{8}+Z^2 n\left[\frac{w}{2m}+\frac{3w^2}{4m^2}+\frac{15w^3}{8m^3}\right]+O(w^4)\right\}. \tag{4.21}$$

$$w = \frac{1}{\zeta_1^2} = \frac{k^2}{\omega^2}\frac{2}{\beta m_1} = \frac{2}{s^2\beta m_1}. \tag{4.22}$$

Inverting the series for $y = Y_c$ gives

$$\begin{aligned} w &= \frac{2my}{m+nZ^2} - \frac{6y^2\left(m\left(m^2+nZ^2\right)\right)}{\left(m+nZ^2\right)^3} \\ &\quad + \frac{6y\left(2m^4+5m^3nZ^2-12m^2nZ^2+5mnZ^2+2n^2Z^4\right)}{m\left(m+nZ^2\right)^3} \end{aligned} \tag{4.23}$$

Finally the sound speed $s^2_{\text{asym}} = 2/w(y \ll 1)$

$$s^2_{\text{asym}} = \frac{\omega_p^2}{\kappa^2} + 3\frac{\omega_1^2v_1^2+\omega_2^2v_2^2}{\omega_p^2} + 6\frac{\kappa^2}{\omega_p^6}\left[\left(\omega_1^2v_1^2+\omega_2^2v_2^2\right)^2 + \frac{5}{2}\omega_1^2\omega_2^2\left(v_1^2-v_2^2\right)^2\right] \tag{4.24}$$

which in units of s_0 is

$$\begin{aligned} s^2_{\text{asym}} &= s_0^2\left\{1+3\frac{\kappa^2}{3\Gamma/\sqrt{n}}\left[\frac{1+q^2p^2/m}{(1+q^2p^2)^2}\right]\right. \\ &\quad \left. +6\left(\frac{\kappa^2}{3\Gamma/\sqrt{n}}\right)^2\left[\frac{\left(1+q^2p^2/m\right)^2}{(1+q^2p^2)^4} + \frac{5}{2}\frac{q^2p^2(1-1/m)^2}{(1+q^2p^2)^4}\right]\right\}. \end{aligned} \tag{4.25}$$

As expected both formulas give s_0 in the $T = 0$ ($\Gamma \to \infty$) limit. An important feature, that will become evident later on, is that the total plasma frequency $\omega_p \propto \sqrt{n_1/m_1 + n_2/m_2}$ and as such is largely determined by the light species. In (Golden, Kalman, and Silvestri, 2018) it was shown that the first expression, eq. (4.20), agreed better than the second with MD simulation As we will see later this is the case here too. In Figs. 4.5-4.7 we show intensity maps of $S_{AB}(k,\omega)$ for three Γ values for three different regions on the κ, Γ phase space of Fig. 4.4. The first plots correspond to a point in the red region, the second to a point in between the contours $Y_c = 0.2848$ and $Y_c = 0.1508$, and the last plots to a point in the dark blue region. Notice how the acoustic mode becomes sharper with increasing Γ. In the plots the black line indicates the mode given by the sound speed $s_{\text{Th,RPA}}$ calculated from eq. (4.20). The red line, instead, is the solution of the $1 - \phi_1(k)\bar{\chi}_1(k,\omega) == 0$ *i.e.* the acoustic mode of an YOCP created entirely

by species 1. Similarly to the Coulomb case this acoustic frequency corresponds to the anti-resonance observable in $S_{22}(k,\omega)$.

4.3 Strong Coupling

In the strongly coupled regime the QLCA has proved to be successfull in the predition of the collective mode spectrum for similar systems; 2D binary yukawa mixture and yukawa one component plasma (Kalman, Hartmann, Donkó, Golden, and Kyrkos, 2013). In the case of a 3D Binary Yukawa Mixture we have that the longitudinal dynamical matrix elements are (see Appendix C.2 for details)

$$C_{11}(k) = \omega_1^2 \left[\frac{k^2}{k^2+\kappa^2} - \frac{1}{2} D_{11}(k,\kappa) + \frac{p^2}{3} W(\kappa) \right] \tag{4.26a}$$

$$C_{12}(k) = \omega_1^2 qp \left[\frac{k^2}{k^2+\kappa^2} - \frac{1}{2} D_{12}(k,\kappa) - \frac{1}{3} W(\kappa) \right] \tag{4.26b}$$

$$C_{22}(k) = \omega_1^2 \left[q^2 p^2 \frac{k^2}{k^2+\kappa^2} - q^2 p^2 \frac{1}{2} D_{22}(k,\kappa) + \frac{q^2}{3} W(\kappa) \right] \tag{4.26c}$$

where

$$D_{AB}(k,\kappa) = \int \frac{dr}{r} \left[\mathcal{K}(kr,\kappa r) - \mathcal{K}(0,\kappa r) \right] h_{AB}(r), \tag{4.27}$$

$$W(\kappa) = 1 + \kappa^2 \int dr r e^{-\kappa r} h_{12}(r). \tag{4.28}$$

The $\mathcal{K}(k,\kappa r)$ are integrals of the interaction potential over the solid angle (see eq. (C.19)). Notice that by taking the limit $\kappa \to 0$ one recovers the dynamical elements of a Binary Coulomb Mixture. As in BIM the first term is the RPA contribution to the mean field and the second and third terms represent (explicit) correlational effect. We stress again that the naïve substitution $h_{AB}(k) = 0$ in eq. (B.19) appears to recover the high-frequency RPA result. However, this substitution does not translate in $h_{AB}(r) = 0$ since this would not cancel the constant

term in $W(\kappa, h_{12} = 0) = 1$. This is easily seen in the expression of $\bar{\chi}_{AB}$

$$\bar{\chi}_{11}(k,\omega) = \frac{n_1}{m_1} k^2 \frac{\omega^2 - H_{22}}{|\omega^2 \mathbf{I} - \mathbf{H}|}, \tag{4.29}$$

$$\bar{\chi}_{12}(k,\omega) = \sqrt{\frac{n_1 n_2}{m_1 m_2}} k^2 \frac{H_{12}}{|\omega^2 \mathbf{I} - \mathbf{H}|}, \tag{4.30}$$

$$\bar{\chi}_{22}(k,\omega) = \frac{n_2}{m_2} k^2 \frac{\omega^2 - H_{11}}{|\omega^2 \mathbf{I} - \mathbf{H}|}, \tag{4.31}$$

where

$$H_{AB} = C_{AB}(k) - \omega_A \omega_B \frac{k^2}{k^2 + \kappa^2} - i\omega R_{AB}. \tag{4.32}$$

For $h_{AB}(r) = 0$ $\bar{\chi}_{12} \neq 0$ while in the RPA $\bar{\chi}_{12} = 0$.

4.3.1 The longitudinal dielectric function

Using the above expressions we can calculate the dielectric matrix elements

$$\varepsilon_{11}(k,\omega) = 1 - 4\pi e^2 \phi(k) \left[Z_1^2 \bar{\chi}_{11} + Z_1 Z_2 \bar{\chi}_{21} \right] \tag{4.33}$$

$$\varepsilon_{12}(k,\omega) = -4\pi e^2 \phi(k) \left[Z_1^2 \bar{\chi}_{12} + Z_1 Z_2 \bar{\chi}_{22} \right] \tag{4.34}$$

$$\varepsilon_{21}(k,\omega) = -4\pi e^2 \phi(k) \left[Z_2^2 \bar{\chi}_{21} + Z_1 Z_2 \bar{\chi}_{11} \right] \tag{4.35}$$

$$\varepsilon_{22}(k,\omega) = 1 - 4\pi e^2 \phi(k) \left[Z_2^2 \bar{\chi}_{22} + Z_1 Z_2 \bar{\chi}_{12} \right] \tag{4.36}$$

where $\phi(k) = 1/(k^2 + \kappa^2)$. The collective modes of the system are given by the zeros of the determinant which is given by

$$\det \varepsilon(k,\omega) = \frac{\det\{\omega^2 \mathbf{I} - \mathbf{G}(k,\omega)\}}{\det\{\omega^2 \mathbf{I} - \mathbf{H}(k,\omega)\}}, \tag{4.37}$$

Further simplification leads to

$$\det\{\varepsilon(k,\omega)\} = \frac{(\omega^2-\omega_+^2)(\omega^2-\omega_-^2)-i\omega\,(R_{11}+R_{22})\,(\omega^2-\omega_{\rm im}^2)}{(\omega^2-\delta_+^2)(\omega^2-\delta_-^2)-i\omega\,(R_{11}+R_{22})\,(\omega^2-D_+(k))} \quad (4.38)$$

$$= \frac{(\omega^2-\omega_+^2)(\omega^2-\omega_-^2)-i\omega\nu\omega_1\,(n+1/m)\,(\omega^2-\omega_{\rm im}^2)}{(\omega^2-\delta_+^2)(\omega^2-\delta_-^2)-i\nu\omega\omega_1\,(n+1/m)\,[\omega^2-D_+(k)]} \quad (4.39)$$

where ν is the nominal collisional frequency, $\omega_\pm$ are the QLCA modes, $\omega_{\rm im}$ is given by eq. (2.41), and $\delta_\pm(k)$ are the zeros of the real part of the denominator and $D_+(k)$ the zero of the imaginary part.

Considering at first the case of negligible damping, we notice that the collective modes correspond to $\omega_\pm$. In the long wavelength limit these are (details of the calculation are given in App. C.2)

$$\omega_+^2(k\to 0) = \omega_{\rm vaa}^2\left[1-\frac{U_+}{(1+p^2)^2}\right]\frac{k^2}{\kappa^2} \quad (4.40)$$

$$\omega_-^2(k\to 0) = \left(\frac{\Omega_{12}^2+\Omega_{21}^2}{3}\right)W(\kappa)+\left(\omega_p^2-\omega_{\rm vaa}^2\right)\left[1-\frac{U_-}{(1-q^2)^2}\right]\frac{k^2}{\kappa^2} \quad (4.41)$$

$$U_+ = U_{11}+2p^2U_{12}+p^4U_{22}, \quad U_- = U_{11}-2q^2U_{12}+q^4U_{22} \quad (4.42)$$

where U_{AB} are the long wavelength limit of the $D_{AB}(k)$ correlational terms (precisely $\lim_{k\to 0} D_{AB} = 2U_{AB}k^2/\kappa^2$). The subscripts "$\pm$" indicate the polarization of the eigenvectors of $\mathbf{C}(k)$; "$+(-)$" the two species are in-phase (out-of-phase). As expected, in a system with short range interaction, the strongly coupled phase continues to be characterized by an acoustic mode with a linear dispersion for $k\to 0$. The difference with the weak coupling phase is in the sound speed of this mode. The sound speed in the strongly coupled phase is lower than the weak coupling. The lowering is twofold. First, the RPA plasma frequency ω_0 is replaced with the hydrodynamics frequency $\omega_{\rm vaa}<\omega_0$. Second, the sound speed is further reduced by correlations, see the term U_+. This is a further indication that one

does not recover the RPA when $h_{AB} = 0$. The transition from weak to strong coupling is further investigated in Sec. 4.5.1.

The other major feature of the strongly coupled phase is the existence of a new gapped mode, $\omega_-(k)$, with gap frequency

$$\omega_-^2(0) = \left(\frac{\Omega_{12}^2 + \Omega_{21}^2}{3}\right) W(\kappa). \tag{4.43}$$

which depends entirely on the inter-particles correlations. In fact, the term

$$\frac{\Omega_{AB}^2}{3} W(\kappa) = \frac{\Omega_{AB}^2}{4\pi} \int d^3 r \psi^L(r) \left[1 + h_{AB}(r)\right] \tag{4.44}$$

represents the average field that a particle of species A experiences in a frozen environment of species B particles. It is important to clarify that these are not the Einstein frequencies which instead are given by

$$\Omega_{E1}^2 = \frac{\omega_1^2 + \Omega_{12}^2}{3} W(\kappa), \quad \Omega_{E2}^2 = \frac{\omega_2^2 + \Omega_{21}^2}{3} W(\kappa). \tag{4.45}$$

Furthermore, it is easy to verify that these frequencies correspond to the short wavelength limit of the collective modes

$$\omega_\pm^2(k \to \infty) = \Omega_{E1,2}^2. \tag{4.46}$$

Looking now at the denominator, in the long wavelength limit we find

$$\delta_+(k \to 0) = -\omega_{\text{vaa}}^2 \frac{U_+}{(1+p^2)^2} \frac{k^2}{\kappa^2}, \tag{4.47}$$

$$\delta_-(k \to 0) = \left(\frac{\Omega_{12}^2 + \Omega_{21}^2}{3}\right) W(\kappa) - \left(\omega_p^2 - \omega_{\text{vaa}}^2\right) \frac{U_-}{(1-q^2)^2} \frac{k^2}{\kappa^2} \tag{4.48}$$

which are none other than the correlational correction to the QLCA modes.
The SK frequencies of a YBM are

$$\omega_{*1}^2(k) = \left(\omega_1^2 + \Omega_{12}^2\right) \frac{k^2}{k^2+\kappa^2} - \frac{\omega_1^2}{2}\left[D_{11}(k) + p^2 D_{12}(k)\right], \tag{4.49a}$$

$$\omega_{*2}^2(k) = \left(\omega_2^2 + \Omega_{21}^2\right) \frac{k^2}{k^2+\kappa^2} - \frac{\omega_2^2}{2}\left[D_{22}(k) + \frac{1}{p^2} D_{12}(k)\right]. \tag{4.49b}$$

Using these we can calculate the zero of the imaginary part of the numerator of $\det \varepsilon(k,\omega)$, $\omega_{\rm im}(k)$. Using eq. (2.41) we find

$$\begin{aligned}
\omega_{\rm im}^2(k) &= \frac{q^2\omega_{*1}^2(k) + p^2\omega_{*2}^2(k)}{q^2+p^2}, \\
&= \omega_{\rm vaa}^2 \frac{k^2}{k^2+\kappa^2} - \frac{\omega_{\rm vaa}^2}{2} \frac{D_{11}(k) + 2p^2 D_{12}(k) + p^4 D_{22}(k)}{(1+p^2)^2}, \\
&= \omega_{\rm vaa}^2 \left[\frac{k^2}{k^2+\kappa^2} - \frac{1}{2}\frac{D_+(k)}{(1+p^2)^2}\right].
\end{aligned} \tag{4.50}$$

The important point to notice is that in the long wavelength limit $\omega_{\rm im}^2(k\to 0) = \omega_+^2(k\to 0)$, which leads to

$$\det\{\varepsilon(k,\omega)\} \propto (\omega^2 - \omega_+^2) \frac{(\omega^2-\omega_-^2) - i\omega\nu\omega_1\,(n+1/m)}{(\omega^2-\delta_+^2)(\omega^2-\omega_-^2) - i\nu\omega\omega_1\,(n+1/m)\,(\omega^2 - U_+(k))}, \tag{4.51}$$

where we also used the fact that $\delta_-(k\to 0) \approx \omega_-(0)$. This shows that only the gap mode is affected by collisional damping while the acoustic mode is likely damped by thermal effects (Landau damping). This simplification was not found in the Binary Coulomb Mixture, and was showed only with plots of $\det \varepsilon(k,\omega)$. In order to consider also thermal effect we use the Extended QLCA formalism as presented in Sec. 2.2.3.
In the following we study the behavior of $\det\{\varepsilon(k,\omega)\}$ as a function of the system parameters.

In Figs. 4.8-4.9 we show plots of the real and imaginary part of $\det \varepsilon(k,\omega)$ as

a function of the dimensionless frequency ω/ω_1 at different values of the coupling parameters Γ and collisional frequency ν. $\det\varepsilon(k,\omega)$ is calculated using the Extended Collisional QLCA, plots of the collisional QLCA are not shown for the sake of clarity. In fact, the only differences between the two models are explained below. All the plots are at the smallest ka value reached by simulations. Starting from Fig. 4.8, we notice that $\det\varepsilon(ka_{\min},\omega=0)$ is positive for $\Gamma\leq 1$ and becomes negative for larger values of Γ. This is due to the change in sign of the isothermal compressibility which becomes negative at strong coupling. This feature is only observable in the Extended Collisional QLCA and not in the collisional QLCA. In fact, one of the main differences between the two models is that the Extended QLCA satisfies the compressibility sum rule while the Collisional QLCA does not. A further difference can be seen in the plot of the imaginary part of $\det\varepsilon(k,\omega)$. At low values of ω we find a peak that gets sharper and close to $\omega=0$ as Γ increases. This is due to Landau damping that vanishes at $T=0$ ($\Gamma\to\infty$). At higher frequencies Landau damping decays exponentially fast, thus the only damping contribution comes from the $\mathbf{R}$ collisional matrix. The discontinuity encountered at high frequencies is at the gap frequency $\omega_-(0)$, since $\delta_-(k\to 0)\approx\omega_-(0)$ as seen from eq. (4.48). At stronger Γ the discontinuity moves to the left indicating the stronger correlational effect of U_-. The frequency δ_+ does not appear as a discontinuity to the fact that $\delta_+^2<0$ ($U_+>0$).

The collective modes are the frequencies at which $\det\varepsilon(k,\omega)=0$. However, since $\det\{\varepsilon(k,\omega)\}$ is a complex function one searches for the zeros of the real part assuming a negligible imaginary part. From the plots we find that the propagating modes are those for which $\mathrm{Re}\{\}\det\varepsilon$ changes from negative to positive. This excludes the first zero in the plots of $\Gamma\leq 1$ because of the large Landau at those frequencies. The acoustic mode is the first (second) zero for $\Gamma>1(\Gamma<1)$ and the gap mode the zero to the right of the discontinuity. Furthermore, Fig. 4.8

shows that at long wavelength collisional damping affects only the gap mode. This is further confirmed by the plots of Fig. 4.9. As the collisional frequency ν increases in magnitude the discontinuity disappears and thus, removing the gap mode. Finally, in Fig. 4.10 we show plots of the behavior of $\det\{\varepsilon(k,\omega)\}$ as a function of ka. The first zero to the left of the discontinuity agrees with the linear dispersion of the QLCA acoustic mode $\omega_+(k)$ indicated by the dashed vertical lines. However, the gap frequency $\omega_-(0)$ disappears due to the denominator of eq. (4.51).

4.4 Comparison with MD simulations

4.4.1 Weak Coupling

The partial dynamic structure functions are calculated via the FDT from the partial external response χ_{AB}. In addition, to the species partial S_{AB} we consider also the total density DSF S_{NN} and total concentration DSF S_{CC} defined in eqs. (1.33)– (1.34) and reproduced here for simplicity

$$S_{NN}(k,\omega) = c_1 S_{11}(k,\omega) + 2\sqrt{c_1 c_2} S_{12}(k,\omega) + c_2 S_{22}(k,\omega), \tag{4.52}$$

and

$$S_{cc}(k,\omega) = c_1 c_2 \left[c_2 S_{11}(k,\omega) - 2\sqrt{c_1 c_2} S_{12}(k,\omega) + c_1 S_{22}(k,\omega) \right]. \tag{4.53}$$

In Figs. 4.11-4.16 we show plots comparing the four DSF's from MD simulations with RPA calculations. The six figures are for $\Gamma = 0.1, 0.3, 0.5$, respectively, corresponding to three different regions of the κ–Γ phase space shown in Figs. 4.2–4.4. At the lowest Γ no clear peak is visible in the DSF's, but only a broad shoulder around $\omega \approx \omega_1$ in S_{22} and S_{NN}. The acoustic peak becomes evident at

the intermediate value $\Gamma = 0.3$, shown in Figs. 4.13-4.14 and gets more defined at higher Γ (see Figs. 4.15-4.16). In all six figures the RPA appears to be give a good reproduction of $S_{AB}(k,\omega)$ around the peak. Disagreement is found in the high frequency tail of $S_{AB}(k,\omega)$ at the lowest ka (blue lines) which however, appears to improve at higher values. Qualitative disagreement is found especially at $\Gamma = 0.5$ with the RPA predicting a sharp well defined acoustic peak in S_{22} and S_{NN} while MD shows a broader peak to a slightly lower frequency. Such disagreement is somewhat expected since the RPA is exact only in the limit $\Gamma \to 0$. Furthermore, for finite Γ, collisional damping prevails over Landau causing a shift of the mode to lower frequencies. In the past, a great deal of work focused on calculating the collisional damping at long wavelengths and it was shown that for any measurable small ka collisional damping would prevail over Landau. The inverse situation, instead, would appear at much smaller ka. This work was done for a One Component Plasma (DuBois, Gilinsky, and Kivelson, 1962; Coste, 1965a; Coste, 1965b), but the arguments remain valid also for a YOCP. In a binary mixture however, the collisional damping remains finite even at $k = 0$ and thus will always prevail over Landau. The interesting point to learn out of this investigation is that the RPA appears to give a good description for $\kappa - \Gamma$ values in the lower regions of phase space. Furthermore, the RPA shows good agreement with MD in reproducing the location of the anti-resonance at the ion-acoustic frequency $\omega_1(k)$.

4.4.2 Strong Coupling

In the strong coupling regime we compare the simulations with the Extended Collisional QLCA and Collisional QLCA. As shown before at long wavelengths $\omega_{\rm im} \approx \omega_+$ which simplifies the denominator of both $\hat{\chi}_{AB}$ and S_{AB}. Using the collisional QLCA expressions of $\mathrm{Im}\{\chi_{AB}(k,\omega)\}$ of eqs. (2.56)–(2.57), we find that

the expressions for S_{AB}

$$S_{11}(k,\omega) = \frac{k^2 n}{\pi\beta m_1}\frac{1}{\left(\omega^2-\omega_+^2\right)^2}\frac{\nu n(\omega^2-\omega_{*2}^2)^2}{\left(\omega^2-\omega_-^2\right)^2+(\omega\nu n)^2\left(1+q^2/p^2\right)^2}, \tag{4.54}$$

$$S_{22}(k,\omega) = \frac{k^2}{\pi\beta m_2}\frac{1}{m}\frac{1}{\left(\omega^2-\omega_+^2\right)^2}\frac{\nu/m(\omega^2-\omega_{*1}^2)^2}{\left(\omega^2-\omega_-^2\right)^2+(\omega\nu n)^2\left(1+q^2/p^2\right)^2}, \tag{4.55}$$

$$S_{12}(k,\omega) = -\frac{k^2}{\pi\beta\sqrt{m_1 m_2}}\sqrt{\frac{1}{m}}\frac{1}{\left(\omega^2-\omega_+^2\right)^2}\frac{\nu(\omega^2-\omega_{*2}^2)(\omega^2-\omega_{*1}^2)}{\left(\omega^2-\omega_-^2\right)^2+(\omega\nu n)^2\left(1+q^2/p^2\right)^2}. \tag{4.56}$$

Using these to calculate the total dynamic structure factors we find, apart from the β^{-1} constant factor

$$S_{NN}(k,\omega) \propto \frac{\nu(1-1/m)^2k^2}{|\mathcal{D}|^2}\left(\omega^2-\frac{\omega_{*2}^2-\omega_{*1}^2/m}{1-1/m}\right)^2, \tag{4.57}$$

and

$$S_{cc}(k,\omega) \approx \frac{\nu(1+q^2/p^2)^2k^2}{|\mathcal{D}|^2}\left(\omega^2-\omega_{\rm im}^2\right)^2. \tag{4.58}$$

Contrary to BIM, we now have anti-resonances in the total DSF's. The anti-resonance in S_{NN}, however, appears only when $Z_2 \neq Z_1$, since for $Z_2 = Z_1$ $\omega_{*2}^2 = q^2\omega_{*1}^2 = \omega_{*1}^2/m$. The anti-resonance of S_{CC}, instead, is equal to $\omega_{\rm im}$ thus it might be cancelled by the acoustic mode at long wavelengths. Comparison with MD simulation is shown in Figs. 4.17-4.18. In these plots the black line represents the MD simulation data, the blue dashed line S_{AB} calculated using the collisional QLCA, and the red dashed line S_{AB} using the extended collisional QLCA. In the partial S_{11} and S_{22} we again find minima at the locations of the SK-frequencies. The first peak at low ω is the acoustic mode while the very broad peak centered around $\omega \approx 2.9\omega_1$ is the gap mode. Notice the large difference between the two widths. As shown before ω_- is primarily affected by collisional damping. Moving to the total DSF S_{NN} and S_{CC} we notice the main discrepancies between the two

QLCA models. It appears that the Collisional QLCA gives a qualitatively better description than the Extended QLCA which wrongly predicts the anti-resonances in S_{NN} and S_{CC}. Furthermore, we notice that the S_{CC} MD line does not show a resonant peak at ω_+, but only a sharp minimum. This is likely due to the fact that the ka value shown in the plot is not small enough so that $\omega_{\rm im}(k) = \omega_+(k)$. Plots at smaller ka values will definitely show no feature. The other important feature to notice is a wide shoulder centered around ω_-. In fact, dispersion plots of the L_{CC} clearly show the presence of the gap mode.

4.4.3 Dispersion

The dispersion of the modes is studied using intensity maps of $L_{AB}(k, \omega)$. These are shown in Figs. 4.19-4.20. Peaks in L_{AB} are indicated by colored regions (yellow-red-white) while dark regions indicate very small values of L_{AB}. Similar to previous figures We show plots for L_{11}, L_{22}, L_{NN}, L_{CC}. The chosen asymmetry parameters represent a mixture with a high concentration of heavy particles (species 1). The solid white lines correspond to the QLCA modes $\omega_\pm(k)$. In L_{11} and L_{22} the dashed lines represent the SK-frequencies while in the plot of L_{CC} the dispersion of $\omega_{\rm im}(k)$. In L_{22} and L_{CC} a high frequency mode that approaches the gap frequency $\omega_-(0)$ is evident. Similarly, an acoustic mode is visible in the plots of L_{11} and L_{NN}. Overall we notice qualitative good agreement with the QLCA modes $\omega_\pm(k)$ over the entire ka regime. At long wavelengths especially we find that the QLCA correctly identifies the sound speed of the acoustic mode ($s = \omega_{\rm vaa}/\kappa$). This suggests a physical picture in which the system behaves like an YOCP with charge and mass given by an average created by the charges and masses of the two components. Additionally, the low ka behaviour of the gap mode is also well reproduced by the QLCA, thus, indicating the existence of a gap at $ka = 0$.

For shorter wavelengths the QLCA correctly reproduce the oscillatory behaviour. In particular, we point out that the existence of a roton minimum around ka 6. As in the case of BIM this has been a long debated issues as many researchers considered the roton minimum an entirely quantum effect. Instead, it appears that it is a feature of strongly coupled liquid, both classical and quantum, caused by the formation of randomly oriented micro-crystals whose averaged dispersion reproduces the minimum (Kalman, Hartmann, Golden, et al., 2010; Kalman, Kyrkos, et al., 2012). Finally, we notice that the MD dispersion approaches the nominal Einstein frequencies of each component at short wavelengths. This was not visible in 2D Yukawa mixtures (Kalman, Hartmann, Donkó, Golden, and Kyrkos, 2013).

As per the SK frequencies, excellent agreement is also evident at long wavelengths, indicated by the black regions in the MD intensity maps. The dark regions in the intensity maps of the heavy species and L_{CC} extend well in $ka = 2$ indicating that the assumption of $R_{AB} \propto \nu$ is valid for finite ka as well. The agreement of the SK-frequencies is not evident in intensity maps of the light species, but it is confirmed in intensity maps of $|L_{12}|$ shown in Fig. 4.21. We recall that the SK-frequencies correspond to the zeros of $L_{12}(k, \omega)$, thus, in a plot of the absolute value this will appear as the lowest possible value. The region in which $L_{12}(k, \omega)$ is positive is the region in between the two zeros, that is the region between the two black dispersion in Fig. 4.21. We point out that similarly to BIM, although not as evident, we find an oscillatory behavior and the intersection of the QLCA modes and SK frequencies corresponds to dark regions between two colored region at the same ω.

4.5 Transition from Weak to Strong Coupling:

4.5.1 Sound Speed and Effective Mass

We have seen that the longitudinal collective mode spectrum is characterized by a longitudinal acoustic mode both in the weakly and strongly coupled phase. At weak coupling the sound speed is primarily characterized by the $T = 0$ RPA sound $s_0 = \omega_0/\kappa$, while at strong coupling it reduces to $c_s = \omega_{\text{vaa}}\sqrt{1 - U_+(\Gamma)}/\kappa$. Even though the QLCA has shown that the transition happens in a non-perturbative way, we can nonethless follow the behavior of the sound speed as function of Γ in order to identify a critical Γ value. In order to reduce the number of parameters we consider a mixture with equal charges $Z_2 = Z_1$, but with different masses and concentration. This simplification further removes the correlational dependence that arises from the difference between $h_{11}(r)$, $h_{22}(r)$, $h_{12}(r)$ – all of them being equal in the case $Z_2 = Z_1$. The sound speed at this point depends only one parameter: the effective mass. Borrowing from a model of two coupled oscillators, or better two coupled LC circuits, we can portray the weak coupling regime as the parallel connection between the two oscillators, while the strong coupling regime as the series connection. In the weak coupling regime we have

$$\omega_0^2 = \omega_1^2 + \omega_2^2 \propto \frac{1}{m_0}, \quad m_0 = \left[\frac{c_1}{m_1} + \frac{c_2}{m_2}\right]^{-1}. \tag{4.59}$$

At strong coupling

$$\omega_{\text{vaa}}^2 \propto \frac{1}{m_{\text{vaa}}}, \quad m_{\text{vaa}} = \frac{c_1 m_1 + c_2 m_2}{n_1 + n_2} \tag{4.60}$$

with $m_{\text{vaa}} > m_0$. These two expressions can be considered as the lower and upper limit of an effective mass, $m_0 < m_{eff}(\Gamma) < m_{\text{vaa}}$. This quantity and the sound speed s will be used to track the transition from weak to strong coupling.

Kalman and collaborators investigated this for a 2D binary Yukawa mixture (Kalman, Hartmann, Donkó, Golden, and Kyrkos, 2013) and in some extent for a 3D mixtures too (Kalman, Donkó, et al., 2011). However, the lowest coupling reached by simulations was still larger than 1 and that did not allow for the exploitation of the "parallel" connection. Advancement in the simulation code have allowed us to reach smaller coupling and this is what we present in this section. Kalman *et al.* showed that the sound speed decreases monotonically, with no evident discontinuity, as coupling increases. This is somewhat surprising inasmuch that correlations appear only as a subtraction term in the QLCA expression and ω_{vaa} is the primary factor for the softening of the sound speed. In the following we will describe first the method used for the extrapolation of the sound speed and effective mass from MD data and then show the results.

4.5.2 Method

The sound speed is calculated from the acoustic peak of $S_{NN}(k,\omega)$. This choice is due to the vicinity of SK-frequencies to the acoustic peak in $S_{22}(k,\omega)$. Furthermore, $S_{NN}(k,\omega)$ is the only measurable quantity in a realistic experiment. The peak of $S_{NN}(k,\omega)$ is located by fitting a model function from which the center and FWHM are extrapolated. The fit is performed using the `lmfit` package for Python. For $\Gamma < 1$ we chose to fit a Voigt profile

$$f(x;A,\mu,\sigma,\gamma) = A\frac{\mathrm{Re}\mathcal{W}(z)}{\sigma\sqrt{2\pi}} \tag{4.61}$$

where

$$\mathcal{W}(z) = e^{-z^2}\,\mathrm{erfc}(-iz), \quad z = \frac{x-\mu+i\gamma}{\sigma\sqrt{2\pi}} \tag{4.62}$$

is the Faddeeva function whose FWHM is is given by 3.6013σ. The parameters to be fitted are the amplitude A, the center of the peak μ, σ and γ. The choice

of this function is motivated by the fact that is the one that closely resembles the $S_{NN}(k,\omega)$ profile from an RPA description. At strong coupling instead we use a Lorentzian profile

$$f(x;A,\mu,\sigma) = \frac{A}{\pi}\frac{\sigma}{(x-\mu)^2+\sigma^2} \tag{4.63}$$

with A, μ, and σ as the fitting parameters. The FWHM is 2σ. The peak's centers are calculated for the three lowest values of ka and then a cubic function of the form

$$f(x;d_1,d_3) = d_1 x + d_3 x^3 \tag{4.64}$$

is fitted from which we extrapolate the sound speed as the coefficient c_1. This specific form is chosen to prevent underestimates of the sound speed due to the large ka regime on which it is fitted. Finally, the effective mass m_{eff} is calculated using the following formula (Kalman, Donkó, et al., 2011; Kalman, Hartmann, Donkó, Golden, and Kyrkos, 2013)

$$\frac{m_{\text{eff}}}{m_1} = \frac{n_1+n_2}{n_1}\left(\frac{1+p^2}{1+n}\right)^2 \frac{1-U_+}{\kappa^2 s^2}. \tag{4.65}$$

The first fraction renormalizes the total density with respect to n_1. The second fraction is to remove effects due different charges for different species and in the case of $Z_2 = Z_1$ the entire fraction is equal to 1. The last fraction is to remove the correlational dependent term from the sound speed expression s

4.5.3 Results and Discussion

In Figs. 4.22-4.23 we show plots of the sound speed as a function of Γ compared with the weak coupling and QLCA formulas. The lowest Γ is the lowest value for which S_{NN} shows a well defined peak. The vertical lines indicate 5% error bars. At low couplings, $\Gamma < 1$, we notice that the sound speed approaches the cold plasma RPA value s_0 while the RPA expressions, obtained in Sec. 4.2, drastically

overestimate the sound speed. The discrepancy increases with higher κ values. The steep increase at low Γ of the RPA formulas is due to thermal effects. This disagreement suggests that the collisionless description is not valid. As a matter of fact comparison of $S_{NN}(k,\omega)$, shown in the top panel of Figs. 4.14 - 4.16, the MD peak is to the left and much wider than the RPA peak. The sound speed values at $\Gamma = 0.2$ in the case of $\kappa = 0.5$ are very likely to be considered outliers, since a closer look at $S_{AB}(k,\omega)$ shows very noisy simulations in which is difficult to identify the real peak. Further simulations at lower $ka_{\min}$ with a smaller $\Delta\omega$ are needed in order to better investigate this low coupling values. It would be interesting if these new simulations were to confirm the results shown here as this sudden lowering of the sound speed is completely unexpected at weak coupling.

For $\Gamma > 1$ we observe an apparent monotonic decay of the sound speed. A closer look, though shows a slight change in slope once the reaches the VAA sound speed $s_{\text{vaa}} = \omega_{\text{vaa}}/\kappa$ (dashed gold line) at $\Gamma = 10$ suggesting a possible boundary between the moderate and strongly coupled regime. Once in the strongly coupled regime one would expect a change in the slope of the sound speed, due only to the correlational term U_+, shown in Fig. 4.24, which being very small and slowly increasing lead to a flatter slope. This behavior is obvious in the QLCA (red) line, but not in the MD data, nonetheless the QLCA prediction remains within the error bars. A possible reason for this disagreement is that the ka values chosen are not small enough. In order to see this we have performed new simulations with $\Gamma = 120$ and an increased number of particles $N = 221,148$ leading to $ka_{\min} = 0.0852$, much smaller than $ka_{\min} = 0.1704$ of the other simulations. The sound speed obtained from this run is the data point indicated by the arrow in the plots of $\kappa = 0.5$. Notice how this data point is almost at the same level as that at $\Gamma = 20$.

Fig. 4.25 shows plots of the effective mass as a function of Γ with 5% error bars.

The effective mass follows the behavior of the sound speed. At small couplings it approaches the RPA value m_0 and $m_{\rm vaa}$ at strong couplings. As explained above the reason for the overshooting of $m_{\rm eff}$ for $\Gamma > 10$ is due to the large $ka_{\rm min}$ of the simulations. The data point obtained from simulations with a much larger particle number is again indicate by an arrow.

The final step is to study the damping mechanism. In Fig. 4.26–4.27 we show plots of the HWHM (FWHM/2) of the MD acoustic peak for the three lowest ka values. The arrows indicate again data point from MD simulations with $N = 221,184$. Different decay slopes are evident in the three regions: $\Gamma < 1$, $1 < \Gamma < 10$ and $\Gamma > 10$. The decay is somewhat surprising as one would expect that in the weakly and moderately coupled regime the system becomes more and more collisional, thus, leading to an increasing HWHM with larger Γ. At strong coupling, $\Gamma > 10$, we notice a somewhat flat slope in the decay, especially at the lowest ka. This behavior is in agreement with the physical picture proposed by the QLCA in which the particles become quasi-localized and therefore reaching the minimum collisional damping. The black lines in the plots indicate a power law fit in the strongly coupled regime $\Gamma > 10$. In the same plot we indicate also the HWHM obtained from simulations with a larger number of particles.

4.6 Fast Sound

Before concluding this chapter, we present the latest results on an interesting feature. In a YBM with a high concentration of light particles we find no trace of a gap mode, but we notice the existence of a single acoustic mode with a sound speed greater than $s_{\rm vaa}$. This is clearly visible in intensity maps of $L_{NN}(k,\omega)$ and $L_{CC}(k,\omega)$ shown in Fig. 4.28. We notice that this "fast" acoustic mode approaches the acoustic QLCA mode at the lowest ka but after a few values it matches the dispersion of the gap mode. We recall that peaks in $L_{CC}(k,\omega)$ represent the dis-

persion of the gap mode.

This new mode can be understood if we look at the dielectric function again. As seen from eq. (4.51), at long wavelengths, the collisional damping influences only the gap mode indicating also that for large ν the discontinuity and thus, the gap mode disappear. This behavior, however, does not hold for finite ka, where $\omega_{\rm im}(k) \neq \omega_+(k)$ as shown in the plots of Fig. 4.29. These plots show again the real and imaginary part of $\det \varepsilon(k,\omega)$, calculated using the Collisional QLCA with a strong collisional frequency, at four different ka values. We notice that at the lowest ka value the real part has one zero at low frequencies, which as explained before corresponds to the acoustic mode. Furthermore, no discontinuity is observed at the gap frequency and consequently no second zero and the function approaches its high frequency limit. At larger ka values, instead, the low frequency zero disappears and a softened λ-shape feature appears at around the gap frequency. As seen from the lower plot, the λ feature is due to the broad peak of the imaginary part of $\det \varepsilon(k,\omega_-)$. In the top plot we also indicate the location of the peaks of $L_{NN}(k,\omega)$ by vertical dashed lines with the same color of $\det \varepsilon(k,\omega)$. The very good agreement therefore suggest that the apparent "fast" acoustic mode is due to a large collisional frequency.

4.7 Conclusion

In this Chapter we have investigated a binary mixture of ions interacting via a Yukawa potential. We have investigated both the weakly and strongly coupled regime and supported theoretical predictions with MD simulations. The primary focus of the investigation was the collective mode structure and the Silvestri–Kalman frequencies. The weakly coupled regime has been investigated using the RPA formalism adapted to a Yukawa potential. We have shown that contrary to the Coulomb mixture there exists a κ–dependent lower limit in Γ below which the system cannot support an acoustic excitation. MD simulations have confirmed this picture. While an acoustic mode has been found for coupling parameters $\Gamma < 1$, its sound speed is in disagreement with the RPA predictions, thus indicating that the mixture is more akin to a liquid mixtures, where the particles interact via short–range binary collisions, in contrast to a Coulomb liquid characterized by long–range interactions.

In the strongly coupled regime the system is characterized by an acoustic and a gap mode whose dispersion are in agreement with the Collisional QLCA. Furthermore, by studying the complex dielectric function we were able to better under the appearance of a single "fast" acoustic mode in mixtures with a high concentration of light particles.

The presence of an acoustic mode both in the weakly and strongly coupled regime provided an important quantity for the study of the transition from weak to strong coupling. The sound speed decays from its RPA value $s_0 = \omega_0/\kappa$, dominated by the total plasma frequency, to its strong coupling value $s_{\rm vaa} = \omega_{\rm vaa}/\kappa$, corresponding to the sound speed of an effective YOCP. Preliminary results on the damping of the acoustic mode have been presented also. The damping of the mode was defined as the HWHM of the acoustic peak. The most important thing was the lack of any distinctive feature in the behavior of the relative HWHM as a function of Γ. The

damping appear to continuously decay from the weak to the moderately coupled regime and to become almost Γ independent in the strongly coupled regime. This Γ independent behavior is somewhat expected since the particles become quasi–localized at high Γ. The continuous decay is the surprising feature as one expects the mixture to become more and more collisional with increasing Γ. Further work on the damping of these modes is needed.

As a reference for future research we list the new features found at strong coupling (vs. weak coupling)

- An entirely correlational dependent gap modes
- An acoustic mode with a different sound speed than at weak coupling
- The appearance of ω_{vaa} as the dominant frequency (vs. ω_0)
- Roton Minimum
- Silvestri–Kalman frequencies (vs. Fano frequencies at weak coupling)
- Γ-dependent effective mass
- "Fast-sound" mode

The above features have been investigated in this Chapter, but many more remain to be investigated, just to mention a few

- Behavior of $S_{AB}(k,\omega)$ as $\omega \to \infty$
- Collective Mode structure dependence on the charge asymmetry parameter Z
- Transverse Collective Modes
- Relation of FWHM of $S_{AB}(k,\omega)$ with transport properties

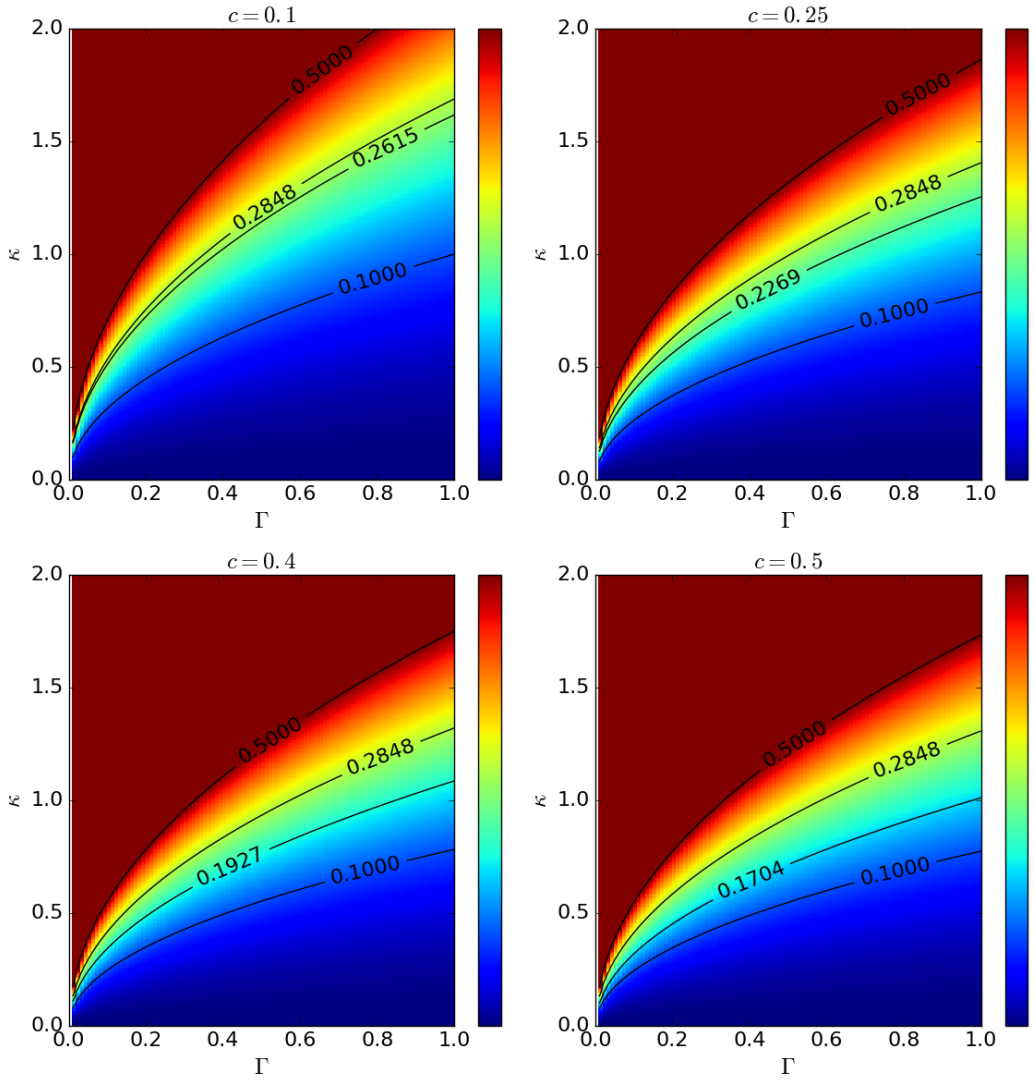

Figure 4.3: Color - Contour maps of Y_c. Blue (red) indicates low (high) values. The maximum color value has been set to $Y_c = 0.5$ for better viewing. In addition, the contours $Y_c[\Pi_{\max}(m = 1)] = 0.2848$ and $Y_c = \Pi_{\max}(m = 0.2)$ are indicated.

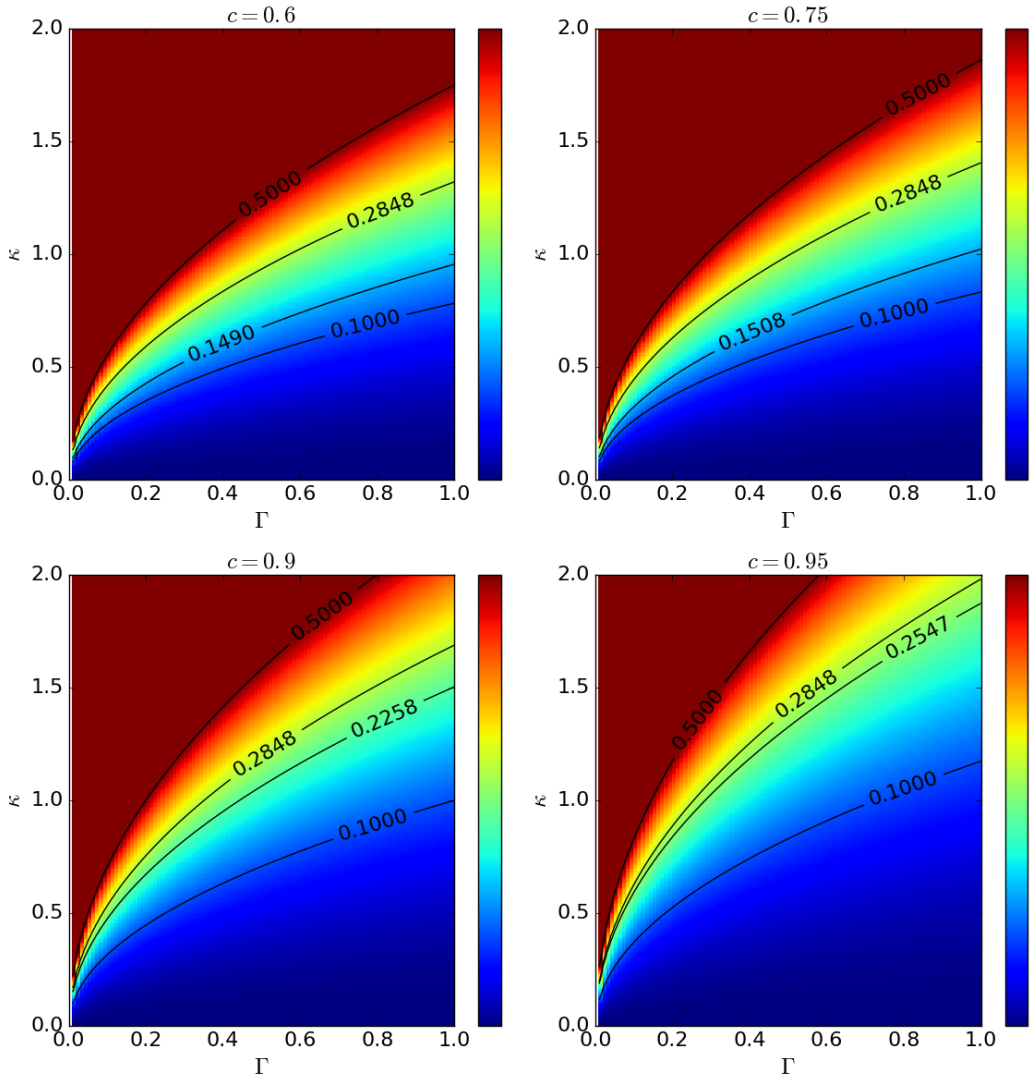

Figure 4.4: Same as in Fig. 4.2 but for $c = \{0.6,\ 0.75,\ 0.9,\ 0.95\}$

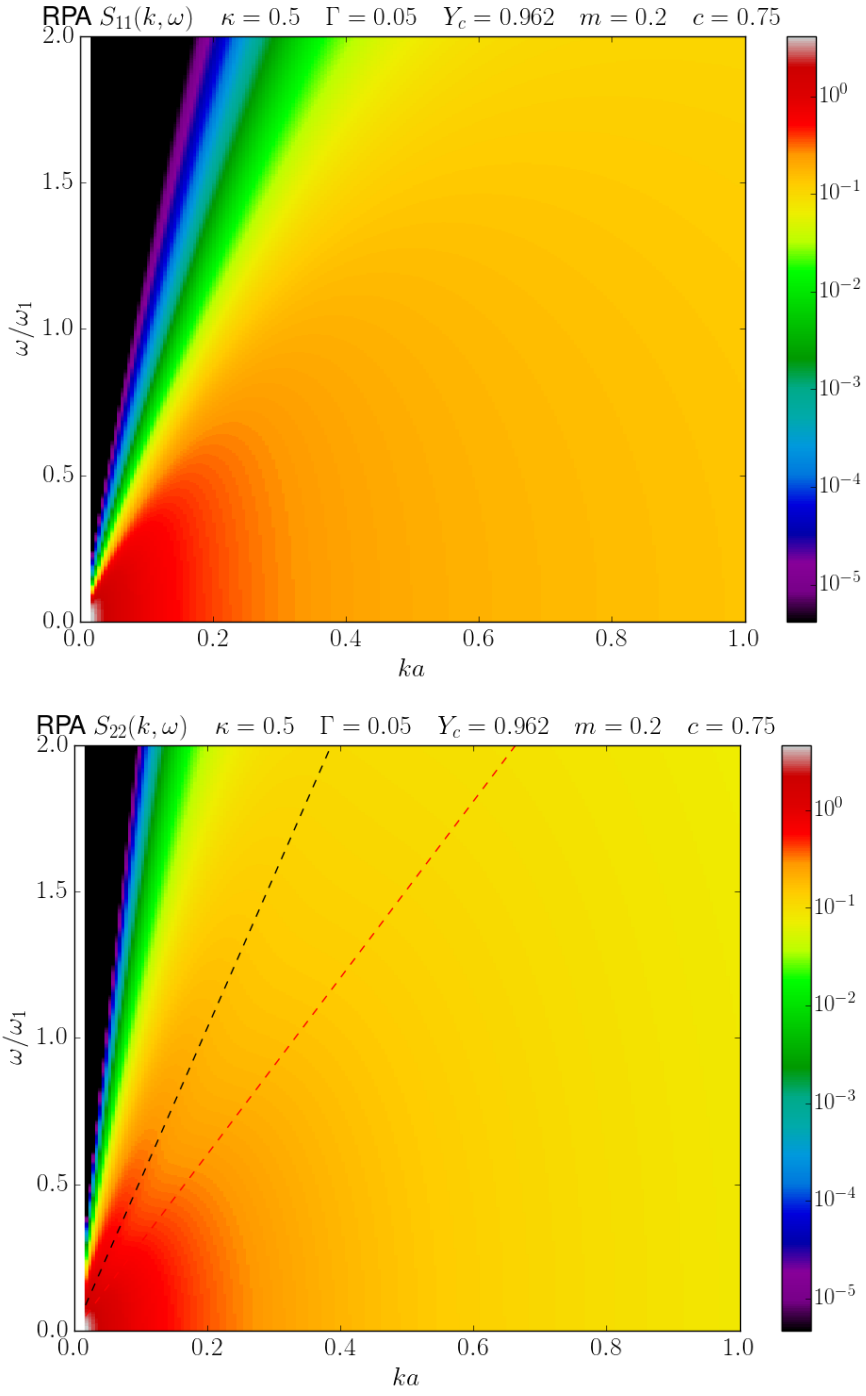

Figure 4.5: Intensity map of RPA $S_{AB}(k,\omega)$. The black lines indicate the mode given by sound speed c_s calculated from eq. (4.20) while the red line is the acoustic mode of a YOCP created by species 1.

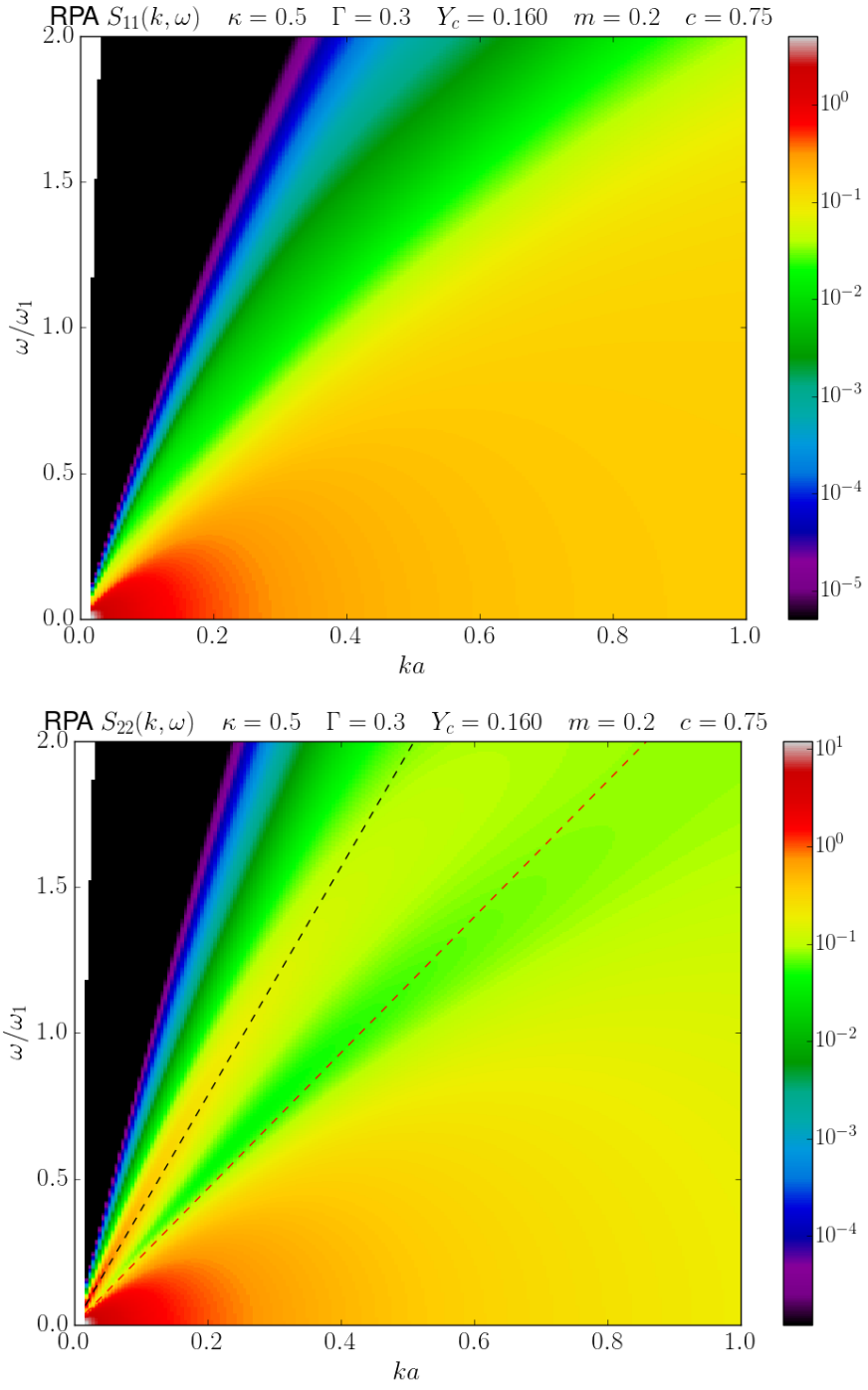

Figure 4.6: Intensity map of RPA $S_{11}(k,\omega)$ (top) and $S_{22}(k,\omega)$ (bottom). The black lines indicates the mode given by sound speed $s_{\text{Th, RPA}}$ calculated from eq. (4.20) while the red line indicates the anti–resonant frequency given by the acoustic mode of an YOCP composed only of species 1.

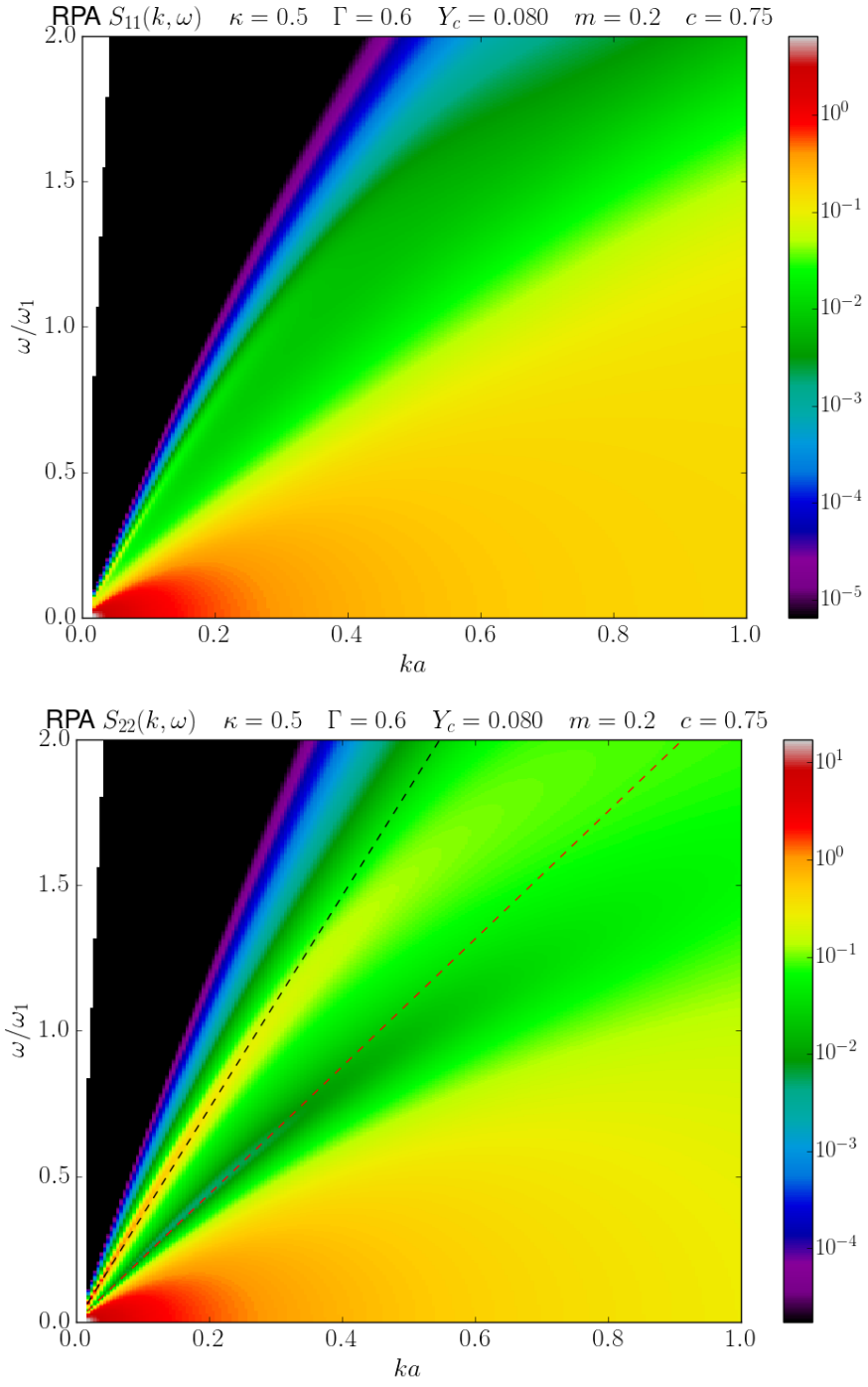

Figure 4.7: Intensity map of RPA $S_{11}(k,\omega)$ (top) and $S_{22}(k,\omega)$ (bottom). The black lines indicates the mode given by sound speed $s_{\text{Th, RPA}}$ calculated from eq. (4.20) while the red line indicates the anti–resonant frequency given by the acoustic mode of an YOCP composed only of species 1.

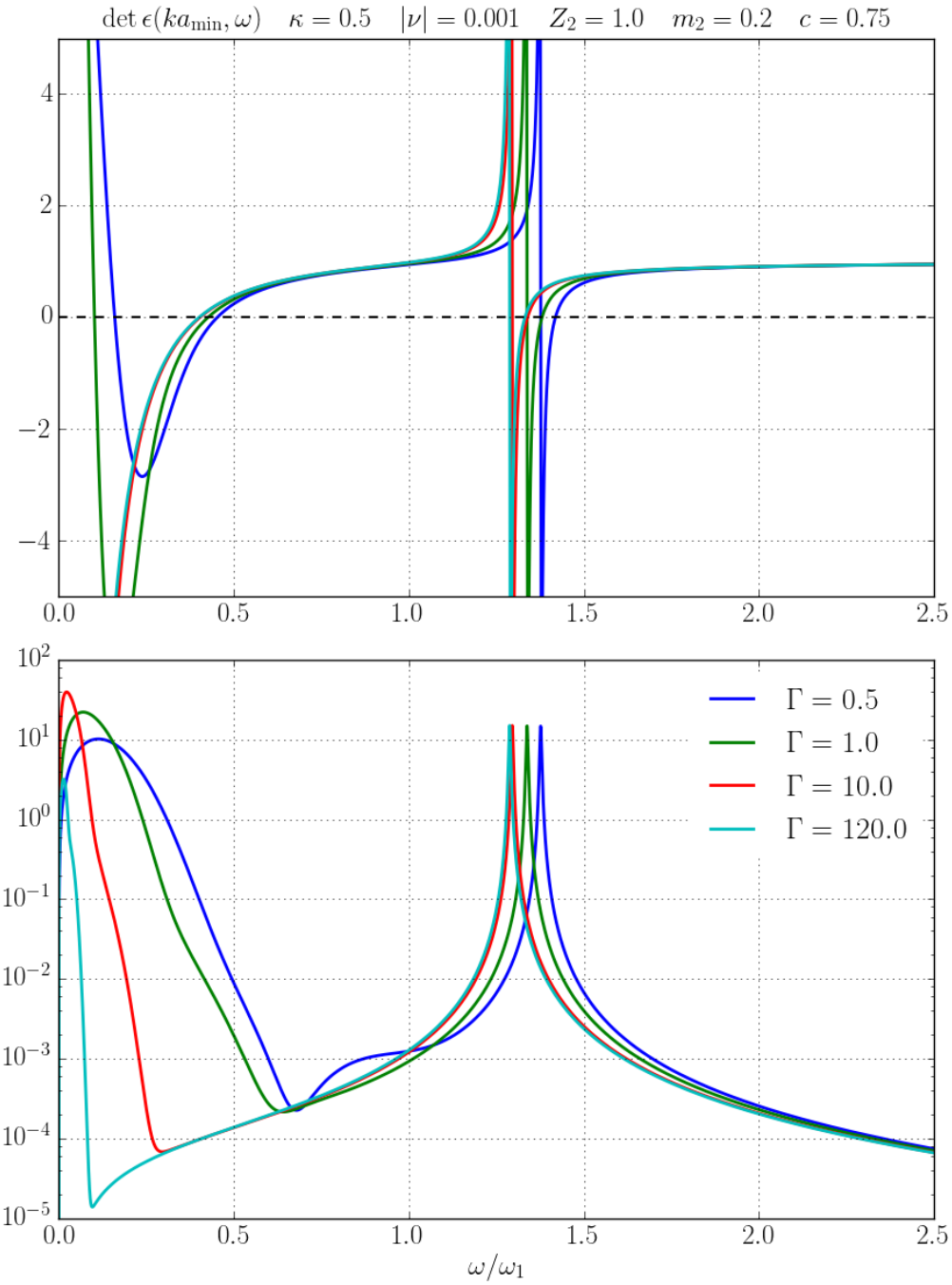

Figure 4.8: Plots of the Real (top) and Imaginary part (bottom) of $\det \varepsilon(k, \omega)$ calculated from the Extended Collisional QLCA at the lowest ka reached in simulation ($ka = 0.170$). Different lines represent different coupling parameter Γ.

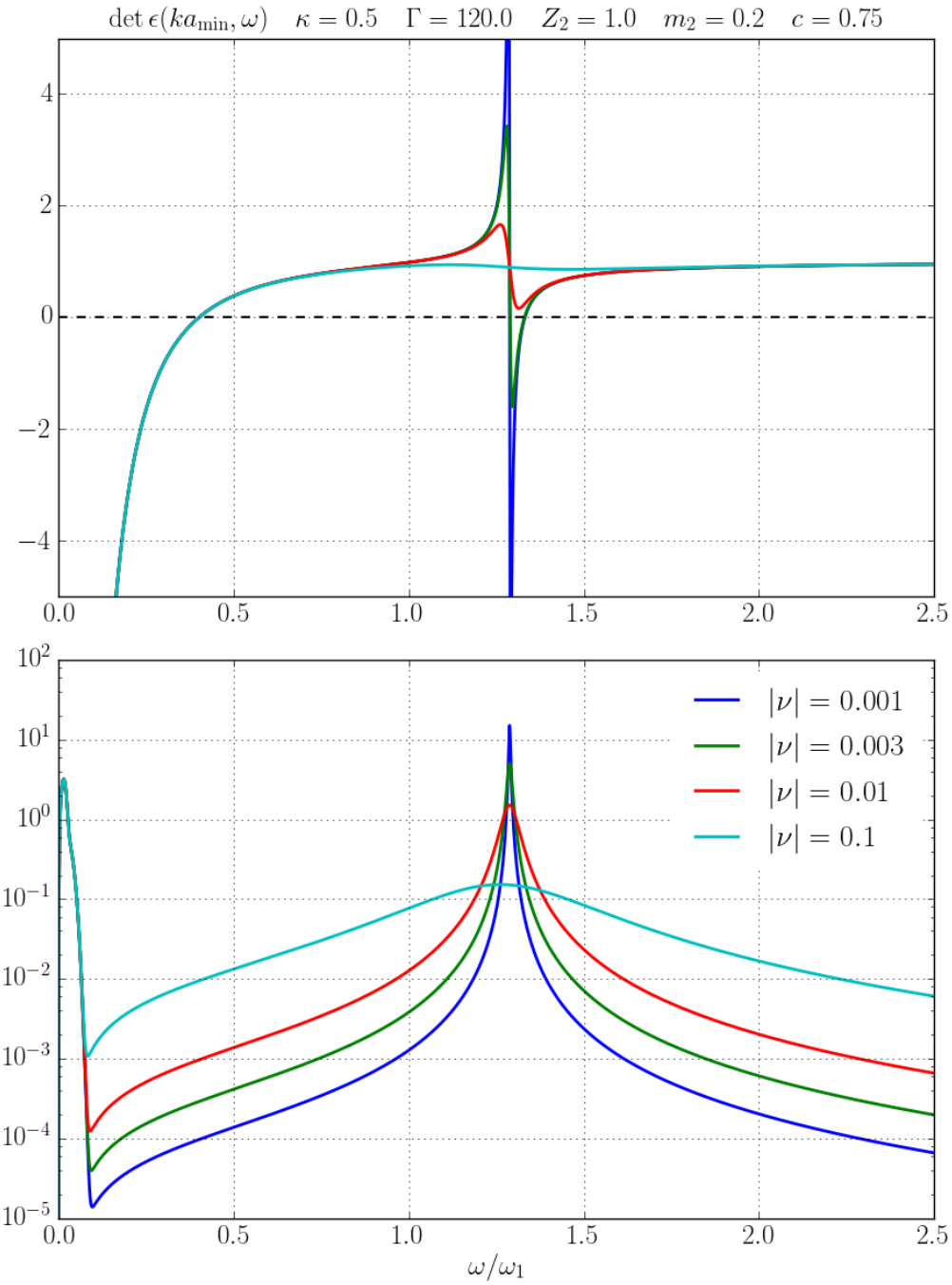

Figure 4.9: Plots of the real (top) and imaginary part (bottom) of $\det \varepsilon(k, \omega)$ calculated from the Extended Collisional QLCA at the lowest ka reached in simulation ($ka = 0.170$). Different lines represent different collisional frequencies ν.

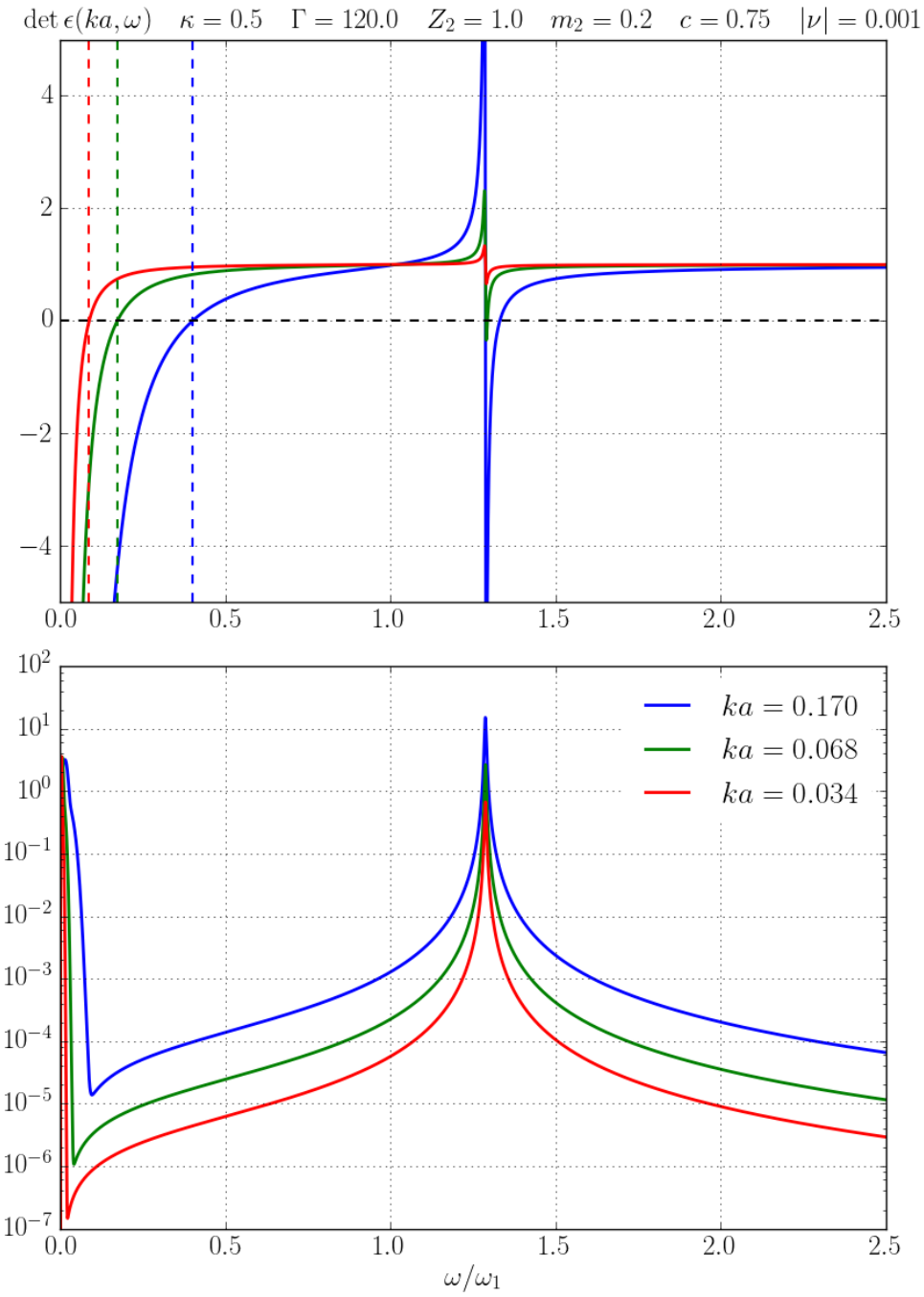

Figure 4.10: Plots of the Real (top) and Imaginary part (bottom) of $\det \varepsilon(k, \omega)$ calculated from the Extended Collisional QLCA. The dashed vertical lines indicate the values of $\omega_+(k)$. Different lines represent different ka values.

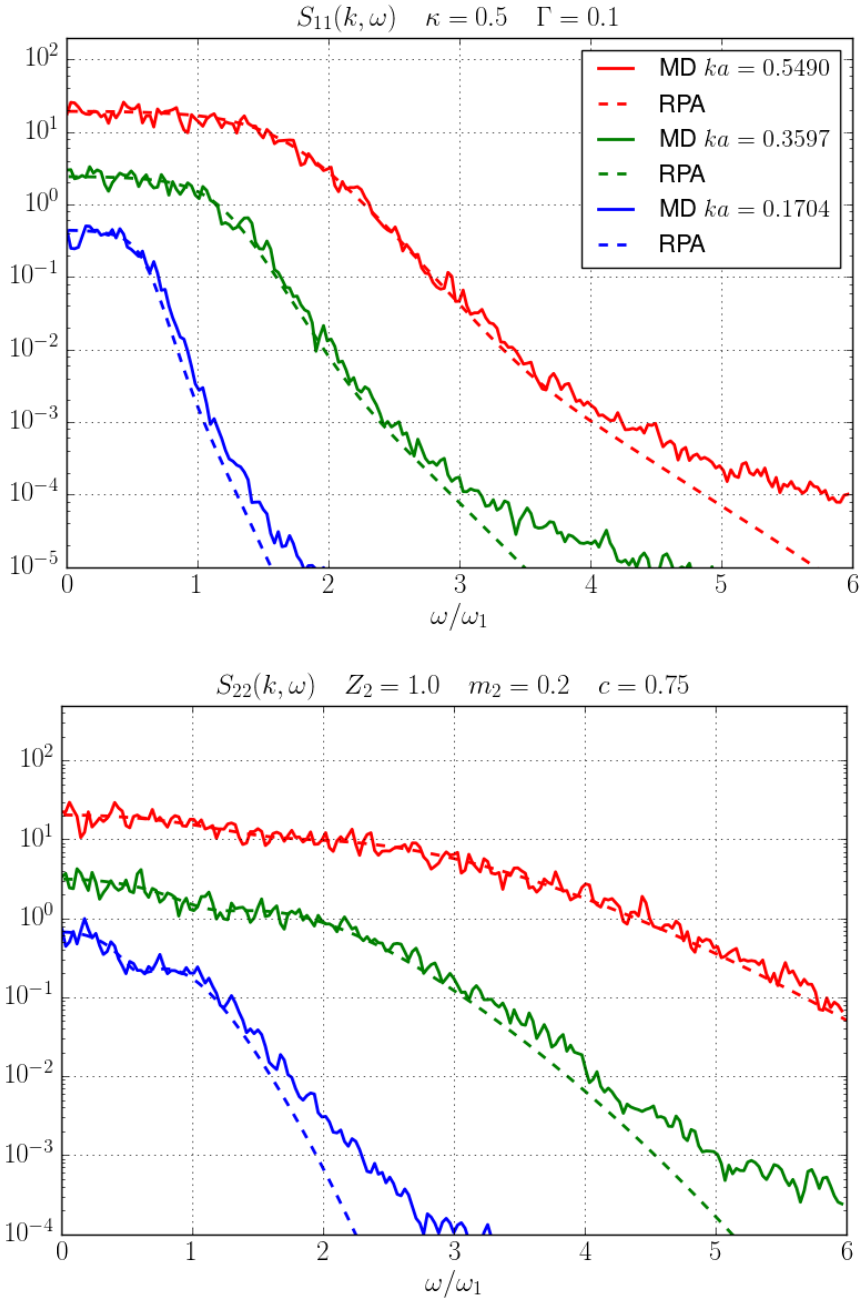

Figure 4.11: Plots of $S_{11}(k,\omega)$ (top) and $S_{22}(k,\omega)$ (bottom) comparing the RPA with MD simulations at the three lowest ka values for $\Gamma = 0.1$. Note that the second (third) ka lines have been shifted upwards by 10 (100) for easier viewing.

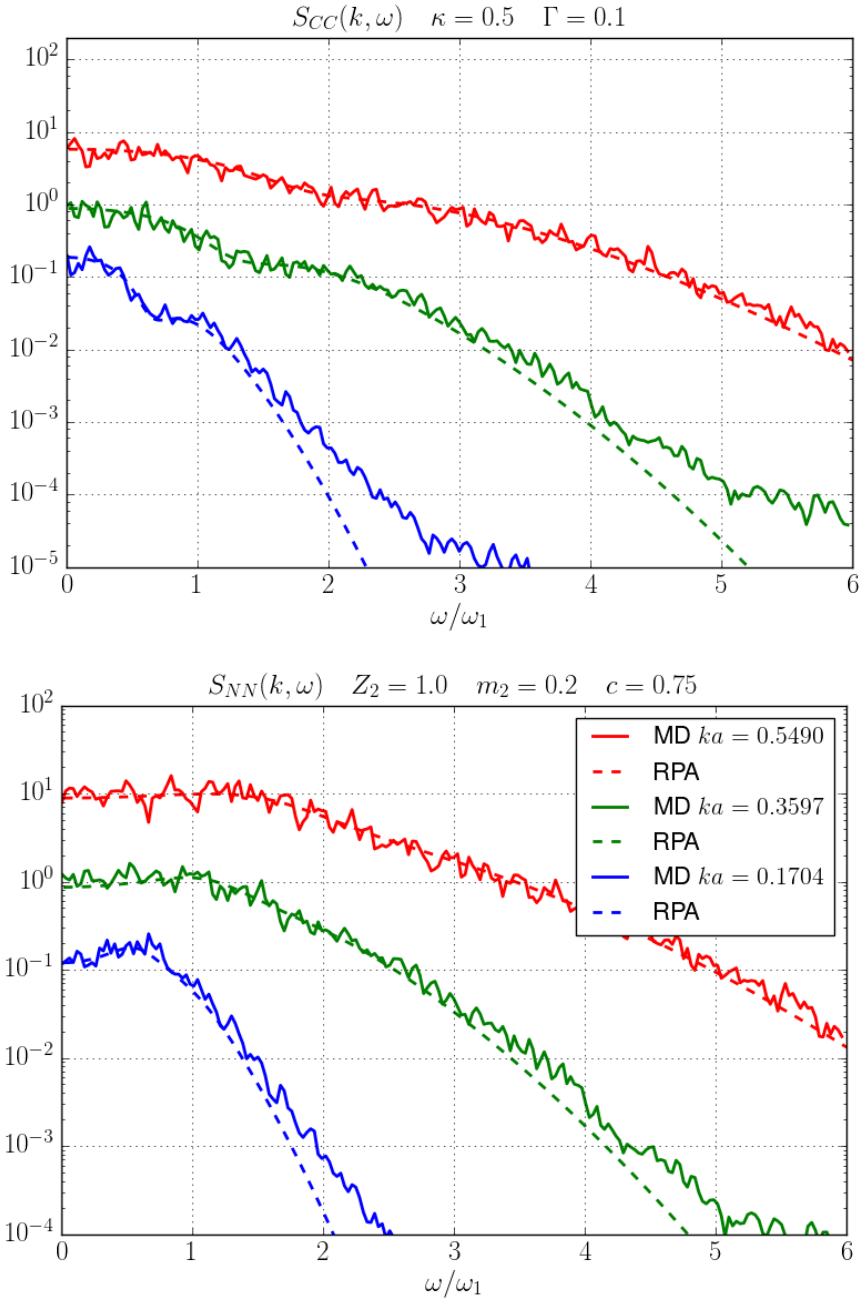

Figure 4.12: Plots of $S_{CC}(k,\omega)$ (top) and $S_{NN}(k,\omega)$ (bottom) comparing the RPA with MD simulations at the three lowest ka values for $\Gamma = 0.1$. Note that the second (third) ka lines have been shifted upwards by 10 (100) for easier viewing.

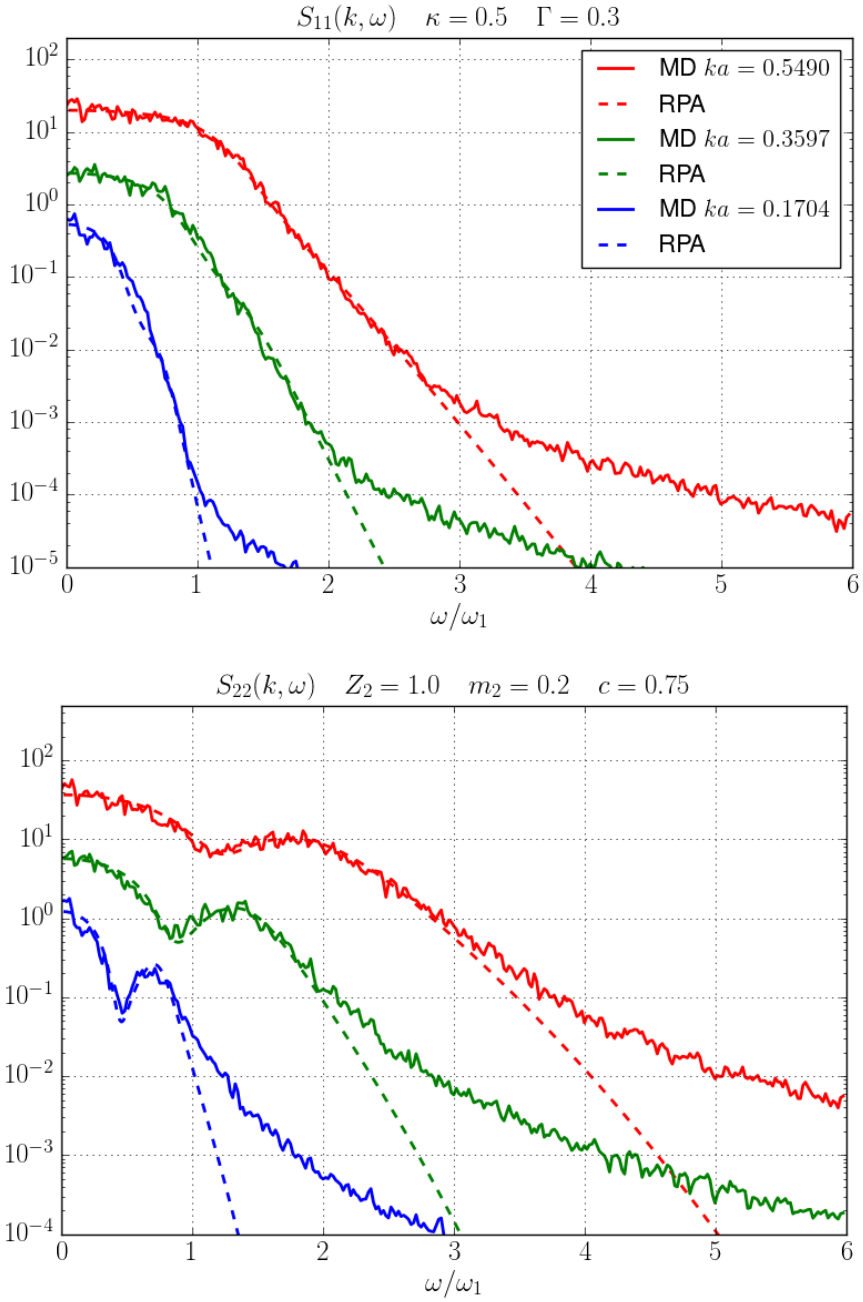

Figure 4.13: Plots of $S_{11}(k,\omega)$ (top) and $S_{22}(k,\omega)$ (bottom) comparing the RPA with MD simulations at the three lowest ka values for $\Gamma = 0.3$. Note that the second (third) ka lines have been shifted upwards by 10 (100) for easier viewing.

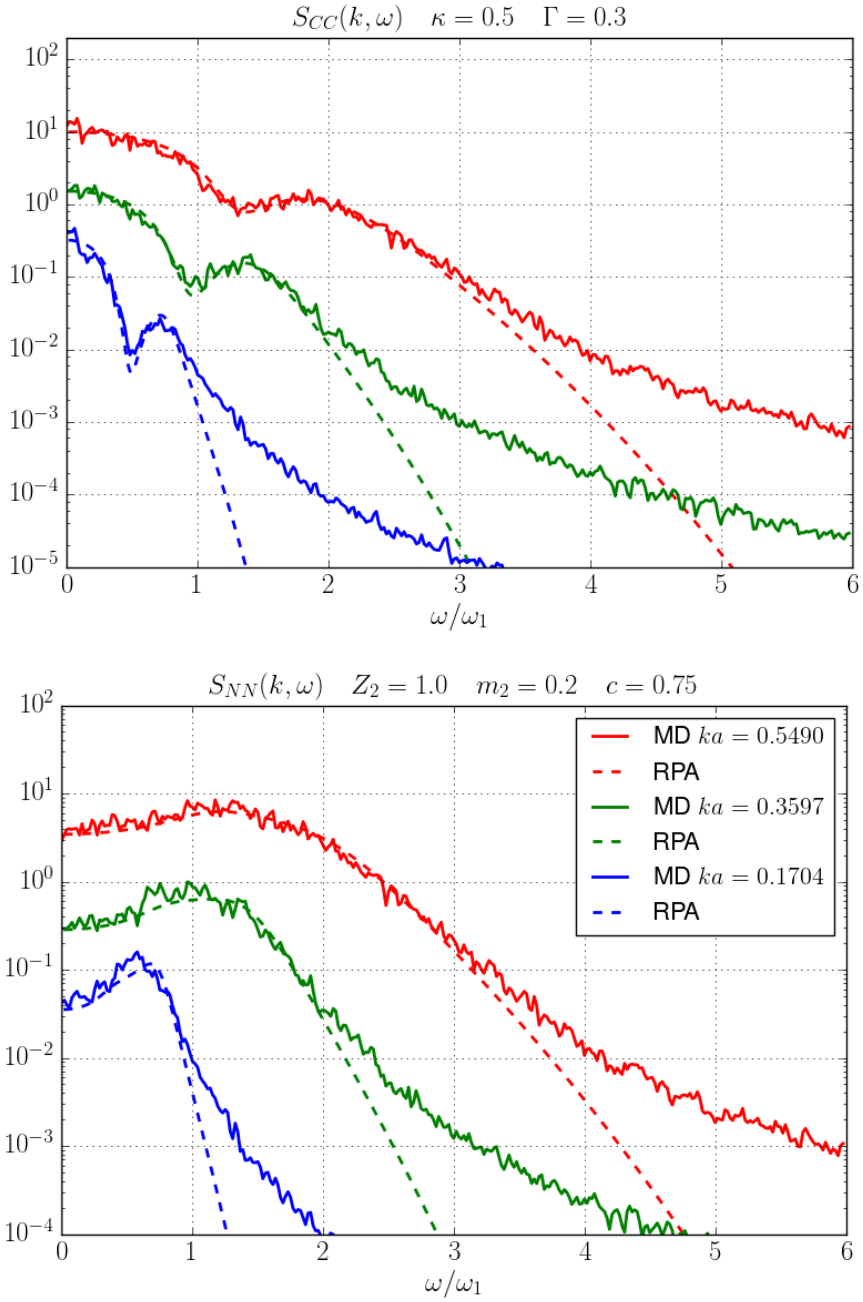

Figure 4.14: Plots of $S_{CC}(k,\omega)$ (top) and $S_{NN}(k,\omega)$ (bottom) comparing the RPA with MD simulations at the three lowest ka values for $\Gamma = 0.3$. Note that the second (third) ka lines have been shifted upwards by 10 (100) for easier viewing.

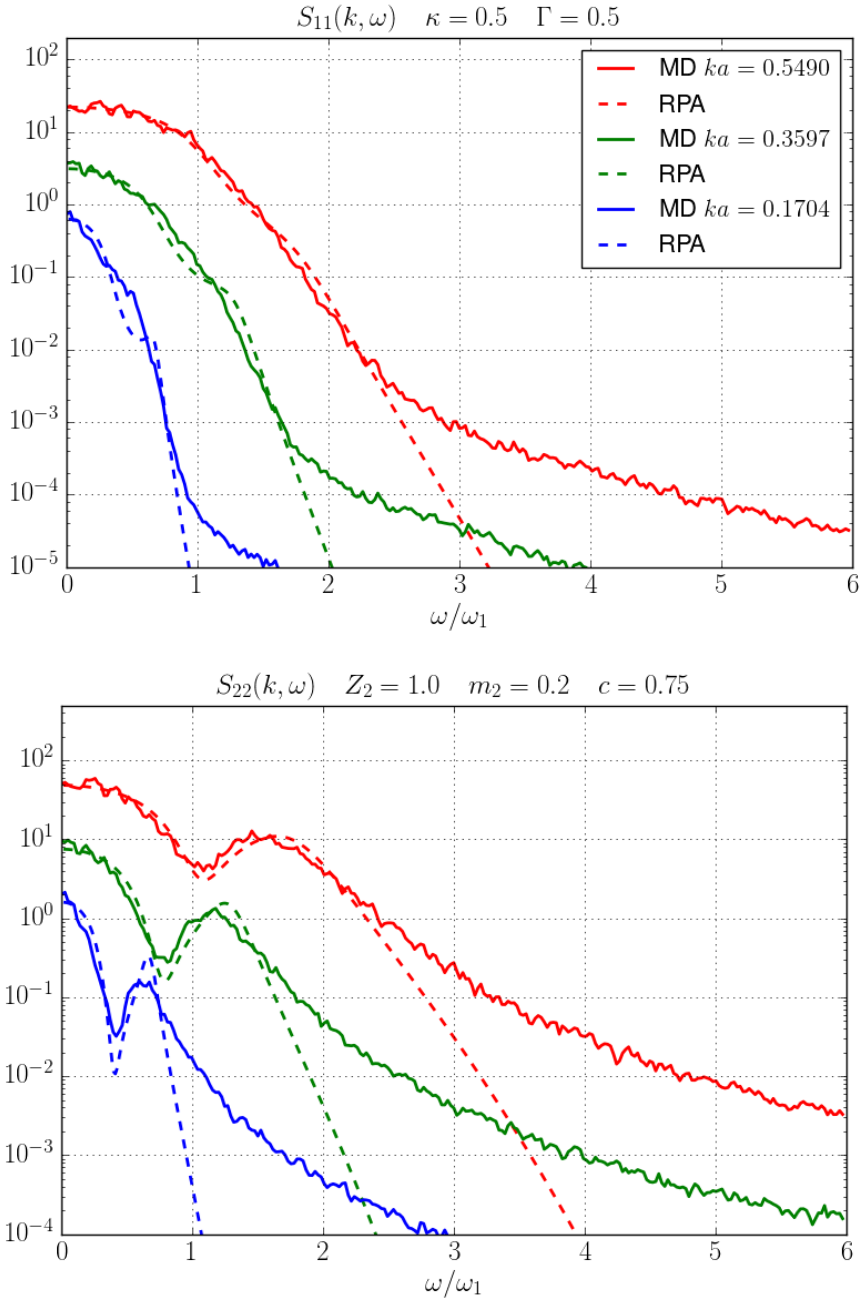

Figure 4.15: Plots of $S_{11}(k,\omega)$ (top) and $S_{22}(k,\omega)$ (bottom) comparing the RPA with MD simulations at the three lowest ka values for $\Gamma = 0.5$. Note that the second (third) ka lines have been shifted upwards by 10 (100) for easier viewing.

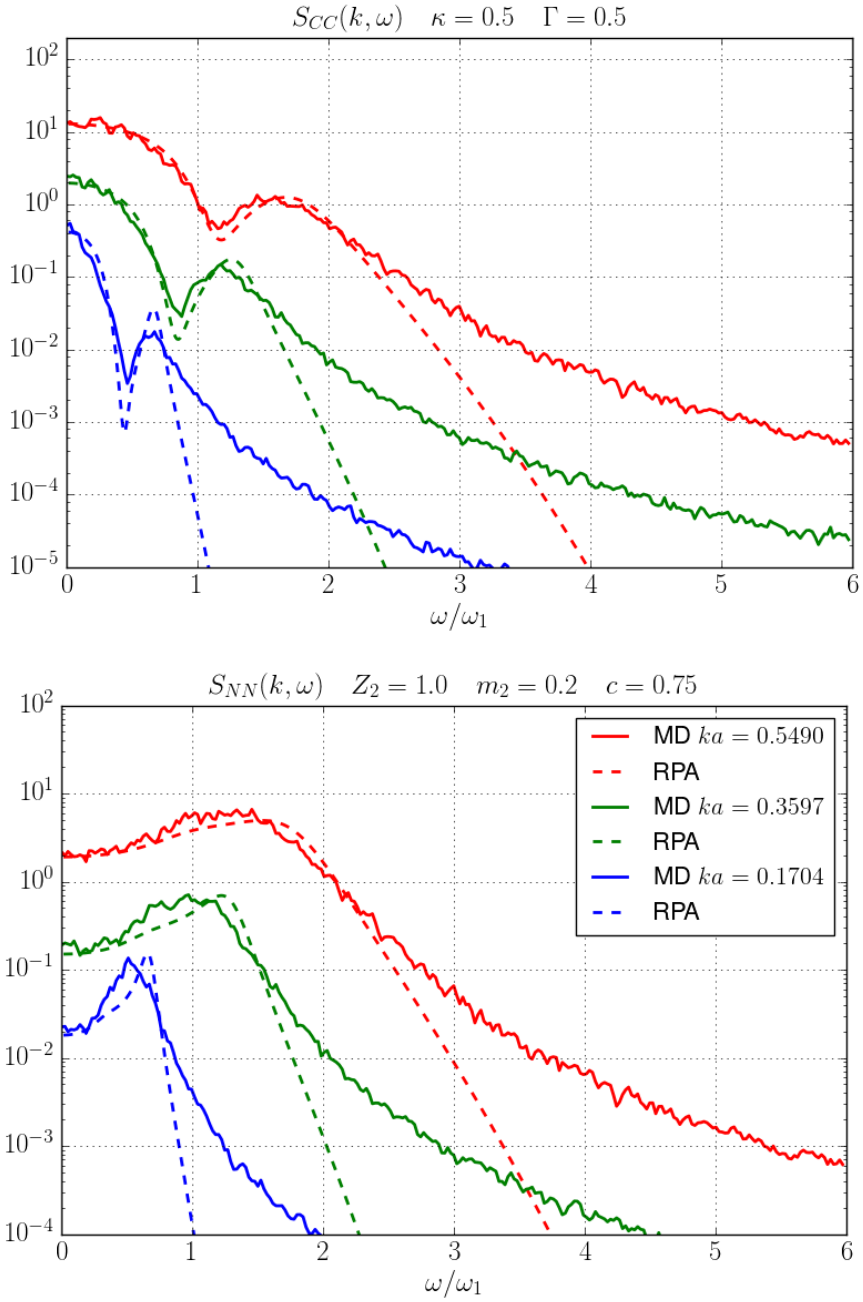

Figure 4.16: Plots of $S_{CC}(k,\omega)$ (top) and $S_{NN}(k,\omega)$ (bottom) comparing the RPA with MD simulations at the three lowest ka values for $\Gamma = 0.5$. Note that the second (third) ka lines have been shifted upwards by 10 (100) for easier viewing.

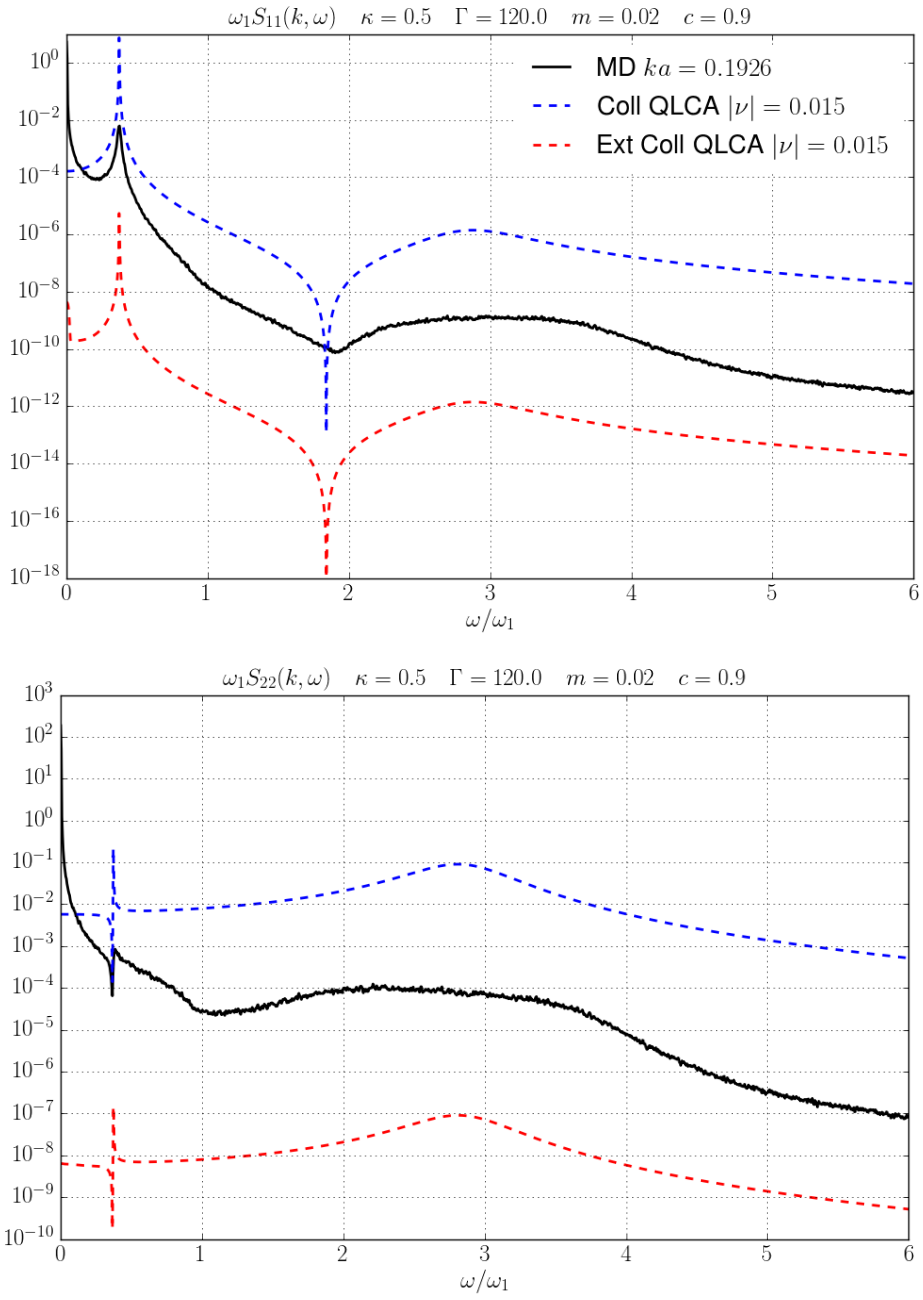

Figure 4.17: Plot comparing the Extended Collisional QLCA and Collisional QLCA with MD Simulations at the lowest ka value. The QLCA models have been shifted upwards and downwards for better viewing.

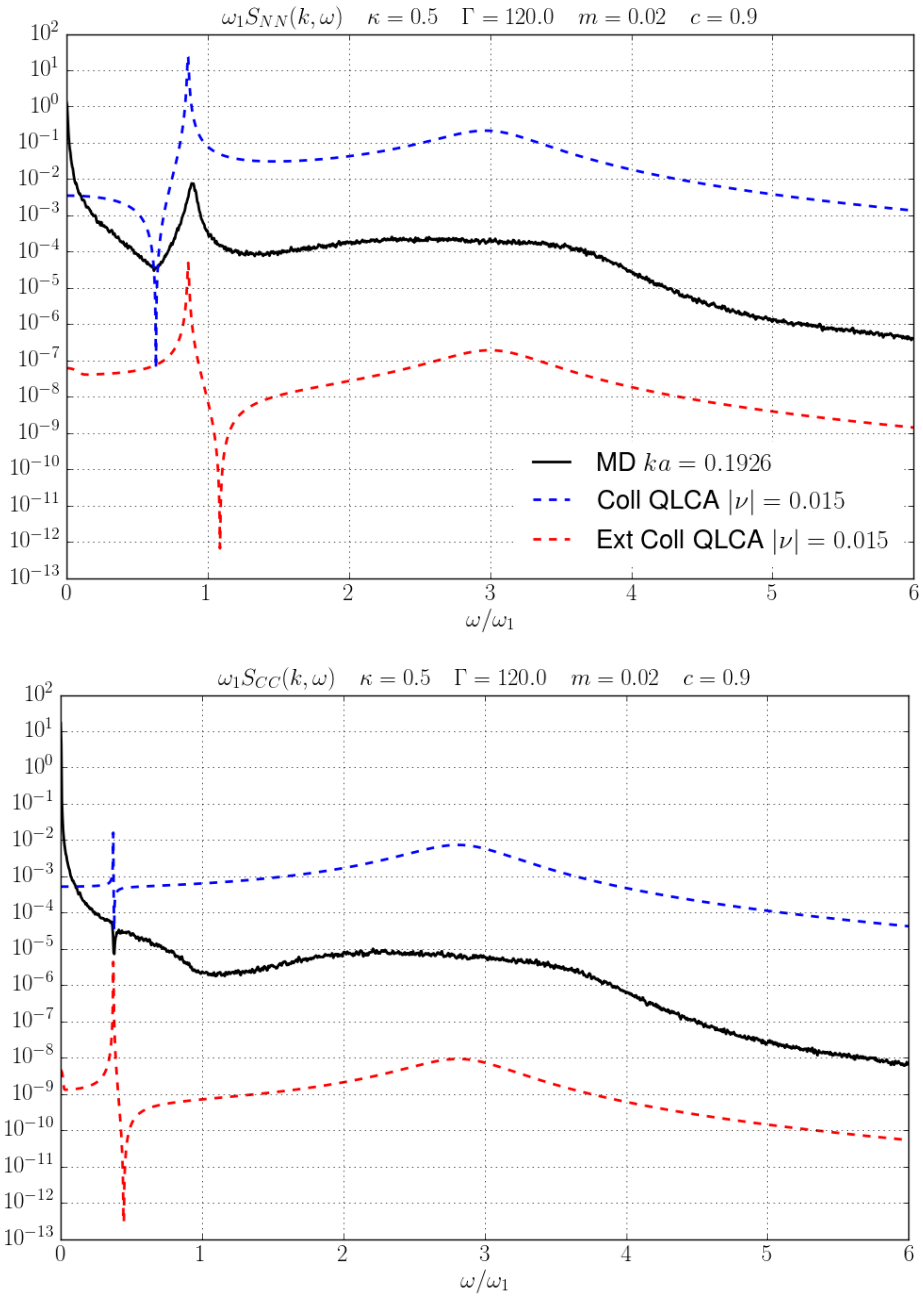

Figure 4.18: Plot comparing the Extended Collisional QLCA and Collisional QLCA with MD Simulations at the lowest ka value. The QLCA models have been shifted upwards and downwards for better viewing.

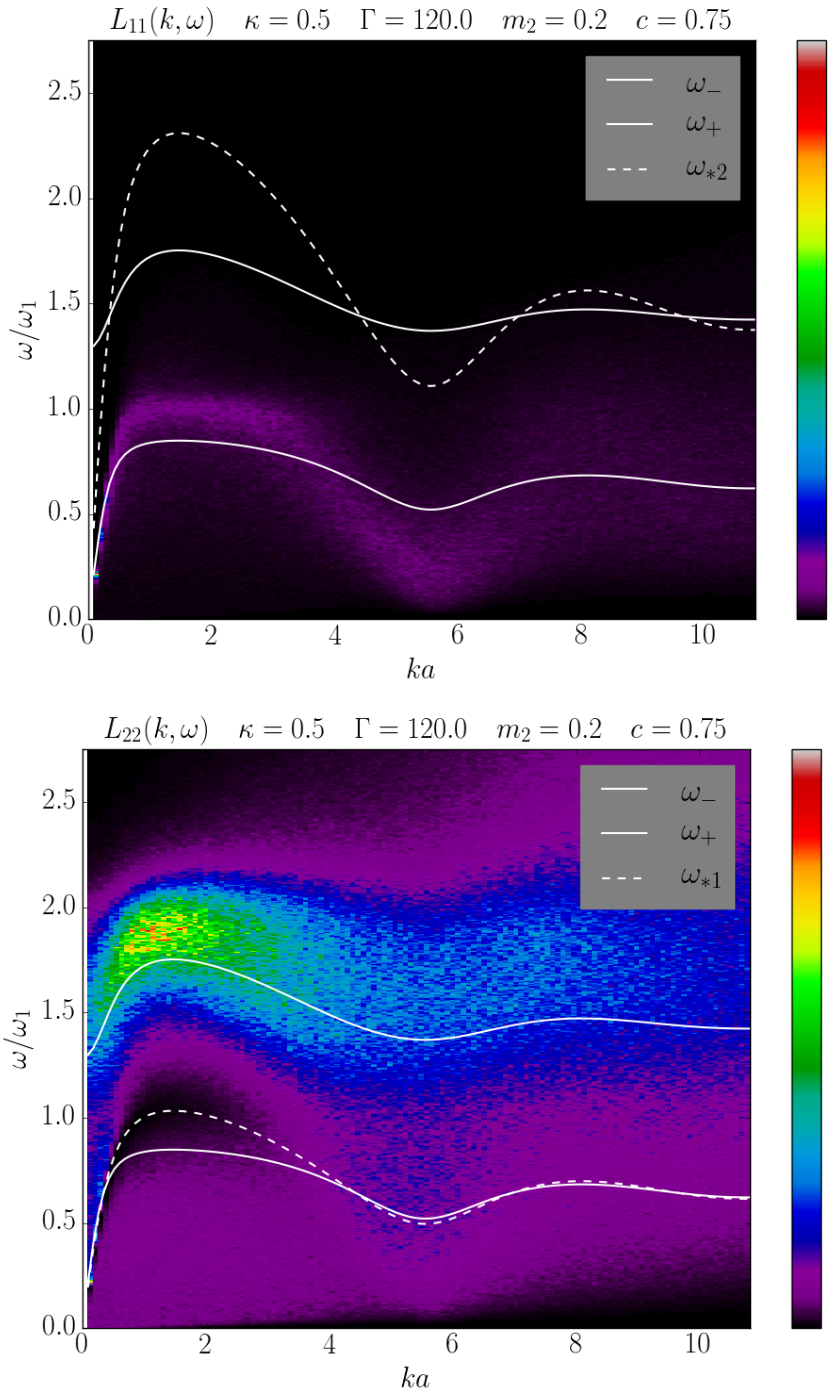

Figure 4.19: Intensity plot of $L_{11}(k,\omega)$ (top) and $L_{22}(k,\omega)$ (bottom) to show the collective mode dispersion. Solid white line identify the QLCA modes, while dashed lines the SK-frequencies.

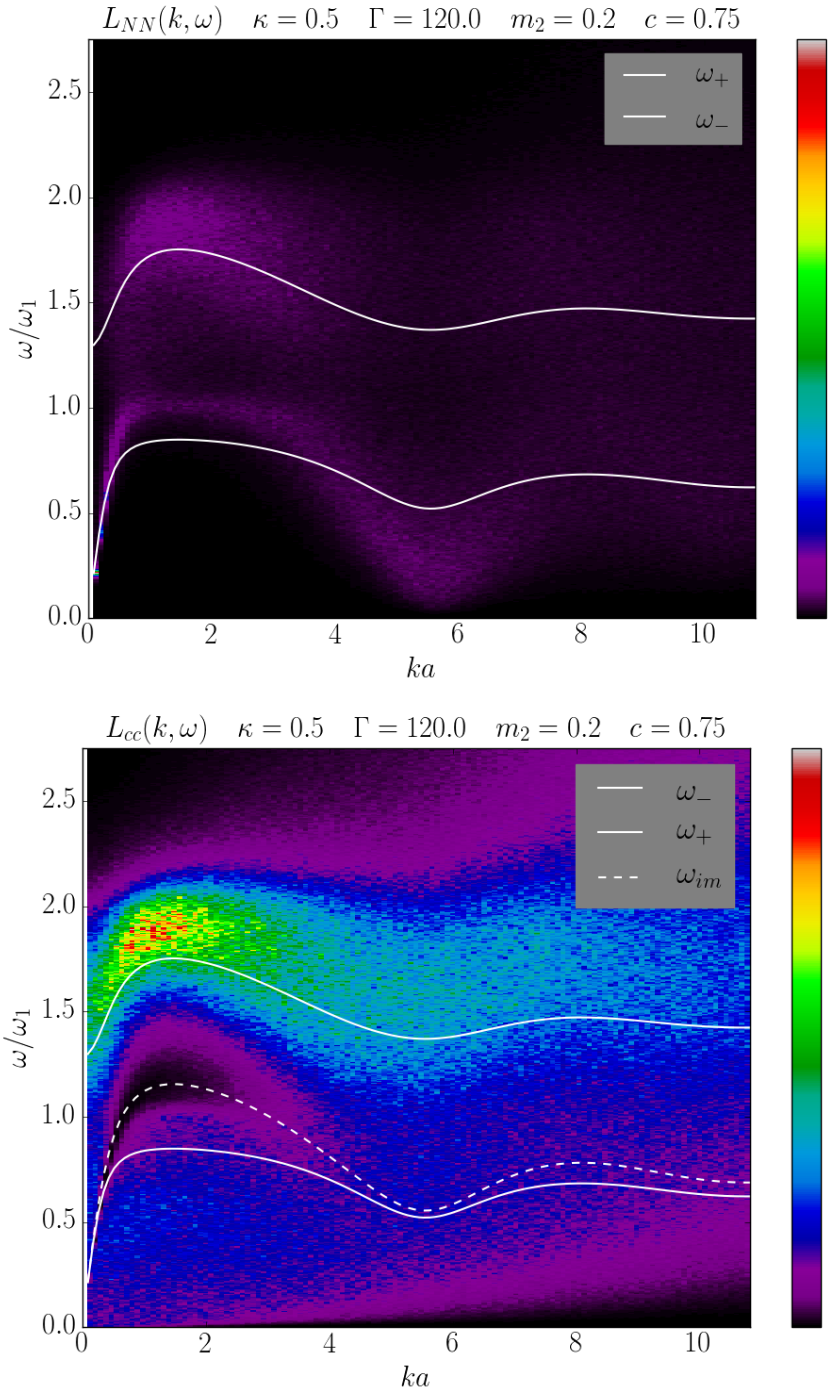

Figure 4.20: Intensity map of L_{AB} to show the collective mode dispersion. Solid white line identify the QLCA modes, while dashed lines the SK-frequencies.

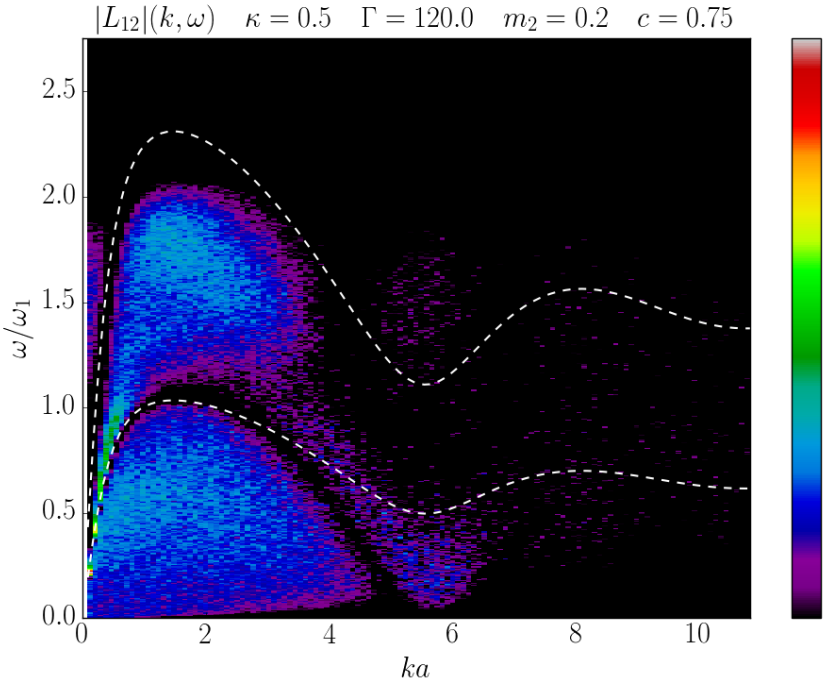

Figure 4.21: Intensity map of L_{AB} to show the collective mode dispersion. Dashed lines represent the SK-frequencies' dispersions.

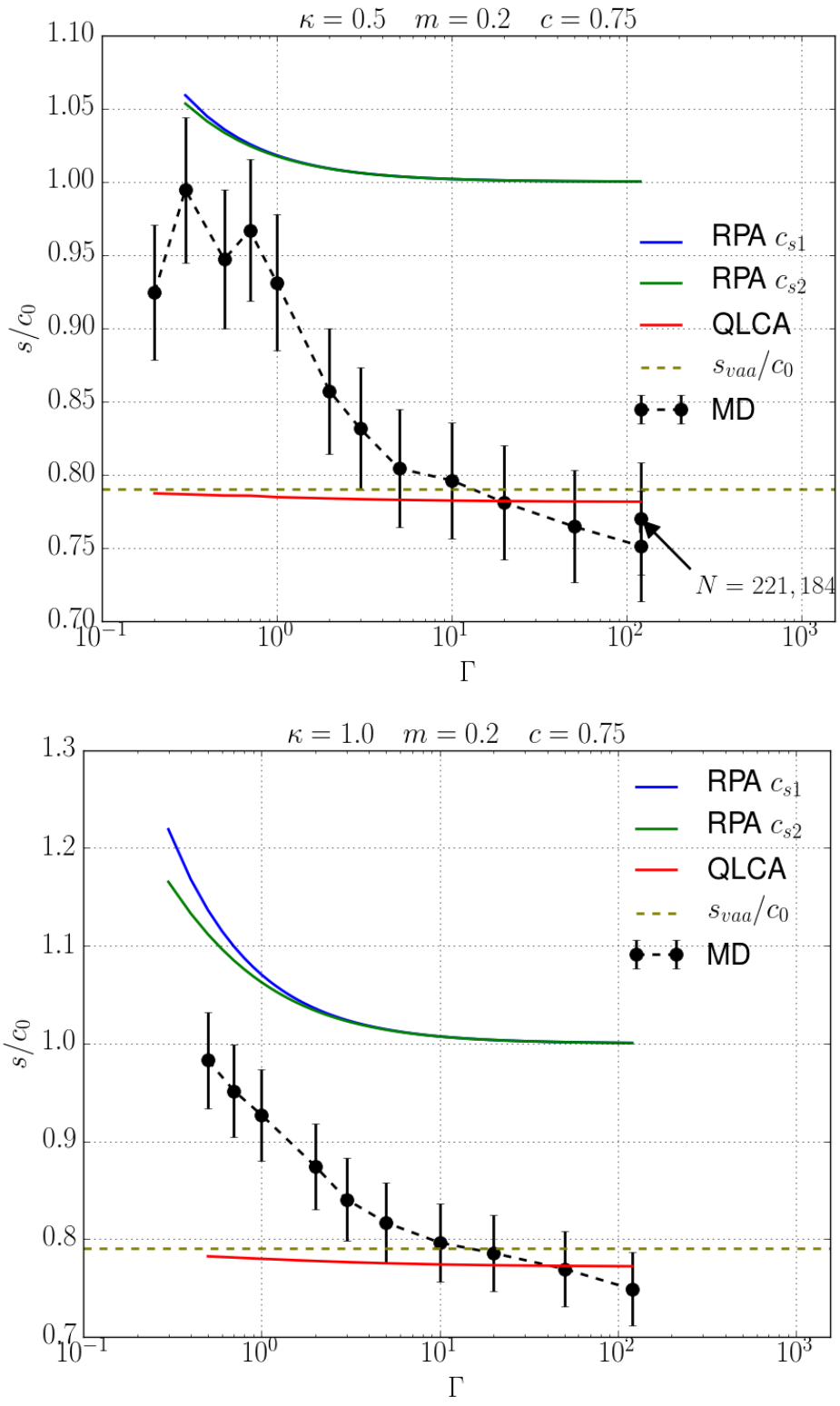

Figure 4.22: Plots of sound speed as a function of Γ for two values of κ. RPA c_{s1} corresponds to eq. (4.25) and RPA c_{s2} to eq. (4.20).

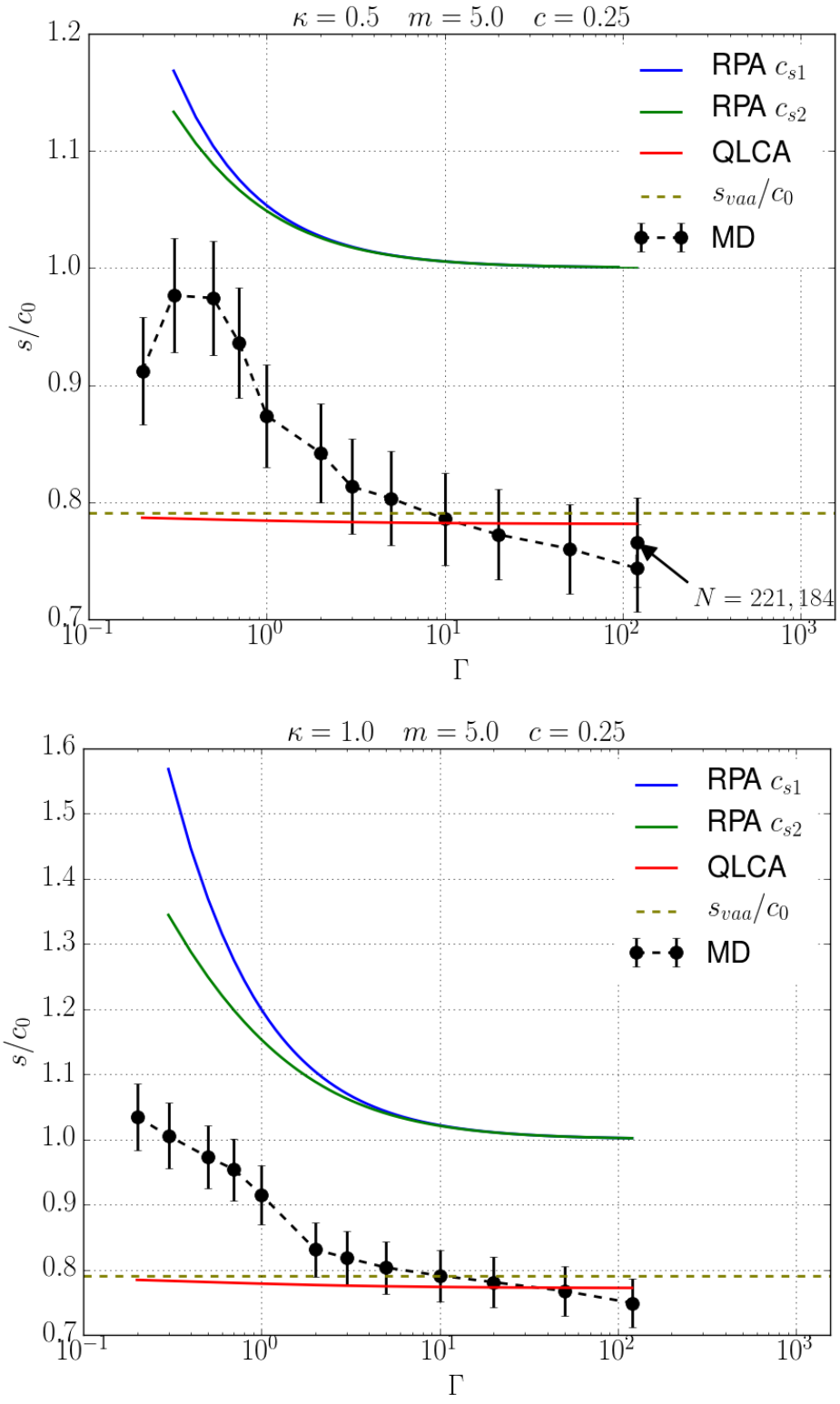

Figure 4.23: Plots of sound speed as a function of Γ for two values of κ. RPA c_{s1} corresponds to eq. (4.25) and RPA c_{s2} to eq. (4.20).

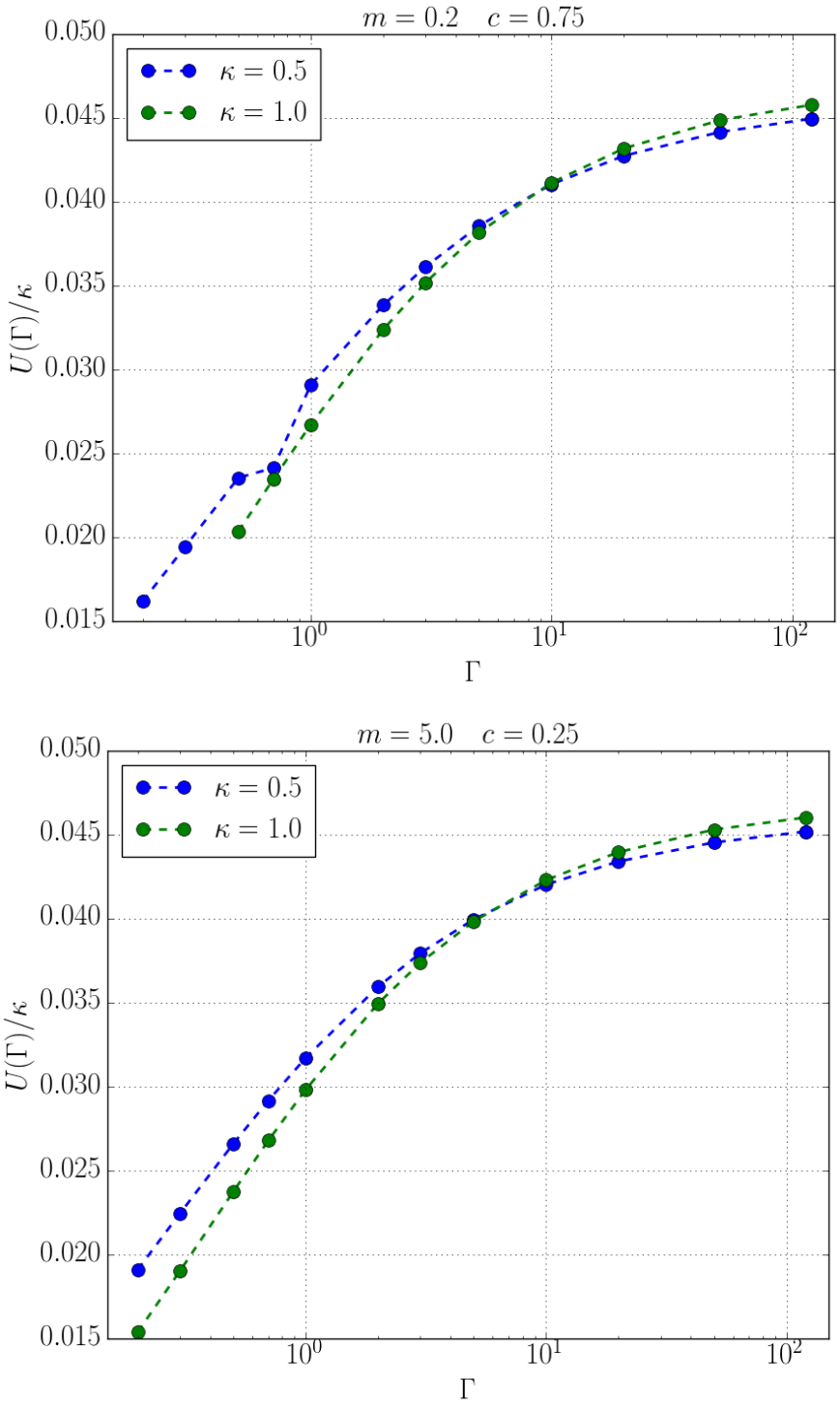

Figure 4.24: Plot of the correlation correction U_+ as a function of Γ for two different mixtures.

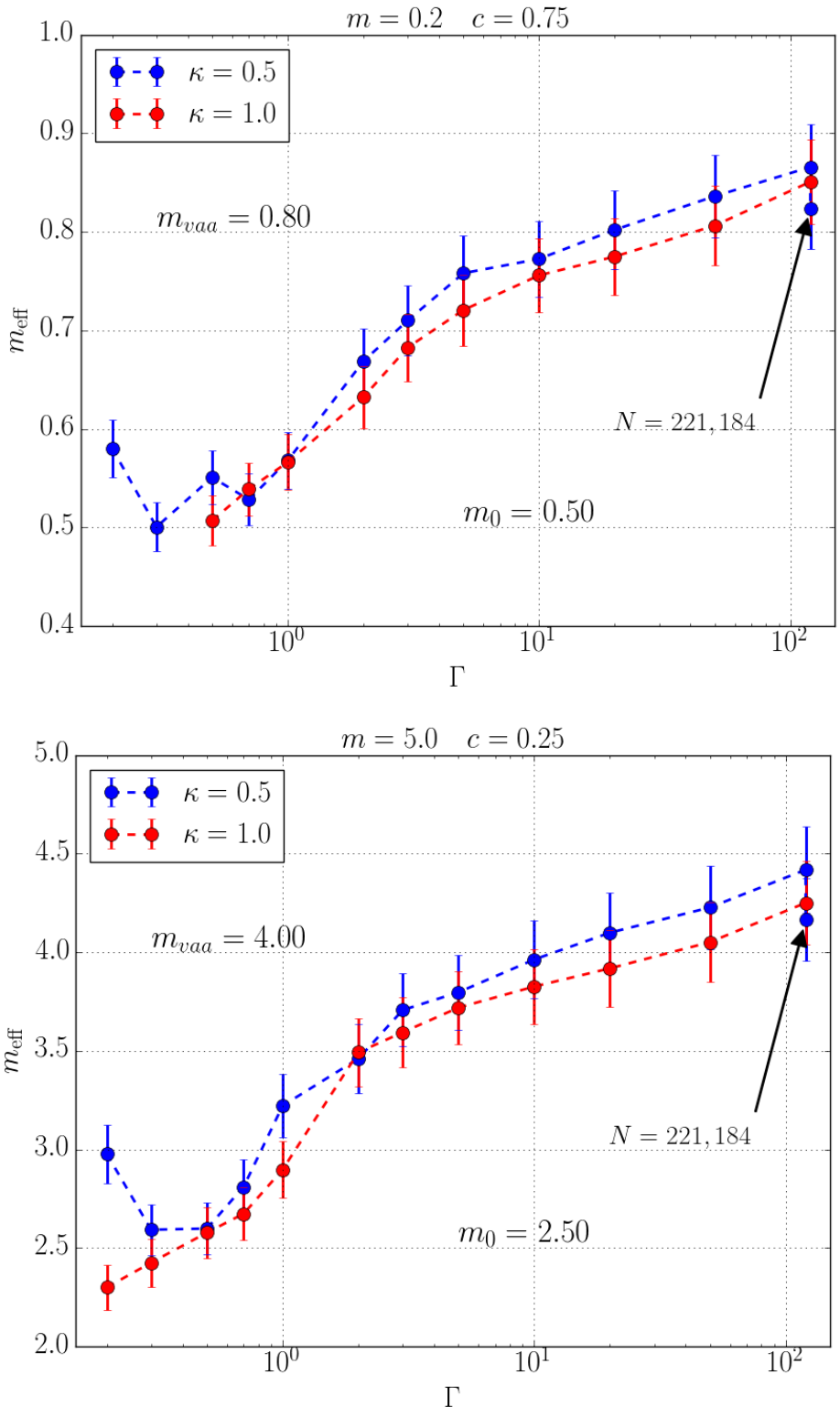

Figure 4.25: Effective Mass calculated using eq. (4.65) for two values of κ.

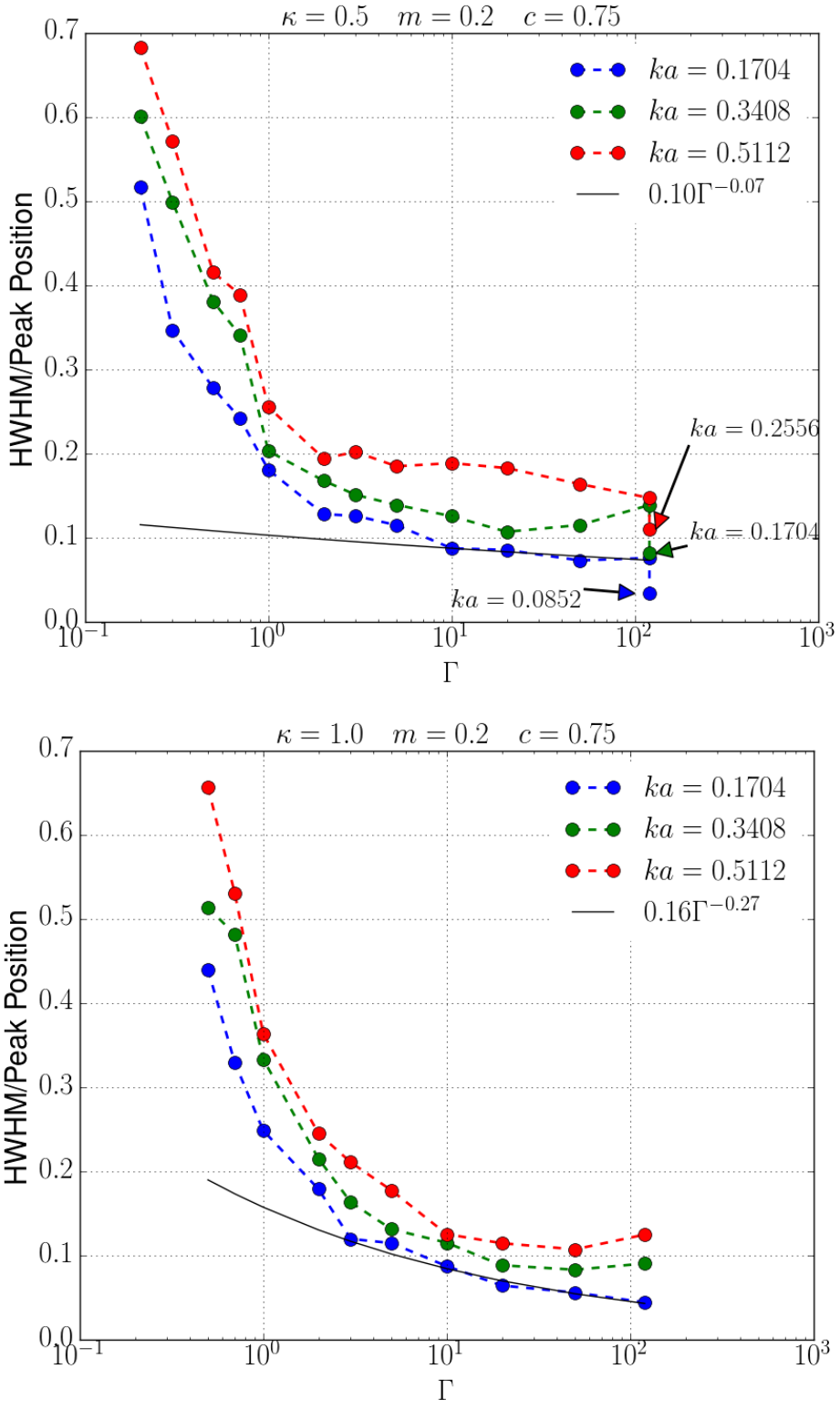

Figure 4.26: Plots of the relative HWHM as a function of Γ for two values of κ.

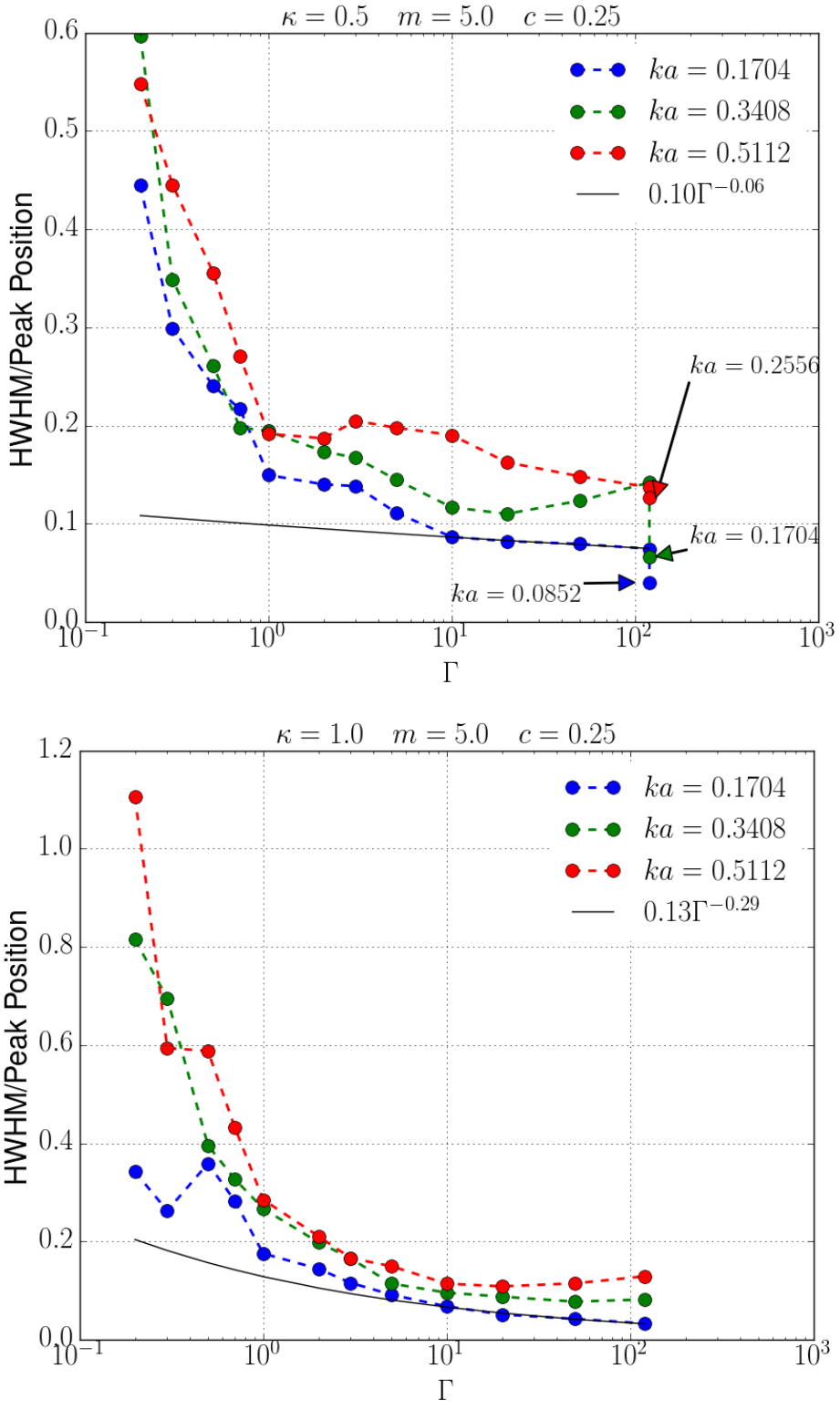

Figure 4.27: Plots of the relative HWHM as a function of Γ for two values of κ.

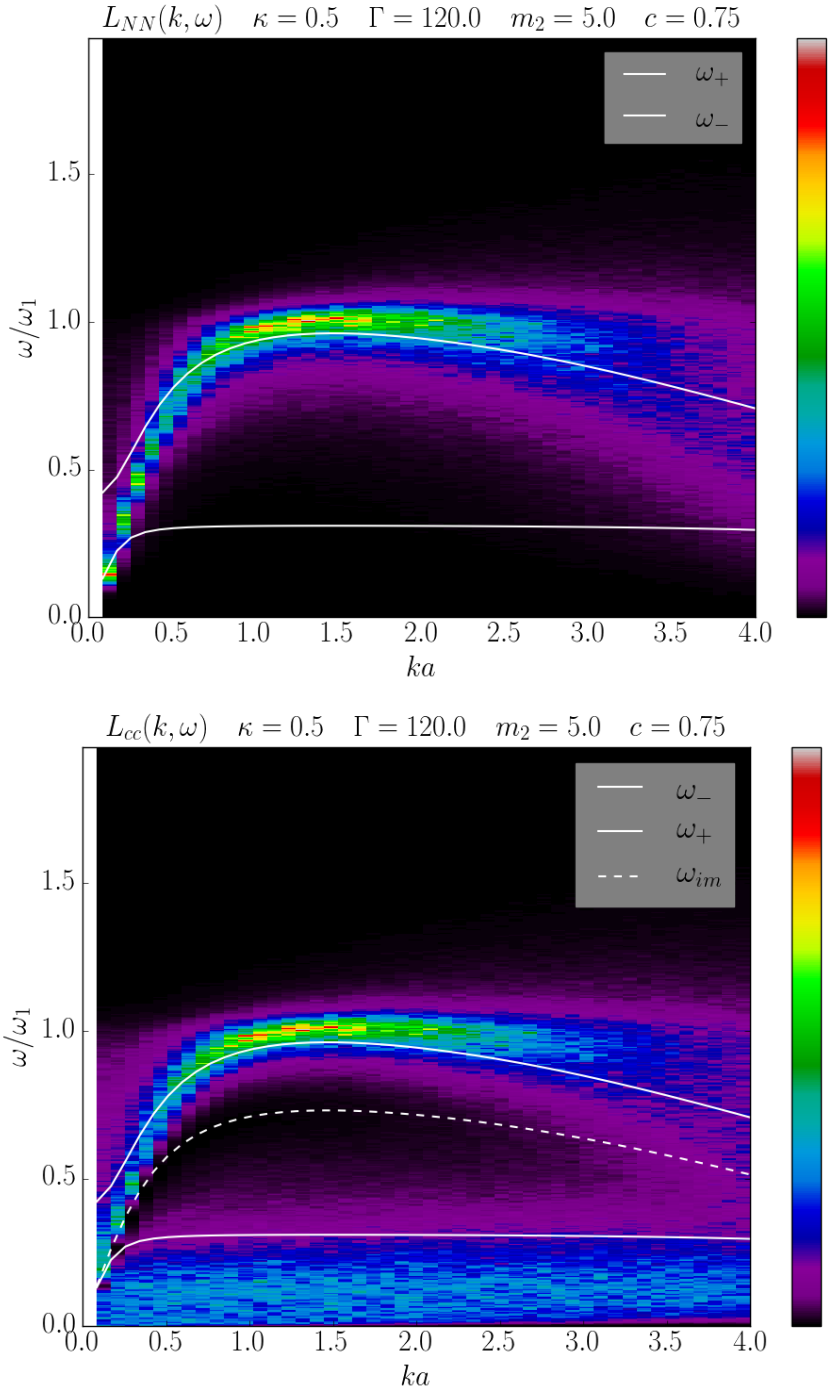

Figure 4.28: Intensity map of $L_{NN}(k,\omega)$ (top) and $L_{CC}(k,\omega)$ (bottom) for a mixture with a high concentration of light particles. Solid white line identify the QLCA modes, while dashed lines ω_{vaa}.

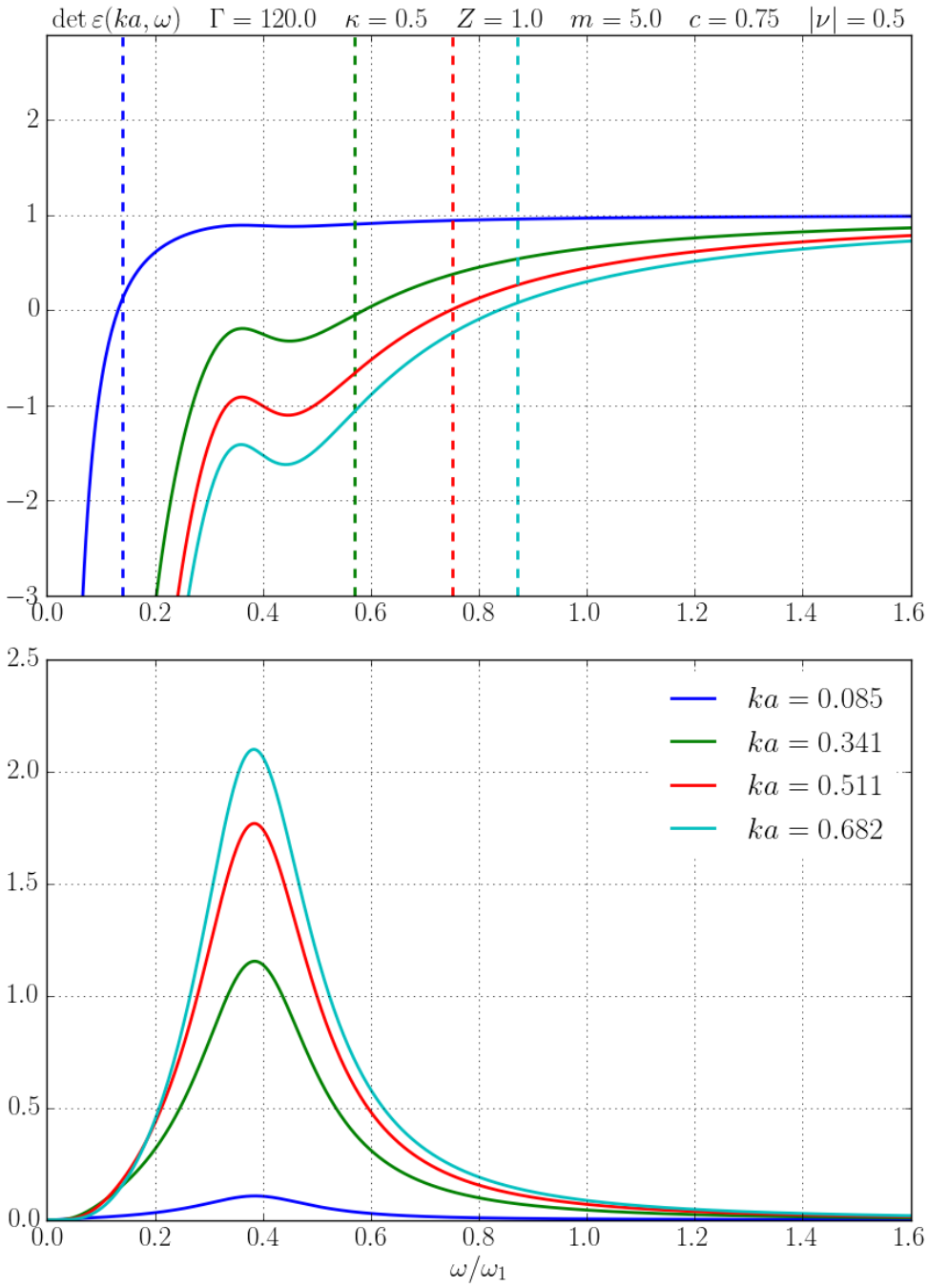

Figure 4.29: Plots of the real (top) and imaginary part (bottom) of $\det \varepsilon(k, \omega)$ calculated using the Collisional QLCA. The dashed vertical lines indicate the position of the peak in $L_{NN}(k, \omega)$ extrapolated from MD data.

CHAPTER V

Yukawa to Coulomb

In this chapter we investigate the collective mode spectrum as a function of κ. In this Chapter as in the entirety of this Thesis we have referred to the polarization of the eigenvector of the QLCA dynamical matrix $\mathbf{C}(k)$. This eigenvectors are the eigenvectors of the matrix of external response functions and as such indicated the "polarization" of the displacement fields $\mathfrak{z}_A$. On the other hand, the polarization of the eigenvectors of the dielectric matrix are associated with the polarization of the Electric Field. Are the two sets of eigenvectors the same at strong coupling? A first look indicates that they should not be since the dielectric matrix is the product of the external χ_{AB} matrix and the singular interaction matrix ϕ_{AB}. At the same time a physical picture suggests that an Electric Field should be proportional to a displacement field. Leaving the answer to this question as future work we investigate the behavior of the polarization of the eigenvectors of $\mathbf{C}$.

A Binary Coulomb Mixture (BIM) is characterized by two plasmon modes while a Yukawa Binary Mixture (YBM) by an acoustic and a gap mode. In the case of BIM looking at the sign of L_{12} we established that the high frequency plasmon corresponds to an in-phase motion of both positive ions while the second plasmon represents an out-of-phase motion between the two ionic species. In a Yukawa mixture, instead, we find the opposite: the high frequency gap mode represents

out-of-phase oscillations and the low frequency acoustic mode in-phase oscillations between the two species. This is shown in plots of $L_{12}(k,\omega)$ at specific values of ka in Fig. 5.1 where the top panel corresponds to BIM and the bottom panel to YBM. Looking at $L_{12}(k,\omega)$ of a Binary Yukawa Mixture, we notice, at the lowest ka value, a large positive acoustic peak at low frequencies and a negative broad peak, representing the gap mode, at higher frequencies. This is in contrast with the top panel where the situation is reversed.

This appears somewhat confusing since one expects that, as $\kappa \to 0$, the acoustic Yukawa mode transforms into the low frequency Coulomb plasmon, by means of the Anderson-Higgs mechanism, while the gap Yukawa mode goes into the high frequency Coulomb plasmon. In fact, this is what is argued in Ref. (Kalman, Donkó, et al., 2014) by Kalman *et al.*. Fig. (5) in Ref. (Kalman, Donkó, et al., 2014) shows a dispersion plot for a series of κ values indicating how the Yukawa mode dispersion approaches that of the Coulomb plasmons. Although, that plot represents lattice modes of a Yukawa crystal the same picture remains valid in the strongly coupled liquid regime.

In Fig. 5.2 we show dispersions of the QLCA Yukawa modes $\omega_{\pm}(k)$ for three values of κ. The horizontal black lines indicate the frequencies of the Coulomb plasmons at $k = 0$ (for the same asymmetry parameters), and the dashed lines, instead, indicate the nominal Einstein frequencies. As expected the Yukawa dispersions approach the Coulomb plasmons as $\kappa \to 0$. These plots, however, need to be compared with the one in Fig. 5.3 where we show the eigenvectors obtained from the diagonalization of the QLCA dynamical matrix $\mathbf{C}(k)$. We plot these eigenvectors in species space, where the horizontal axis indicate species 1 and the vertical axis species 2. The high frequency Coulomb plasmon is in the first quadrant indicating that the two species are in-phase, while the second plasmon is in the third quadrant representative of the two species being out-of-phase. From the

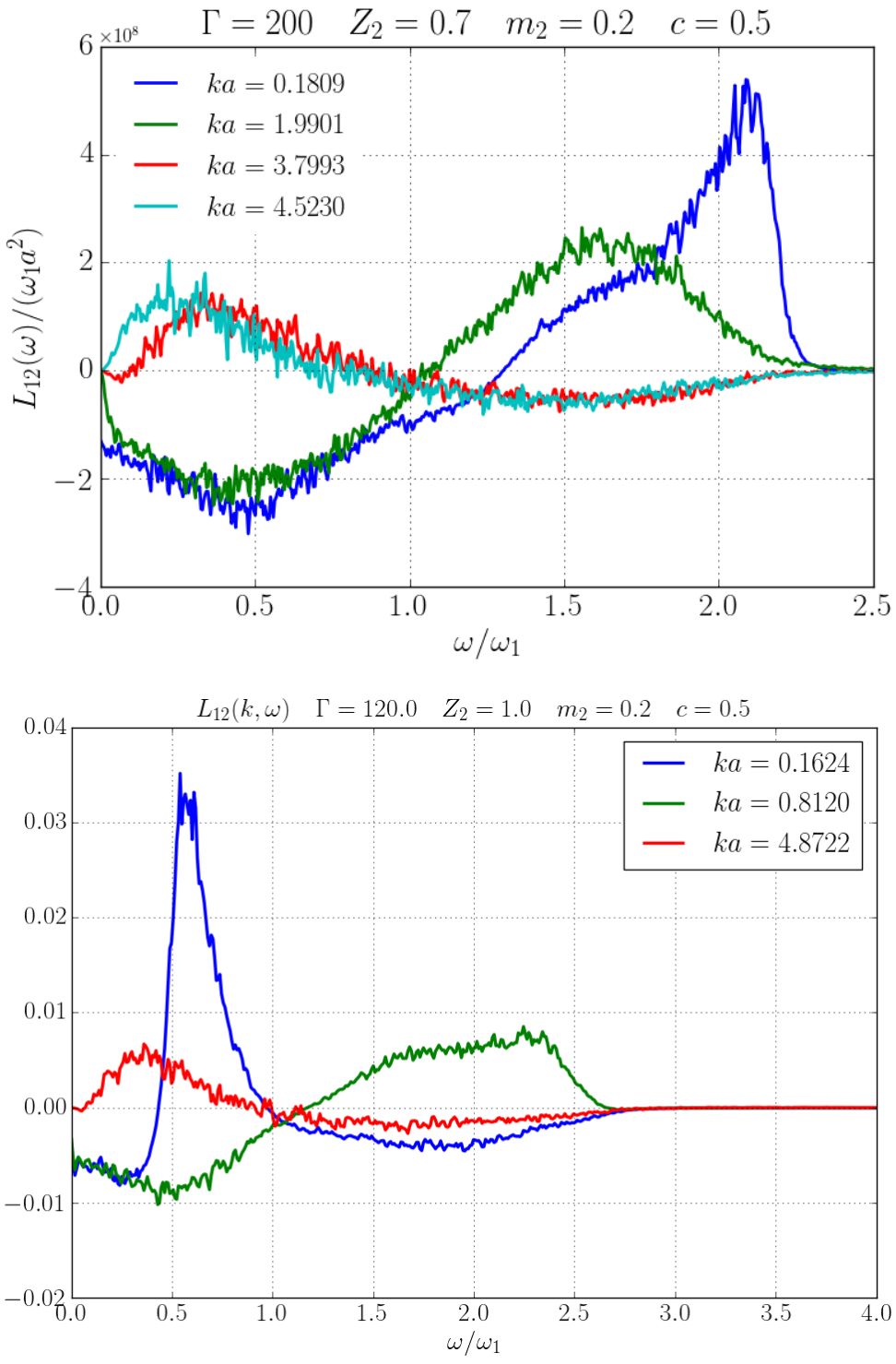

Figure 5.1: Plot of L_{12} at different ka values showing how the sign change after the collective modes interesect the anti-resonances. Top panel $L_{12}(k,\omega)$ for a Binary Coulomb Mixture. Bottom panel for a Binary Yukawa Mixture.

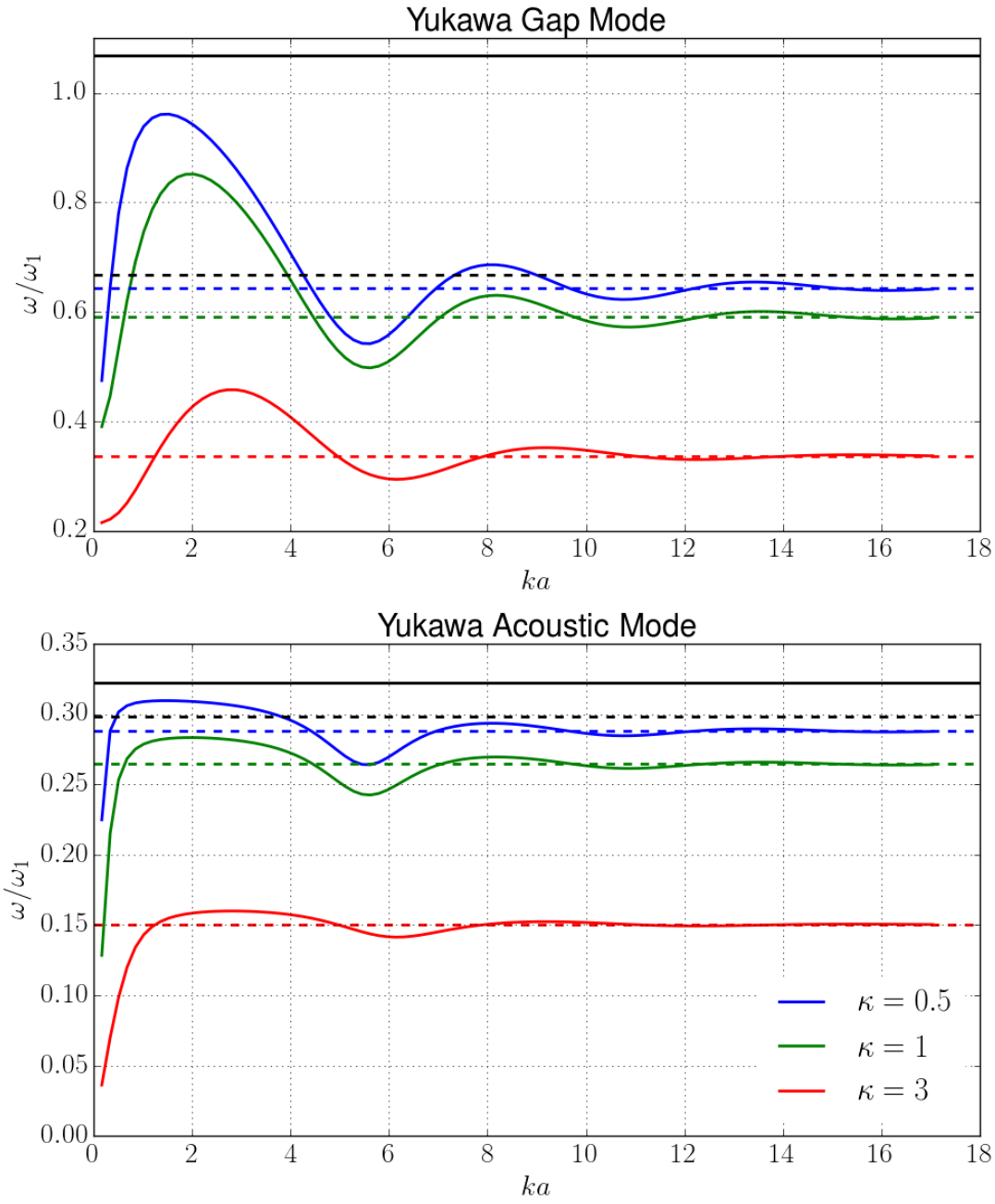

Figure 5.2: Dispersion of the QLCA Yukawa collective modes for three values of screening parameter κ for a mixture with $Z_2 = 1.0$, $m_2 = 5.0$, and $c = 0.75$. The black lines indicate the frequencies of the Coulomb plasmons for a mixture with similar asymmetry parameters.

plot in Fig. 5.2 one would expect to find the Yukawa acoustic eigenvectors in the third quadrant and the Yukawa gap eigenvectors in the first quadrant, but this is not the case. Hence, the question how does one reconcile the dispersion plot with the polarization of the modes?

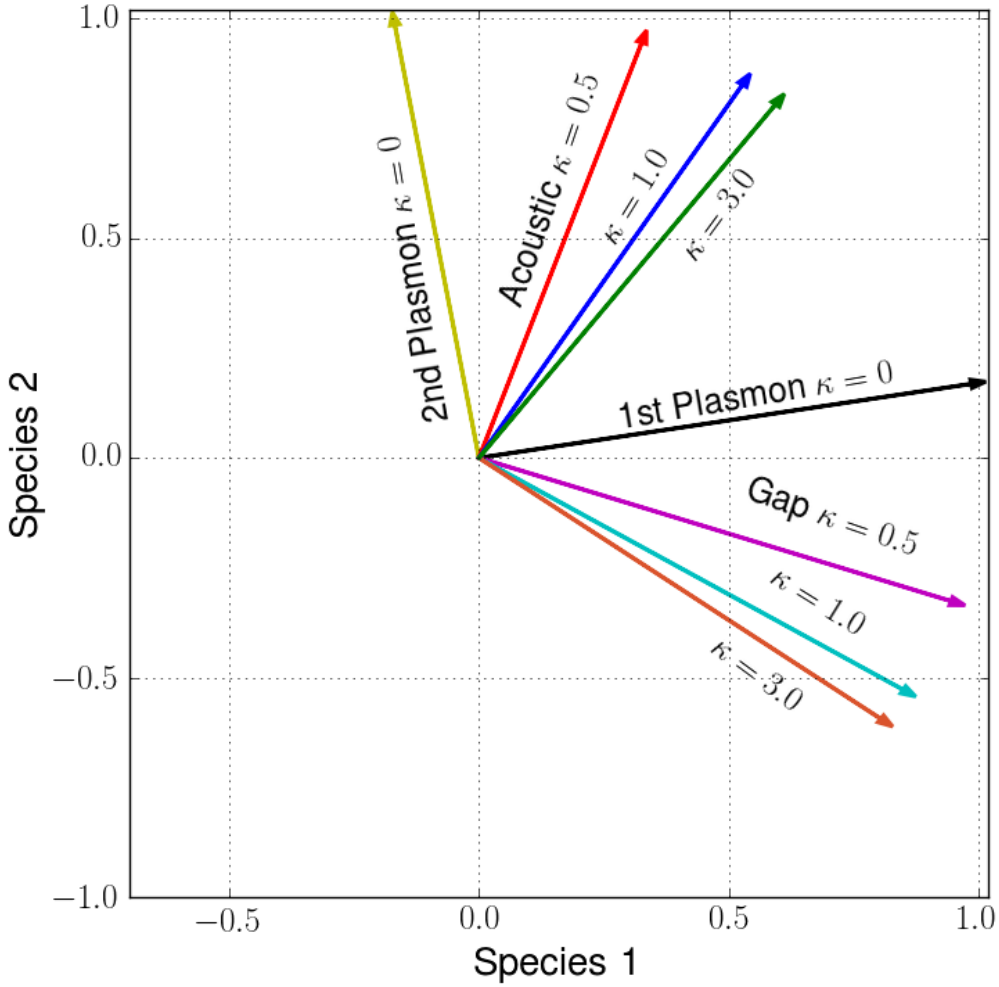

Figure 5.3: Eigenvectors of the dynamical matrix $\mathbf{C}(k)$ in species space at the lowest ka values of Yukawa MD simulations.

The answer lies in the sign of the off-diagonal element of the dynamical matrix, C_{12}. A negative sign of C_{12} leads to an in-phase mode with a lower frequency than

the out-of-phase mode. This is also found in the toy model of two coupled harmonic oscillators (see eq. (2.68). The higher frequency of the out-of-phase mode is due to the sum of the natural frequencies and the coupling frequency. Undergraduate texts often give the following reasoning: in order for the two oscillator to move opposite of each other the system requires energy to overcome the coupling and thus a finite frequency at $k = 0$. If C_{12} is positive, instead, the out-of-phase mode will have a lower frequency than the in-phase one since the coupling between the two oscillators creates an effective attraction.

In Fig. 5.4 we show plots of the dispersion of all the relevant frequencies of a BIM (top plot) and a YBM (bottom plot) for a sample set of asymmetry parameters. The top plot is the same in Fig. 3.3, reproduced here for the sake of clarity. The first thing to notice is the opposite signs of C_{12} at low ka which is negative in the case of YBM and positive in BIM. Similar to the BIM case the SK frequencies are found above and below the in-phase mode, $\omega_+(k)$. In addtion, in both plots we notice that the SK frequencies intersect the collective modes whenever $C_{12}(k) = 0$. This happens at much lower frequencies in YBM than in BIM.

To further prove that the sign of C_{12} determines the polarization of the modes, we show plots of the dispersion with the corresponding eigenvectors in Figs. 5.5 – 5.6. As expected as the sign of C_{12} changes the eigenvectors start to rotate counter-clockwise. As ka increases further the eigenvectors oscillate around the species axis until the finally settle on $\{-1, 0\}$ $\{0, -1\}$ at $k \to \infty$ where $C_{12} = 0$.

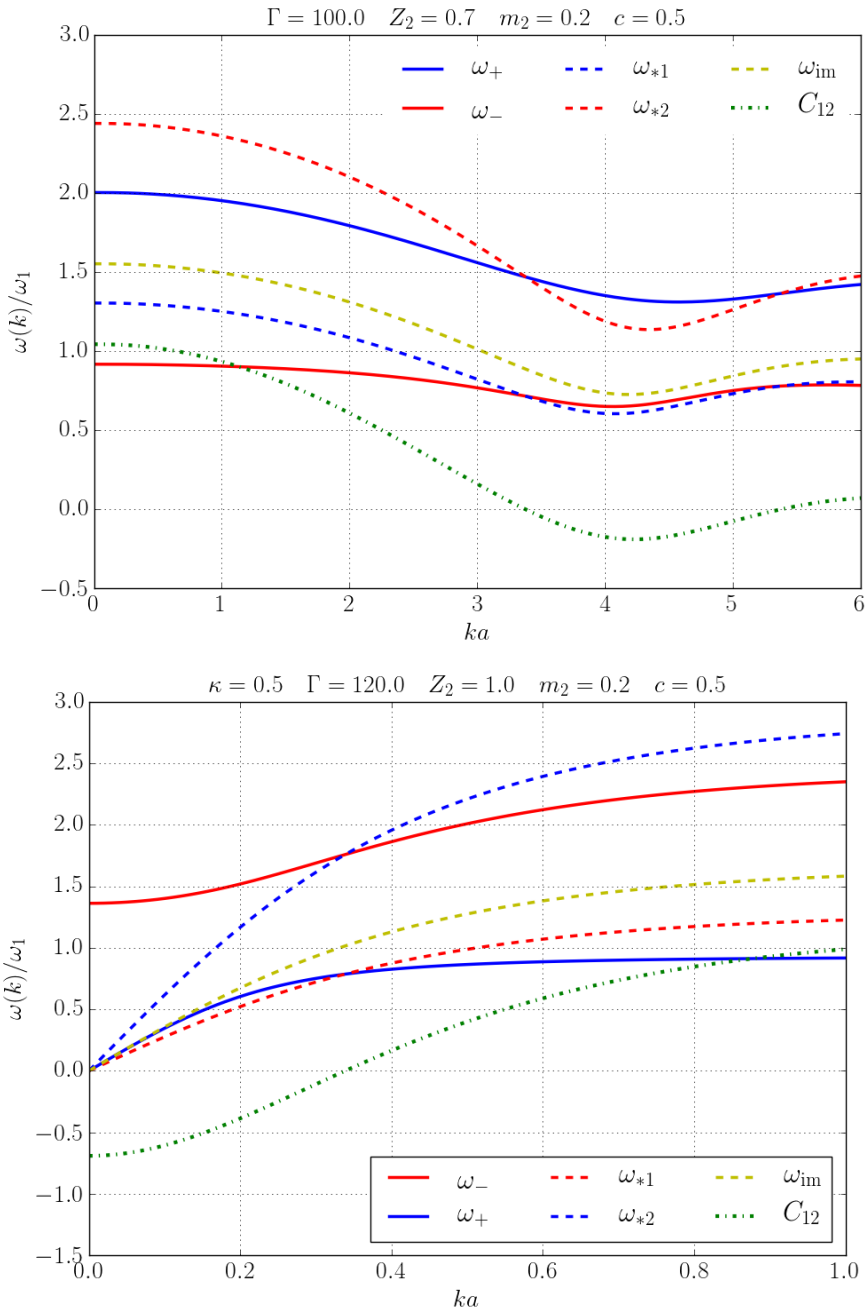

Figure 5.4: Dispersions of the relevant QLCA frequencies in units of ω_1. The collective mode are indicated by solid lines, Silvestri–Kalman frequencies by dashed lines, QLCA Dynamical matrix elements by dashed-dot lines.

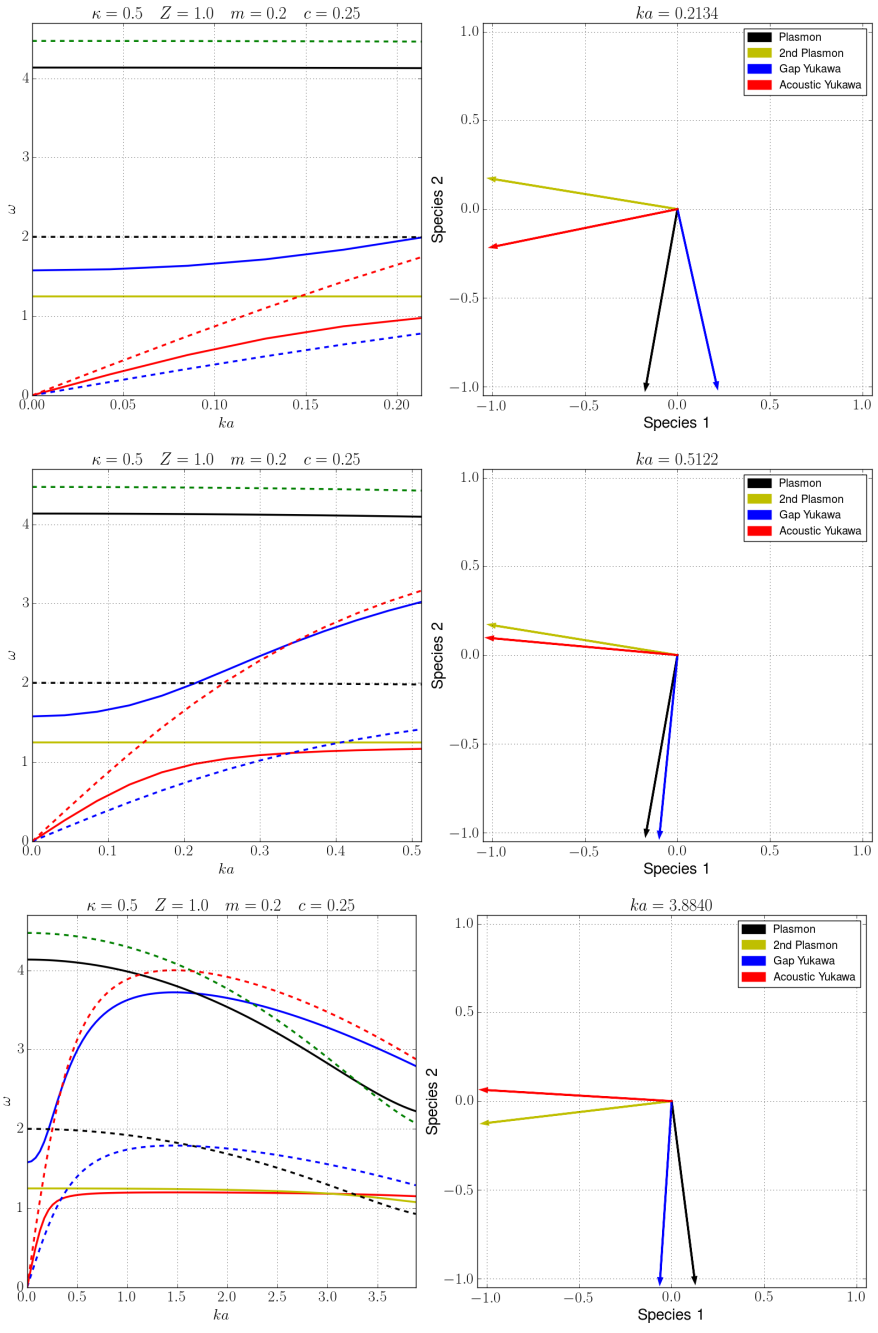

Figure 5.5: Dispersions of the relevant QLCA frequencies in units of ω_1. (Left) Collective modes are indicated by solid lines (Yukawa: red and blue, Coulomb: black and yellow), Silvestri–Kalman frequencies by dashed lines (Yukawa: red and blue, Coulomb: balck and green). (Right) Eigenvectors in species space corresponding to the last ka values shown in the left panel. Color code is kept the same between the two panels.

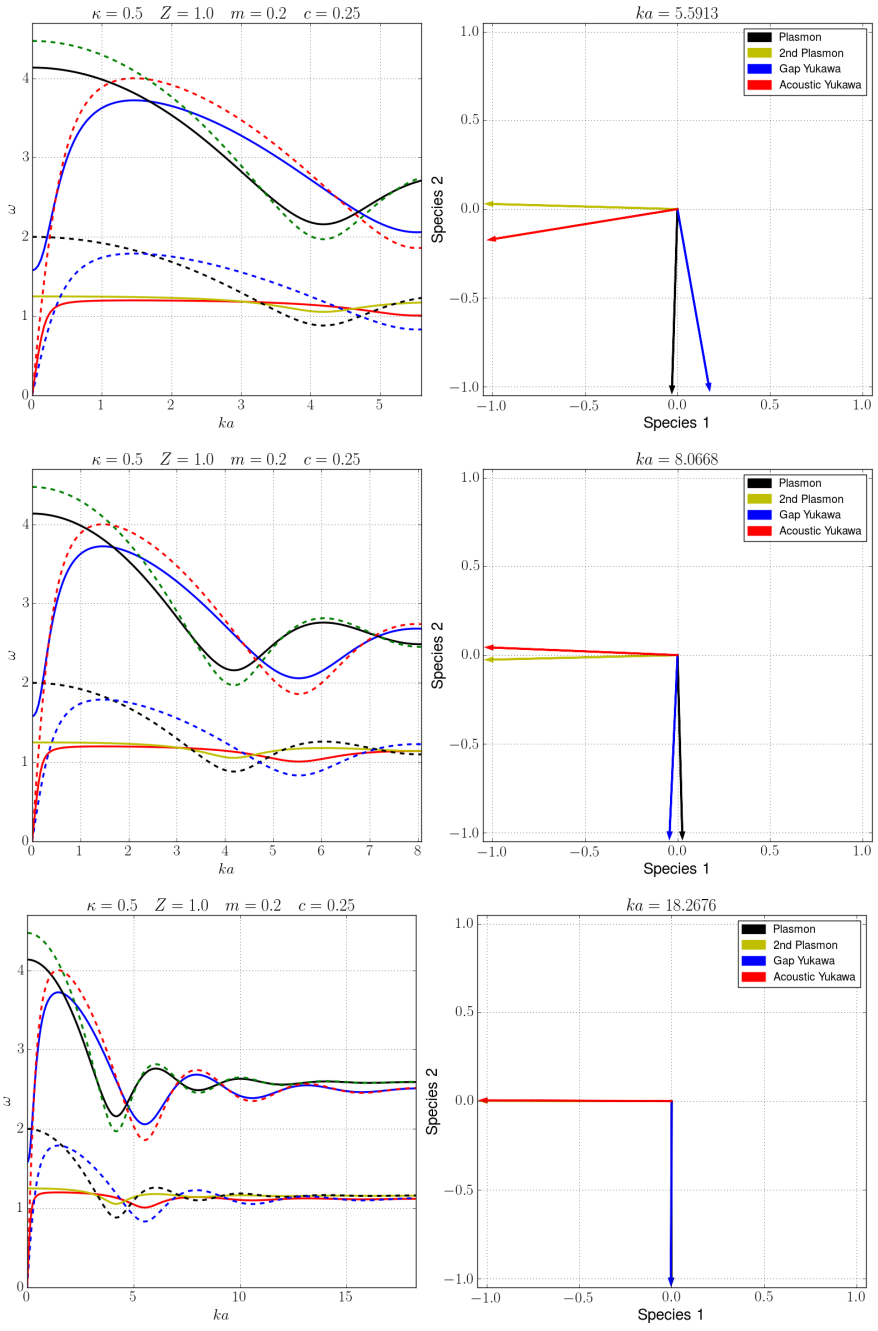

Figure 5.6: Dispersions of the relevant QLCA frequencies in units of ω_1. (Left) Collective modes are indicated by solid lines (Yukawa: red and blue, Coulomb: black and yellow), Silvestri–Kalman frequencies by dashed lines (Yukawa: red and blue, Coulomb: balck and green). (Right) Eigenvectors in species space corresponding to the last ka values shown in the left panel. Color code is kept the same between the two panels.

CHAPTER VI

Bilayer

Charged particle bilayers are parallel conducting planes separated by a distance, d, comparable to the inter-particle distance within the layers, a. These systems can be viewed as a binary system, where the two species are distinguished from each other, not by different parameters, but by the difference between the intra–layer and inter–layer potentials. In this chapter we will refer to symmetric bilayers as those systems in which the charged particles have equal mass and concentrations and as asymmetric bilayers as those in which the particle mass and/or number density of one layer is different than the other. For example, systems in which both layers are populated by electrons ($e-e$) with the same effective mass, or one layer by electrons and the other by holes ($e-h$) and same effective mass, are considered symmetric.

The literature on this topic is vast due to the promising technological applications of such layered devices. Originally the interest stemmed from the ability to create low dimensional (1D and 2D) electron liquids using a combination of metal and semiconductors layered structures (Giuliani and Vignale, 2005). Nowadays similar 2D electron liquids can be created using graphene or van-der Walls materials (Basov, Averitt, and Hsieh, 2017). Research on these systems has been mostly directed towards transport properties, in particular, on the Coulomb drag effect

(Rojo, 1999; Narozhny and Levchenko, 2016) mentioned in Chap. I.

The creation of low dimensional electron liquids had also attracted the attention of the strongly coupled plasma community as these systems are able to reach the strong coupling regime $r_s \sim 20$. Early works focused on the collective excitations of these systems and the problem was studied within the STLS formalism. The latter predicted only correlational corrections to order k^2 to the weak coupling spectrum, constituted by a quasi-acoustic ($\omega \sim \sqrt{k}$) and acoustic ($\omega \sim k$) modes (Neilson et al., 1993; Świerkowski, Neilson, and Szymański, 1993; Szyma ński, Świerkowski, and Neilson, 1994; Liu et al., 1996). Kalman and collaborators, using the QLCA formalism, instead, suggested that at strong coupling the acoustic mode be replaced by gap (Kalman and Golden, 1998; Kalman, Valtchinov, and Golden, 1999; Kalman, Valtchinov, and Golden, 2003). Subsequent MD simulations have confirmed the existence of a gap but at higher frequency than the one predicted by the QLCA (Donkó, Hartmann, Kalman, and Golden, 2003; Donkó, Kalman, Hartmann, et al., 2003; Ranganathan and Johnson, 2004; Golden, Mahassen, Kalman, et al., 2005; Golden, Mahassen, Senatore, et al., 2006; Kalman, Hartmann, Donkó, and Golden, 2007). Later on, strongly coupled bilayers were created using dusty plasmas experiments (Hartmann, Donkó, et al., 2009). This did not unequivocally confirmed the existence of the gap, but gave strong proof of its existence. As per the case of asymmetric bilayers, preliminary theoretical work was conducted by Golden and collaborators (Mahassen et al., 2006; Golden, Kalman, Hartmann, et al., 2012) predicting the existence of gap also in this case. MD simulations were carried out for bilayers with different densities, but focused primarily on static properties and transport (Ranganathan and Johnson, 2008). An interesting finding of Ref. (Ranganathan and Johnson, 2008) was no evidence of a fluid-solid phase transition at $\Gamma > 80$ as it was found in the case of symmetric bilayers (Ranganathan and Johnson, 2006).

In this Chapter we extend the theoretical work and present computer simulations on mass asymmetric $e-e$ bilayers. We will show that also in this case the collective spectrum of the strongly coupled regime consists of a longitudinal quasi-acoustic in-phase and a gap out-of-phase mode. The latter appears around $\Gamma \sim 10$ and its value at $k = 0$ does not seem to change at higher coupling values. The computer simulations cover a large range of the coupling parameter extending into the moderately to weakly coupled regime. In this case simulation results do not show the presence of an acoustic mode even in the absence of the gapped excitation. The effect of the asymmetry appears in the lowest order (in k) correlation-independent contribution to the quasi-acoustic mode. Charge particle asymmetric bilayers can provide a confirmation on the existence of the SK frequencies since in such experiments it is possible to probe only one of the layers and thus providing the partial $S_{AB}(k, \omega)$

6.1 Model and Definitions

The system under consideration is composed of two 2D layers of classical charged particles, exchange and other quantum effects are neglected. The duality of the system is due to the different interaction between particles on different layers

$$\phi_{11}(r) = \frac{Z_1^2 e^2}{r}, \quad \phi_{12}(r) = \frac{Z_1 Z_2 e^2}{\sqrt{r^2 + d^2}} \tag{6.1}$$

and respective Fourier transforms

$$\phi_{11}(k) = \frac{2\pi Z_1^2 e^2}{k}, \quad \phi_{12}(k) = \frac{2\pi Z_1 Z_2 e^2}{k} e^{-kd}. \tag{6.2}$$

Note that the subscripts indicate the layer, r is the projected 2D distance between particles in the same layer, and d the distance between the two layers. The charge number Z_A indicates the sign of the charges, whether we are considering

an electron-electron ($Z_1 = Z_2 = -1$) or an electron-hole ($Z_2 = 1 = -Z_1$) bilayer. In either case the sign is incorporated in the asymmetry parameters

$$p^2 = \frac{Z_2 n_2}{Z_1 n_1}, \qquad q^2 = \frac{Z_2}{m_2}\frac{m_1}{Z_1}. \tag{6.3}$$

The plasma and nominal Einstein frequencies are defined as

$$\omega_{AB}^2 = \frac{2\pi e^2}{a}\frac{Z_A Z_B \sqrt{n_A n_B}}{\sqrt{m_A m_B}}, \qquad \Omega_{AB}^2 = \frac{2\pi e^2}{a}\frac{Z_A}{m_A} Z_B n_B \tag{6.4}$$

where a is the Wigner-Seitz radius given by

$$\pi a^2 = \frac{1}{\sqrt{n_1 n_2}} \tag{6.5}$$

Finally, the coupling parameter is defined as

$$\Gamma = \frac{e^2}{a k_B T}. \tag{6.6}$$

6.2 Collective Modes

6.2.1 Weak Coupling

The long wavelength limit of the dielectric response, using the RPA (Das Sarma and Madhukar, 1981), is

$$\varepsilon(k,\omega) = 1 - \left[\frac{\omega_1^2 + \omega_2^2}{\omega^2} ka + 3\frac{\omega_1^2 v_1^2 + \omega_2^2 v_2^2}{\omega^4 a^2}(ka)^3\right] + \frac{\omega_1^2 \omega_2^2}{\omega^4}(ka)^2\left(1 - e^{-2kd}\right), \tag{6.7}$$

whose solutions are

$$\omega_\pm^2 = \frac{\omega_1^2 + \omega_2^2}{2} ka \left[1 \pm \sqrt{1 - 4\left(\frac{\omega_1 \omega_2}{\omega_1^2 + \omega_2^2}\right)^2 \frac{1 - e^{-2kd}}{ka} + 12\frac{\omega_1^2 v_1^2 + \omega_2^2 v_2^2}{(\omega_1^2 + \omega_2^2)^2}\frac{ka}{a^2}}\right]. \tag{6.8}$$

To first order in d these become: *(i)* a quasi-acoustic mode

$$\omega_+^2(k) = \left(\omega_1^2 + \omega_2^2\right) ka \left[1 - 2\left(\frac{\omega_1^2\omega_2^2}{\omega_p^4}\frac{d}{a} - 3\frac{\omega_1^2 v_1^2 + \omega_2^2 v_2^2}{\omega_p^4 a^2}\right)(ka)\right], \tag{6.9}$$

in which particles on different layers move in-phase, and *(ii)* an acoustic out-of-phase mode

$$\omega_-^2 = 2\left(\frac{\omega_1^2\omega_2^2}{\omega_p^2}\right)k^2 d - 3\left(\frac{\omega_1^2 v_1^2 + \omega_2^2 v_2^2}{\omega_p^2 a^2}\right)(ka)^2, \tag{6.10}$$

where we have defined $\omega_p^2 = \omega_1^2 + \omega_2^2$ and v_A the thermal speed of the particles. We verify that in the limit $d \to \infty$, when the two layers are completely separated, the collective modes are simply the quasi-acoustic plasmons of a 2D classical electron liquid

$$\omega_+^2 = \omega_1^2 ka, \quad \omega_-^2 = \omega_2^2 ka. \tag{6.11}$$

At the same time, in the opposite limit $d \to 0$ we recover

$$\omega_+^2(k) = \left(\omega_1^2 + \omega_2^2\right) ka \tag{6.12}$$

6.2.2 Strong Coupling

In the strongly coupled regime we again use the QLCA longitudinal dynamical matrix whose elements are

$$C_{11}(k) = \omega_1^2\left[ka + D_{11}(ka) + p^2 W\right], \tag{6.13}$$

$$C_{22}(k) = \omega_1^2\left\{q^2 p^2\left[ka + D_{22}(ka)\right] + q^2 W\right\}, \tag{6.14}$$

$$C_{12}(k) = qp\omega_1^2\left[kae^{-kd} + D_{12}(ka) - W\right] \tag{6.15}$$

where

$$D_{11}(ka) = \frac{a}{2}\int \frac{dr}{r^2} h_{11}(r)\left[1 - J_0(kr) + 3J_2(kr)\right], \tag{6.16}$$

$$D_{12}(ka) = \frac{a}{2}\int \frac{dr\, r\, h_{12}(r)}{(r^2+d^2)^{3/2}}\left\{1 - J_0(kr) + 3J_2(kr) - \frac{3d^2}{r^2+d^2}\left[1 - J_0(kr) + J_2(kr)\right]\right\}, \tag{6.17}$$

$$W = a\int \frac{dr\, r h_{12}(r)}{(r^2+d^2)^{3/2}}\left(\frac{3}{2}\frac{r^2}{r^2+d^2} - 1\right) = \frac{a}{2}\int \frac{dr\, r h_{12}(r)}{(r^2+d^2)^{3/2}}\left(1 - 3\frac{d^2}{r^2+d^2}\right), \tag{6.18}$$

$J_\nu(x)$ are Bessel functions of the first kind. Details of the derivation of these formulas are reported in Appendix C.3. Notice that the C_{AB} elements have been divided into the mean-field RPA (the first terms) and correlational terms (second and third terms). Contrary to the case of a Binary Yukawa Mixture, setting $h_{AB}(r) = 0$ one does recover the RPA expressions. Furthermore, we verify that in the limit $d \to 0$ we recover the case of a 2D Coulomb liquid and for $d \to \infty$ the entire $C_{12}(k)$ term vanishes indicating two separated 2D layers.

The collective modes are calculated from the zeros of $|\omega^2\mathbf{I} - \mathbf{C}(k)| = 0$ which in units of ω_1^2 are

$$\omega_+^2(k\to 0) = \omega_1^2\frac{q^2(1+p^2)^2}{q^2+p^2}ka - \omega_1^2\frac{2q^2p^2}{p^2+q^2}\left[\frac{d}{a} + \frac{(1+p^2)^2(1-q^2)^2}{2W(p^2+q^2)^2} - U_+\right](ka)^2 \tag{6.19}$$

$$\omega_-^2(k\to 0) = \omega_1^2\left(p^2+q^2\right)W + \omega_1^2\frac{p^2(1-q^2)^2}{q^2+p^2}ka + \omega_1^2\frac{2q^2p^2}{p^2+q^2}\left[\frac{d}{a} + \frac{(1+p^2)^2(1-q^2)^2}{2W(p^2+q^2)^2} + U_-\right](ka)^2. \tag{6.20}$$

$$U_+ = \frac{U_{11} + 2p^2U_{12} + p^4U_{22}}{2p^2}, \quad U_- = \frac{U_{11} - 2q^2U_{12} + q^4U_{22}}{2q^2} \tag{6.21}$$

U_{AB} are the $k \to 0$ limits of the D_{AB} terms. The collective modes become: *(i)* an in-phase quasi-acoustic mode

$$\omega_+^2(k\to 0) = \omega_{vaa}^2 ka - \Pi(d, U_+)(ka)^2, \tag{6.22}$$

and *(ii)* an out-of-phase gap mode

$$\omega_{-}^{2}(k\to 0)=\left(\omega_{1}^{2}+\omega_{2}^{2}\right)W+\left(\omega_{p}^{2}-\omega_{\mathrm{v}aa}^{2}\right)ka+\mathit{\Pi}(d,U_{-})(ka)^{2}. \tag{6.23}$$

where

$$\mathit{\Pi}(d,U_{\pm})=\frac{2\omega_{1}^{2}\omega_{2}^{2}}{\omega_{1}^{2}+\omega_{2}^{2}}\left[\frac{d}{a}+\frac{1}{2W}\frac{\omega_{\mathrm{v}aa}^{2}\left(\omega_{p}^{2}-\omega_{\mathrm{v}aa}^{2}\right)}{\omega_{1}^{2}\omega_{2}^{2}}\mp U_{\pm}\right]. \tag{6.24}$$

The above equations have been derived by making use of the identity (Hansen, McDonald, and Vieillefosse, 1979)

$$\omega_{1}^{2}\frac{p^{2}(1-q^{2})^{2}}{q^{2}+p^{2}}=\omega_{p}^{2}-\omega_{\mathrm{v}aa}^{2}>0. \tag{6.25}$$

We point out that this spectrum resembles that of a binary Yukawa mixture. The similarity are: *(i)* the softening of the quasi-acoustic sound speed by the exchange $\omega_{p}^{2}\to\omega_{\mathrm{vaa}}^{2}$, *(ii)* the existence of an entirely correlational dependent gap frequency $\omega_{-}(k=0)$, already predicted in the symmetric bilayer.

The Silvestri–Kalman frequencies are

$$\omega_{*1}^{2}(k)=\omega_{1}^{2}\left(1+p^{2}e^{-kd}\right)ka+\omega_{1}^{2}\left[D_{11}+p^{2}D_{12}\right], \tag{6.26}$$

$$\omega_{*2}^{2}(k)=\omega_{1}^{2}\left(q^{2}p^{2}+q^{2}e^{-kd}\right)ka+\omega_{1}^{2}\left[q^{2}p^{2}D_{11}+q^{2}D_{12}\right], \tag{6.27}$$

which in the long wavelength limit become

$$\omega_{*1}^{2}(k\to 0)=\omega_{1}^{2}\left(2k-dk^{2}\right)+\omega_{1}^{2}\left[U_{11}+U_{12}\right](ka)^{2}, \tag{6.28}$$

$$\omega_{*2}^{2}(k\to 0)=\omega_{2}^{2}\left(2k-dk^{2}\right)+\omega_{2}^{2}\left[U_{11}+U_{12}\right](ka)^{2} \tag{6.29}$$

We again find similarities with a Binary Yukawa mixture with the SK frequencies surrounding the quasi-acoustic mode at small ka, leading to

$$\omega_{\text{im}}(k \to 0) = \omega_{+}(k \to 0). \tag{6.30}$$

In the symmetric case $q^2 = 1$, $\omega_{*1} = \omega_{*2} = \omega_{+}$ and thus, no anti-resonance can be observed.

6.3 Results and Discussion

In this section we show preliminary results on the ongoing work on asymmetric bilayers. Similarly, to the previous chapters the dispersion relations are portrayed via intensity maps of $L_{AB}(k,\omega)$. In addition, to $L_{11}(k,\omega)$ and $L_{22}(k,\omega)$ we define the total $L_{AB}(k,\omega)$ as

$$L_{+}(k,\omega) = L_{11}(k,\omega) + L_{22}(k,\omega) + 2L_{12}(k,\omega) \tag{6.31}$$

$$L_{-}(k,\omega) = L_{11}(k,\omega) + L_{22}(k,\omega) - 2L_{12}(k,\omega) \tag{6.32}$$

These two functions, albeit not real physical quantities, are used to highlight the dispersion of modes. The collective mode representative of an in-phase oscillations between particles of different layers will be visible in $L_{+}(k,\omega)$ since $L_{12}(k,\omega_{\text{in-phase}}) > 0$. On the other hand the collective mode representative of an out-of-phase oscillations, instead, would be visible in $L_{-}(k,\omega)$, $L_{12}(k,\omega_{\text{out-phase}}) < 0$. Furthermore, given that $L_{12}(k,\omega_{\text{out-phase}}) < 0$ a sharp minimum will be visible in $L_{+}(k,\omega_{\text{out-phase}})$ indicative of $L_{+}(k,\omega_{\text{out-phase}}) = 0$. Note that these functions are similar to $L_{NN}(k,\omega)$ and $L_{CC}(k,\omega)$ of a Binary Yukawa Mixture with equal concentrations.

We start by looking at dispersion plots in the weakly coupled regime. Figs. 6.1–6.2

shows intensity plots of $L_{AB}(k,\omega)$ for a sample set of system parameters. The yellow dashed lines indicate the RPA modes eq. (6.9)–(6.10) while the white dashed lines are the RPA modes without thermal effects (second term in the equations). The important thing to notice is that the plots are missing the acoustic mode inclusive of the thermal term, $\omega_-(k,\Gamma)$. This is due to the fact that the second term is greater than the d/a term, thus, leading to an imaginary frequency, $\omega_-^2(k,\Gamma) < 0$. The white dashed line, $\omega_-(k)$, is plotted instead. Although, the intensity plot of $L_-(k,\omega)$, bottom plot of Fig. 6.2, shows good agreement with the acoustic mode, we cannot make a conclusive argument on its existence. The blue region observed in this plot is likely due to the proportionality factor ω^2/k^2 between $L_{AB}(k,\omega)$ and $S_{AB}(k,\omega)$. This is further confirmed by looking at line plots of $S_\pm(k,\omega)$ shown in Fig. 6.3. In these plots the vertical dashed lines indicate, the quasi-acoustic mode, $\omega_+(k,\Gamma)$, in the top panel and acoustic mode $\omega_-(k)$ (without the Γ–term) in the bottom panel. The quasi-acoustic peak is evident while, although hints of a peak are visible, the claim of this being a peak is far–fetched because of the large $\Delta\omega$ between two consecutive data points. In other words the peak is given only by three data point stretched over a relatively large ω range. Further simulations are needed.

Moving to the strongly coupled regime, Figs. 6.4–6.11 show intensity plots of $L_{AB}(k,\omega)$ for two sets of system parameter. As usual the solid white lines represent the QLCA modes $\omega_\pm(k)$ while the dashed white lines the SK frequencies. As mentioned above, the quasi-acoustic mode corresponds to in–phase oscillations between particles of different layers, therefore it is visible in $L_+(k,\omega)$, while the gap mode, representative of out–of–phase oscillations, instead, is be visible in $L_-(k,\omega)$. In all these plots we notice the presence of a quasi–acoustic mode and its good agreement with QLCA predictions at low ka. As per the gap mode we notice some discrepancies in the case of $m = 0.5$ and $d = 0.1$, while excellent agreement for

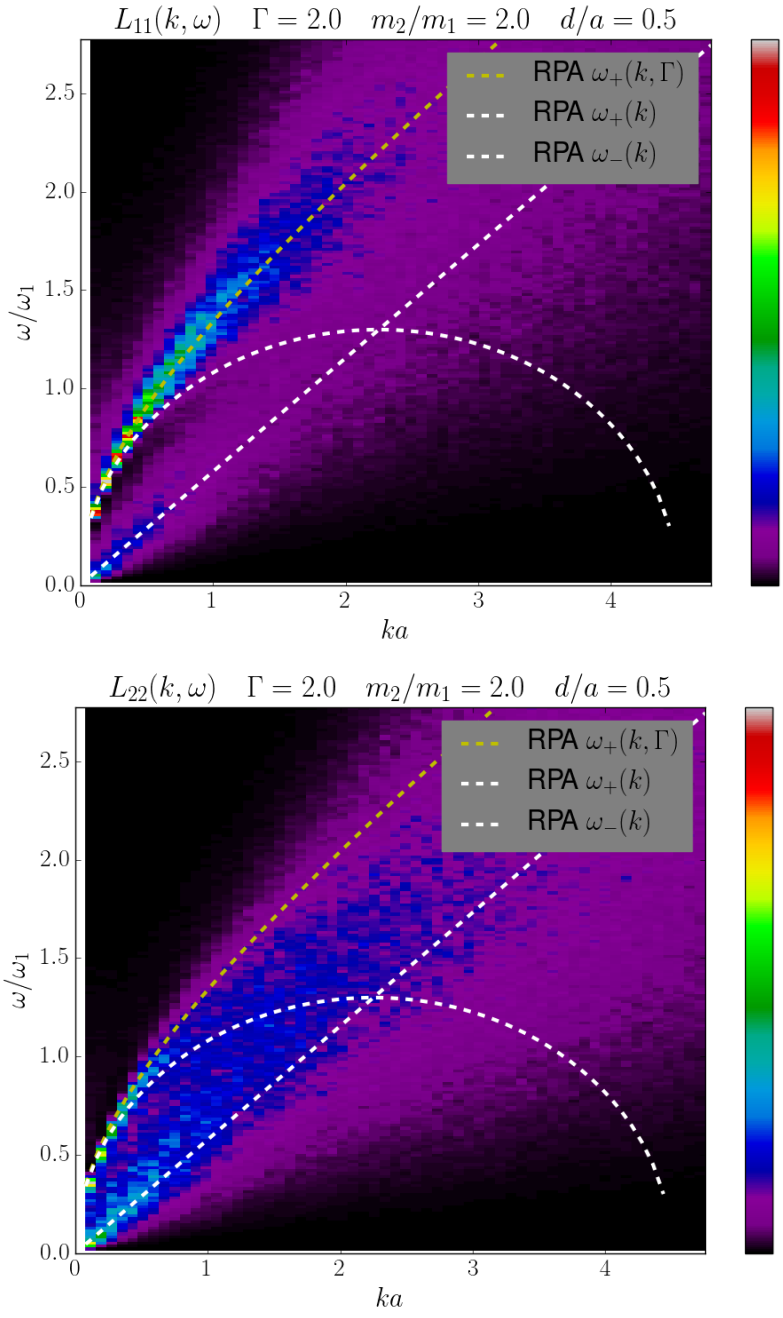

Figure 6.1: Intensity plots of $L_{11}(k,\omega)$ (top) and $L_{22}(k,\omega)$ (bottom). Yellow (White) dashed lines indicate the RPA modes with (without) the thermal term.

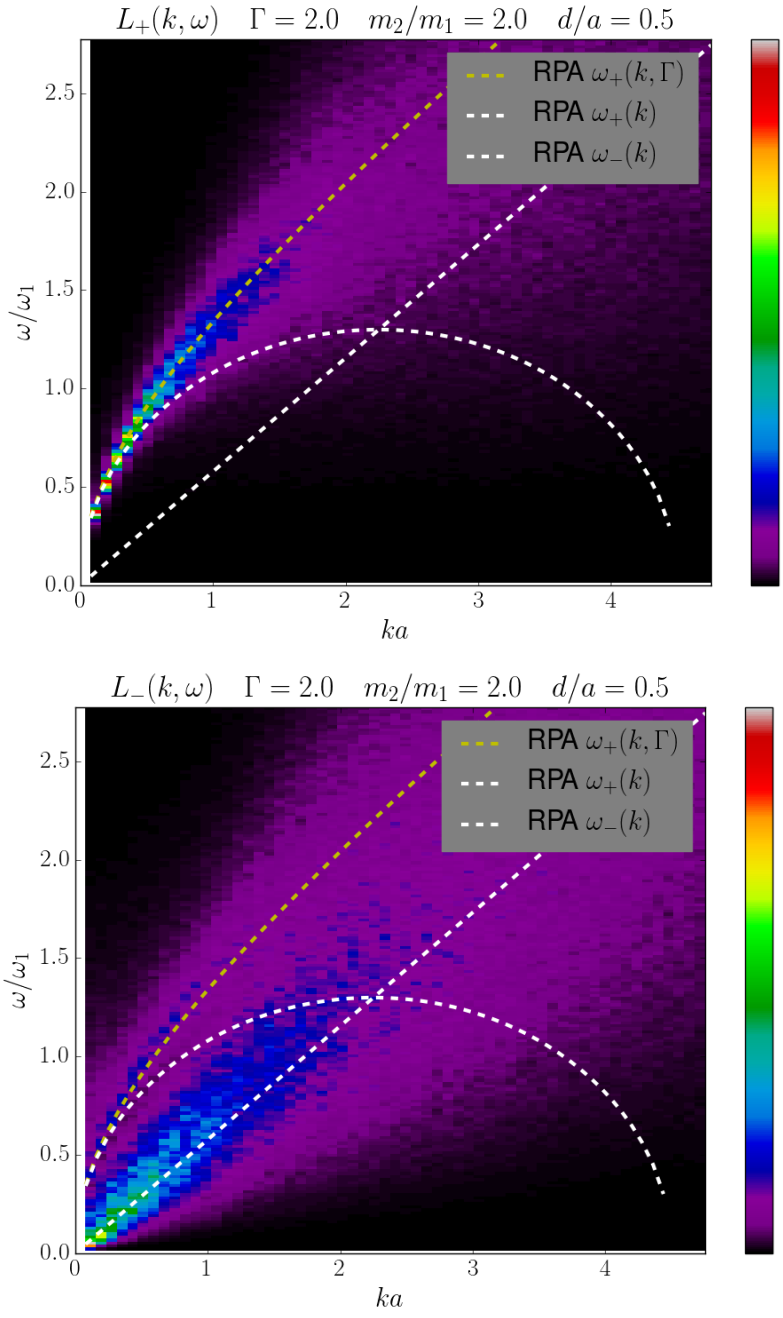

Figure 6.2: Intensity plots of $L_+(k,\omega)$ (top) and $L_-(k,\omega)$ (bottom). Yellow (White) dashed lines indicate the RPA modes with (without) the thermal term.

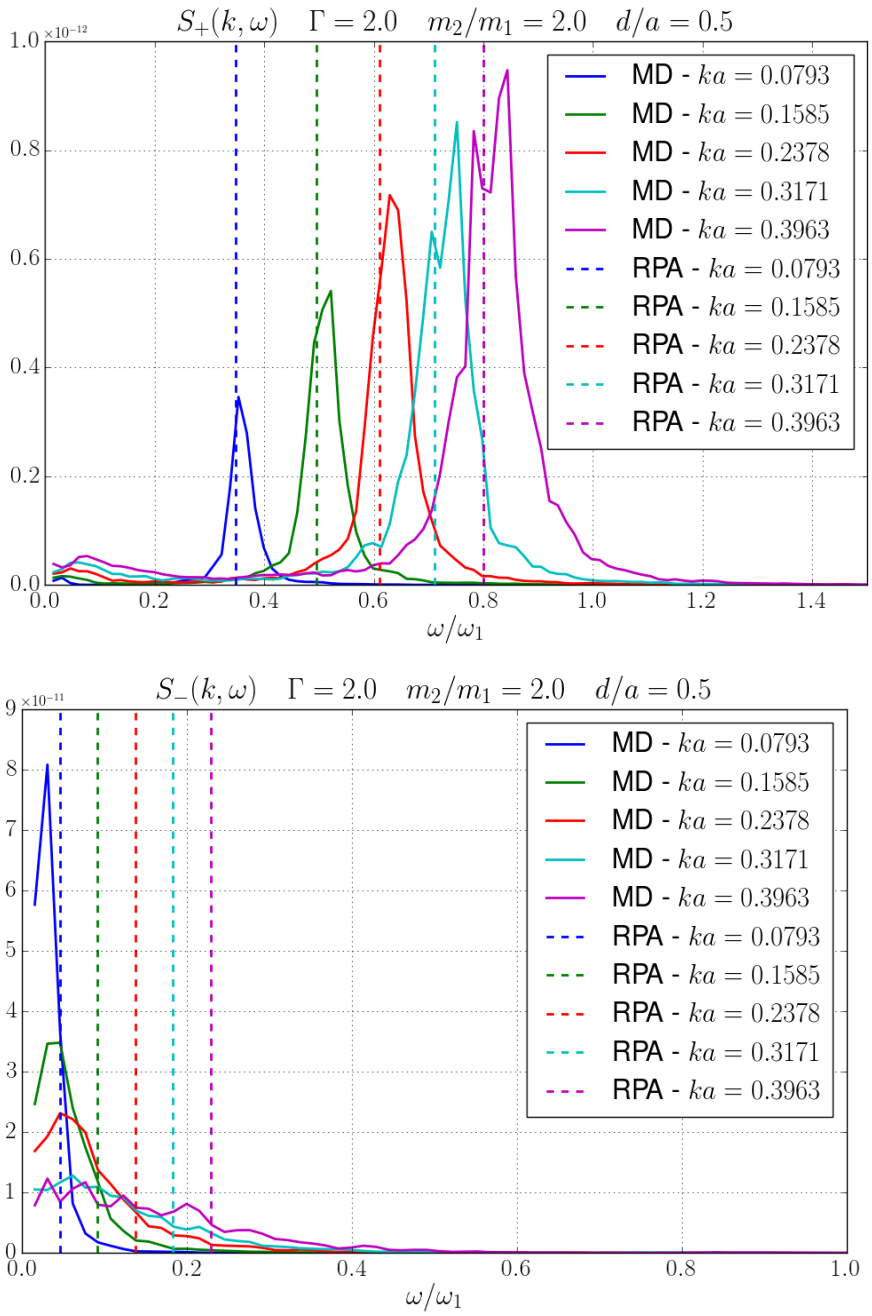

Figure 6.3: Line plot of $S_+(k,\omega)$ (top) and $S_-(k,\omega)$ (bottom) for the first four ka values. The vertical dashed lines indicate the location of the RPA quasi-acoustic mode (top) and acoustic mode (bottom).

$m = 5$ and $d = 0.7$. The higher gap frequency found in the former is a well known issue of the QLCA as it was found also in symmetric bilayers (Donkó, Hartmann, Kalman, and Golden, 2003; Donkó, Kalman, Hartmann, et al., 2003; Hartmann, Donkó, et al., 2009). Recent findings, however, have shown that at $d = 0.1$ the two layers are so close to each other that the system is effectively a single 2D layer. This does not preclude the existence of a gap since the system is still composed by two species and for this we refer the reader to compare Fig. 6.8 with Fig. 3.33 in Sec. 3.6 where we talk of 2D Binary Coulomb Mixtures.

The gap frequency is certainly evidence of strong coupling effects therefore we investigated its behaviour as a function of Γ. In Fig. 6.12 we show a plot of the gap frequency as a function of Γ. The value of the gap was obtained from MD simulations by fitting a Lorentzian profile to $S_-(k, \omega)$. The vertical error bars represent FWHM obtained from the fit. The interesting feature is the lack of a gap mode for $\Gamma < 10$, it appears at $\Gamma = 10$ and its value does not change over the entire regime. This is in agreement with the QLCA calculations, shown as solid lines in the plot. The integral W, eq. (6.18) does not vary appreciably as a function of Γ.

The behavior of the gap frequency as a function of the interlayer distance is shown in Fig. 6.13 for two different mass ratios. We notice that the largest disagreement between the QLCA and the MD at $d/a = 0.1$.

We conclude this section with a comparison between MD and collisional QLCA. In Fig. 6.14 we show plots of $S_{AB}(k, \omega)$ obtained from MD and Collisional QLCA calculations for various values of the nominal collisional frequency ν. We notice a similar behavior as that of Binary Yukawa Mixture. We find again the low frequency mode unaffected by the different ν values while the gap mode widens with increasing ν.

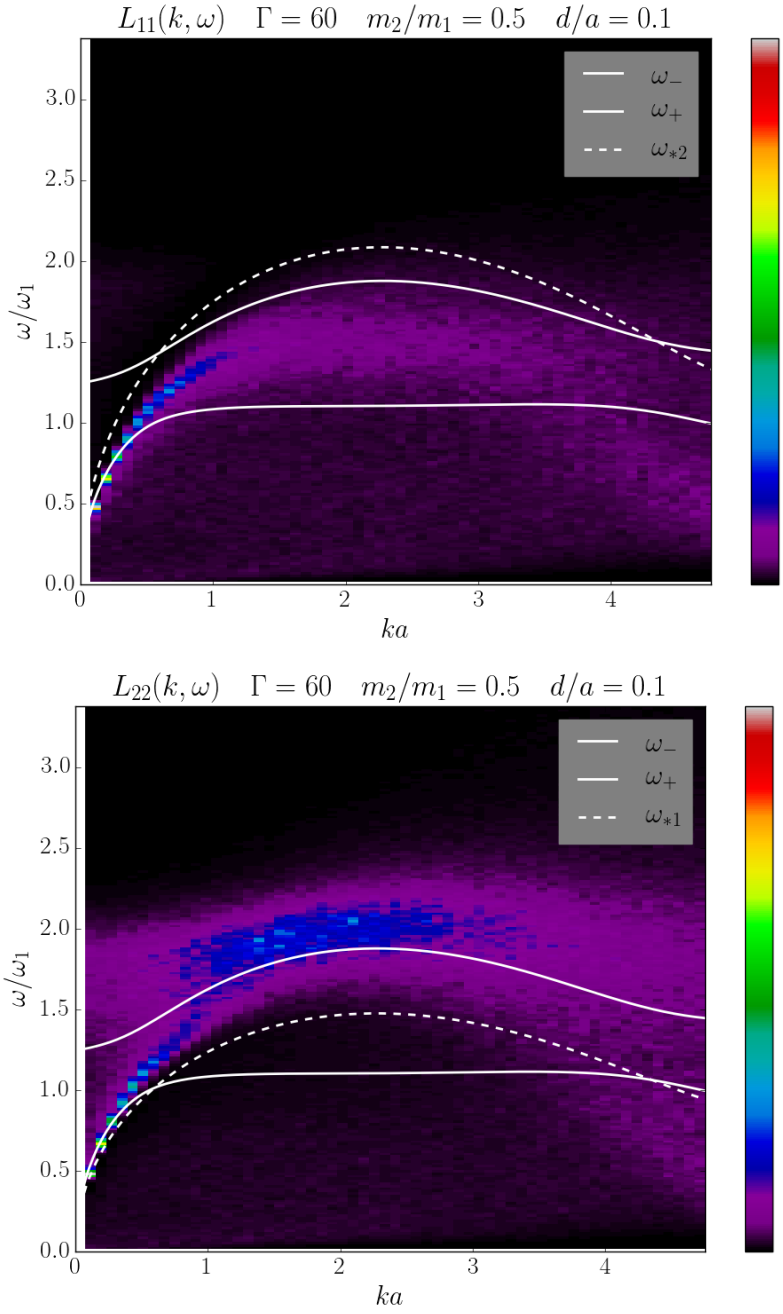

Figure 6.4: Intensity plots of $L_{11}(k,\omega)$ (top) and $L_{22}(k,\omega)$ (bottom). Solid black lines indicate the QLCA collective modes and dashed black lines the SK frequencies.

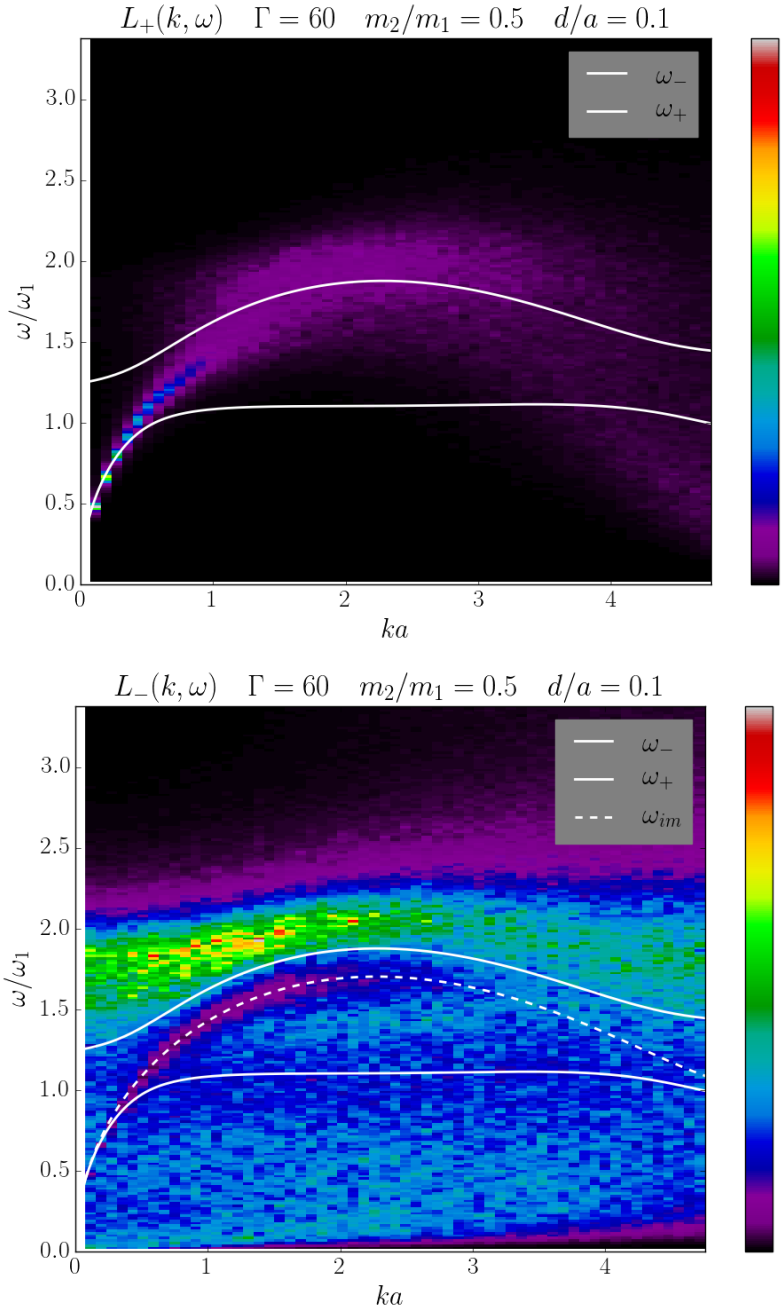

Figure 6.5: Intensity plots of $L_{11}(k,\omega)$ (top) and $L_{22}(k,\omega)$ (bottom). Solid black lines indicate the QLCA collective modes and dashed black lines the SK frequencies.

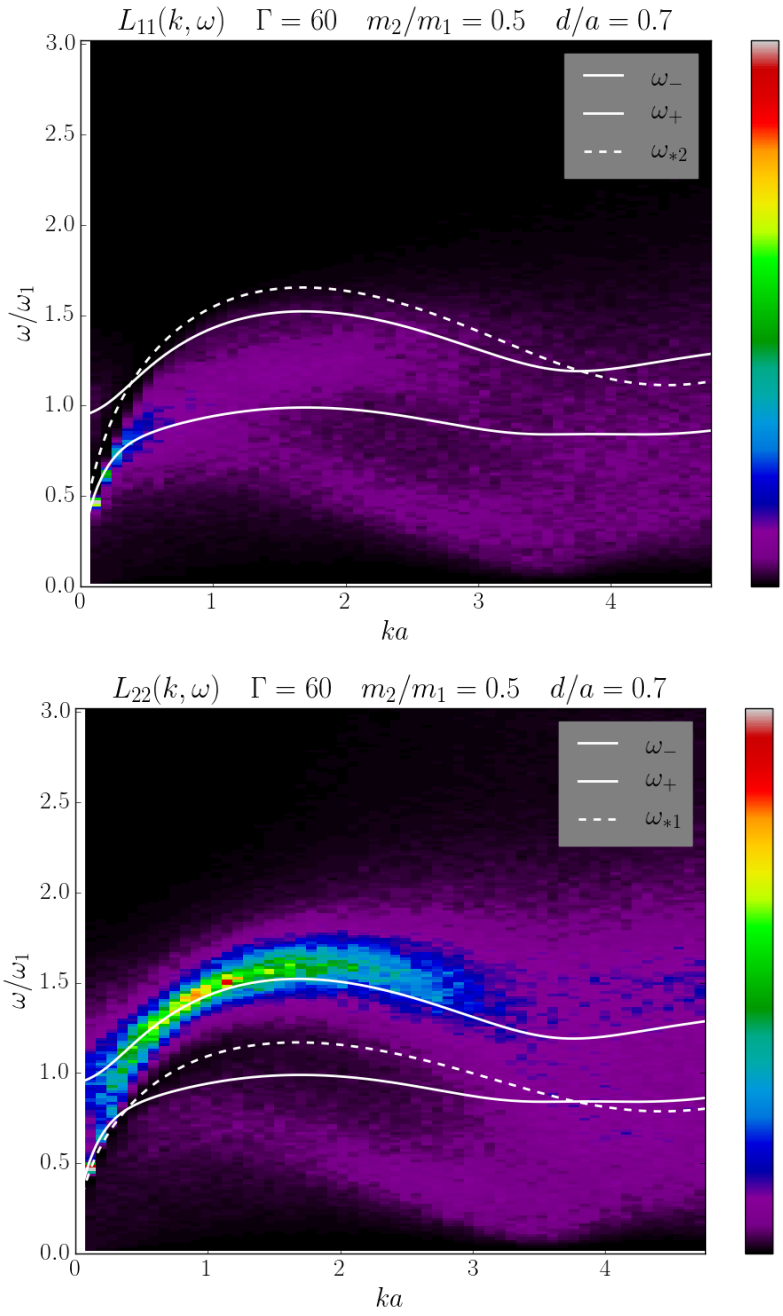

Figure 6.6: Intensity plots of $L_{11}(k,\omega)$ (top) and $L_{22}(k,\omega)$ (bottom). Solid black lines indicate the QLCA collective modes and dashed black lines the SK frequencies.

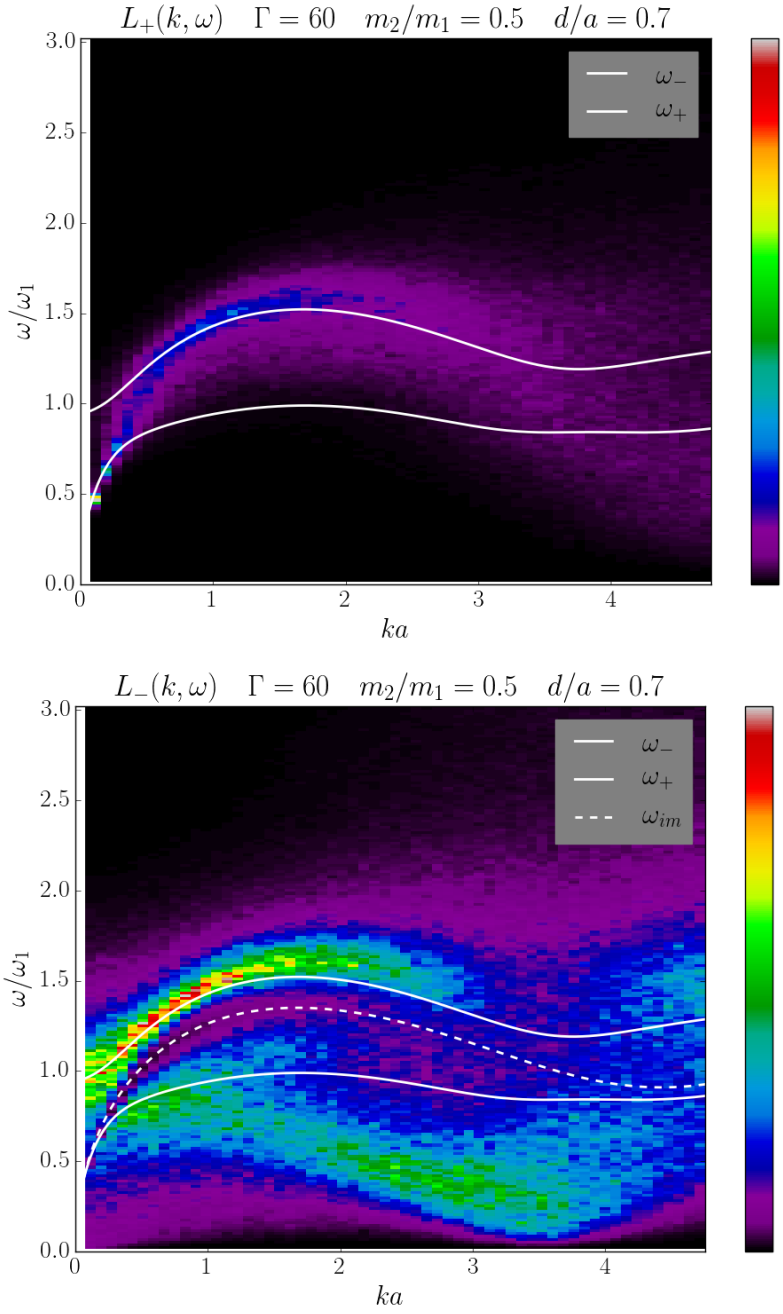

Figure 6.7: Intensity plots of $L_{11}(k,\omega)$ (top) and $L_{22}(k,\omega)$ (bottom). Solid black lines indicate the QLCA collective modes and dashed black lines the SK frequencies.

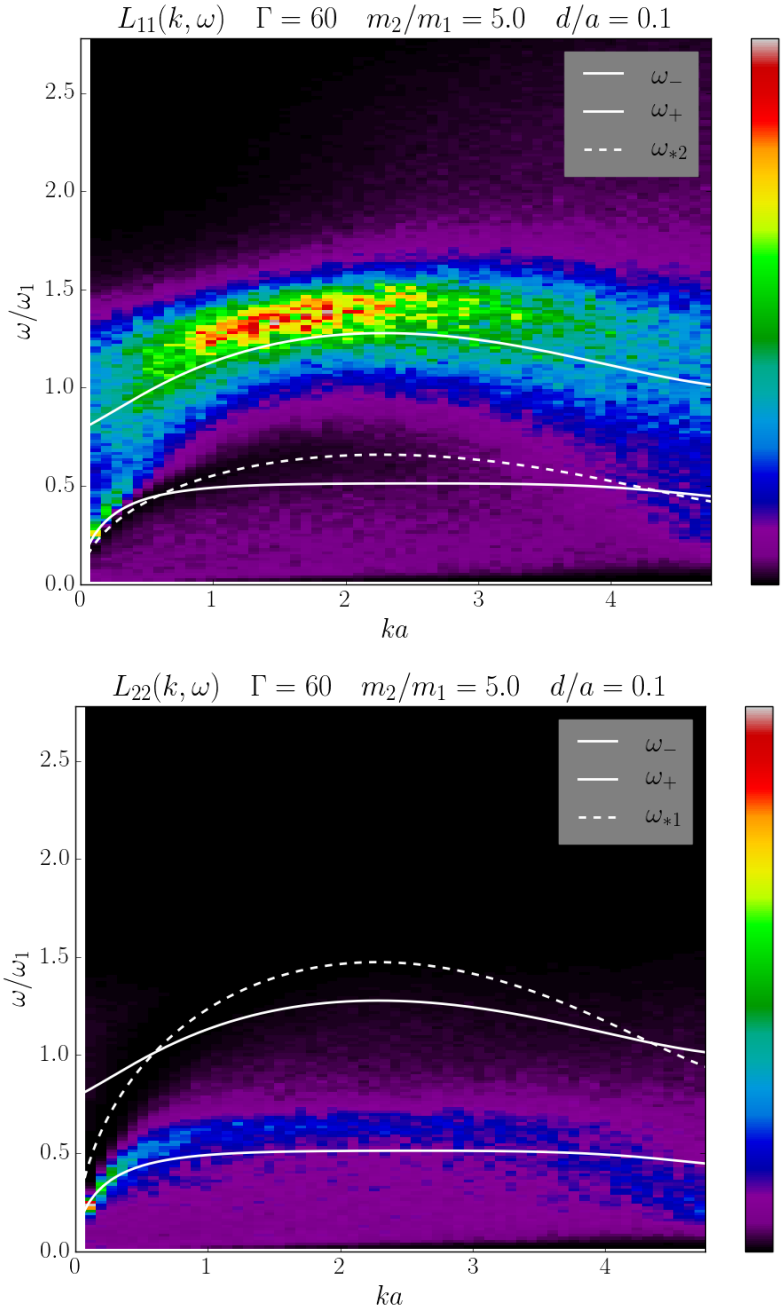

Figure 6.8: Intensity plots of $L_{11}(k,\omega)$ (top) and $L_{22}(k,\omega)$ (bottom). Solid black lines indicate the QLCA collective modes and dashed black lines the SK frequencies.

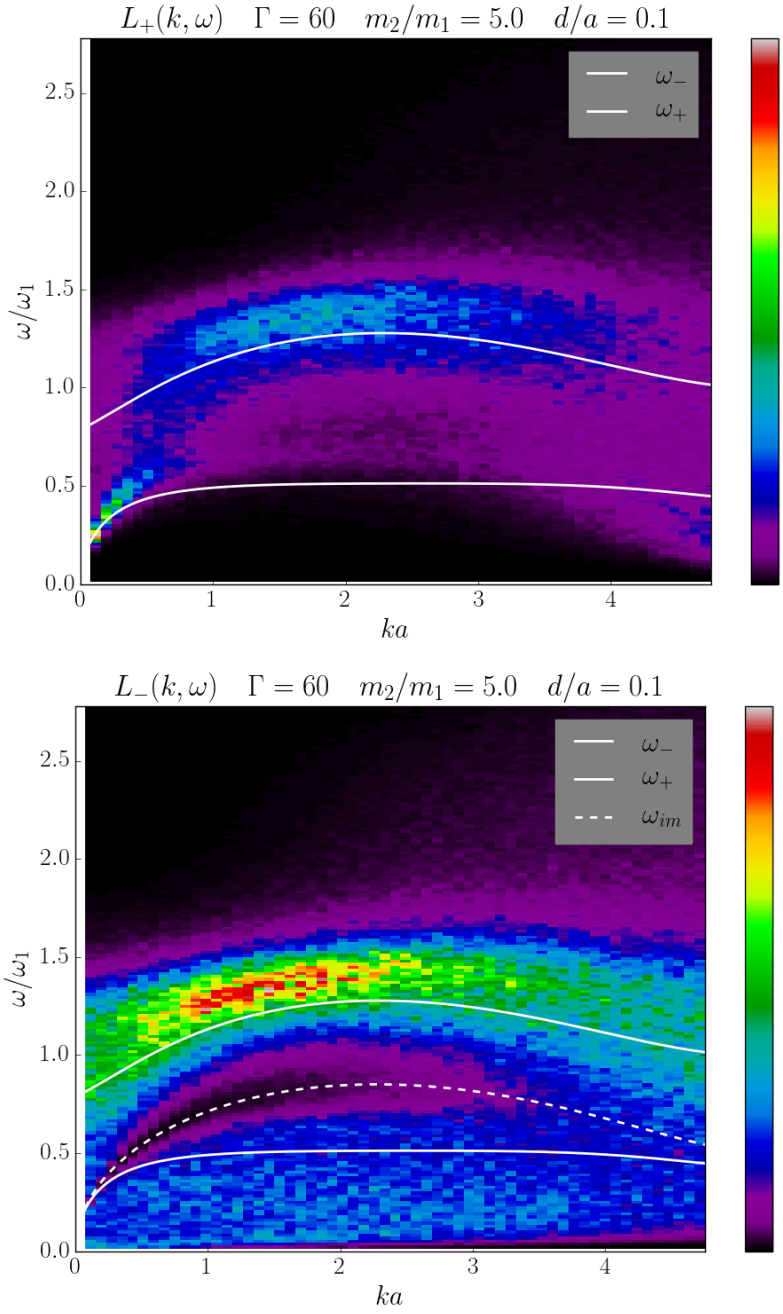

Figure 6.9: Intensity plots of $L_{11}(k,\omega)$ (top) and $L_{22}(k,\omega)$ (bottom). Solid black lines indicate the QLCA collective modes and dashed black lines the SK frequencies.

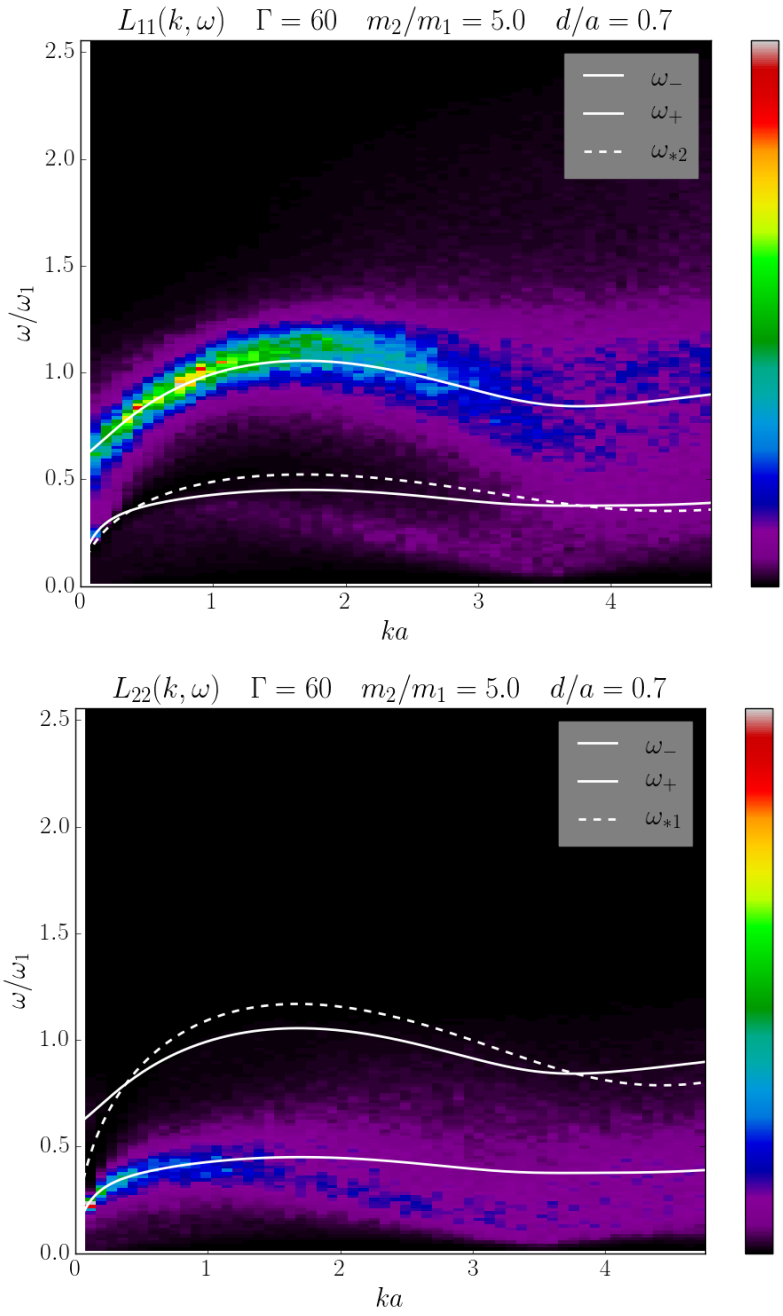

Figure 6.10: Intensity plots of $L_{11}(k,\omega)$ (top) and $L_{22}(k,\omega)$ (bottom). Solid black lines indicate the QLCA collective modes and dashed black lines the SK frequencies.

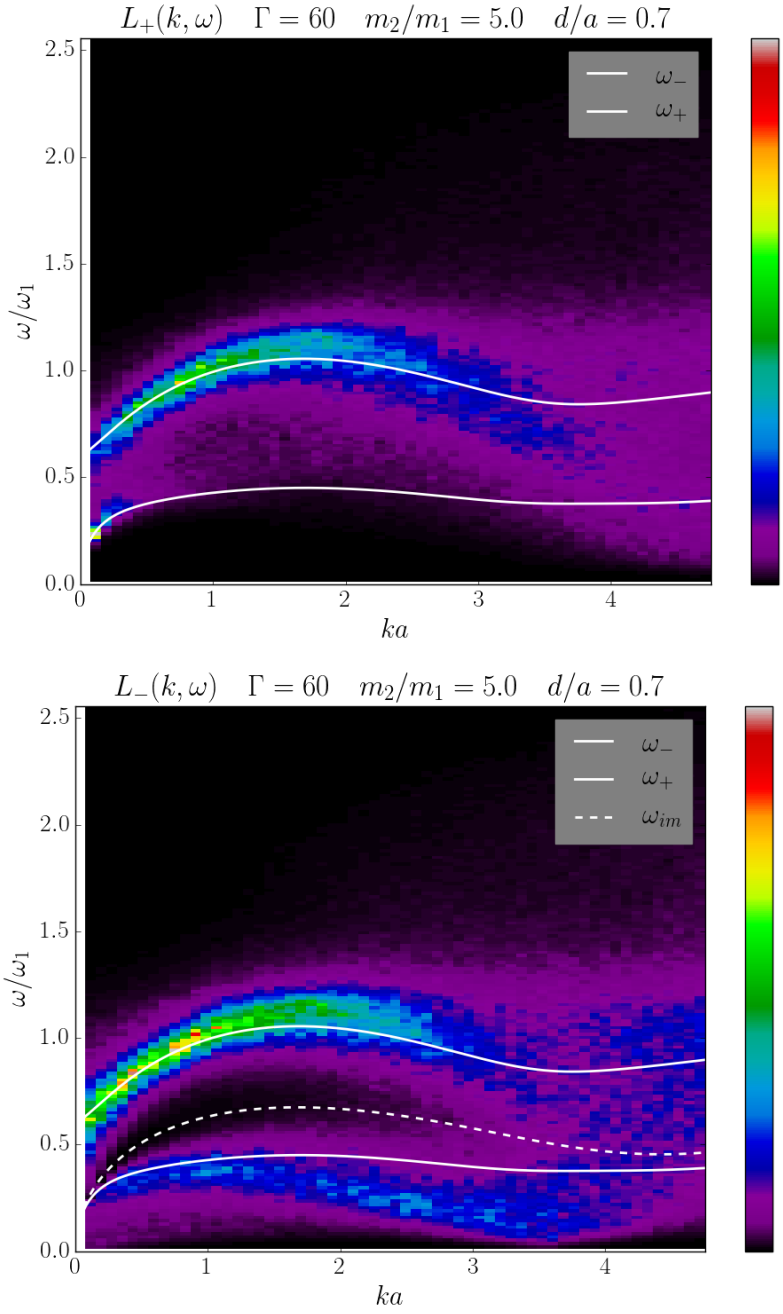

Figure 6.11: Intensity plots of $L_{11}(k,\omega)$ (top) and $L_{22}(k,\omega)$ (bottom). Solid black lines indicate the QLCA collective modes and dashed black lines the SK frequencies.

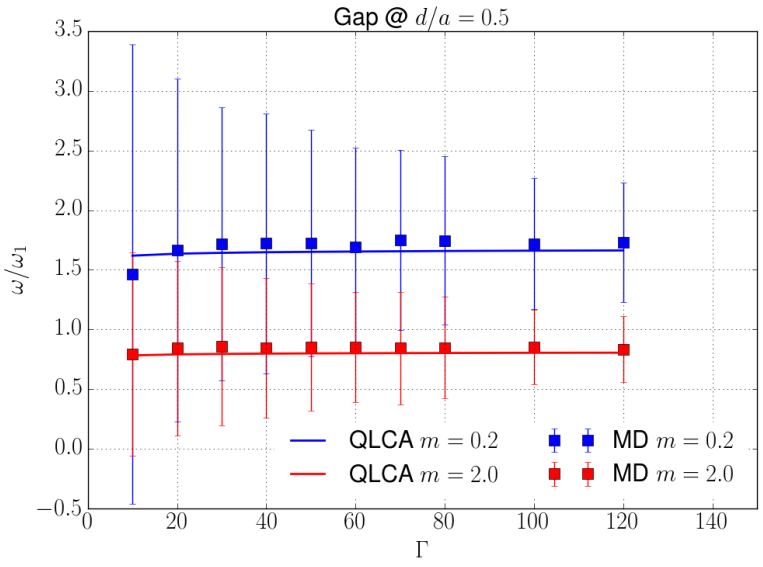

Figure 6.12: Plots of the gap frequency at $ka = 0$ as a function of Γ.

6.4 Conclusion

In this chapter we have presented preliminary results on the asymmetric bilayers. At small coupling we find that MD simulations showed good agreement with the RPA quasi–acoustic mode while no evidence of the presence of the acoustic mode is found. We mention, though, that the lowest Γ investigated in our simulations is still greater than 1, therefore, no conclusive argument can be made on the existence of the acoustic mode. Furthermore, finite Γ effects lead to imaginary frequencies according to eq. (6.10).

The collective mode spectrum in the strongly coupled regime is correctly predicted by the QLCA. The quasi-acoustic mode shows a reduced speed from that of the weak coupling regime primarily due to a different dominant frequency in the system; ω_p at weak coupling and ω_{vaa} at strong coupling. Furthermore, MD simulations show the existence of the QLCA predicted gap mode at high frequencies. This mode appears at $\Gamma = 10$ and its frequency does not vary with Γ. As in the case of symmetric bilayers the QLCA disagrees with MD in the location of the gap frequency at small d/a. In light of recent results we argue that for small

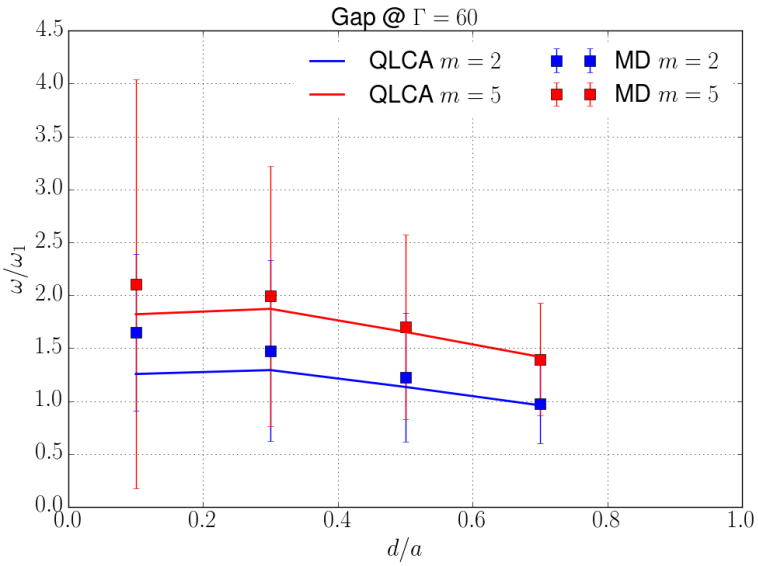

Figure 6.13: Plots of the gap frequency at $ka = 0$ as a function of d/a.

inter–layer separation, $d/a \sim 0.1$, the system is to be considered as a single 2D Coulomb liquid.

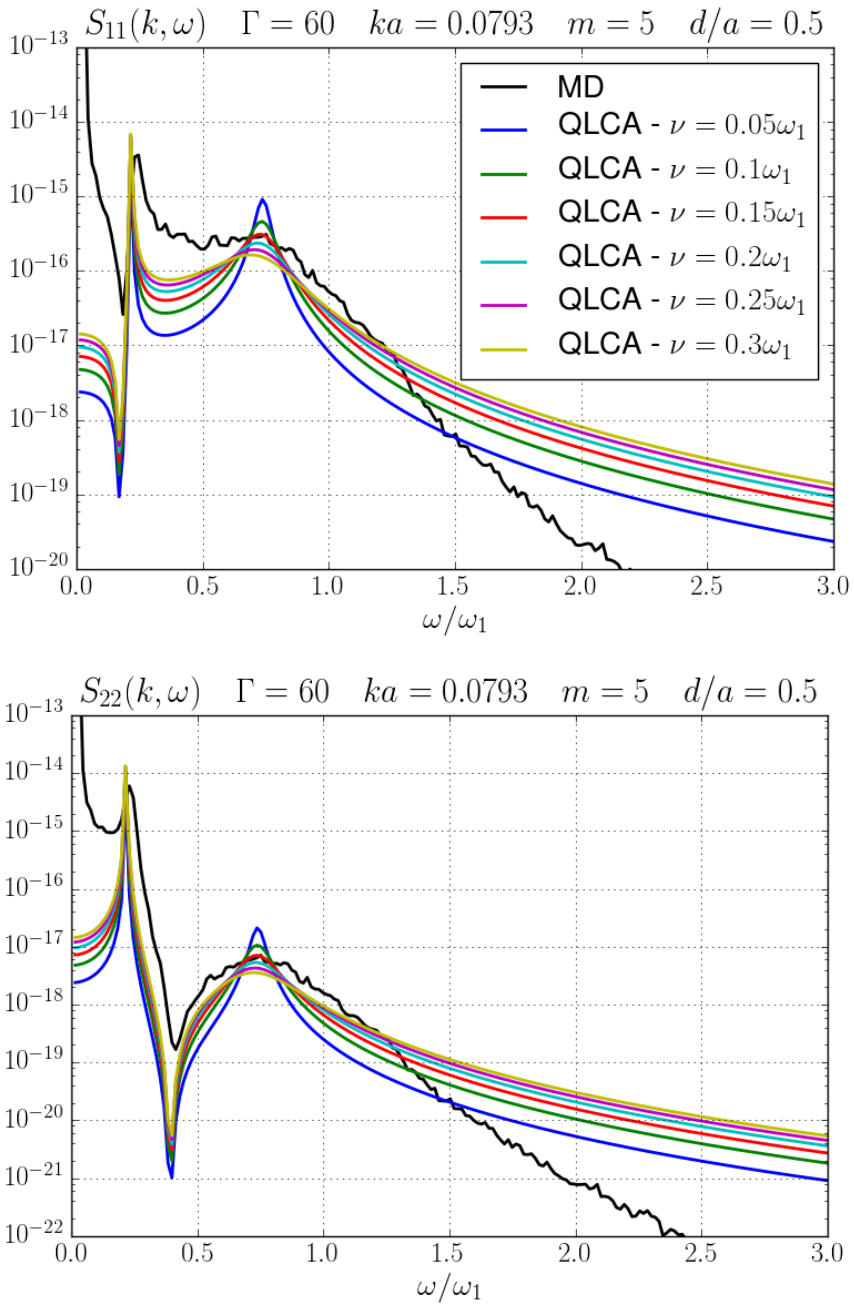

Figure 6.14: Line plot of $S_{11}(k,\omega)$ (top) and $S_{22}(k,\omega)$ (bottom) at the lowest ka value. The vertical dashed lines indicate the location of the SK frequencies.

CHAPTER VII

Conclusion and Future Directions

In this thesis I have investigated the dynamics of classical many–body systems composed of two species of positively charged particles. The investigation was carried both on the theoretical and computational level. The theoretical study involved the calculation of plasma response functions via the Collisional Quasi–Localized Charge Approximation, in the strongly coupled regime, and via the Random Phase Approximation, in the weakly coupled regime. Three systems were studied in particular: a binary mixtures of ions interacting via the long–range Coulomb potential, a binary mixture of charged particles interacting via the short–range Yukawa potential, and a mass–asymmetric electronic bilayer.

The main scope of this study was to discover and explain new physical behaviors of strongly coupled binary plasmas. The most important discovery are the Silvestri–Kalman frequencies which are new characteristic frequencies that appear as anti–resonances in the partial dynamic structure functions. They arise from a drag force proportional to the relative microscopic current between the two species. A simple toy model of driven coupled harmonic oscillators has been presented for a better understanding. The Silvestri–Kalman are novel inasmuch they represent the zeros of the imaginary part of partial response functions and not of their real part. Furthermore, they do not depend on strength of inter–species damping nor

on the strength of the coupling parameter, despite being contigent on their existence. As a matter of fact, in the weakly coupled regime, in which particles' correlations are entirely neglected, the zeros of the imaginary and real part coincide and are exactly the well known plasma frequencies of each species.

The introduction of damping in the QLC formalism not only allowed for the explicit calculation of partial dynamic structure function, but also led to a better description of the collective modes of binary plasma mixtures. As expected a relatively large damping dramatically changes the collective mode spectrum predicted by the QLCA. In the case of a binary Yukawa mixture with a large concentration of light particles we find that a single acoustic–like mode, instead, of a gap and an acoustic mode. The Collisional QLCA has showed that the large damping cancels the gap mode at small k leaving only the acoustic mode, while for larger k the opposite situation is true, with only the gap mode surviving.

As in the case of any research, the discovery of a new phenomenon opens up a lot more questions than it answers. Below I list some of the few topics that arised from this thesis and should be investigated

- **Electron–Ion Plasma:** Such a system is of particular importance, not only in statistical physics, but also in laboratory experiments. The recent advances in laser technologies allows for the investigation of a new state of matter: Warm Dense Matter (WDM). In these systems the high temperatures prohibit the use of well known condensed matter techniques, while the high number densities prevent the use of weak coupling plasma physics. The application of the YOCP model to WDM as already shown its limitation. So to what extent can we apply the Collisional QLCA formalism to the case of an electron–ion plasma? A first modification would be to substitute the Coulomb potential with a pseudo-potential with a repulsive core. This leads to different equations for response functions since many of the simplifications

found in BIM and YBM are no more valid.

- **Mixtures with more than two species:** Obviously there is no need to stop at mixtures with only two components. The QLCA is easily extendable to N species. However, questions arise concerning the existence of anti-resonances N-component mixtures. Preliminary work on three component mixtures continues to show the existence of anti-resonances in the equilibrium spectrum and suggests their existence for any number of species. The anti-resonances are created due to inter-species interaction; therefore, their existence in mixtures of N species is not surprising. However, an exact calculation and a general formula for their identification is still missing.

- **A derivation of the collisional damping from first principles:** Even though the anti-resonances do not depend on the strength of damping between particles, their existence is rooted in the presence of collisions between particles of different species. An interesting project would be to derive the anti–resonances from a kinetic description using the Velocity Average Approximation.

- **Electron Liquid:** A particular interesting project that emerged from this Thesis, is to apply the Collisional QLCA to a strongly coupled electron liquid. This system can be considered to be composed by two components with different spins, but equal charge and mass. Preliminary work shows that in addition to the well known high frequency plasmon mode, such a binary system, in the strongly coupled phase, supports a second plasmon mode at a low non–zero frequency. This excitation is maintained by the out–of–phase oscillations of the spin-up and spin-down densities of the electron liquid, but governed solely by the Coulomb interaction between the particles. The frequency square of this mode is proportional to the overlap ($r = 0$) (abso-

lute) value of the spin–up/spin–down correlation function, and thus slightly affected by the degree of polarization of the electron liquid. From its dispersion and its satisfaction of the 3rd frequency sum rule this mode is identified with the conjectured magnetic excitation in the homogeneous electron gas (Goodman and Sjölander, 1973). The Collisional QLCA, thus, give a first principle derivation of such a mode, and a compelling argument could be made once the quantum exchange–correlation effects are incorporated in the model.

- **Behavior of $S_{AB}(k,\omega)$ at $\omega = 0$ and $\omega \to \infty$:** An important topic not covered in this Thesis is conductivity of the plasma. In an OCP it can be shown that $S(k,\omega = 0)$ is directly proportional to the DC conductivity σ. In a BIM such relation involves $S_{ZZ}(k,\omega)$. The Collisional QLCA predicts a $S_{ZZ} \xrightarrow{\omega \to 0} 0$ while MD simulation show that it reaches a finite value. MD simulations show also a very fast power law decay, ω^{-p} $(p > 10)$ not predicted by any theoretical model. These shortcomings of the QLCA are somewhat expected since the Collisional QLCA represents $S_{AB}(k,\omega)$ as a product of Lorentzians, therefore, new ideas are needed. An interesting new tool that became available only recently is the reconstruction of the entire real and imaginary part of the dielectric and total response functions from MD data of $S_{AB}(k,\omega)$. This was done in the case of an OCP by using the FDT to convert $S(k,\omega)$ into $\mathrm{Im}\{\varepsilon^{-1}(k,\omega)\}$ and then applying Kramers–Kronig relations to obtain $\mathrm{Re}\{\varepsilon(k,\omega)\}$. An extension of this procedure to binary mixtures will help provide new insights for the study of $S_{AB}(k,\omega)$.

- **Computer Simulations:** Finally, one very important aspect is the data. The investigation of binary mixtures (especially in the case of Coulomb interaction) remain incomplete due to a lack of data. For example, the investi-

gation of the weak to strong coupling transition of binary Coulomb mixtures could be improved by more simulations. In fact, MD simulations spanning a large set of Γ values was available only for one set of asymmetry parameters. More asymmetry parameters are needed in order to reach a conclusive picture of the transition. Furthermore, the available high Γ MD simulations showed that a certain class of asymmetry parameters did not show the presence of the low frequency plasmon predicted by the QLCA. Is Γ large enough for the mixture to be considered strongly coupled? Does the mode really exists or is it masked by damping as in the case of a binary Yukawa mixture? All of the above and more are some of the questions that a larger set of MD simulations could help answer.

APPENDICES

APPENDIX A

Real and Imaginary part of Matrices

In this appendix we show the calculation of the real and imaginary part of the inverse of a matrix with complex elements. Take the matrix

$$\mathbf{Z} = \begin{pmatrix} z_{11} & z_{12} \\ z_{12} & z_{22} \end{pmatrix}, \tag{A.1}$$

with $z_{jk} \in \mathbb{C}$, $z_{jk} = a_{jk} + ib_{jk}$ and the inverse is

$$\chi = \mathbf{Z}^{-1} = \frac{1}{\det \mathbf{Z}} \begin{pmatrix} z_{22} & -z_{12} \\ -z_{21} & z_{11} \end{pmatrix}. \tag{A.2}$$

The determinant can be written in the following forms

$$\begin{aligned} \det \mathbf{Z} &= a_{11}a_{22} - a_{12}^2 - (b_{11}b_{22} - b_{12}b_{21}) + i\,(a_{11}b_{22} + b_{11}a_{22} - a_{12}b_{21} - a_{21}b_{12}) \\ &= \det \mathbf{A} - \det \mathbf{B} + i\left[b_{11}\left(a_{22} - \frac{b_{12}}{b_{11}}a_{21}\right) + b_{22}\left(a_{11} - \frac{b_{21}}{b_{22}}a_{12}\right)\right] \qquad \text{(A.3)} \\ &= \det \mathbf{A} - \det \mathbf{B} + i\sum_{m,n}(-1)^{m+n}a_{m,n}b_{mn} \qquad \text{(A.4)} \\ &= \mathrm{Re}\{\det \mathbf{Z}\} + i\,\mathrm{Im}\{\det \mathbf{Z}\}. \qquad \text{(A.5)} \end{aligned}$$

Considering the case $z_{12} = z_{21}$, the real part of the diagonal element, say χ_{22}, can be expressed in the following forms

$$\begin{aligned}
\mathrm{Re}\{\chi_{22}\} &= \frac{1}{|\det \mathbf{Z}|^2}\left[a_{11}\,\mathrm{Re}\{\det \mathbf{Z}\} + b_{11}\,\mathrm{Im}\{\det \mathbf{Z}\}\right] && \text{(A.6)}\\
&\propto a_{22}\left(a_{11}^2 + b_{11}^2\right) - a_{21}b_{11}b_{12} - a_{12}b_{11}b_{21} + a_{11}\left(b_{12}b_{21} - a_{12}a_{21}\right)\\
&= a_{11}\det \mathbf{A} + b_{11}^2\left(a_{22} - \frac{b_{12}}{b_{11}}a_{21}\right) + b_{12}b_{21}\left(a_{11} - \frac{b_{11}}{b_{12}}a_{12}\right) && \text{(A.7)}
\end{aligned}$$

and its imaginary part

$$\begin{aligned}
\mathrm{Im}\{\chi_{22}\} &= \frac{1}{|\det \mathbf{Z}|^2}\left[b_{11}\,\mathrm{Re}\{\det \mathbf{Z}\} - a_{11}\,\mathrm{Im}\{\det \mathbf{Z}\}\right] && \text{(A.8)}\\
&\propto b_{11}\left[a_{11}a_{22} - a_{12}^2 - (b_{11}b_{22} - b_{12}^2)\right]\\
&\quad -a_{11}\left[b_{11}\left(a_{22} - \frac{b_{12}}{b_{11}}a_{12}\right) + b_{22}\left(a_{11} - \frac{b_{12}}{b_{22}}a_{12}\right)\right]\\
&= -b_{22}\left(a_{11} - \frac{b_{12}}{b_{22}}a_{12}\right)^2 - \left(\frac{a_{12}^2}{b_{22}} + b_{11}\right)\det \mathbf{B} && \text{(A.9)}
\end{aligned}$$

The real part of the off diagonal elements is

$$\begin{aligned}
\mathrm{Re}\{\chi_{12}\} &= -\frac{1}{|\det \mathbf{Z}|^2}\left[a_{21}\,\mathrm{Re}\{\det \mathbf{Z}\} + b_{21}\,\mathrm{Im}\{\det \mathbf{Z}\}\right] && \text{(A.10)}\\
&\propto a_{12}\left(a_{21}^2 + b_{21}^2\right) + b_{11}\left(a_{21}b_{22} - a_{22}b_{21}\right)\\
&\quad -a_{11}\left(a_{21}a_{22} + b_{21}b_{22}\right)\\
&= -a_{21}\det \mathbf{A} - b_{11}b_{21}\left(a_{22} - \frac{b_{22}}{b_{21}}a_{21}\right)\\
&\quad -b_{12}b_{22}\left(a_{11} - \frac{b_{21}}{b_{22}}a_{12}\right) && \text{(A.11)}
\end{aligned}$$

and the imaginary part

$$\begin{aligned}
\mathrm{Im}\{\chi_{12}\} &= -\frac{1}{|\det \mathbf{Z}|^2}\left[b_{12}\,\mathrm{Re}\{\det \mathbf{Z}\} - a_{12}\,\mathrm{Im}\{\det \mathbf{Z}\}\right] && \text{(A.12)}\\
&\propto -b_{12}\left[a_{11}a_{22} - a_{12}^2 - (b_{11}b_{22} - b_{12}^2)\right]\\
&\quad +a_{12}\left[b_{11}\left(a_{22} - \frac{b_{12}}{b_{11}}a_{12}\right) + b_{22}\left(a_{11} - \frac{b_{12}}{b_{22}}a_{12}\right)\right]\\
&= -b_{12}\left[a_{12}^2 - a_{12}\left(\frac{b_{11}}{b_{12}}a_{22} + \frac{b_{22}}{b_{12}}a_{11}\right) + a_{11}a_{22} - \det \mathbf{B}\right]\\
&= -b_{12}\left[\left(a_{12} - \frac{b_{11}}{b_{12}}a_{22}\right)\left(a_{12} - \frac{b_{22}}{b_{12}}a_{11}\right) - \frac{b_{11}b_{22}}{b_{12}^2}a_{11}a_{22} + a_{11}a_{22} - \det \mathbf{B}\right]\\
&= -\frac{b_{11}b_{22}}{b_{12}}\left(a_{11} - \frac{b_{12}}{b_{22}}a_{12}\right)\left(a_{22} - \frac{b_{12}}{b_{11}}a_{12}\right) + \det \mathbf{B}\left(b_{12} + \frac{a_{11}a_{22}}{b_{12}}\right). && \text{(A.13)}
\end{aligned}$$

The above result can be extended to the case of a 3x3 matrix

$$\mathbf{Z} = \begin{pmatrix} z_{11} & z_{12} & z_{13} \\ z_{12} & z_{22} & z_{23} \\ z_{13} & z_{23} & z_{33} \end{pmatrix}. \qquad \text{(A.14)}$$

The determinant is expressed as

$$\begin{aligned}
\det \mathbf{Z} &= \mathrm{Re}\{\det \mathbf{Z}\} + i\,\mathrm{Im}\{\det \mathbf{Z}\} && \text{(A.15)}\\
&= \det \mathbf{A} - \sum_{m,n}(-1)^{m+n}a_{mn}b_{m,n}\\
&\quad +i\left[\sum_{m,n}(-1)^{m+n}a_{m,n}b_{mn} - \det \mathbf{B}\right] && \text{(A.16)}
\end{aligned}$$

where $c_{m,n}$ represent the absolute value of the (m,n)-minor.

APPENDIX B

QLCA Dynamical Matrix Derivation

In this appendix, we provide a detailed derivation of QLCA dynamical matrix $\mathbf{C}$. The starting point for the calculation is eq.(38) in (Golden and Kalman, 2000). The microscopic equation of motion for the i-th particle of species A:

$$-m\omega^2\xi^{\alpha}_{A,i}(\omega)+\sum_{B}\sum_{j}K^{\alpha\beta}_{AB,ij}\xi^{\beta}_{B,j}(\omega)=Z_A e\hat{E}^{\alpha}(\mathbf{x}_{A,i},\omega) \tag{B.1}$$

where $\xi^{\alpha}_{A,i}(t)$ is the perturbed amplitude of the particle's small excursion about its equilibrium site $\mathbf{x}_{A,i}$; $\hat{E}^{\alpha}(\mathbf{x}_{A,i},t)$ is the full external electric field perturbation originating from external vector and scalar potential sources. Indices i,j,l enumerate particles,

A, B, C designate different species, α, β (μ, ν in (Golden and Kalman, 2000)) are the 3D vector indices. We note that there is a slight change in the notation. In (Golden and Kalman, 2000) the indices A, B, C (α, β) are used as superscript (subscript) while in this supplemental material are used as subscript (superscript). The reason for the change is so this supplemental material is consistent with the notation used in this work. The interaction term $K^{\alpha\beta}_{AB,ij}$, see eq. (39) of (Golden and Kalman, 2000), takes account of the uniform neutralizing background contribution, n_b, and can be divided into its diagonal ($\delta_{AB}\delta_{ij}$) and off-diagonal ($1 - \delta_{AB}\delta_{ij}$) contributions, as follows

$$\begin{aligned} K^{\alpha\beta}_{AB,ij} &= (1 - \delta_{AB}\delta_{ij}) \frac{\partial^2}{\partial x^{\alpha}_{A,i} \partial x^{\beta}_{B,j}} \phi_{AB} \left(|\mathbf{x}_{A,i} - \mathbf{x}_{B,j}| \right) \\ &\quad -\delta_{AB}\delta_{ij} \left\{ \sum_l \sum_C (1 - \delta_{AC}\delta_{il}) \frac{\partial^2}{\partial x^{\alpha}_{A,i} \partial x^{\beta}_{C,l}} \phi_{AC} \left(|\mathbf{x}_{A,i} - \mathbf{x}_{C,l}| \right) + n_b \int d^3 y_b \frac{\partial^2}{\partial x^{\alpha}_{A,i} \partial y^{\beta}_{b}} \phi_{Ab} \left(|\mathbf{x}_{A,i} - \mathbf{y}_b| \right) \right\}. \end{aligned} \tag{B.2}$$

The diagonal terms originates from the displacement of a particle in a fixed environment of the other particles, while the off-diagonal from the fluctuating environment. In the first stage of the derivation, we introduce collective coordinates $\xi^{\alpha}_{A,\mathbf{q}}(\omega)$ via the Fourier representation

$$\xi^{\alpha}_{A,i}(\omega) = \frac{1}{\sqrt{N_A m_A}} \sum_{\mathbf{q}} e^{i\mathbf{q}\cdot\mathbf{x}_{A,i}} \xi^{\alpha}_{A,\mathbf{q}}(\omega) \tag{B.3}$$

This is formally similar to the coordinates used in the harmonic approximation of lattice vibrations. We then substitute eq. (B.3)

into eq. (B.1), multiply by $e^{-i\mathbf{k}\cdot\mathbf{x}_{A,i}}$, and sum over the i particles comprising plasma species A to obtain

$$-m_A\omega^2\sum_{\mathbf{p}} n_{A,\mathbf{k}-\mathbf{p}}\xi^{\alpha}_{A,\mathbf{p}}(\omega)+\sum_B\sqrt{\frac{m_AN_A}{m_BN_B}}\sum_{\mathbf{p}}\sum_{i,j}e^{-i\mathbf{k}\cdot\mathbf{x}_{A,i}}e^{i\mathbf{p}\cdot\mathbf{x}_{B,j}}K^{\alpha\beta}_{AB,ij}\xi^{\beta}_{B,\mathbf{p}}(\omega)=\frac{Z_Ae\sqrt{m_AN_A}}{V}\sum_{\mathbf{p}}n_{A,\mathbf{k}-\mathbf{p}}\hat{E}^{\alpha}(\mathbf{p},\omega). \tag{B.4}$$

where we recall

$$n_{A,\mathbf{k}-\mathbf{p}}=\sum_i e^{-i(\mathbf{k}-\mathbf{p})\cdot\mathbf{x}_{A,i}} \tag{B.5}$$

is the usual microscopic density in the present classical derivation. The second term in the first line of eq. (B.4) is calculated as follows

$$\begin{aligned}
\sum_{i,j}e^{-i\mathbf{k}\cdot\mathbf{x}_{A,i}}e^{i\mathbf{p}\cdot\mathbf{x}_{B,j}}K^{\alpha\beta}_{AB,ij} &= \frac{1}{V}\sum_{ij}\sum_{\mathbf{q}}q^{\alpha}q^{\beta}\Bigg\{(1-\delta_{AB}\delta_{ij})\,\phi_{AB}(q)e^{-i(\mathbf{k}-\mathbf{q})\cdot\mathbf{x}_{A,i}}e^{-i(\mathbf{q}-\mathbf{p})\cdot\mathbf{x}_{B,j}} \\
&\quad -\delta_{AB}\left[\delta_{ij}\sum_C\phi_{AC}(q)e^{-i(\mathbf{k}-\mathbf{q})\cdot\mathbf{x}_{A,i}}e^{i\mathbf{p}\cdot\mathbf{x}_{B,j}}n_{C,\mathbf{q}}-\phi_{AA}(q)n_{A,\mathbf{k}-\mathbf{p}}\right]\Bigg\} \\
&= \frac{1}{V}\sum_{\mathbf{q}}q^{\alpha}q^{\beta}\Bigg\{\phi_{AB}(q)\left[n_{A,\mathbf{k}-\mathbf{q}}n_{B,\mathbf{q}-\mathbf{p}}-\delta_{AB}n_{A,\mathbf{k}-\mathbf{p}}\right] \\
&\quad -\delta_{AB}\left[\sum_C\phi_{AC}(q)n_{A,\mathbf{k}-\mathbf{p}-\mathbf{q}}n_{C,\mathbf{q}}-\phi_{AA}(q)n_{A,\mathbf{k}-\mathbf{p}}\right]\Bigg\}
\end{aligned} \tag{B.6}$$

with $\phi_{AB}(q)=4\pi Z_AZ_Be^2/q^2$ being the 3D Fourier transform of the Coulomb interaction between species A and B. Further

development of eq. (B.6) gives

$$\sum_B \sum_{\mathbf{p}} \sum_{i,j} e^{-i\mathbf{k}\cdot\mathbf{x}_{A,i}} e^{i\mathbf{p}\cdot\mathbf{x}_{B,j}} K^{\alpha\beta}_{AB,ij} \xi^{\beta}_{B,\mathbf{p}}(\omega) = \sum_B \sum_{\mathbf{qp}} \frac{q^\alpha q^\beta}{V} \left\{ \phi_{AB}(q) n_{A,\mathbf{k-q}} n_{B,\mathbf{q-p}} - \delta_{AB} \sum_C \phi_{AC}(q) n_{A,\mathbf{k-p-q}} n_{C,\mathbf{q}} \right\} \xi^{\beta}_{B,\mathbf{p}}(\omega). \quad \text{(B.7)}$$

The principal assumption of the QLCA consists of replacing the $n_{A,\mathbf{k-q}} n_{B,\mathbf{q-p}}$ and $n_{A,\mathbf{k-p-q}} n_{C,\mathbf{q}}$ terms by their ensemble averages,

$$\langle n_{A,\mathbf{k-p}} \rangle = N_A \delta_{\mathbf{k-p}}, \quad \text{(B.8)}$$

$$\langle n_{A,\mathbf{k-q}} n_{B,\mathbf{q-p}} \rangle = \sqrt{N_A N_B} S_{AB} \left(|\mathbf{k}-\mathbf{q}| \right) \delta_{\mathbf{k-p}} + N_A N_B \delta_{\mathbf{k-q}} \delta_{\mathbf{q-p}}, \quad \text{(B.9)}$$

$$\langle n_{A,\mathbf{k-q-p}} n_{C,\mathbf{q}} \rangle = \sqrt{N_A N_C} S_{AC} \left(q \right) \delta_{\mathbf{k-p}} + N_A N_C \delta_{\mathbf{k-p}} \delta_{\mathbf{q}}. \quad \text{(B.10)}$$

Note that the product $\delta_{\mathbf{k-p-q}} \delta_{\mathbf{q}}$ is equivalent to $\delta_{\mathbf{k-p}} \delta_{\mathbf{q}}$. Carrying out these operations amounts to replacing eq. (B.4) by

$$- m_A \omega^2 \sum_{\mathbf{p}} \langle n_{A,\mathbf{k-p}} \rangle \, \xi^{\alpha}_{A,\mathbf{p}}(\omega) + \sum_B \sqrt{\frac{m_A N_A}{m_B N_B}} \sum_{\mathbf{p}} \langle \sum_{i,j} e^{-i\mathbf{k}\cdot\mathbf{x}_{A,i}} e^{i\mathbf{p}\cdot\mathbf{x}_{B,j}} K^{\alpha\beta}_{AB,ij} \rangle \, \xi^{\beta}_{B,\mathbf{p}}(\omega) = \frac{Z_A e \sqrt{m_A N_A}}{V} \sum_{\mathbf{p}} \langle n_{A,\mathbf{k-p}} \rangle \, \hat{E}^{\alpha}(\mathbf{p}, \omega) \quad \text{(B.11)}$$

where

$$\begin{aligned}
\sum_{\mathbf{p}} \langle \sum_{i,j} e^{-i\mathbf{k}\cdot\mathbf{x}_{A,i}} e^{i\mathbf{p}\cdot\mathbf{x}_{B,j}} K^{\alpha\beta}_{AB,ij} \rangle \, \xi^{\beta}_{B,\mathbf{p}}(\omega) &= \frac{1}{V} \sum_{\mathbf{qp}} q^{\alpha} q^{\beta} \left\{ \phi_{AB}(q) \, \langle n_{A,\mathbf{k}-\mathbf{q}} n_{B,\mathbf{q}-\mathbf{p}} \rangle - \delta_{AB} \sum_{C} \phi_{AC}(q) \, \langle n_{A,\mathbf{k}-\mathbf{p}-\mathbf{q}} n_{C,\mathbf{q}} \rangle \right\} \xi^{\beta}_{B,\mathbf{p}}(\omega) \\
&= \sum_{\mathbf{q}} q^{\alpha} q^{\beta} \left\{ \phi_{AB}(q) \, [\sqrt{n_A n_B} S_{AB} \left(|\mathbf{k}-\mathbf{q}| \right) + n_A N_B \delta_{\mathbf{k}-\mathbf{q}}] \right. \\
&\quad \left. - \delta_{AB} \sum_{C} \phi_{AC}(q) \, [\sqrt{n_A n_C} S_{AC} \left(q \right) + n_A N_C \delta_{\mathbf{q}}] \right\} \xi^{\beta}_{B,\mathbf{k}}(\omega) \qquad \text{(B.12)} \\
&= \sum_{\mathbf{q}} q^{\alpha} q^{\beta} \left\{ \phi_{AB}(q) \, [n_A n_B h_{AB} \left(|\mathbf{k}-\mathbf{q}| \right) + \sqrt{n_A n_B} \delta_{AB} + n_A N_B \delta_{\mathbf{k}-\mathbf{q}}] \right. \\
&\quad \left. - \delta_{AB} \sum_{C} \phi_{AC}(q) \, [n_A n_C h_{AC} \left(q \right) + \sqrt{n_A n_C} \delta_{AC} + n_A N_C \delta_{\mathbf{q}}] \right\} \xi^{\beta}_{B,\mathbf{k}}(\omega) \qquad \text{(B.13)} \\
&= \sum_{\mathbf{q}} q^{\alpha} q^{\beta} \left\{ \phi_{AB}(q) \, [n_A n_B h_{AB} \left(|\mathbf{k}-\mathbf{q}| \right) + n_A N_B \delta_{\mathbf{k}-\mathbf{q}}] \right. \\
&\quad \left. - \delta_{AB} \sum_{C} \phi_{AC}(q) \, [n_A n_C h_{AC} \left(q \right) + n_A N_C \delta_{\mathbf{q}}] \right\} \xi^{\beta}_{B,\mathbf{k}}(\omega) \qquad \text{(B.14)}
\end{aligned}$$

In going from eq. (B.12) to eq. (B.14), the static structure function have been replaced by the notationally more convenient equilibirum pair correlation functions via, *e.g.*

$$S_{AB} \left(|\mathbf{k}-\mathbf{q}| \right) = \delta_{AB} + \sqrt{n_A n_B} h_{AB} \left(|\mathbf{k}-\mathbf{q}| \right). \qquad \text{(B.15)}$$

Note that in the first line of eq. (B.13) the term proportional to $\sqrt{n_A n_B}\delta_{AB}$ is cancelled by the term in the second line proportional to $-\delta_{AB}\sum_C \sqrt{n_A n_C}\delta_{AC}$. The QLCA equation of motion readily follows from substituting eq. (B.14) into eq. (B.11):

$$\sum_B \left\{\omega^2 \delta_{AB}\delta^{\alpha\beta} - C_{AB}^{\alpha\beta}(\mathbf{k})\right\} \xi_{B,\mathbf{k}}^{\alpha}(\omega) = -\frac{Z_A e n_A}{\sqrt{m_A N_A}} \hat{E}^{\alpha}(\mathbf{k},\omega) \tag{B.16}$$

$$\begin{aligned}
C_{AB}^{\alpha\beta}(\mathbf{k}) &= \sqrt{\frac{n_A n_B}{m_A m_B}} \frac{1}{V} \sum_{\mathbf{q}} q^{\alpha} q^{\beta} \left\{ \phi_{AB}(q) \left[h_{AB}\left(|\mathbf{k}-\mathbf{q}|\right) + V\delta_{\mathbf{k}-\mathbf{q}} \right] - \delta_{AB} \sum_C \frac{n_C}{n_A} \phi_{AC}(q) h_{AC}(q) \right\} && \text{(B.17)} \\
&= \sqrt{\frac{n_A n_B}{m_A m_B}} k^{\alpha} k^{\beta} \phi_{AB}(k) + \sqrt{\frac{n_A n_B}{m_A m_B}} \frac{1}{V} \sum_{\mathbf{q}} q^{\alpha} q^{\beta} \left\{ \phi_{AB}(q) h_{AB}\left(|\mathbf{k}-\mathbf{q}|\right) - \delta_{AB} \sum_C \frac{n_C}{n_A} \phi_{AC}(q) h_{AC}(q) \right\} && \text{(B.18)} \\
&= \sqrt{\frac{n_A n_B}{m_A m_B}} k^{\alpha} k^{\beta} \phi_{AB}(k) + H_{AB}(\mathbf{k}) && \text{(B.19)}
\end{aligned}$$

This is the principal element of the QLCA from which all the dynamical quantity will be calculated. The next stage of the derivation consists in casting the dynamical matrix eq. (B.19) in a form where the equilibrium correlation functions are functions of r since MD simulation provide the quantity $g_{AB}(r)$.

r-conversion

The conversion proceeds as follows:

$$\begin{aligned}
\frac{1}{V}\sum_{\mathbf{q}} q^\alpha q^\beta \phi_{AB}(q) h_{AB}\left(|\mathbf{k}-\mathbf{q}|\right) &= \int d^3r \phi_{AB}(r) \frac{1}{V}\sum_{\mathbf{q}} q^\alpha q^\beta h_{AB}\left(|\mathbf{k}-\mathbf{q}|\right) e^{-i\mathbf{q}\cdot\mathbf{r}} \\
&= -\int d^3r \phi_{AB}(r) \frac{\partial^2}{\partial r^\alpha \partial r^\beta} \frac{1}{V}\sum_{\mathbf{q}} h_{AB}\left(|\mathbf{k}-\mathbf{q}|\right) e^{-i\mathbf{q}\cdot\mathbf{r}} \\
&= -\int d^3r \phi_{AB}(r) \frac{\partial^2}{\partial r^\alpha \partial r^\beta} \left[e^{-i\mathbf{k}\cdot\mathbf{r}} \frac{1}{V}\sum_{\mathbf{q}} h_{AB}\left(|\mathbf{k}-\mathbf{q}|\right) e^{i(\mathbf{k}-\mathbf{q})\cdot\mathbf{r}} \right] \\
&= -\int d^3r \phi_{AB}(r) \frac{\partial^2}{\partial r^\alpha \partial r^\beta} \left[e^{-i\mathbf{k}\cdot\mathbf{r}} h_{AB}(r) \right] \\
&= \int d^3r \left[\frac{\partial}{\partial r^\alpha} \phi_{AB}(r) \right] \frac{\partial}{\partial r^\beta} \left[e^{-i\mathbf{k}\cdot\mathbf{r}} h_{AB}(r) \right] \\
&= -\int d^3r \left[e^{-i\mathbf{k}\cdot\mathbf{r}} h_{AB}(r) \right] \frac{\partial^2}{\partial r^\alpha \partial r^\beta} \phi_{AB}(r) \qquad \text{(B.20)} \\
\frac{1}{V}\sum_{\mathbf{q}} q^\alpha q^\beta \phi_{AC}(q) h_{AC}\left(q\right) &= -\int d^3r h_{AC}(r) \frac{\partial^2}{\partial r^\alpha \partial r^\beta} \phi_{AC}(r). \qquad \text{(B.21)}
\end{aligned}$$

In the first and last line of eq. (B.20), replacement of $h\left(|\mathbf{k}-\mathbf{q}|\right)$ by $V\delta_{\mathbf{k}-\mathbf{q}}$ and $h_{AB}(r)$ by unity provides

$$\int d^3r e^{-i\mathbf{k}\cdot\mathbf{r}} \frac{\partial^2}{\partial r^\alpha \partial r^\beta} \phi_{AB}(r) = -k^\alpha k^\beta \phi_{AB}(k). \qquad \text{(B.22)}$$

The final formula is then

$$\begin{aligned} C_{AB}^{\alpha\beta}(\mathbf{k}) &= -\sqrt{\frac{n_A n_B}{m_A m_B}} \int d^3r \left\{ \left[1 + h_{AB}(r)\right] e^{-i\mathbf{k}\cdot\mathbf{r}} \frac{\partial^2}{\partial r^\alpha \partial r^\beta} \phi_{AB}(r) - \delta_{AB} \sum_C \frac{n_C}{n_A} \left[1 + h_{AC}(r)\right] \frac{\partial^2}{\partial r^\alpha \partial r^\beta} \phi_{AC}(r) \right\} + \delta_{AB}\delta^{\alpha\beta} \sum_C \frac{\Omega_{AC}^2}{3} \\ &= -\int \frac{d^3r}{4\pi} \left\{ \omega_{AB}^2 \psi^{\alpha\beta}(r) \left[1 + h_{AB}(r)\right] e^{-i\mathbf{k}\cdot\mathbf{r}} + \delta_{AB} \sum_C \Omega_{AC}^2 \psi^{\alpha\beta}(r) \left[1 + h_{AC}(r)\right] \right\} + \delta_{AB}\delta^{\alpha\beta} \sum_C \frac{1}{3} \Omega_{AC}^2, \end{aligned} \tag{B.23}$$

where

$$\psi^{\alpha\beta}(r) = \frac{\partial^2}{\partial r^\alpha \partial r^\beta} \frac{1}{r} = \frac{1}{r^3} \left(3 \frac{r^\alpha r^\beta}{r^2} - \delta^{\mu\nu} \right) - \frac{4\pi}{3} \delta^{\alpha\beta} \delta(\mathbf{r}), \tag{B.24}$$

$$\omega_{AB}^2 = \frac{4\pi e^2 Z_A Z_B \sqrt{n_A n_B}}{m}, \quad \Omega_{AC}^2 = \frac{4\pi e^2 Z_A Z_C n_C}{m_A}. \tag{B.25}$$

The last $\delta(\mathbf{r})$ term in eq. (B.24) comes from the Poisson equation $\nabla^2 \frac{1}{r} = -4\pi\delta(\mathbf{r})$. Further explanation on the way eq. (B.23) is obtained is needed since the passages are not obvious. The first term $\psi^{\alpha\beta} \times e^{-i\mathbf{k}\cdot\mathbf{r}}$ comes from the mean field term $-k^\alpha k^\beta \phi(k)$. The addition of "1" in the $[1 + h_{AC}(r)]$ term gives, in the longitudinal elements,

$$\frac{\Omega_{AC}^2}{4\pi} \int d^3r \left[-\frac{4\pi}{3} \delta(\mathbf{r}) \right] = -\frac{\Omega_{AC}^2}{3}. \tag{B.26}$$

The latter is cancelled by adding the equal opposite value, hence the last constant term in eq. (B.23).

APPENDIX C

QLCA Dynamical Matrix Elements Calculation

In this appendix we show detailed derivation of the QLCA longitudinal dynamical matrix elements for all the systems considered in the thesis.

C.1 3D Coulomb

In this appendix we give details on the calculation of the elements of the dynamical matrix. The starting point is

$$C_{AB}^{\mu\nu}(\mathbf{k}) = -\frac{\omega_{AB}^2}{4\pi}\int d^3r\psi^{\mu\nu}(\mathbf{r})e^{-i\mathbf{k}\cdot\mathbf{r}}\left[1+h_{AB}(r)\right] + \delta_{AB}\sum_C \frac{\Omega_{AC}^2}{4\pi}\int d^3r\psi^{\mu\nu}(\mathbf{r})\left[1+h_{AC}(r)\right] + \delta_{AB}\delta^{\mu\nu}\sum_C \frac{1}{3}\Omega_{AC}^2 \tag{C.1}$$

where $\psi^{\mu\nu}(r)$ is the harmonic approximation of the Coulomb potential given by eq. (B.24) and the frequencies ω_{AB} and Ω_{AB} are given by eq. (B.25). The first two lines of (C.1) can be simplified as follows

$$\begin{aligned}
& -\int \frac{d^3r}{4\pi}\left\{\omega_{AB}^2\left[\frac{1}{r^3}\left(3\frac{r^\mu r^\nu}{r^2}-\delta^{\mu\nu}\right)-\frac{4\pi}{3}\delta^{\mu\nu}\delta(\mathbf{r})\right]e^{-i\mathbf{k}\cdot\mathbf{r}}\left[1+h_{AB}(r)\right]-\delta_{AB}\sum_{C\neq A}\Omega_{AC}^2\left[\frac{1}{r^3}\left(3\frac{r^\mu r^\nu}{r^2}-\delta^{\mu\nu}\right)-\frac{4\pi}{3}\delta^{\mu\nu}\delta(\mathbf{r})\right]\left[1+h_{AC}(r)\right]\right\} \\
= & -\frac{\omega_{AB}^2}{4\pi}\int\frac{d^3r}{r^3}\left(3\frac{r^\mu r^\nu}{r^2}-\delta^{\mu\nu}\right)\left[1+h_{AB}(r)\right]e^{-i\mathbf{k}\cdot\mathbf{r}}+\delta_{AB}\sum_{C=A}\frac{\Omega_{AC}^2}{4\pi}\int\frac{d^3r}{r^3}\left(3\frac{r^\mu r^\nu}{r^2}-\delta^{\mu\nu}\right)\left[1+h_{AC}(r)\right] \\
= & -\frac{\omega_{AB}^2}{4\pi}\int\frac{d^3r}{r^3}\left(3\frac{r^\mu r^\nu}{r^2}-\delta^{\mu\nu}\right)\left[1+h_{AB}(r)\right]e^{-i\mathbf{k}\cdot\mathbf{r}}. \qquad \text{(C.2)}
\end{aligned}$$

In the first step we made the fact that particles do not overlap, $h_{AB}(r\to 0)=-1$ while in the second, the $\mathbf{k}$-independent integrals vanish due to isotropy (see (D.2)). The dynamical matrix elements, thus, become

$$C_{AB}^{\mu\nu}(\mathbf{k})=-\frac{\omega_{AB}^2}{4\pi}\int\frac{d^3r}{r^3}\left\{\left(3\frac{r^\mu r^\nu}{r^2}-\delta^{\mu\nu}\right)\left[1+h_{AB}(r)\right]e^{-i\mathbf{k}\cdot\mathbf{r}}\right\}+\delta_{AB}\delta^{\mu\nu}\sum_{C=A}\frac{1}{3}\Omega_{AC}^2, \qquad \text{(C.3)}$$

whose longitudinal components are

$$\begin{aligned}
C_{AB}^{L}(k) &= -\frac{\omega_{AB}^2}{4\pi}\int\frac{dr}{r}g_{AB}(r)\int_{-1}^{1}d\mu\left(3\mu^2-1\right)e^{-ikr\mu}\int_0^{2\pi}d\phi+\delta_{AB}\sum_{C=A}\frac{\Omega_{AC}^2}{3} \qquad \text{(C.4)} \\
&= -\frac{\omega_{AB}^2}{2}\int\frac{dr}{r}\left[1+h_{AB}(r)\right]\left[4\frac{\sin(kr)}{kr}+12\frac{\cos(kr)}{(kr)^2}-12\frac{\sin(kr)}{(kr)^3}\right]+\delta_{AB}\sum_{C=A}\frac{\Omega_{AC}^2}{3}. \qquad \text{(C.5)}
\end{aligned}$$

Further integrating the h_{AB}-independent parts we obtain

$$C^L_{AB}(k) = 2\omega^2_{AB}\left[\frac{1}{3} - D_{AB}(k)\right] + \delta_{AB}\sum_C \frac{\Omega^2_{AC}}{3} \tag{C.6}$$

$$D_{AB}(k) = \int \frac{dr}{r} h_{AB}(r)\left[\frac{\sin(kr)}{kr} + 3\frac{\cos(kr)}{(kr)^2} - 3\frac{\sin(kr)}{(kr)^3}\right]. \tag{C.7}$$

Writing out explicitly each matrix element in terms of the asymmetry parameter p, q we have

$$C^L_{11}(k) = \omega^2_1\left[1 + \frac{1}{3}p^2 - 2D_{11}(k)\right] \tag{C.8a}$$

$$C^L_{12}(k) = \omega^2_1\left[\frac{2}{3}pq - 2pqD_{12}(k)\right] \tag{C.8b}$$

$$C^L_{22}(k) = \omega^2_1\left[q^2p^2 + \frac{1}{3}q^2 - 2q^2p^2D_{22}(k)\right] \tag{C.8c}$$

Long wavelength limit

In the limit $k \to 0$ the $D_{AB}(k)$ integrals become

$$D_{AB}(k) \approx -\frac{k^2}{15}\int dr r h_{AB}(r) = -\frac{k^2}{15} I_{AB} \tag{C.9}$$

which gives

$$C_{11}^L(k\to 0) = \omega_1^2\left[1+\frac{1}{3}p^2+\frac{2}{15}k^2 I_{11}\right] \tag{C.10a}$$

$$C_{12}^L(k\to 0) = \omega_1^2\left[\frac{2}{3}pq+\frac{2}{15}pqk^2 I_{12}\right] \tag{C.10b}$$

$$C_{22}^L(k\to 0) = \omega_1^2\left[p^2q^2+\frac{1}{3}q^2+\frac{2}{15}p^2q^2k^2 I_{22}\right] \tag{C.10c}$$

Short wavelength limit

In the $k\to\infty$ limit we make the substitution $r\to x/k$ and recall that $h_{AB}(0)=-1$

$$\lim_{k\to\infty} D_{AB}(k) = \lim_{k\to\infty}\int \frac{dx}{x} h_{AB}(x/k)\left[4\frac{\sin x}{x}+12\frac{\cos x}{x^2}-12\frac{\sin x}{x^3}\right] = \frac{1}{3} \tag{C.11}$$

$$C_{11}^L(k\to\infty) = \omega_1^2\frac{1+p^2}{3} = \frac{\omega_1^2+\Omega_{12}^2}{3} \tag{C.12a}$$

$$C_{12}^L(k\to\infty) = 0 \tag{C.12b}$$

$$C_{22}^L(k\to\infty) = \omega_1^2\frac{q^2p^2+q^2}{3} = \frac{\omega_2^2+\Omega_{21}^2}{3} \tag{C.12c}$$

which are the Einstein frequencies of each component.

C.2 3D Yukawa

In the case of a Binary Yukawa Mixture the QLCA dynamical matrix elements are again obtained from the r-conversion of eq. (B.19) which leads to

$$C^{\mu\nu}_{AB}(\mathbf{k}) = -\int \frac{d^3r}{4\pi}\left\{\omega^2_{AB}\psi^{\mu\nu}(r)e^{-i\mathbf{k}\cdot\mathbf{r}}\left[1+h_{AB}(r)\right] - \delta_{AB}\sum_C \Omega^2_{AC}\psi^{\mu\nu}(r)\left[1+h_{AC}(r)\right]\right\} \tag{C.13}$$

where the frequencies ω_{AB} and Ω_{AB} are again given by eq. (B.25) and $\psi^{\mu\nu}$ is now

$$\psi^{\mu\nu}(r) = \frac{e^{-y}}{r^3}\left[3\frac{r^\mu r^\nu}{r^2}a(y) - \delta^{\mu\nu}b(y)\right] - \frac{4\pi}{3}\delta^{\mu\nu}\delta(\mathbf{r}) \tag{C.14}$$

$$a(y) = 1 + y + \frac{y^2}{3}, \quad b(y) = 1 + y, \quad y = \kappa r. \tag{C.15}$$

The $\delta(\mathbf{r})$ term in $\psi^{\mu\nu}$ is now due to the Helmholtz equation

$$\left(\nabla^2 - \kappa^2\right)\frac{e^{-\kappa r}}{r} = -4\pi\delta(\mathbf{r}) \tag{C.16}$$

Contrary to the 3D Coulomb case no additional term is needed to compensate the terms arising from $\delta(\mathbf{r})$, since

$$\int \frac{d^3r}{4\pi}\psi^{\mu\mu} = \int \frac{d^3r}{4\pi}\left[\frac{e^{-y}}{r^3}\left[3\cos\theta a(y) - b(y)\right] - \frac{4\pi}{3}\delta(\mathbf{r})\right] = \left[\frac{1}{3} - \frac{1}{3}\right] = 0. \tag{C.17}$$

The calculation of the longitudinal elements then proceeds as follows

$$\begin{aligned} C^L_{AB}(k) &= -\frac{\omega^2_{AB}}{4\pi}\int d^3r \frac{e^{-\kappa r}}{r^3}\left[3a(\kappa r)\cos^2\theta - b(\kappa r)\right]\left[1 + h_{AB}(r)\right]\left[e^{-ikr\cos\theta} - \delta_{AB}\right] \\ &\quad +\delta_{AB}\sum_{C\neq A}\frac{\Omega^2_{AC}}{4\pi}\int d^3r\frac{e^{-\kappa r}}{r^3}\left[3a(\kappa r)\cos^2\theta - b(\kappa r)\right]\left[1 + h_{AC}(r)\right] \end{aligned} \tag{C.18}$$

The angular integral are evaluated as follows

$$\begin{aligned} \mathcal{K}(u,y) &= \int_{-1}^{1} d\mu\left[3a(y)\mu^2 - b(y)\right]e^{-iu\mu}e^{-y} \\ &= 2\left\{[3a(y) - b(y)]\frac{\sin u}{u} + 6a(y)\frac{\cos u}{u^2} - 6a(y)\frac{\sin u}{u^3}\right\}e^{-y} \end{aligned} \tag{C.19}$$

$$\mathcal{K}(0,y) = \int_{-1}^{1} d\mu\left[3a(y)\mu^2 - b(y)\right]e^{-y} = 2[a(y) - b(y)]e^{-y} = \frac{2}{3}y^2e^{-y}. \tag{C.20}$$

Thus, eq. (C.18) becomes

$$C_{AB}^{L}(k) = -\frac{\omega_{AB}^2}{2}\int \frac{dr}{r}\left[\mathcal{K}(u,y) - \delta_{AB}\mathcal{K}(0,y)\right]\left[1 + h_{AB}(r)\right] + \delta_{AB}\sum_{C\neq A}\frac{\Omega_{AC}^2}{2}\int \frac{dr}{r}\mathcal{K}(0,y)\left[1 + h_{AC}(r)\right]. \tag{C.21}$$

The h_{AB}-independent parts integrate to

$$\int \frac{dr}{r}\mathcal{K}(u,y) = 2\left(\frac{1}{3} - \frac{k^2}{k^2+\kappa^2}\right), \quad \int \frac{dr}{r}\mathcal{K}(0,y) = \frac{2}{3}\kappa^2\int dr\, re^{-\kappa r} = \frac{2}{3} \tag{C.22}$$

Notice that in the limit $\kappa \to 0$ the first integral $\to -4/3$ and the kernel $\mathcal{K}(0,y) \to 0$ which are the results found in the 3D Coulomb case. Further defining

$$D_{AB}(k,\kappa) = \int \frac{dr}{r}\left[\mathcal{K}(u,y) - \mathcal{K}(0,y)\right]h_{AB}(r), \quad W(\kappa) = 1 + \kappa^2\int dr re^{-\kappa r}h_{12}(r) \tag{C.23}$$

the longitudinal elements can be rewritten as

$$C_{11}^{L}(k) = \omega_{11}^2\left[\frac{k^2}{k^2+\kappa^2} - \frac{1}{2}D_{11}(k,\kappa) + \frac{p^2}{3}W(\kappa)\right] \tag{C.24a}$$

$$C_{12}^{L}(k) = \omega_{11}^2 qp\left[\frac{k^2}{k^2+\kappa^2} - \frac{1}{2}D_{12}(k,\kappa) - \frac{1}{3}W(\kappa)\right] \tag{C.24b}$$

$$C_{22}^{L}(k) = \omega_{11}^2\left[q^2p^2\frac{k^2}{k^2+\kappa^2} - q^2p^2\frac{1}{2}D_{22}(k,\kappa) + \frac{q^2}{3}W(\kappa)\right] \tag{C.24c}$$

The first term of each of these equation is the mean-field RPA term and while the last two terms contain all the correlational dependence.

Long wavelength limit

In the long wavelength limit, $k \to 0$, we have

$$\mathcal{K}(u,y) - \mathcal{K}(0,y) \approx -\frac{4}{15}u^2 e^{-y}\left(1 + y + \frac{3}{4}y^2\right) + \mathcal{O}(u^4) \tag{C.25}$$

$$D_{AB} = -\frac{4}{15}\frac{k^2}{\kappa^2}\int dy y(1 + y + \frac{3}{4}y^2)e^{-y}h_{AB}(y/\kappa) = 2U_{AB}\frac{k^2}{\kappa^2} \tag{C.26}$$

w which simplifies eq. (C.24)

$$C_{11}^L(k \to 0) = \omega_{11}^2\left[(1 - U_{11})\frac{k^2}{\kappa^2} + \frac{p^2}{3}W\right] \tag{C.27a}$$

$$C_{12}^L(k \to 0) = \omega_{11}^2 qp\left[(1 - U_{12})\frac{k^2}{\kappa^2} - \frac{1}{3}W\right] \tag{C.27b}$$

$$C_{22}^L(k \to 0) = \omega_{11}^2\left[q^2p^2(1 - U_{22})\frac{k^2}{\kappa^2} + \frac{q^2}{3}W\right] \tag{C.27c}$$

Short wavelength limit

On the other hand, in the limit $k \to \infty$ the integral

$$\int \frac{dr}{r} \mathcal{K}(kr, \kappa r) \left[1 + h_{AB}(r/k)\right] \to 0 \tag{C.28}$$

due to the fact that $[1 + h_{AB}(x \to 0)] \to 0$ fast enough. Thus,

$$C_{11}^L(k \to \infty) = \omega_1^2 \frac{1+p^2}{3} W = \frac{\omega_{11}^2 + \Omega_{12}^2}{3} W \tag{C.29a}$$

$$C_{12}^L(k \to \infty) = 0 \tag{C.29b}$$

$$C_{22}^L(k \to \infty) = \omega_1^2 \frac{q^2(1+p^2)}{3} W = \frac{\omega_{22}^2 + \Omega_{21}^2}{3} W \tag{C.29c}$$

and we recover the Einstein frequencies of each species times a factor of W.

Collective Modes

The collective modes are obtained from the zeros of $||\omega^2 - \mathbf{C}^L||$.

$$\omega_{\mp}^2 = \frac{C_{11} + C_{22}}{2} \pm \sqrt{\left(\frac{C_{11} - C_{22}}{2}\right)^2 + C_{12}^2} = \frac{1}{2}\left\{B(k,\kappa) \pm \sqrt{[B(k,\kappa)]^2 - 4\Delta(k,\kappa)}\right\} \tag{C.30}$$

$$B = \frac{p^2+q^2}{3}W(\kappa) + (1+q^2p^2)\frac{k^2}{k^2+\kappa^2} - \frac{1}{2}\left[D_{11}(k,\kappa) + q^2p^2D_{22}(k,\kappa)\right] \tag{C.31}$$

$$\Delta = \frac{q^2(1+p^2)^2}{3}W\left[\frac{k^2}{k^2+\kappa^2} - \frac{D_{11}+2p^2D_{12}+p^4D_{22}}{(1+p^2)^2}\right] - \frac{1}{2}q^2p^2\frac{k^2}{k^2+\kappa^2}\left(D_{11}-2D_{12}+D_{22}\right) + \frac{q^2p^2}{4}\left(D_{11}D_{22}-D_{12}^2\right) \tag{C.32}$$

Long wavelength limit

$$\omega_{\mp}^2 = \frac{1}{2}\left(B \pm \sqrt{B^2-4\Delta}\right) \tag{C.33}$$

with

$$B = \left(\frac{p^2+q^2}{3}\right)W + \left[\left(1+q^2p^2\right) - \left(U_{11}+p^2q^2U_{22}\right)\right]\frac{k^2}{\kappa^2} \tag{C.34}$$

$$\Delta = \frac{q^2\left(1+p^2\right)^2}{3}\left[1 - \frac{U_{11}+2p^2U_{12}+p^4U_{22}}{(1+p^2)^2}\right]\frac{k^2}{\kappa^2}W - q^2p^2\frac{k^4}{\kappa^4}\left[U_{11}-2U_{12}+U_{22}-(U_{11}U_{22}-U_{12}^2)\right] \tag{C.35}$$

You can see then that in the $\kappa \to 0$ limit the only term that survives in Δ is $q^2(1+p^2)^2$ and obtain the Coulomb modes.

$$\omega_+^2(k) \approx \omega_1^2\frac{q^2(1+p^2)^2}{q^2+p^2}\left[1 - \frac{U_{11}+2p^2U_{12}+p^4U_{22}}{(1+p^2)^2}\right]\frac{k^2}{\kappa^2} \tag{C.36}$$

$$\omega_-^2(k) \approx \omega_1^2\left(\frac{p^2+q^2}{3}\right)W + \omega_1^2\frac{p^2(1-q^2)^2}{q^2+p^2}\frac{k^2}{\kappa^2}\left[1 - \frac{U_{11}-2q^2U_{12}+q^4U_{22}}{(1-q^2)^2}\right] \tag{C.37}$$

Notice that the subscript sign indicates whether the two components move in-phase (+) or out-of-phase (−).

Short wavelength limit

In this limit the collective modes become exactly

$$\omega_+^2 = \omega_1^2 \frac{1+p^2}{3} W, \quad \omega_-^2 = \omega_1^2 \frac{q^2(1+p^2)}{3} W, \tag{C.38}$$

C.3 Asymmetric $e-e$ Bilayer

The elements of the longitudinal dynamical matrix are

$$C_{AB}(\mathbf{k}) = -\sqrt{\frac{n_A n_B}{m_A m_B}} \int d\mathbf{r} \left[\left(\frac{\mathbf{k}\cdot\nabla}{k} \right)^2 \phi_{AB}(r) \right] \left(e^{-i\mathbf{k}\cdot\mathbf{r}} - \delta_{AB} \right) g_{AB}(r) + \delta_{AB} \sum_{C\neq A} \sqrt{\frac{n_A n_C}{m_A m_B}} \int d\mathbf{r} \left[\left(\frac{\mathbf{k}\cdot\nabla}{k} \right)^2 \phi_{AC}(r) \right] g_{AC}(r) \tag{C.39}$$

where $\mathbf{r}$ is the 2D distance between two particles in a 2D layer and d is the (vertical) distance between the two layers. In the following $d\mathbf{r} = rdrd\theta$ indicate the 2D infinitesimal surface. The potential ϕ_{AB} is

$$\phi_{11}(r) = \frac{(Z_1 e)^2}{r}, \quad \phi_{12}(r) = \pm \frac{Z_1 Z_2 e^2}{\sqrt{r^2+d^2}} \tag{C.40}$$

where the sign of $\phi_{12}(r)$ is determined whether we are considering an electron-electron (+) or an electron-hole (−) bilayer. In any case we can incorporate the sign in the asymmetry parameters

$$p^2 = Zn, \qquad q^2 = Z/m, \qquad \omega_{22}^2/\omega_{11}^2 = Z^2 n/m = q^2 p^2. \tag{C.41}$$

Hence, $p^2 = -n$ and $q^2 = -1/m$ in the case of an electron-hole bilayer. Using

$$\omega_{AB}^2 = \frac{2\pi Z_A Z_B e^2 \sqrt{n_A n_B}}{\sqrt{m_A m_B}a}, \qquad \Omega_{AB}^2 = \frac{2\pi Z_A Z_B e^2 n_B}{m_A a}, \quad \pi a^2 = 1/\sqrt{n_1 n_2} \tag{C.42}$$

We can rewrite eq. (C.39) as

$$C_{AB}(\mathbf{k}) = -\omega_{AB}^2 \frac{a}{2\pi}\int d\mathbf{r}\left[\left(\frac{\mathbf{k}\cdot\nabla}{k}\right)^2 \phi_{AB}(r)\right]\left(e^{-i\mathbf{k}\cdot\mathbf{r}} - \delta_{AB}\right) g_{AB}(r) + \delta_{AB}\sum_{C\neq A}\Omega_{AB}^2 \frac{a}{2\pi}\int d\mathbf{r}\left[\left(\frac{\mathbf{k}\cdot\nabla}{k}\right)^2 \phi_{AC}(r)\right] g_{AC}(r), \tag{C.43}$$

It is important to notice that the argument of g_{12} is the distance r not $\rho = \sqrt{r^2 + d^2}$ since this is what is computed in MD simulations. The way is calculated is by counting the number of particles that fall into a circle of radius r and then dividing by the total areal density. The calculations goes as follows. We start by evaluating the longitudinal projection of the potentials

$$\left[\left(\frac{\mathbf{k}\cdot\nabla}{k}\right)^2 \phi_{11}(r)\right] = \frac{e^2}{r^3}\left(3\cos^2\theta - 1\right), \quad \left[\left(\frac{\mathbf{k}\cdot\nabla}{k}\right)^2 \phi_{12}(r)\right] = \frac{e^2}{(r^2+d^2)^{3/2}}\left(3\frac{r^2\cos^2\theta}{r^2+d^2} - 1\right). \tag{C.44}$$

Writing explicitly each element we have

$$C_{11}(k) = -\omega_1^2 \frac{a}{2\pi} \int \frac{d\mathbf{r}}{r^3} \left(3\cos^2\theta - 1\right) \left(e^{-i\mathbf{k}\cdot\mathbf{r}} - 1\right) g_{11}(r) + \omega_1^2 \frac{p^2 a}{2\pi} \int \frac{d\mathbf{r}}{(r^2+d^2)^{3/2}} \left(3\frac{r^2\cos^2\theta}{r^2+d^2} - 1\right) g_{12}(r), \tag{C.45}$$

$$C_{22}(k) = -\omega_1^2 q^2 p^2 \frac{a}{2\pi} \int \frac{d\mathbf{r}}{r^3} \left(3\cos^2\theta - 1\right) \left(e^{-i\mathbf{k}\cdot\mathbf{r}} - 1\right) g_{22}(r) + \omega_1^2 \frac{q^2 a}{2\pi} \int \frac{d\mathbf{r}}{(r^2+d^2)^{3/2}} \left(3\frac{r^2\cos^2\theta}{r^2+d^2} - 1\right) g_{12}(r), \tag{C.46}$$

$$C_{12}(k) = -\omega_1^2 qp \frac{a}{2\pi} \int \frac{d\mathbf{r}\, g_{12}(r)}{(r^2+d^2)^{3/2}} \left(3\frac{r^2\cos^2\theta}{r^2+d^2} - 1\right) e^{-i\mathbf{k}\cdot\mathbf{r}}. \tag{C.47}$$

Rewriting $g_{AB}(r) = 1 + h_{AB}(r)$ and carrying out the calculation, using some useful integrals eqs. (D.6),(D.7),(D.9) and some relations between the Bessel functions eq. (D.10), we obtain the diagonal element

$$\begin{aligned} C_{11}(k) &= \omega_1^2 \left\{ ka + \frac{a}{2} \int \frac{dr}{r^2} h_{11}(r) \left[1 - J_0(kr) + 3J_2(kr)\right] + p^2 a \int \frac{dr\, r h_{12}(r)}{(r^2+d^2)^{3/2}} \left(\frac{3}{2}\frac{r^2}{r^2+d^2} - 1\right) \right\} && \text{(C.48)} \\ &= \omega_1^2 \left\{ ka + D_{11}(ka) + p^2 W \right\} && \text{(C.49)} \end{aligned}$$

where the first term comes from eq. (D.6) and is referred to as the RPA term and we have defined

$$D_{11}(ka) = \frac{a}{2} \int \frac{dr}{r^2} h_{11}(r) \left[1 - J_0(kr) + 3J_2(kr)\right], \tag{C.50}$$

$$W = a\int \frac{dr\, r h_{12}(r)}{(r^2+d^2)^{3/2}}\left(\frac{3}{2}\frac{r^2}{r^2+d^2}-1\right) = \frac{a}{2}\int \frac{dr\, r h_{12}(r)}{(r^2+d^2)^{3/2}}\left(1-3\frac{d^2}{r^2+d^2}\right) \tag{C.51}$$

Now onto the off-diagonal

$$\begin{aligned}
C_{12}(k) &= -\omega_1^2 qp\frac{a}{2\pi}\int \frac{d\mathbf{r} g_{12}(r)}{(r^2+d^2)^{3/2}}\left(3\frac{r^2\cos^2\theta}{r^2+d^2}-1\right)e^{-i\mathbf{k}\cdot\mathbf{r}} && \text{(C.52)}\\
&= -\omega_1^2 qp\left\{\frac{a}{2\pi}\int \frac{d\mathbf{r}[1+h_{12}(r)]}{(r^2+d^2)^{3/2}}\left(3\frac{r^2\cos^2\theta}{r^2+d^2}-1\right)\left(e^{-i\mathbf{k}\cdot\mathbf{r}}-1+1\right)\right\} && \text{(C.53)}\\
&= \omega_1^2 qp\left\{kae^{-kd}-\frac{a}{2\pi}\int \frac{d\mathbf{r}\, h_{12}(r)}{(r^2+d^2)^{3/2}}\left(3\frac{r^2\cos^2\theta}{r^2+d^2}-1\right)\left(e^{-i\mathbf{k}\cdot\mathbf{r}}-1\right)-\frac{a}{2\pi}\int \frac{d\mathbf{r}\, h_{12}(r)}{(r^2+d^2)^{3/2}}\left(3\frac{r^2\cos^2\theta}{r^2+d^2}-1\right)\right\} && \text{(C.54)}\\
&= \omega_1^2 qp\left\{kae^{-kd}-\frac{a}{2\pi}\int \frac{d\mathbf{r}\, h_{12}(r)}{(r^2+d^2)^{3/2}}\left(3\frac{r^2\cos^2\theta}{r^2+d^2}-1\right)\left(e^{-i\mathbf{k}\cdot\mathbf{r}}-1\right)-a\int \frac{dr\, r h_{12}(r)}{(r^2+d^2)^{3/2}}\left(\frac{3}{2}\frac{r^2}{r^2+d^2}-1\right)\right\}. && \text{(C.55)}
\end{aligned}$$

At this point we make some remarks on the next steps. There are two ways for this to be solved. One is the easy way: plug the second integral in the computer software `Mathematica` and simplify the Bessel functions to obtain

$$\begin{aligned}
C_{12}(k) &= \omega_1^2 qp\left\{kae^{-kd}-a\int \frac{dr\, r h_{12}(r)}{(r^2+d^2)^{3/2}}\left\{[1-J_0(kr)]+\frac{3}{2}\frac{r^2}{r^2+d^2}\left[1-J_0(kr)+J_2(kr)\right]\right\}-W\right\} && \text{(C.56)}\\
&= \omega_1^2 qp\left\{kae^{-kd}-L_{12}(ka)-W\right\} && \text{(C.57)}
\end{aligned}$$

where we have defined

$$L_{12}(ka) = a \int \frac{dr\, r h_{12}(r)}{(r^2+d^2)^{3/2}} \left\{ [1 - J_0(kr)] - \frac{3}{2} \frac{r^2}{r^2+d^2} [1 - J_0(kr) + J_2(kr)] \right\}. \tag{C.58}$$

However, in the literature we find the expression

$$D_{12}(ka) = \frac{a}{2} \int dr \frac{r\, h_{12}(r)}{(r^2+d^2)^{3/2}} \left\{ 1 - J_0(kr) + 3J_2(kr) - \frac{3d^2}{r^2+d^2} [1 - J_0(kr) + J_2(kr)] \right\}. \tag{C.59}$$

Therefore, in order to be consistent with the previous papers published by Golden and Kalman we will use the other more difficult way which consist in making the substitution $\rho^2 = r^2 + d^2$. This gives

$$dr\, r = d\rho\, \rho, \quad \frac{dr\, r}{r^2+d^2} = \frac{d\rho}{\rho^2}, \quad 3\frac{r^2 \cos^2\theta}{r^2+d^2} - 1 = \left(3\cos^2\theta - 1\right) - 3\frac{d^2}{\rho^2}\cos^2\theta, \tag{C.60}$$

and the second term becomes

$$-\int \frac{d\mathbf{r}\, h_{12}(r)}{(r^2+d^2)^{3/2}}\left(3\frac{r^2\cos^2\theta}{r^2+d^2}-1\right)\left(e^{-i\mathbf{k}\cdot\mathbf{r}}-1\right) = -\int \frac{d\rho}{\rho^2}h_{12}(r)\int_0^{2\pi}\left[\left(3\cos^2\theta-1\right)-3\frac{d^2}{\rho^2}\cos^2\theta\right]\left(e^{-i\mathbf{k}\cdot\mathbf{r}}-1\right) \quad \text{(C.61)}$$

$$= \pi\int \frac{d\rho}{\rho^2}h_{12}(r)\left[1-J_0(kr)+3J_2(kr)\right]$$

$$+3d^2\int \frac{d\rho}{\rho^4}h_{12}(r)\int_0^{2\pi}d\theta\cos^2\theta\left(e^{-ikr\cos\theta}-1\right) \quad \text{(C.62)}$$

Calculating the second term with `Mathematica` again

$$3d^2\int \frac{d\rho}{\rho^4}h_{12}(r)\int_0^{2\pi}d\theta\cos^2\theta\left(e^{-ikr\cos\theta}-1\right) = -3\pi\frac{d^2}{\rho^2}\left\{1+2J_2(kr)-{}_0F_1\left[;2;-(kr)^2/4\right]\Gamma(2)\right\} \quad \text{(C.63)}$$

where ${}_0F_1\left(;2;-x^2/4\right)\Gamma(2)$ is the regularized confluent hypergeometric limit functions and it is related to the Bessel functions by

$$J_\alpha(x) = \frac{(x/2)^\alpha}{\Gamma(\alpha+1)}{}_0F_1\left(;\alpha+1;-\tfrac{1}{4}x^2\right). \quad \text{(C.64)}$$

Eq. (C.63) thus, becomes

$$-3\pi\frac{d^2}{\rho^2}\left\{1+2J_2(kr)-{}_0F_1\left[;2;-(kr)^2/4\right]\Gamma(2)\right\} = -3\pi\frac{d^2}{\rho^2}\left\{1+2J_2(kr)-2J_1(kr)\right\} \quad \text{(C.65)}$$

$$= -3\pi\frac{d^2}{\rho^2}\left[1-J_0(kr)+J_2(kr)\right]. \quad \text{(C.66)}$$

The off-diagonal element $C_{12}(k)$ can now be rewritten as

$$C_{12}(k) = \omega_1^2 qp\left\{kae^{-kd}-\frac{a}{2\pi}\int\frac{d\mathbf{r}\,h_{12}(r)}{(r^2+d^2)^{3/2}}\left(3\frac{r^2\cos^2\theta}{r^2+d^2}-1\right)\left(e^{-i\mathbf{k}\cdot\mathbf{r}}-1\right)-\frac{a}{2\pi}\int\frac{d^2r\,h_{12}(r)}{(r^2+d^2)^{3/2}}\left(3\frac{r^2\cos^2\theta}{r^2+d^2}-1\right)\right\} \quad \text{(C.67)}$$

$$= \omega_1^2 qp\left\{kae^{-kd}-a\int\frac{dr\,rh_{12}(r)}{(r^2+d^2)^{3/2}}\left(\frac{3}{2}\frac{r^2}{r^2+d^2}-1\right)\right.$$
$$\left.+\frac{a}{2}\int\frac{d\rho}{\rho^2}h_{12}(r)\left[1-J_0(kr)+3J_2(kr)\right]-\frac{3ad^2}{2}\int\frac{d\rho}{\rho^4}h_{12}(r)\left[1-J_0(kr)+J_2(kr)\right]\right\} \quad \text{(C.68)}$$

$$= \omega_1^2 qp\left\{kae^{-kd}+D_{12}(ka)-W\right\}, \quad \text{(C.69)}$$

where we have defined

$$D_{12}(ka)=\frac{a}{2}\int dr\frac{r\,h_{12}(r)}{(r^2+d^2)^{3/2}}\left\{1-J_0(kr)+3J_2(kr)-\frac{3d^2}{r^2+d^2}\left[1-J_0(kr)+J_2(kr)\right]\right\}. \quad \text{(C.70)}$$

Put everything in units of ω_1^2 we rewrite

$$C_{11}(k) = ka + D_{11}(ka) + p^2 W, \tag{C.71}$$

$$C_{22}(k) = q^2 p^2 \left[ka + D_{22}(ka)\right] + q^2 W, \tag{C.72}$$

$$C_{12}(k) = qp \left[kae^{-kd} + D_{12}(ka) - W\right] \tag{C.73}$$

where

$$D_{11}(ka) = \frac{a}{2} \int \frac{dr}{r^2} h_{11}(r) \left[1 - J_0(kr) + 3J_2(kr)\right], \tag{C.74}$$

$$D_{12}(ka) = \frac{a}{2} \int dr \frac{r\, h_{12}(r)}{(r^2+d^2)^{3/2}} \left\{1 - J_0(kr) + 3J_2(kr) - \frac{3d^2}{r^2+d^2}\left[1 - J_0(kr) + J_2(kr)\right]\right\}. \tag{C.75}$$

$$W = a \int \frac{dr\, r h_{12}(r)}{(r^2+d^2)^{3/2}} \left(\frac{3}{2}\frac{r^2}{r^2+d^2} - 1\right) = \frac{a}{2} \int \frac{dr\, r h_{12}(r)}{(r^2+d^2)^{3/2}} \left(1 - 3\frac{d^2}{r^2+d^2}\right) \tag{C.76}$$

Long Wavelength limit

In this limit $D_{AB}(ka) \to I_{AB}(ka)$

$$I_{11}(ka) = \frac{5}{8}\frac{a}{2} \int \frac{dr}{r^2} (kr)^2 h_{11}(r) \tag{C.77}$$

$$I_{12}(ka) = \frac{5}{8}\frac{a}{2} \int dr \frac{r\,(kr)^2 h_{12}(r)}{(r^2+d^2)^{3/2}} \left\{1 - \frac{9}{5}\frac{d^2}{r^2+d^2}\right\}. \tag{C.78}$$

Collective Modes

The collective modes are the solutions to the equation

$$\left|\omega^2\mathbf{I} - \mathbf{C}(\mathbf{k})\right| = 0 \tag{C.79}$$

which are, expressed in units ω_1

$$\omega_{\mp}^2 = \frac{C_{11}+C_{22}}{2} \pm \sqrt{\left(\frac{C_{11}-C_{22}}{2}\right)^2 + C_{12}^2} = \frac{1}{2}\left\{B(k,d) \pm \sqrt{[B(k,d)]^2 - 4\Delta(k,d)}\right\} \tag{C.80}$$

$$B(k,d) = \left(p^2+q^2\right)W + \left(1+p^2q^2\right)k + D_{11}(k) + p^2q^2D_{22}(k) \tag{C.81}$$

$$\begin{aligned}
\Delta(k,d) &= \left\{q^2\left(1+2p^2e^{-kd}+p^4\right)W + q^2p^2\left[D_{11}(k) - 2e^{-kd}D_{12}(k,d) + D_{22}(k)\right]\right\}ka + q^2p^2\left(1-e^{-2kd}\right)(ka)^2 \\
&\quad + q^2p^2\left[D_{11}(k)D_{22}(k) - D_{12}^2(k,d)\right] + q^2\left[D_{11}(k) + 2p^2D_{12}(k,d) + p^4D_{22}(k)\right]W \qquad \text{(C.82)} \\
&= q^2(1+p^2)^2W\left\{\left[1 - \frac{2p^2\left(1-e^{-kd}\right)}{(1+p^2)^2}\right]ka + \frac{D_{11}(k) + 2p^2D_{12}(k,d) + p^4D_{22}(k)}{(1+p^2)^2}\right\} \\
&\quad + q^2p^2\left\{\left(1-e^{-2kd}\right)(ka)^2 + \left[D_{11}(k) - 2e^{-kd}D_{12}(k,d) + D_{22}(k)\right]ka + D_{11}(k)D_{22}(k) - D_{12}^2(k,d)\right\} \qquad \text{(C.83)}
\end{aligned}$$

where the d-dependence in $B(k,d)$ is in $W = W(d)$.

Long wavelength limit

$$B \to \left(p^2+q^2\right) W + \left(1+p^2q^2\right) k + U_{11}(ka)^2 + p^2q^2U_{22}(ka)^2 \tag{C.84}$$

$$\Delta \to q^2(1+p^2)^2 W \left[ka + 2\frac{d}{a}(ka)^2 + \frac{U_{11}+2p^2U_{12}+p^4U_{22}}{(1+p^2)^2}(ka)^2\right] \tag{C.85}$$

which gives

$$\omega_+^2(k) \approx \frac{q^2(1+p^2)^2}{q^2+p^2}ka - \frac{2q^2p^2}{p^2+q^2}\left[\frac{d}{a} + \frac{\left(1+p^2\right)^2\left(1-q^2\right)^2}{2W\left(p^2+q^2\right)^2} - \frac{U_{11}+2p^2U_{12}+p^4U_{22}}{2p^2}\right](ka)^2 \tag{C.86}$$

$$\omega_-^2(k) \approx \left(p^2+q^2\right) W + \frac{p^2(1-q^2)^2}{q^2+p^2}ka + \frac{2q^2p^2}{p^2+q^2}\left[\frac{d}{a} + \frac{\left(1+p^2\right)^2\left(1-q^2\right)^2}{2W\left(p^2+q^2\right)^2} + \frac{U_{11}-2q^2U_{12}+q^4U_{22}}{2q^2}\right](ka)^2 \tag{C.87}$$

Notice that the subscript sign indicates whether the two components move in-phase (+) or out-of-phase (−).

Anti-resonances

The anti-resonances in the asymmetric bilayers are

$$\omega_{*1}^2(k) = C_{11} + \frac{p}{q}C_{12} = \left(1+p^2e^{-kd}\right)ka + D_{11}(ka) + p^2D_{12}(ka) \tag{C.88}$$

$$\omega_{*2}^2(k) = C_{22} + \frac{q}{p}C_{12} = q^2\left(e^{-kd}+p^2\right)ka + q^2p^2D_{11}(ka) + q^2D_{12}(ka) \tag{C.89}$$

APPENDIX D

Useful Relations

In this appendix we report useful integrals and formulas used in the thesis.

$$\lim_{k\to 0}\int d^3r \frac{1}{\mathbf{r}^3}\left(3\frac{r^\mu r^\nu}{r^2}-\delta^{\mu\nu}\right)e^{-i\mathbf{k}\cdot\mathbf{r}} = -\frac{4\pi}{3}\left(3\frac{k^\mu k^\nu}{k^2}-\delta^{\mu\nu}\right) \tag{D.1}$$

$$\int d^3r \frac{1}{\mathbf{r}^3}\left(3\frac{r^\mu r^\nu}{r^2}-\delta^{\mu\nu}\right) = \int dr r^2 \int d\phi \left\{\int_{-1}^{1} d\mu(3\mu^2-1) = 0\right\} \text{ i}sotropy \tag{D.2}$$

$$\int_{-1}^{1} d\mu(3\mu^2-1)e^{-ikr\mu} = 4\frac{\sin(kr)}{kr} + 12\frac{\cos(kr)}{(kr)^2} - 12\frac{\sin(kr)}{(kr)^3} \tag{D.3}$$

$$\int_{0}^{\infty} dx\frac{1}{x}\left[4\frac{\sin(x)}{x} + 12\frac{\cos(x)}{x^2} - 12\frac{\sin(x)}{x^3}\right] = -\frac{4}{3} \tag{D.4}$$

$$\lim_{k\to 0}\left[4\frac{\sin(kr)}{kr} + 12\frac{\cos(kr)}{(kr)^2} - 12\frac{\sin(kr)}{(kr)^3}\right] = -\frac{4}{15}k^2r^2 \tag{D.5}$$

Asymmetric $e-e$ Bilayer

$$\int \frac{dr\,r}{r^3}\int_0^{2\pi} d\theta\left(3\cos^2\theta-1\right)\left(e^{-ikr\cos\theta}-1\right) = -\int\frac{dr}{r^2}\pi\left[1-4J_0(kr)+6\frac{J_1(kr)}{kr}\right] = -2\pi k \tag{D.6}$$

$$\int dr\frac{r}{(r^2+d^2)^{3/2}}\int_0^{2\pi} d\theta\left(3\frac{r^2}{r^2+d^2}\cos^2\theta-1\right) = 2\pi\int dr\frac{r}{(r^2+d^2)^{3/2}}\left(\frac{3}{2}\frac{r^2}{r^2+d^2}-1\right) = 0 \tag{D.7}$$

$$\begin{aligned}
\int\frac{d\mathbf{r}}{(r^2+d^2)^{3/2}}\left(3\frac{r^2\cos^2\theta}{r^2+d^2}-1\right)\left(e^{-ikr\cos\theta}-1\right) &= \int\frac{dr2\pi r}{(r^2+d^2)^{3/2}}\left[1-\frac{3}{2}\frac{r^2}{r^2+d^2}-\left(1-\frac{3}{2}\frac{r^2}{r^2+d^2}\right)J_0(kr)-\frac{3}{2}\frac{r^2}{r^2+d^2}J_2(kr)\right] \\
&= \int\frac{dr2\pi r}{(r^2+d^2)^{3/2}}\left\{[1-J_0(kr)]-\frac{3}{2}\frac{r^2}{r^2+d^2}\left[1-J_0(kr)+J_2(kr)\right]\right\} \qquad \text{(D.8)} \\
&= -2\pi k e^{-kd} \qquad \text{(D.9)}
\end{aligned}$$

$$\frac{J_1(kr)}{kr} = \frac{1}{2}\left[J_0(kr) + J_2(kr)\right], \quad 1 - 4J_0(kr) + 6\frac{J_1(kr)}{kr} = 1 - J_0(kr) + 3J_2(kr). \tag{D.10}$$

BIBLIOGRAPHY

Agarwal, A. et al. (2014). "Long-lived spin plasmons in a spin-polarized two-dimensional electron gas". In: *Phys. Rev. B* 90 (15), p. 155409. DOI: 10.1103/PhysRevB.90.155409.

Anderson, P. W. (1963). "Plasmons, Gauge Invariance, and Mass". In: *Phys. Rev.* 130 (1), pp. 439–442. DOI: 10.1103/PhysRev.130.439.

Atzeni, S. and J. Meyer-ter-Vehn (2004). *The Physics of Inertial Fusion*. International Series of Monographs on Physics. Oxford University Press. ISBN: 9780198562641. DOI: 10.1093/acprof:oso/9780198562641.001.0001.

Baalrud, S. D. and J. Daligault (2013). "Effective Potential Theory for Transport Coefficients across Coupling Regimes". In: *Phys. Rev. Lett.* 110.23, p. 235001. DOI: 10.1103/PhysRevLett.110.235001.

Balescu, R. (1960). "Irreversible Processes in Ionized Gases". In: *The Physics of Fluids* 3.1, pp. 52–63. DOI: 10.1063/1.1706002. eprint: https://aip.scitation.org/doi/pdf/10.1063/1.1706002.

Basov, D. N., R. D. Averitt, and D. Hsieh (2017). "Towards properties on demand in quantum materials". In: *Nature Materials* 16, p. 1077.

Baus, M. (1977a). "Microscopic theory of the long-wavelength modes of two component plasmas and ionic liquids: I. The transverse modes". In: *Physica A: Statistical Mechanics and its Applications* 88.2, pp. 319–335. ISSN: 0378-4371. DOI: https://doi.org/10.1016/0378-4371(77)90007-3.

— (1977b). "Microscopic theory of the long-wavelength modes of two-component plasmas and ionic liquids: II. The longitudinal modes". In: *Physica A: Statistical Mechanics and its Applications* 88.2, pp. 336–346. ISSN: 0378-4371. DOI: https://doi.org/10.1016/0378-4371(77)90008-5.

— (1977c). "Microscopic theory of the long-wavelength modes of two-component plasmas and ionic liquids: III. The space-time correlation functions". In: *Physica A: Statistical Mechanics and its Applications* 88.3, pp. 591–599. ISSN: 0378-4371. DOI: https://doi.org/10.1016/0378-4371(77)90130-3.

— (1978). "Temperature Dependence of the Plasma Frequency of Two-Component Ionic Fluids". In: *Phys. Rev. Lett.* 40 (12), pp. 793–796. DOI: 10.1103/PhysRevLett.40.793.

Baus, M. and J.-P. Hansen (1980). "Statistical mechanics of simple coulomb systems". In: *Physics Reports* 59.1, pp. 1–94. ISSN: 0370-1573. DOI: https://doi.org/10.1016/0370-1573(80)90022-8.

Belbasi, S., M. Ebrahim Foulaadvand, and Y. S. Joe (2014). "Anti-resonance in a one-dimensional chain of driven coupled oscillators". In: *American Journal of Physics* 82.1, pp. 32–38. DOI: 10.1119/1.4827277.

Bhatia, A. B. and D. E. Thornton (1970). "Structural Aspects of the Electrical Resistivity of Binary Alloys". In: *Phys. Rev. B* 2 (8), pp. 3004–3012. DOI: 10.1103/PhysRevB.2.3004.

Bhatia, A. B. and D. E. Thornton (1971). "Structural Aspects of the Electrical Resistivity of Binary Alloys. II. Long-Wavelength Limit of the Structure Factors for a Solid Alloy". In: *Phys. Rev. B* 4 (8), pp. 2325–2328. DOI: 10.1103/PhysRevB.4.2325.

Bhatia, A. B., D. E. Thornton, and N. H. March (1974). "Dynamical structure factors for a fluid binary mixture in the hydrodynamic limit". In: *Physics and Chemistry of Liquids* 4.2-3, pp. 97–111. DOI: 10.1080/00319107408084276.

Bhatnagar, P. L., E. P. Gross, and M. Krook (1954). "A Model for Collision Processes in Gases. I. Small Amplitude Processes in Charged and Neutral One-Component Systems". In: *Phys. Rev.* 94.3, pp. 511–525. DOI: 10.1103/PhysRev.94.511.

Bildsten, L. and D. M. Hall (2001). "Gravitational Settling of 22Ne in Liquid White Dwarf Interiors". In: *The Astrophysical Journal Letters* 549.2, p. L219.

Bohm, D. and E. P. Gross (1949a). "Theory of Plasma Oscillations. A. Origin of Medium-Like Behavior". In: *Phys. Rev.* 75 (12), pp. 1851–1864. DOI: 10.1103/PhysRev.75.1851.

— (1949b). "Theory of Plasma Oscillations. B. Excitation and Damping of Oscillations". In: *Phys. Rev.* 75 (12), pp. 1864–1876. DOI: 10.1103/PhysRev.75.1864.

Bohm, D. and D. Pines (1953). "A Collective Description of Electron Interactions: III. Coulomb Interactions in a Degenerate Electron Gas". In: *Phys. Rev.* 92 (3), pp. 609–625. DOI: 10.1103/PhysRev.92.609.

Brown, E. F. (2000). "Nuclear Heating and Melted Layers in the Inner Crust of an Accreting Neutron Star". In: *The Astrophysical Journal* 531.2, p. 988.

Brush, S. G., H. L. Sahlin, and E. Teller (1966). "Monte Carlo Study of a One-Component Plasma. I". In: *The Journal of Chemical Physics* 45.6, pp. 2102–2118. DOI: 10.1063/1.1727895. eprint: https://doi.org/10.1063/1.1727895.

Callen, H. B. and T. A. Welton (1951). "Irreversibility and Generalized Noise". In: *Phys. Rev.* 83 (1), pp. 34–40. DOI: 10.1103/PhysRev.83.34.

Coste, J. (1965a). "Longitudinal dielectric constant of the classical plasma — I". In: *Nuclear Fusion* 5.4, pp. 284–292. ISSN: 0029-5515. DOI: 10.1088/0029-5515/5/4/005.

Coste, J. (1965b). "Longitudinal dielectric constant of the classical plasma — II". In: *Nuclear Fusion* 5.4, pp. 293–298. ISSN: 0029-5515. DOI: 10.1088/0029-5515/5/4/006.

Crookes, W. (1879). *On radiant matter: a lecture delivered to the British Association for the Advancement of Science, at Sheffield, Friday, August 22, 1879.* eng. London.

— (1880). "I. On a fourth state of matter, in a letter to the Secretary." In: *Proceedings of the Royal Society of London* 30.200–205, pp. 469–472. DOI: 10.1098/rspl.1879.0147. eprint: http://rspl.royalsocietypublishing.org/content/30/200-205/469.full.pdf+html.

Daligault, J. (2006). "Liquid-State Properties of a One-Component Plasma". In: *Phys. Rev. Lett.* 96 (6), p. 065003. DOI: 10.1103/PhysRevLett.96.065003.

Daligault, J. (2012). "Diffusion in Ionic Mixtures across Coupling Regimes". In: *Phys. Rev. Lett.* 108 (22), p. 225004. DOI: 10.1103/PhysRevLett.108.225004.

Daligault, J., K. Ø. Rasmussen, and S. D. Baalrud (2014). "Determination of the shear viscosity of the one-component plasma". In: *Phys. Rev. E* 90 (3), p. 033105. DOI: 10.1103/PhysRevE.90.033105.

Das Sarma, S. and A. Madhukar (1981). "Collective modes of spatially separated, two-component, two-dimensional plasma in solids". In: *Phys. Rev. B* 23 (2), pp. 805–815. DOI: 10.1103/PhysRevB.23.805.

DeWitt, H. E. (1994). "Strongly Coupled Ionic Mixtures and the H/He EOS". In: *The Equation of State in Astrophysics, International Astronomical Union Colloquium*. Vol. 147. Cambridge University Press, pp. 330–346. DOI: 10.1017/S0252921100026439.

Diaw, A. and M. S. Murillo (2016). "A Dynamic Density Functional Theory Approach to Diffusion in White Dwarfs and Neutron Star Envelopes". In: *The Astrophysical Journal* 829.1, p. 16.

Donkó, Z., P. Hartmann, and G. J. Kalman (2003). "Molecular dynamics simulations of strongly coupled plasmas: Localization and microscopic dynamics". In: *Physics of Plasmas* 10.5, pp. 1563–1568. DOI: 10.1063/1.1560612. eprint: https://doi.org/10.1063/1.1560612.

Donkó, Z., P. Hartmann, G. J. Kalman, and K. I. Golden (2003). "Simulations of strongly coupled charged particle systems: static and dynamical properties of classical bilayers". In: *Journal of Physics A: Mathematical and General* 36.22, p. 5877.

Donkó, Z., P. Hartmann, P. Magyar, et al. (2017). "Higher order structure in a complex plasma". In: *Physics of Plasmas* 24.10, p. 103701. ISSN: 1070-664X. DOI: 10.1063/1.4990510.

Donkó, Z., G. J. Kalman, and K. I. Golden (2002). "Caging of Particles in One-Component Plasmas". In: *Phys. Rev. Lett.* 88 (22), p. 225001. DOI: 10.1103/PhysRevLett.88.225001.

Donkó, Z., G. J. Kalman, P. Hartmann, et al. (2003). "Dynamical Structure Functions, Collective Modes, and Energy Gap in Charged-Particle Bilayers". In: *Phys. Rev. Lett.* 90 (22), p. 226804. DOI: 10.1103/PhysRevLett.90.226804.

Dornheim, T. et al. (2018). "Ab initio Path Integral Monte Carlo Results for the Dynamic Structure Factor of Correlated Electrons: From the Electron Liquid to Warm Dense Matter". In: *Phys. Rev. Lett.* 121 (25), p. 255001. DOI: 10.1103/PhysRevLett.121.255001.

DuBois, D. F., V. Gilinsky, and M. G. Kivelson (1962). "Collision Damping of Plasma Oscillations". In: *Physical Review Letters* 8.11, pp. 419–421. DOI: 10.1103/PhysRevLett.8.419.

Fano, U. (1961). "Effects of Configuration Interaction on Intensities and Phase Shifts". In: *Phys. Rev.* 124 (6), pp. 1866–1878. DOI: 10.1103/PhysRev.124.1866.

Fano, U. (1935). "Sullo spettro di assorbimento dei gas nobili presso il limite dello spettro d'arco". In: *Il Nuovo Cimento (1924-1942)* 12.3, pp. 154–161. ISSN: 1827-6121. DOI: 10.1007/BF02958288.

Felde, A. vom, J. Sprösser-Prou, and J. Fink (1989). "Valence-electron excitations in the alkali metals". In: *Phys. Rev. B* 40 (15), pp. 10181–10193. DOI: 10.1103/PhysRevB.40.10181.

Fortov, V. E. et al. (2005). "Complex (dusty) plasmas: Current status, open issues, perspectives". In: *Physics Reports* 421.1, pp. 1–103. ISSN: 0370-1573. DOI: https://doi.org/10.1016/j.physrep.2005.08.007.

Geim, A. K. and I. V. Grigorieva (2013). "Van der Waals heterostructures". In: *Nature* 499.7459, pp. 419–425. ISSN: 0028-0836. DOI: 10.1038/nature12385.

Gell-Mann, M. and K. A. Brueckner (1957). "Correlation Energy of an Electron Gas at High Density". In: *Phys. Rev.* 106 (2), pp. 364–368. DOI: 10.1103/PhysRev.106.364.

Gericke, D. O. et al. (2010). "Structural properties of warm dense matter". In: *Journal of Physics: Conference Series* 220.1, p. 012001.

Giammichele, N. et al. (2018). "A large oxygen-dominated core from the seismic cartography of a pulsating white dwarf". In: *Nature* 554.7690, pp. 73–76. DOI: 10.1038/nature25136.

Giuliani, G. and G. Vignale (2005). *Quantum Theory of the Electron Liquid*. Cambridge: Cambridge University Press, p. 777. ISBN: 9780511619915. DOI: 10.1017/CBO9780511619915.

Glenzer, S. H., O. L. Landen, et al. (2007). "Observations of Plasmons in Warm Dense Matter". In: *Phys. Rev. Lett.* 98 (6), p. 065002. DOI: 10.1103/PhysRevLett.98.065002.

Glenzer, S. H. and R. Redmer (2009). "X-ray Thomson scattering in high energy density plasmas". In: *Rev. Mod. Phys.* 81 (4), pp. 1625–1663. DOI: 10.1103/RevModPhys.81.1625.

Golden, K. I. (2018). "Higher-order fluctuation-dissipation relations in plasma physics: Binary Coulomb systems". In: *Phys. Rev. E* 97 (5), p. 052104. DOI: 10.1103/PhysRevE.97.052104.

Golden, K. I., F. Green, and D. Neilson (1985a). "Dynamical theory of binary ionic mixtures". In: *Phys. Rev. A* 31 (5), pp. 3529–3532. DOI: 10.1103/PhysRevA.31.3529.

— (1985b). "Nonlinear-response-function approach to binary ionic mixtures: Dynamical theory". In: *Phys. Rev. A* 32 (3), pp. 1669–1692. DOI: 10.1103/PhysRevA.32.1669.

Golden, K. I. and J. T. Heath (2016a). "Erratum to: Generalized Nonlinear Fluctuation-Dissipation Relation for the One-Component Plasma". In: *Journal of Statistical Physics* 163.1, pp. 210–210. ISSN: 0022-4715. DOI: 10.1007/s10955-016-1454-7.

— (2016b). "Generalized Nonlinear Fluctuation-Dissipation Relation for the One-Component Plasma". In: *Journal of Statistical Physics* 162.1, pp. 199–217. ISSN: 0022-4715. DOI: 10.1007/s10955-015-1395-6.

Golden, K. I. and G. Kalman (1982). "Plasma response functions, fluctuation-dissipation relations and the velocity-average-approximation". In: *Annals of Physics* 143.1, pp. 160–178. ISSN: 0003-4916. DOI: https://doi.org/10.1016/0003-4916(82)90217-2.

Golden, K. I. and G. J. Kalman (1969). "The electrodynamics and statistical mechanics of linear plasma response functions". In: *Journal of Statistical Physics* 1.3, pp. 415–466. ISSN: 1572-9613. DOI: 10.1007/BF01106580.

— (1979). "Approximation scheme for strongly coupled plasmas: Dynamical theory". In: *Phys. Rev. A* 19 (5), pp. 2112–2128. DOI: 10.1103/PhysRevA.19.2112.

— (2000). "Quasilocalized charge approximation in strongly coupled plasma physics". In: *Phys. Plasmas* 7.1, pp. 14–32. DOI: 10.1063/1.873814.

— (2001). "Erratum: "Quasilocalized charge approximation in strongly coupled plasma physics" [Phys. Plasmas 7, 14 (2000)]". In: *Physics of Plasmas* 8.11, pp. 5064–5064. DOI: 10.1063/1.1408622. eprint: https://doi.org/10.1063/1.1408622.

Golden, K. I., G. J. Kalman, P. Hartmann, et al. (2012). "Collective Modes in Classical Mass–Asymmetric Bilayers". In: *Contributions to Plasma Physics* 52.2, pp. 130–134. DOI: 10.1002/ctpp.201100068.

Golden, K. I., G. J. Kalman, and M. B. Silevitch (1972). "Nonlinear fluctuation-dissipation theorem". In: *Journal of Statistical Physics* 6.2-3, pp. 87–118. DOI: 10.1007/BF01023681.

— (1974). "New Approach to a Strongly Coupled Electron Plasma". In: *Phys. Rev. Lett.* 33 (26), pp. 1544–1547. DOI: 10.1103/PhysRevLett.33.1544.

Golden, K. I., G. J. Kalman, and L. G. Silvestri (2018). "Is the Vlasov equation valid for Yukawa plasmas?" In: *Physical Sciences and Technology* 4.1, pp. 9–14.

Golden, K. I., H. Mahassen, G. J. Kalman, et al. (2005). "Dielectric matrix and plasmon dispersion in strongly coupled electronic bilayer liquids". In: *Phys. Rev. E* 71 (3), p. 036401. DOI: 10.1103/PhysRevE.71.036401.

Golden, K. I., H. Mahassen, G. Senatore, et al. (2006). "Transverse dielectric matrix and shear mode dispersion in strongly coupled electronic bilayer liquids". In: *Phys. Rev. E* 74 (5), p. 056405. DOI: 10.1103/PhysRevE.74.056405.

Golden Kenneth I. and De-xin, L. (1982). "Dynamical three-point correlations and quadratic response functions in binary ionic mixture plasmas". In: *Journal of Statistical Physics* 29.2, pp. 281–307. ISSN: 1572-9613. DOI: 10.1007/BF01020787.

Goodman, B. and A. Sjölander (1973). "Application of the Third Moment to the Electric and Magnetic Response Function". In: *Phys. Rev. B* 8 (1), pp. 200–214. DOI: 10.1103/PhysRevB.8.200.

Grad, H. (1969). "Plasmas". In: *Phys. Today* 22.12, pp. 34–44. ISSN: 0031-9228. DOI: 10.1063/1.3035293.

Guernsey, R. L. (1962). "Kinetic Equation for a Completely Ionized Gas". In: *Physics of Fluids* 5.3, p. 322. ISSN: 00319171. DOI: 10.1063/1.1706617.

Haack, J. R., C. D. Hauck, and M. S. Murillo (2017). "A Conservative, Entropic Multispecies BGK Model". In: *J. Stat. Phys.* 168.4, pp. 826–856. DOI: 10.1007/s10955-017-1824-9.

Hansen, J.-P. (1973). "Statistical Mechanics of Dense Ionized Matter. I. Equilibrium Properties of the Classical One-Component Plasma". In: *Phys. Rev. A* 8 (6), pp. 3096–3109. DOI: 10.1103/PhysRevA.8.3096.

Hansen, J.-P. and I. R. McDonald (2013). *Theory of Simple Liquids*. Elsevier, p. 619. ISBN: 9780123870322. DOI: 10.1016/C2010-0-66723-X.

Hansen, J.-P., I. R. McDonald, and E. L. Pollock (1975). "Statistical mechanics of dense ionized matter. III. Dynamical properties of the classical one-component plasma". In: *Phys. Rev. A* 11 (3), pp. 1025–1039. DOI: 10.1103/PhysRevA.11.1025.

Hansen, J.-P., I. R. McDonald, and P. Vieillefosse (1979). "Statistical mechanics of dense ionized matter. VIII. Dynamical properties of binary ionic mixtures". In: *Phys. Rev. A* 20 (6), pp. 2590–2602. DOI: 10.1103/PhysRevA.20.2590.

Hartmann, P., Z. Donkó, et al. (2009). "Collective Dynamics of Complex Plasma Bilayers". In: *Phys. Rev. Lett.* 103 (24), p. 245002. DOI: 10.1103/PhysRevLett.103.245002.

Hartmann, P., G. J. Kalman, et al. (2009). "Collective excitations in strongly coupled ultra-relativistic plasmas". In: *Journal of Physics A: Mathematical and Theoretical* 42.21, p. 214018. DOI: 10.1088/1751-8113/42/21/214018.

Haxhimali, T. et al. (2014). "Diffusivity in asymmetric Yukawa ionic mixtures in dense plasmas". In: *Phys. Rev. E* 90 (2), p. 023104. DOI: 10.1103/PhysRevE.90.023104.

— (2015). "Shear viscosity for dense plasmas by equilibrium molecular dynamics in asymmetric Yukawa ionic mixtures". In: *Phys. Rev. E* 92 (5), p. 053110. DOI: 10.1103/PhysRevE.92.053110.

Hockney, R. and J. Eastwood (1981). *Computer Simulation Using Particles*. Advanced book program: Addison-Wesley. McGraw-Hill. ISBN: 9780070291089.

Höll, A. et al. (2004). "X-ray Thomson scattering in warm dense matter". In: *The European Physical Journal D - Atomic, Molecular, Optical and Plasma Physics* 29.2, pp. 159–162. DOI: 10.1140/epjd/e2004-00059-5.

Horowitz, C. J., A. S. Schneider, and D. K. Berry (2010). "Crystallization of Carbon-Oxygen Mixtures in White Dwarf Stars". In: *Phys. Rev. Lett.* 104 (23), p. 231101. DOI: 10.1103/PhysRevLett.104.231101.

Hughto, J. et al. (2012). "Direct molecular dynamics simulation of liquid-solid phase equilibria for a three-component plasma". In: *Phys. Rev. E* 86 (6), p. 066413. DOI: 10.1103/PhysRevE.86.066413.

Ichimaru, S. (2004a). *Statistical Plasma Physics, Volume I: Basic Principles*. Westview Press, p. 408. ISBN: 9780429497155.

— (2004b). *Statistical Plasma Physics, Volume II: Condensed Plasmas*. Westview Press, p. 304. ISBN: 9780813341798.

Ichimaru, S., H. Iyetomi, and S. Ogata (1988). "Freezing transition and phase diagram of dense carbon-oxygen mixtures in white dwarfs". In: *The Astrophysics Journal Letters* 334, pp. L17–L20. DOI: 10.1086/185303.

Ichimaru, S., S. Mitake, et al. (1985). "Theory of interparticle correlations in dense, high-temperature plasmas. I. General formalism". In: *Phys. Rev. A* 32 (3), pp. 1768–1774. DOI: 10.1103/PhysRevA.32.1768.

Igarashi, T., N. Nakao, and H. Iyetomi (2001). "Chemical Stability of Binary Coulomb Compounds". In: *Contributions to Plasma Physics* 41.4, pp. 319–322. DOI: 10.1002/1521-3986(200107)41:4<319::AID-CTPP319>3.0.CO;2-J.

Igarashi, T. and H. Iyetomi (2003). "Phase characteristics and elastic properties of binary Coulomb compounds". In: *Journal of Physics A: Mathematical and General* 36.22, p. 6197.

Joe, Y. S., A. M. Satanin, and C. S. Kim (2006). "Classical analogy of Fano resonances". In: *Phys. Scr.* 74.2, pp. 259–266. ISSN: 0031-8949. DOI: 10.1088/0031-8949/74/2/020.

Jones, H. B. (1870). eng. In: *The life and letters of Faraday*. London Longmans, Green, pp. 215–217.

Kählert, H., G. J. Kalman, and M. Bonitz (2014). "Dynamics of strongly correlated and strongly inhomogeneous plasmas". In: *Phys. Rev. E* 90 (1), p. 011101. DOI: 10.1103/PhysRevE.90.011101.

— (2015). "Linear Fluid Theory for Weakly Inhomogeneous Plasmas with Strong Correlations". In: *Contributions to Plasma Physics* 55.5, pp. 352–359. DOI: 10.1002/ctpp.201400085.

Kalman, G. J., Z. Donkó, et al. (2011). "Strong Coupling Effects in Binary Yukawa Systems". In: *Phys. Rev. Lett.* 107 (17), p. 175003. DOI: 10.1103/PhysRevLett.107.175003.

Kalman, G. J. and K. I. Golden (1984). "Theory of partial response functions in multicomponent plasmas". In: *Phys. Rev. A* 29 (2), pp. 844–853. DOI: 10.1103/PhysRevA.29.844.

— (1990). "Response function and plasmon dispersion for strongly coupled Coulomb liquids". In: *Phys. Rev. A* 41 (10), pp. 5516–5527. DOI: 10.1103/PhysRevA.41.5516.

— (1998). "Energy gap in the bilayer: Understanding the failure of the Singwi-Tosi-Land-Sjolander approximation". In: *Phys. Rev. B* 57 (15), pp. 8834–8837. DOI: 10.1103/PhysRevB.57.8834.

Kalman, G. J., K. I. Golden, Z. Donkó, et al. (2005). "The quasilocalized charge approximation". In: *Journal of Physics: Conference Series* 11.1, p. 254.

Kalman, G. J., K. I. Golden, and L. G. Silvestri (2016). "Correlation induced out-of-phase plasmon in an electron liquid". In: arXiv: 1609.09029.

Kalman, G. J., P. Hartmann, Z. Donkó, and K. I. Golden (2007). "Collective Excitations in Electron-Hole Bilayers". In: *Phys. Rev. Lett.* 98 (23), p. 236801. DOI: 10.1103/PhysRevLett.98.236801.

Kalman, G. J., P. Hartmann, Z. Donkó, K. I. Golden, and S. Kyrkos (2013). "Collective modes in two-dimensional binary Yukawa systems". In: *Phys. Rev. E* 87 (4), p. 043103. DOI: 10.1103/PhysRevE.87.043103.

Kalman, G. J., P. Hartmann, K. I. Golden, et al. (2010). "Correlational origin of the roton minimum". In: *EPL (Europhysics Letters)* 90, p. 55002. DOI: 10.1209/0295-5075/90/55002. arXiv: 1002.3516.

Kalman, G. J., K. Kempa, and M. Minella (1991). "Dynamical correlation effects in alkali metals". In: *Phys. Rev. B* 43 (17), pp. 14238–14240. DOI: 10.1103/PhysRevB.43.14238.

Kalman, G. J., S. Kyrkos, et al. (2012). "The Roton Minimum: Is it a General Feature of Strongly Correlated Liquids?" In: *Contributions to Plasma*

Physics 52.3, pp. 219–223. DOI: 10.1002/ctpp.201100095. eprint: https://onlinelibrary.wiley.com/doi/pdf/10.1002/ctpp.201100095.

Kalman, G. J., M. Rosenberg, and H. E. DeWitt (2000). "Collective Modes in Strongly Correlated Yukawa Liquids: Waves in Dusty Plasmas". In: *Phys. Rev. Lett.* 84 (26), pp. 6030–6033. DOI: 10.1103/PhysRevLett.84.6030.

Kalman, G. J., V. Valtchinov, and K. I. Golden (1999). "Collective Modes in Strongly Coupled Electronic Bilayer Liquids". In: *Phys. Rev. Lett.* 82 (15), pp. 3124–3127. DOI: 10.1103/PhysRevLett.82.3124.

— (2003). "Erratum: Collective Modes in Strongly Coupled Electronic Bilayer Liquids [Phys. Rev. Lett. 82, 003124 (1999)]". In: *Phys. Rev. Lett.* 91 (15), p. 159901. DOI: 10.1103/PhysRevLett.91.159901.

Kalman, G., Z. Donkó, et al. (2014). "Second plasmon and collective modes in binary Coulomb systems". In: *EPL (Europhysics Letters)* 107.3, p. 35001.

Kamenev, A. and Y. Oreg (1995). "Coulomb drag in normal metals and superconductors: Diagrammatic approach". In: *Phys. Rev. B* 52 (10), pp. 7516–7527. DOI: 10.1103/PhysRevB.52.7516.

Khrapak, S. A. and H. M. Thomas (2015). "Fluid approach to evaluate sound velocity in Yukawa systems and complex plasmas". In: *Phys. Rev. E* 91 (3), p. 033110. DOI: 10.1103/PhysRevE.91.033110.

Killian, T. C. et al. (2007). "Ultracold neutral plasmas". In: *Physics Reports* 449.4, pp. 77–130. ISSN: 0370-1573. DOI: https://doi.org/10.1016/j.physrep.2007.04.007.

Korolov, I. et al. (2015). "The Dynamical Structure Function of the One-Component Plasma Revisited". In: *Contributions to Plasma Physics* 55.5, pp. 421–427. ISSN: 1521-3986. DOI: 10.1002/ctpp.201400098.

Kreil, D. et al. (2018). "Resonant and anti-resonant modes of the dilute, spin-inbalanced, two-dimensional electron liquid including correlations". EN. In: *Contributions to Plasma Physics* 58.2-3. ISSN: 1521-3986. DOI: 10.1002/ctpp.201700147.

Kubo, R. (1957). "Statistical-Mechanical Theory of Irreversible Processes. I. General Theory and Simple Applications to Magnetic and Conduction Problems". In: *Journal of the Physical Society of Japan* 12.6, pp. 570–586. ISSN: 0031-9015. DOI: 10.1143/JPSJ.12.570.

Kubo, R., M. Yokota, and S. Nakajima (1957). "Statistical-Mechanical Theory of Irreversible Processes. II. Response to Thermal Disturbance". In: *Journal of the Physical Society of Japan* 12.11, pp. 1203–1211. ISSN: 0031-9015. DOI: 10.1143/JPSJ.12.1203.

Landau, L. D. (1965a). "ON THE VIBRATIONS OF THE ELECTRONIC PLASMA". In: *Collected Papers L.D. Landau*. Ed. by D. ter Haar. Pergamon, pp. 445–460. ISBN: 9780080105864. DOI: 10.1016/B978-0-08-010586-4.50066-3.

— (1965b). "THE TRANSPORT EQUATION IN THE CASE OF COULOMB INTERACTIONS". In: *Collected Papers L.D. Landau*. Ed. by D. ter Haar. Pergamon, pp. 163–170. ISBN: 9780080105864. DOI: 10.1016/B978-0-08-010586-4.50029-8.

Lenard, A. (1960). "On Bogoliubov's kinetic equation for a spatially homogeneous plasma". In: *Ann. Phys. (N. Y).* 10.3, pp. 390–400. ISSN: 0003-4916. DOI: 10.1016/0003-4916(60)90003-8.

Liboff, R. L. (2003). *Kinetic Theory.* Graduate Texts in Contemporary Physics. New York: Springer-Verlag, pp. XX, 572. ISBN: 0-387-95551-8. DOI: 10.1007/b97467.

Liu, L. et al. (1996). "Static and dynamic properties of coupled electron-electron and electron-hole layers". In: *Phys. Rev. B* 53 (12), pp. 7923–7931. DOI: 10.1103/PhysRevB.53.7923.

Magyar, P. et al. (2016). "Factorization of 3-Point Static Structure Functions in 3D Yukawa Liquids". In: *Contributions to Plasma Physics* 56.9, pp. 816–829. ISSN: 08631042. DOI: 10.1002/ctpp.201500062.

Mahassen, H. et al. (2006). "Longitudinal collective modes in asymmetric charged-particle bilayers". In: *Journal of Physics A: Mathematical and General* 39.17, p. 4601.

Martin, P. C. (1967). "Sum Rules, Kramers-Kronig Relations, and Transport Coefficients in Charged Systems". In: *Phys. Rev.* 161 (1), pp. 143–155. DOI: 10.1103/PhysRev.161.143.

Merlino, R. L. and J. A. Goree (2004). "Dusty Plasmas in the Laboratory, Industry, and Space". In: *Physics Today* 57.7, pp. 32–38. DOI: 10.1063/1.1784300.

Miroshnichenko, A. E., S. Flach, and Y. S. Kivshar (2010). "Fano resonances in nanoscale structures". In: *Rev. Mod. Phys.* 82.3, pp. 2257–2298. ISSN: 0034-6861. DOI: 10.1103/RevModPhys.82.2257.

Mithen, J. P., J. Daligault, B. J. B. Crowley, et al. (2011). "Density fluctuations in the Yukawa one-component plasma: An accurate model for the dynamical structure factor". In: *Phys. Rev. E* 84 (4), p. 046401. DOI: 10.1103/PhysRevE.84.046401.

Mithen, J. P., J. Daligault, and G. Gregori (2011). "Extent of validity of the hydrodynamic description of ions in dense plasmas". In: *Phys. Rev. E* 83 (1), p. 015401. DOI: 10.1103/PhysRevE.83.015401.

Morfill, G. E. and A. V. Ivlev (2009). "Complex plasmas: An interdisciplinary research field". In: *Rev. Mod. Phys.* 81 (4), pp. 1353–1404. DOI: 10.1103/RevModPhys.81.1353.

Murillo, M. S. (2010). "X-ray Thomson scattering in warm dense matter at low frequencies". In: *Phys. Rev. E* 81 (3), p. 036403. DOI: 10.1103/PhysRevE.81.036403.

Narozhny, B. N. and A. Levchenko (2016). "Coulomb drag". In: *Rev. Mod. Phys.* 88 (2), p. 025003. DOI: 10.1103/RevModPhys.88.025003.

Neilson, D. et al. (1993). "Excitations of the strongly correlated electron liquid in coupled layers". In: *Phys. Rev. Lett.* 71 (24), pp. 4035–4038. DOI: 10.1103/PhysRevLett.71.4035.

Nozières, P. and D. Pines (1958). "Electron Interaction in Solids. General Formulation". In: *Phys. Rev.* 109 (3), pp. 741–761. DOI: 10.1103/PhysRev.109.741.

Nyquist, H. (1928). "Thermal Agitation of Electric Charge in Conductors". In: *Phys. Rev.* 32 (1), pp. 110–113. DOI: 10.1103/PhysRev.32.110.

Oberman, C., A. Ron, and J. Dawson (1962). "High-Frequency Conductivity of a Fully Ionized Plasma". In: *Physics of Fluids* 5.12, p. 1514. ISSN: 00319171. DOI: 10.1063/1.1706560.

Ogasawara, M. (1963). "Collisional Damping of Plasma Oscillation". In: *Journal of the Physical Society of Japan* 18.7, pp. 1066–1073. ISSN: 0031-9015. DOI: 10.1143/JPSJ.18.1066.

Peng, F., E. F. Brown, and J. W. Truran (2007). "Sedimentation and Type I X-Ray Bursts at Low Accretion Rates". In: *The Astrophysical Journal* 654.2, p. 1022.

Pines, D. and D. Bohm (1952). "A Collective Description of Electron Interactions: II. Collective vs Individual Particle Aspects of the Interactions". In: *Phys. Rev.* 85 (2), pp. 338–353. DOI: 10.1103/PhysRev.85.338.

Pogrebinskii, M. B. (1977). "Mutual drag of carriers in a semiconductor-insulator-semiconductor system". In: *Soviet Physics-Semiconductors* 11.4, pp. 372–376.

Pollock, E. L. and J.-P. Hansen (1973). "Statistical Mechanics of Dense Ionized Matter. II. Equilibrium Properties and Melting Transition of the Crystallized One-Component Plasma". In: *Phys. Rev. A* 8 (6), pp. 3110–3122. DOI: 10.1103/PhysRevA.8.3110.

Ranganathan, S. and R. E. Johnson (2004). "Plasmon modes and energy gap in electronic bilayers". In: *Phys. Rev. B* 69, p. 085310. DOI: 10.1103/PhysRevB.69.085310.

— (2006). "Phase diagram of classical electronic bilayers". In: *J. Phys. A Math. Theor.* 39, pp. 4595–4600. DOI: 10.1088/0305-4470/39/17/S44.

— (2008). "Asymmetric electron bilayer: A molecular dynamics study of correlations and diffusion". In: *Phys. Rev. B* 78, p. 195323. DOI: 10.1103/PhysRevB.78.195323.

Rojo, A. G. (1999). "Electron-drag effects in coupled electron systems". In: *Journal of Physics: Condensed Matter* 11.5, R31–R52. ISSN: 0953-8984. DOI: 10.1088/0953-8984/11/5/004.

Rosenberg, M. and G. J. Kalman (1997). "Dust acoustic waves in strongly coupled dusty plasmas". In: *Phys. Rev. E* 56 (6), pp. 7166–7173. DOI: 10.1103/PhysRevE.56.7166.

Salin, G. (2007). "Hydrodynamic limit of the Yukawa one-component plasma". In: *Physics of Plasmas* 14.8, p. 082316. DOI: 10.1063/1.2759881. eprint: http://dx.doi.org/10.1063/1.2759881.

Salpeter, E. E. (1954). "Electron Screening and Thermonuclear Reactions". In: *Aust. J. Phys.* 7.3, p. 373. ISSN: 0004-9506. DOI: 10.1071/PH540373.

Sawada, K. et al. (1957). "Correlation Energy of an Electron Gas at High Density: Plasma Oscillations". In: *Phys. Rev.* 108 (3), pp. 507–514. DOI: 10.1103/PhysRev.108.507.

Schneider, A. S. et al. (2012). "Direct molecular dynamics simulation of liquid-solid phase equilibria for two-component plasmas". In: *Phys. Rev. E* 85 (6), p. 066405. DOI: 10.1103/PhysRevE.85.066405.

Selwyn, G. S., J. Singh, and R. S. Bennett (1989). "*In situ* laser diagnostic studies of plasma-generated particulate contamination". In: *Journal of Vacuum Sci-*

ence & Technology A: Vacuum, Surfaces, and Films 7.4, pp. 2758–2765. ISSN: 0734-2101. DOI: 10.1116/1.576175.

Singwi, K. S., A. Sjölander, et al. (1969). "Electron correlations at metallic densities - III". In: *Solid State Communications* 7.20, pp. 1503–1505. ISSN: 0038-1098. DOI: https://doi.org/10.1016/0038-1098(69)90030-1.

— (1970). "Electron Correlations at Metallic Densities. IV". In: *Phys. Rev. B* 1 (3), pp. 1044–1053. DOI: 10.1103/PhysRevB.1.1044.

Singwi, K. S., M. P. Tosi, et al. (1968). "Electron Correlations at Metallic Densities". In: *Phys. Rev.* 176 (2), pp. 589–599. DOI: 10.1103/PhysRev.176.589.

Slattery, W. L., G. D. Doolen, and H. E. DeWitt (1980). "Improved equation of state for the classical one-component plasma". In: *Phys. Rev. A* 21 (6), pp. 2087–2095. DOI: 10.1103/PhysRevA.21.2087.

Stanton, L. G. and M. S. Murillo (2016). "Ionic transport in high-energy-density matter". In: *Phys. Rev. E* 93 (4), p. 043203. DOI: 10.1103/PhysRevE.93.043203.

Strickler, T. S. et al. (2016). "Experimental Measurement of Self-Diffusion in a Strongly Coupled Plasma". In: *Phys. Rev. X* 6 (2), p. 021021. DOI: 10.1103/PhysRevX.6.021021.

Stringfellow, G. S., H. E. DeWitt, and W. L. Slattery (1990). "Equation of state of the one-component plasma derived from precision Monte Carlo calculations". In: *Phys. Rev. A* 41 (2), pp. 1105–1111. DOI: 10.1103/PhysRevA.41.1105.

Świerkowski, L., D. Neilson, and J. Szymański (1993). "Electron liquid in double-layer structures." In: *Australian Journal of Physics* 46, p. 423. DOI: 10.1071/PH930423.

Szyma ński, J., L. Świerkowski, and D. Neilson (1994). "Correlations in coupled layers of electrons and holes". In: *Phys. Rev. B* 50 (15), pp. 11002–11007. DOI: 10.1103/PhysRevB.50.11002.

The Plasma Dispersion Function (1961). Elsevier, p. 426. ISBN: 9781483229294. DOI: 10.1016/C2013-0-12176-9.

Thiele, R. et al. (2008). "Plasmon resonance in warm dense matter". In: *Phys. Rev. E* 78 (2), p. 026411. DOI: 10.1103/PhysRevE.78.026411.

Thomson, J. J. (1897). "Cathode Rays". In: *Philosophical Magazine*. 5th ser. 44.269, pp. 293–316. DOI: 10.1080/14786449708621070. eprint: https://doi.org/10.1080/14786449708621070.

Ticknor, C. et al. (2016). "Transport properties of an asymmetric mixture in the dense plasma regime". In: *Phys. Rev. E* 93 (6), p. 063208. DOI: 10.1103/PhysRevE.93.063208.

Tonks, L. (1967). "The Birth of "Plasma"". In: *American Journal of Physics* 35.9, pp. 857–858. DOI: 10.1119/1.1974266.

Tonks, L. and I. Langmuir (1929). "Oscillations in Ionized Gases". In: *Phys. Rev.* 33 (2), pp. 195–210. DOI: 10.1103/PhysRev.33.195.

Vashishta, P. and K. S. Singwi (1972). "Electron Correlations at Metallic Densities. V". In: *Phys. Rev. B* 6 (3), pp. 875–887. DOI: 10.1103/PhysRevB.6.875.

Vlasov, A. A. (1938). "The vibrational properties of an electron gas". In: *Zh. Eksp. Theor. Fiz.* 8.3. (in Russian), p. 291.

Vlasov, A. A. (1967). “The vibrational properties of an electron gas”. In: *Usp. Fiz. Nauk* 93.11. (in Russian), pp. 444–470. DOI: 10.3367/UFNr.0093.196711f.0444.

— (1968). “The vibrational properties of an electron gas”. In: *Phys. Usp.* 10.6. (English Translation), pp. 721–733. DOI: 10.1070/PU1968v010n06ABEH003709.

Whitley, H. D. et al. (2015). “ Localization and Screening Enhancement in Asymmetric Binary Ionic Mixtures”. In: *Contributions to Plasma Physics* 55.5, pp. 413–420.